Direct Numerical Simulation and Modelling of Thermodiffusively-Unstable Lean Premixed Hydrogen Flames for Carbon-Free Internal Combustion Engines

Edward Frederick Hunt

School of Engineering

Newcastle University

Doctor of Philosophy

January 2025

Abstract

Thermodiffusively (TD) unstable lean hydrogen flames, a promising alternative to the combustion of hydrocarbons, have been studied using direct numerical simulation with complex chemistry over a wide range of reactant and turbulent conditions to develop a better understanding of the fundamental behaviour of TD-unstable flames, with a specific focus on the flame speed, which will be used to inform turbulent flame speed models used for device scale simulations.

Firstly the thesis investigates the fundamental behaviour of the TD-instability for 3-dimensional laminar freely-propagating flames over a wide range of reactant conditions. It is shown that the instability parameter ω_2 extends well to 3-dimensions and a model is proposed that has good predictive capabilities for local flame acceleration and thinning arising from the reactant conditions.

Next, the work is extended to turbulent flames at a scale over a wide range of reactant and turbulent conditions. It is found that turbulence intensifies the TD-response and is found that the mean local flame speed scales well. This the square-root of the Karlovitz number, provided the laminar TD-instability is accounted for using ω_2.

Next, the integral length scale as well as the Karlovitz number over a range of reactant conditions are considered to evaluate the combined effect of reactant conditions, turbulent intensity and length scale on both the local and global flame statistics with a focus on the turbulent flame speed. It is found that length scale does not effect the local flame statistics, but does effect the global flame statistics where the turbulent flame speed adheres to Damköhler's small scale limit.

Lastly, a method for a well resolved (DNS-style) G-equation capable of simulating TD-unstable flames is proposed and presented, which could be used in future studies to simulate larger domains due to its lower computational cost.

Acknowledgements

Firstly I would like to acknowledge my PhD supervisor Dr. Andrew Aspden. The advice, support and opportunities he has provided me have resulted in a thesis and papers of which I am truly proud. Andy is an outstanding researcher and mentor with a strong focus on high quality research and novel ideas, it has been a true privilege to work with and learn from him and I am forever grateful.

I would like to thank both the Engineering and Physical Sciences Research Council and Realis simulation (formerly Ricardo Software) for their financial support through this Industrial CASE studentship.

I would like to give special thanks to Dr. Thomas Howarth (RWTH Aachen University) whom I thank for countless discussions, the development of interesting ideas, debugging code and double checking my mathematics, it has been a pleasure to work with him and I hope to continue our work in the future.

I would like to give a thanks to Dr. Charles Turquand d'Auzay for his support, mentorship and guidance on the industrial side of the PhD, it has been a pleasure working with him. I also would like to acknowledge Drs Evgeniy Shapiro and Ignacio Hernandez (Realis simulation) for their support. I also acknowledge Dr. Marcus Day (National Renewable Energy Laboratory) for discussion and feedback on research in addition guidance on programming related issues within the AMReX framework.

I would like to thank Newcastle University for their support and facilities, Rocket (Newcastle University's HPC facility) has been an essential tool used throughout my work. I would also like to acknowledged the UK Consortium on Turbulent Reacting Flows for providing access and compute resources on the EPSRC's HPC facility Archer2.

I dedicate this work to my wife Lydia, whom without her unwavering support this work would not have been possible.

Contents

List of Figures

List of Tables

Chapter 1. Introduction

The combustion of hydrocarbons in the form of fossil fuels has been the backbone of society since the industrial revolution. Fossil fuels have become essential to almost every aspect of modern life, from transportation to food production. Despite the benefits to society, the combustion of hydrocarbons has significant and severe effects on global and local climate as well as human and environmental health [11]. It is now widely accepted that a swift transition away from fossil fuels is essential, and significant global research, innovation and societal change is required to facilitate the green energy transition.

There are many potential alternatives to burning hydrocarbons; clean electrification has formed a central component of the energy transition, with promising uses and adoption in heating, passenger vehicles and public transportation; in recent years there has even been some adoption for electric heavy-goods vehicles (HGVs) [84]. However, there are several disadvantages to electrification. Firstly the required infrastructure development required to supply clean renewable energy at a high demand is a challenge, which can be even more difficult in rural areas [128]. This challenge becomes even more complex in developing countries or countries that are large energy importers with limited space for renewable energy generation. There are still around 1.4billion (2011) people lacking access to electricity [26]. Additionally, some industrial processes and transport (such as long-hall flights and maritime transport) do not have a clear path to electrification, with some major hurdles still to overcome. The energy intensive, typically polluting process of mining and manufacturing large batteries has significant environmental impacts which currently disproportionately effects developing nations [155].

It is the view of the author that it is likely that to fully decarbonise and achieve net-zero, electrification alone will not suffice. Therefore, significant effort to investigate alternatives have been explored. The most promising options involve burning liquid fuels or gasses which have a net-zero carbon release. Examples of these include biofuels (see [69] for review), ammonia (see [175] for review) and the focus on this project, hydrogen. Hydrogen is a carbon-free fuel with a high energy density that can be used as a clean energy carrier and

allows the combination of electricity, heating and transportation into a single energy market [95]. Naturally, hydrogen combustion is a promising substitute for carbon emitting traditional fuels for transport, heating and re-electrification [177]. Due to the unique characteristics of hydrogen, its combustion can be performed lean, resulting in the stable operation at lower combustion temperatures, significantly reducing NO_x [64] which is a pollutant harmful for humans and the environment [37]. However, lean hydrogen can be thermodiffusivly (TD) unstable. The flame physics during combustion are different than traditional fuels which can result in hotter and faster flames than would usually be expected. Therefore, a better understanding of the underlying physics of hydrogen and modification of the models used to develop hydrogen combustors to facilitate future global adoption [161].

1.1 Device Scale Simulations and the Scope of Direct Numerical Simulations

Typically, engine (combustor) designers heavily utilise simulations; namely computational-fluid-dynamics to perform design tasks. It is important that the simulation codes achieve answers quickly with minimal computational costs. A great deal of small scale physics cannot be directly computed from fundamental equations of motion and chemical kinetics, thus models must be used to approximate the large scale effects of the small scale physics. The more accurate the model, the more useful to designers the code will be. One of the key values to calculate is the consumption based turbulent flame speed (the speed of which the flame burns fuel). This global value depends entirely on the small scale physics, and how turbulence and chemistry interact, which cannot be calculated at the device scales hence, a model must be used. This becomes increasingly challenging with TD-unstable hydrogen flames, which typically deviate from the well understood physics used in existing turbulent flame speed models. Existing turbulent flame speed models have been developed mostly with traditional carbon-based fuels in-mind, which are TD-stable. TD-unstable flames which often burn hotter and faster than their stable counterparts result in inaccurate turbulent flame speed predictions from traditional turbulent flame speed models. This project studies TD-unstable flames to gain better insight into the fundamental physics of a TD-unstable hydrogen flames to propose modifications to turbulent flame speed models. There are two historically appropriate ways to study the fundamental physics of flames, experimentally (typically with a bunsen

flame) or numerically utilising direct numerical simulations. Experiments, despite being able to study real world effects, often lack the ability to study the small scales behaviours which enhance our understanding of the underlying physics. This project focuses on using DNS to study the underlying flame physics.

DNS is a method of performing numerical simulations where all turbulent scales are resolved on the computational grid from the large integral scale to the small Kolmogorov micro-scales, therefore no turbulence modelling is required. Combustion follows a similar philosophy where the flame scales must also be resolved. For DNS of reacting flows, both the turbulence and the flame have to be fully resolved. For turbulence, the grid size must be sufficient to resolve the smallest scale with a domain size large enough to capture the larger turbulent length scale. As turbulent intensity increases the smallest scales that need to be resolved decrease, which will increase the computational cost of the simulation [139]. Additionally, pressure decreases the flame scale which then requires a finer computational grid to resolve the flame. Thus highly turbulent flames at pressure (which is typical for most combustors) require significant computational expenditure and cannot be undertaken at device scales. A practical example of this is shown in Figure 1.1 which shows the surface of a turbulent hydrogen flame (burning out towards the reader) using DNS at high pressure (40 atm). The flame has a domain width of only 0.8 mm and consists of 768 computation cells across the domain width requiring a total of 1.8 billion computational cells to simulate. If this same simulation was to be conducted at the size of a combustor with similar conditions (a reciprocating internal combustion engine for a HGV, for example) an estimated 4000 trillion computational cells would be required. Due to the extra size, the flame would take longer to burn though the computational domain thus requiring more time steps, totalling unfeasible computational requirements. For reference, for device scale simulation codes, the size of the entire domain of Figure 1.1 is roughly the size of one computational cell.

1.2 Vectis and the Reciprocating Internal Combustion Engine

Realis Simulation develop Vectis, a 3-dimensional simulation tool for device scale internal combustion engines. Vectis is capable of simulating the entire engine cycle, allowing for essential insight into engine behaviour for more effective design and optimisation [2]. To

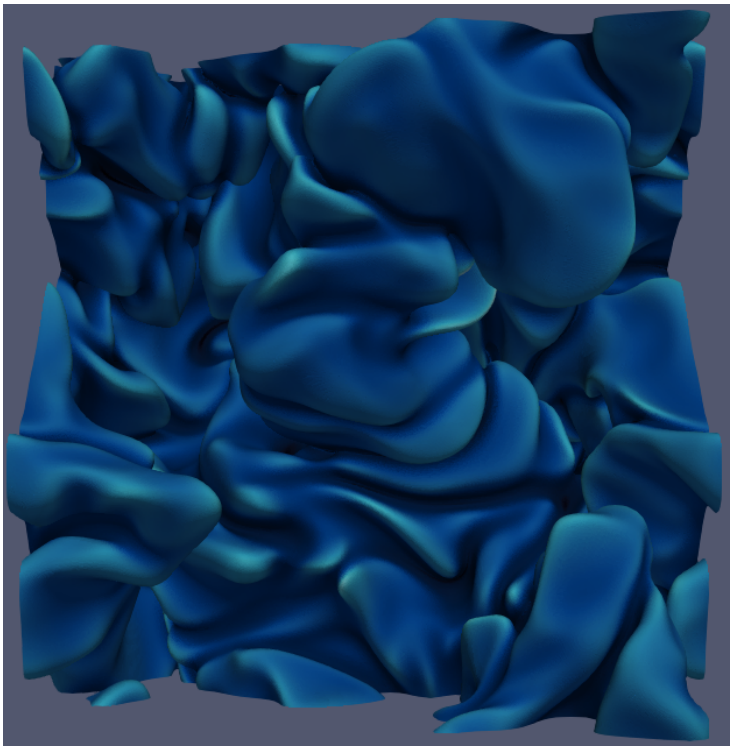

Figure 1.1: Example of a turbulent hydrogen flame isosurface in DNS.

achieve device scale simulations, Vectis utilises the unsteady Reynolds Averaged Navier-Stokes Equations for laminar or turbulent, in-compressible or compressible flows [166]. Coupled with tabulated kinetics with laminar and turbulent flame speed models to allow for the simulation of combustion, Vectis also utilises an unstructured grid and moving boundaries for the simulation of a full engine cycle [2]. A reciprocating internal combustion engine converts chemical energy stored in a liquid or gaseous fuel, such as hydrogen, into mechanical and thermal energy through the combustion of the fuel. Hydrogen reciprocating internal combustion engines follow a typical Otto cycle where:

- Air is drawn into the combustion chamber via an expanding cylinder and hydrogen is injected into the chamber and mixes with the turbulent air, creating a premixed air-fuel mixture.
- The piston compresses the air-fuel mixture.
- A spark plug ignites the mixture via a spark resulting in a small flame kernel. The flame kernel rapidly burns through the mixture, expanding the products through adiabatic

expansion forcing the piston and cylinder head apart, increasing the cylinder volume.

- The exhaust gases are expelled from the cylinder.

1.3 Aims and Thesis Structure

The aims of this project are, by utilising direct numerical simulations, to improve the current understanding of the underlying flame physics of TD-unstable premixed hydrogen flames. Specifically, how flame conditions such as pressure, temperature, equivalence ratio and turbulence affect the underlying flame physics relevant to turbulent flame speed modelling. In particular, the local flame speeds and structure (Chapters 4 and 5), global flame structure and the turbulent flame speed (Chapter 6). Using this insight, an appropriate modified turbulent flame speed model(s) will be proposed, to be used in device scale simulation codes such as Vectis.

This thesis is organised into the following chapters:

- Chapter 2, background; focuses on the key theory and background relevant to understanding the main concepts utilised throughout this thesis. This includes the fundamental equations of motion for reacting flows, relevant turbulence theory, laminar premixed flames, both flat unstretched and multidimensional freely-propagating flames and the consequences of Lewis number, turbulent flames and turbulent flame speed modelling.

- Chapter 3, methods; focuses on the methods used to conduct the simulations and analysis, starting with the direct numerical simulation code and the turbulence forcing, followed by the resolution requirements and the methods used to attain flame statistics.

- Chapter 4, focuses on laminar, freely-propagating flames, where the effects of flame conditions (pressure, temperature and equivalence ratio) have on the freely propagating flame speed, thickness and structure. This chapter also proposes a local freely propagating flame speed and thickness model.

- Chapter 5, builds upon chapter 4 by studying the effect of flame conditions and turbulent intensity on the local flame speed, thickness and flame structure. Chapter 4, also

proposes a model used for predicting the local flame acceleration and thinning under a variety of flame and turbulent conditions.

- Chapter 6, focuses on the effects of the TD-instability, turbulent intensity and turbulent integral length scale on the local and global flame statistics. Chapter 6 also uses the data from Chapter 5 to develop and propose an improved turbulent flame speed model.
- Chapter 7, proposes a DNS style G-equation for simulating lean hydrogen flames without the computational cost of computing chemistry.
- Chapter 8, concludes the thesis with a summary of the key findings of the work and recommended future considerations.

Chapter 2. Background

The goal of this chapter is to introduce the fundamental concepts required to follow the proceeding research chapters. The background chapter will be divided into the following key sections: Conservation equations for reacting flows, Fundamentals of turbulence, Fundamentals of unperturbed laminar premixed flames, Laminar freely-propagating flames, Turbulent flames and turbulent flame speed modelling. The thesis is solely focused on sub-sonic premixed flames, thus non-premixed flames and compressible reacting flows will not be covered in this background. This assumption is sensible provided the combustion velocity (and fluid velocity) is independent of pressure waves, which usually correlates with flame speeds and flows sufficiently slower than the speed of sound (Ma). The flows used throughout this project will be adequately sub-sonic (approximately $0.01\mathrm{Ma}$). A premixed flame is a flame where the fuel and oxidiser is supplied premixed. This means that, ahead of the flame, the gas will contain a fuel (for this project, the fuel is Hydrogen H_2), Oxygen O_2 and Nitrogen N_2. Given sufficient reactant conditions, nitrogen will not be an inert gas and can react to form NOx, however nitrogen kinetics are beyond the scope of this project and will not be discussed further.

2.1 Conservation Equations for Reacting Flows

The following section provides an overview of the fundamental equations of energy conservation in incompressible reacting flows. The equation below will be revisited again when discussing the direct numerical simulation code base (PeleLM) in Section 3.1.

Typically, in three-dimensional reacting flows there are $5 + N$ variables:

- The three velocity components.
- The energy, which can be expressed as a temperature, enthalpy or pressure.
- The fraction of species (typically given as a mass fraction of each of the N species).

2.1.1 The Control Volume

To attain the conservation equations, a control volume approach will be used. Detailed explanations of the control volume approach and the corresponding conservation equations are summarised in [100] and [10] (other supplementary reading includes [27, 173, 139, 137]). The premise of the control volume approach is to take a blob of fluid with a volume V, a surface S and a unit normal vector $\boldsymbol{n}$ as a fixed frame of reference. The control volume has a velocity vector $\boldsymbol{u}$ flowing through it. Simply, the density-weighted velocity is caused by the sum of the velocity of each species ($\rho_k \boldsymbol{u}_k$), where k is the kth species. The difference between the individual species velocity and the bulk velocity is the molecular diffusion

$$\boldsymbol{U}_k = \boldsymbol{u}_k - \boldsymbol{u}. \tag{2.1}$$

The momentum of the fluid is also equal to sum of the momentum of each species in the fluid

$$\sum_{k=1}^{N} \rho_k \boldsymbol{u}_k = \rho \boldsymbol{u}. \tag{2.2}$$

where N is the number of species and ρ_k is the density of species k. Given a fluid property Φ and the corresponding "density" of Φ per unit volume of fluid ϕ, then the rate of change of Φ, is the sum of the change of Φ within the fluid blob volume V and the gain and losses of Φ as the result of fluxes through the surface is defined as [100]

$$\frac{\delta \Phi}{\delta t} = \frac{\partial}{\partial t} \int_V \phi \, \mathrm{d}V + \int_S \phi (\boldsymbol{u} \cdot \boldsymbol{n}) \, \mathrm{d}S. \tag{2.3}$$

By using Gauss's divergence theorem, which for a given vector field $\boldsymbol{\mathcal{V}}$ in a fluid blob of volume V with surface S

$$\iiint_V (\nabla \cdot \boldsymbol{\mathcal{V}}) \, \mathrm{d}V = \iint_S (\boldsymbol{\mathcal{V}} \cdot \boldsymbol{n}) \, \mathrm{d}S, \tag{2.4}$$

allows for the following to be true

$$\int_V (\nabla \cdot \phi \boldsymbol{u}) \, \mathrm{d}V = \int_S \phi (\boldsymbol{u} \cdot \boldsymbol{n}) \, \mathrm{d}S. \tag{2.5}$$

This then allows for the definition of the rate of change of a fluid property, as

$$\frac{\delta \Phi}{\delta t} = \int_V \left(\frac{\partial \phi}{\partial t} + \nabla \cdot \phi \boldsymbol{u} \right) \mathrm{d}V. \tag{2.6}$$

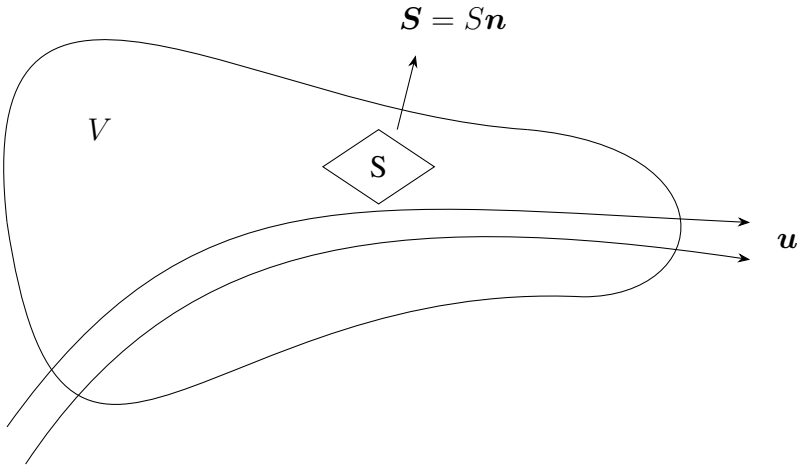

Figure 2.1: Visualisation of the control volume, as influenced by Law's book [100].

2.1.2 Conservation of Mass

The rate of change of the mass is the sum of the loss and gain of mass through fluxes across the surface S of the fluid blob and the temporal change of mass within the fluid volume, therefore by substituting mass m and density ρ into Equation (2.6) the conservation of mass can be written as

$$\frac{\delta m}{\delta t} = \int_V \left(\frac{\partial \rho}{\partial t} + \nabla \cdot \rho \boldsymbol{u} \right) \mathrm{d}V. \tag{2.7}$$

As mass cannot be created or destroyed

$$\int_V \left(\frac{\partial \rho}{\partial t} + \nabla \cdot \rho \boldsymbol{u} \right) \mathrm{d}V = 0, \tag{2.8}$$

and as the control volume is arbitrary, the continuity equation can be defined as

$$\boxed{\frac{\partial \rho}{\partial t} + \nabla \cdot (\rho \boldsymbol{u}) = 0.} \tag{2.9}$$

2.1.3 Conservation of Momentum

There are several steps to defining the momentum equation. Firstly, we must define the temporal change in momentum using Equation (2.6) and substituting Φ for momentum $\boldsymbol{M}$ of the flow and the ϕ for the momentum flux $\rho \boldsymbol{u}$. The temporal change in momentum is then

$$\frac{\delta \boldsymbol{M}}{\delta t} = \int_V \left(\frac{\partial \rho \boldsymbol{u}}{\partial t} + \nabla \cdot \rho \boldsymbol{u} \boldsymbol{u} \right) \mathrm{d}V. \tag{2.10}$$

By adhering to Newton's second law of motion the rate of change of momentum depends on the force acting on the fluid. This force can be divided into a surface force and volume force. The surface force can be represented by the stress tensor $\boldsymbol{\sigma}$ and the density weighted volumetric force $\boldsymbol{\mathcal{F}}$. The rate of change of momentum can then be defined as a sum of the surface and volume forces

$$\frac{\delta \boldsymbol{M}}{\delta t} = -\int_S (\boldsymbol{\sigma} \cdot \boldsymbol{n})\, \mathrm{d}S + \int_V \boldsymbol{\mathcal{F}}. \tag{2.11}$$

By combing Equation (2.4) and (2.11)

$$\frac{\delta \boldsymbol{M}}{\delta t} = -\int_V (-\nabla \cdot \boldsymbol{\sigma} + \boldsymbol{\mathcal{F}})\, \mathrm{d}V. \tag{2.12}$$

Then, by combining Equation (2.10) with equation (2.12), the momentum equation becomes

$$\boxed{\frac{\partial \rho \boldsymbol{u}}{\partial t} + \nabla \cdot \rho \boldsymbol{u}\boldsymbol{u} = -\nabla \cdot \boldsymbol{\sigma} + \boldsymbol{\mathcal{F}}.} \tag{2.13}$$

For this project, volume forces are limited by the forcing used to maintain homogeneous and isotropic turbulence. Details on this method will be detailed in Section 3.1.3.

2.1.4 Conservation of Species

In reacting flows there are more than one species (for example in the Burke mechanism [46] there are 13 species), which must be conserved. Unlike mass, the species mass can change due to both combustion and diffusion. It is now important to define the conservation of species by taking Equation 2.6 for the mass and density of the kth species, then

$$\frac{\delta m_k}{\delta t} = \int_V \left(\frac{\partial \rho_k}{\partial t} + \nabla \cdot \rho_k \boldsymbol{u} \right) \mathrm{d}V. \tag{2.14}$$

The presence of chemical reactions can result in the production or destruction of species k, thus $\dot{\omega}_k$ is the production of species k per unit volume. The diffusive transport is caused through molecular collisions which has a magnitude proportional to the mass flux $\rho_k \boldsymbol{U}_k$ caused by the random motion of the molecules, therefore

$$\frac{\delta m_k}{\delta t} = \underbrace{\int_V \dot{\omega}_k \, \mathrm{d}V}_{\text{reaction}} - \underbrace{\int_S (\rho_k \boldsymbol{U}_k \cdot \boldsymbol{n})\, \mathrm{d}S}_{\text{diffusion}}, \tag{2.15}$$

$$\frac{\delta m_k}{\delta t} = \int_V (\dot{\omega}_k - \nabla \cdot \rho_k \boldsymbol{U}_k)\, \mathrm{d}V. \tag{2.16}$$

When Equation 2.14 and 2.16 are combined, the conservation of species is defined as

$$\frac{\partial \rho_k}{\partial t} = \dot{\omega}_k - \nabla \cdot \left(\rho_k \left(\boldsymbol{u} + \boldsymbol{U}_k\right)\right). \tag{2.17}$$

Typically Equation 2.17 is presented as a species mass fraction Y_k where

$$Y_k = \frac{\rho_k}{\rho}. \tag{2.18}$$

Therefore Equation 2.17 becomes

$$\boxed{\frac{\partial \rho Y_k}{\partial t} = \dot{\omega}_k - \nabla \cdot \left(\rho Y_k \left(\boldsymbol{u} + \boldsymbol{U}_k\right)\right).} \tag{2.19}$$

2.1.5 Conservation of Energy

The internal energy E within the system must be conserved. The total internal energy is the sum of the sensible e_s, chemical e_c and kinetic $u^2/2$. Therefore using the control volume approach Equation 2.6 becomes

$$\frac{\delta E}{\delta t} = \int_V \left(\frac{\partial \rho \left(e_s + e_c + (u^2/2)\right)}{\partial t} + \nabla \cdot \rho \boldsymbol{u} \left(e_s + e_c + \left(u^2/2\right)\right) \right) \mathrm{d}V. \tag{2.20}$$

The internal energy can be changed by three sources [100]:

- Q_1 the energy flux $\boldsymbol{\mathcal{Q}}$ normal to boundary of the system.
- Q_2 the work done on the fluid blob by the surface force $\boldsymbol{F}_s$.
- Q_3 the work done by the body forces on the kth species $\boldsymbol{F}_{V,k}$.

Therefore the rate of change of internal energy is

$$\frac{\partial E}{\partial t} = Q_1 + Q_2 + Q_3. \tag{2.21}$$

Q_1 can be defined as

$$Q_1 = -\int_S (\boldsymbol{\mathcal{Q}} \cdot \boldsymbol{n}) \, \mathrm{d}S = -\int_V \nabla \cdot \boldsymbol{\mathcal{Q}} \, \mathrm{d}V, \tag{2.22}$$

Q_2 can be defined as

$$Q_2 = -\int_S \boldsymbol{u} \, \mathrm{d}\boldsymbol{F}_s = -\int_S \boldsymbol{u} \cdot (\boldsymbol{\sigma} \cdot \boldsymbol{n}) \, \mathrm{d}S = -\int_V \nabla \cdot (\boldsymbol{u} \cdot \boldsymbol{\sigma}) \, \mathrm{d}V, \tag{2.23}$$

where the negative sign means that the velocity vector $\boldsymbol{u}$ is pointed in the same direction of the surface force $\mathrm{d}\boldsymbol{F}_s$ away from the surface, then work is being added to the fluid. Q_3 can be defined as

$$Q_3 = \sum_{k=1}^{N} \int_V \boldsymbol{u}_k \cdot \, \mathrm{d}\boldsymbol{F}_{V,k} = \sum_{k=1}^{N} \int_V \boldsymbol{u}_k \cdot (\rho_k \boldsymbol{f}_k) \, \mathrm{d}V, \tag{2.24}$$

as $U_k = \boldsymbol{u}_k - \boldsymbol{u}$

$$Q_3 = \sum_{k=1}^{N} \int_V (\boldsymbol{U}_k + \boldsymbol{u}) \cdot (\rho_k \boldsymbol{f}_k) \, \mathrm{d}V. \tag{2.25}$$

Equation (2.21) now becomes

$$\frac{\partial E}{\partial t} = -\int_V \nabla \cdot \boldsymbol{\mathcal{Q}} \, \mathrm{d}V - \int_V \nabla \cdot (\boldsymbol{u} \cdot \boldsymbol{\sigma}) \, \mathrm{d}V + \sum_{k=1}^{N} \int_V (\boldsymbol{U}_k + \boldsymbol{u}) \cdot (\rho_k \boldsymbol{f}_k) \, \mathrm{d}V. \tag{2.26}$$

Then, by combining with Equation (2.20), yields

$$\begin{aligned} \frac{\partial \rho \left(e_s + e_c + (u^2/2)\right)}{\partial t} + \nabla \cdot \rho \boldsymbol{u} \left(e_s + e_c + \left(u^2/2\right)\right) = \\ -\nabla \cdot \boldsymbol{\mathcal{Q}} - \nabla \cdot (\boldsymbol{u} \cdot \boldsymbol{\sigma}) + \sum_{k=1}^{N} (\boldsymbol{U}_k + \boldsymbol{u}) \cdot (\rho_k \boldsymbol{f}_k) \, . \end{aligned} \tag{2.27}$$

Following [137] the energy equation can be defined in terms of enthalpy

$$\frac{\partial \rho h}{\partial t} + \nabla \cdot (\rho h \boldsymbol{u} + \boldsymbol{\mathcal{Q}}) = \rho \sum_{k=1}^{N} (\boldsymbol{U}_k + \boldsymbol{u}) \cdot (Y_k f_k). \tag{2.28}$$

For the cases studied throughout this thesis the RHS is equal to zero, thus reduces to

$$\boxed{\frac{\partial \rho h}{\partial t} + \nabla \cdot (\rho h \boldsymbol{u} + \boldsymbol{\mathcal{Q}}) = 0.} \tag{2.29}$$

2.1.6 Species Transport and Diffusive Fluxes

When at rest, species can still be transported through molecular diffusion. The kth species diffusive flux vector is defined as

$$\boldsymbol{F}_k = -\sum_{l=1}^{N} \rho D_{k,l} \boldsymbol{d}_l - \frac{\rho Y_k D_{th,k}}{T} \nabla T, \tag{2.30}$$

where $D_{th,k}$ is the thermal diffusion coefficient of species k, $D_{k,l}$ is the mass diffusion coefficient of species k to species l, $\boldsymbol{d}_l$ is the driving diffusion force of species l and T is the

temperature. The temperature gradient term represents the Soret effect, and historically is absent in most combustion codes. The thermal conductivity is defined as

$$D_t = \frac{\lambda}{\rho c_p}, \tag{2.31}$$

where λ is the thermal conductivity and c_p is the specific heat capacity. The driving diffusion force is defined as

$$\boldsymbol{d}_l = \nabla X_l \frac{X_l - Y_l}{p} \nabla p, \tag{2.32}$$

where p is the pressure field and X_l is the mole fraction of species l. Each species of mass fraction requires a transport equation and can be given by

$$\boxed{\frac{\partial \rho Y_k}{\partial t} + \nabla \cdot (\rho Y_k \boldsymbol{u}) = -\nabla \cdot \boldsymbol{F}_k + \rho \dot{\omega}_k.} \tag{2.33}$$

2.1.7 Chemical Kinetics

Given a chemical system that contains N number of species which have M number of reaction for a given kth species $\mathcal{S}_k$, the reversible reaction can be generalised as

$$\sum_{k=1}^{N} \mathcal{C}_{k,l}^{f} \mathcal{S}_k \rightleftharpoons \sum_{k=1}^{N} \mathcal{C}_{k,l}^{b} \mathcal{S}_k, \tag{2.34}$$

where $\mathcal{C}_{k,l}^{f}$ and $\mathcal{C}_{k,l}^{b}$ is the forward and backward stoichiometric coefficient for the kth species in the lth reaction. The rate of change in the concentration of the kth species is given by

$$\frac{\mathrm{d}c_k}{\mathrm{d}t} = W_k = \sum_{l=1}^{N_R} \left(\mathcal{C}_{k,l}^{f} - \mathcal{C}_{k,l}^{b}\right) \left(W_{k,l}^{f} - W_{k,l}^{b}\right) \quad \text{for} \quad l = 1, N_R, \tag{2.35}$$

where $W_{k,l}^{f}$ and $W_{k,l}^{b}$ is the forward and backward reaction rate of species k from reaction j, and N_R is the number of reactions. Forward and backward reaction rates can be modeled by

$$W_{k,l}^{f} = K_k^{f} \rho^{\sum_{k=1}^{N-1} \mathcal{C}_{k,l}^{f}} \prod_{k=1}^{N-1} \left(\frac{Y_k}{M_k}\right)^{\mathcal{C}_{k,l}^{f}} \tag{2.36}$$

and

$$W_{k,l}^{b} = K_k^{b} \rho^{\sum_{k=1}^{N-1} \mathcal{C}_{k,l}^{b}} \prod_{k=1}^{N-1} \left(\frac{Y_k}{M_k}\right)^{\mathcal{C}_{k,l}^{b}}, \tag{2.37}$$

where M_k is the molar weight of species k and K_k^{f} and K_k^{b} are the forward and backward reaction rate constants. $N-1$ is used because the Nth species is associated with a third body

reaction [108]. The molar weight of species are approximated from the generalised Arrhenius empirical relation

$$K_k^f = \mathcal{A}_k^f \exp\left(-\frac{\mathcal{E}_l^f}{R_o T}\right), \tag{2.38}$$

and

$$K_k^b = \mathcal{A}_k^b \exp\left(-\frac{\mathcal{E}_l^b}{R_o T}\right), \tag{2.39}$$

where $\mathcal{E}_l^f$ and $\mathcal{E}_l^b$ is the activation energy for forward and backward reaction l. R_0 is the universal gas constant and $\mathcal{A}_k^f$ and $\mathcal{A}_k^b$ is the forward and backward pre-exponential which can be divided into a constant and a temperature exponent

$$\mathcal{A}_k^f = A_k^f T^{B_k^f}, \tag{2.40}$$

and

$$\mathcal{A}_k^b = A_k^b T^{B_k^b}, \tag{2.41}$$

where A_k^f, B_k^f, A_k^b and B_k^f are constants. From these, the reaction rate of kth species $\dot{\omega}_k$ can be given as

$$\rho\dot{\omega}_k = \sum_{l=1}^{N_R} \left(\mathcal{C}_{k,l}^b - \mathcal{C}_{k,l}^f\right)\left(W_{k,l}^f - W_{k,l}^b\right). \tag{2.42}$$

2.2 Fundamentals of Turbulence

Turbulence is present in almost all real world combustors, especially internal combustion engines. It will therefore be important to establish a fundamental understanding of how turbulence behaves so it can later be studied in the context of turbulent flame interactions as-well as to gain an appreciation and justification for the appropriate methodology. Turbulence as defined by Bradshaw [41] is "*a 3-dimensional time dependent motion in which vortex stretching causes velocity fluctuations to spread to all wavelengths between a maximum, determined by the boundary conditions of the flow and minimum determined by viscous forces*". Turbulence in the context of this project will mostly be assumed as statistically stationary, in-compressible, homogeneous and isotropic (HIT). The turbulence's statistical properties are independent of the coordinate axes, spatial position and time. Unless stated otherwise, the section below has made the HIT assumption.

2.2.1 Structural Description of Turbulence

To better describe the structure of turbulence, there are four key velocities; the instantaneous velocity ($\mathbf{u}(\mathbf{x},t)$), the mean flow velocity (which is the ensemble average of the instantaneous velocity ($\langle\mathbf{u}(\mathbf{x},t)\rangle$) , the instantaneous velocity fluctuation

$$\mathbf{u}''(\mathbf{x},t) = \mathbf{u}(\mathbf{x},t) - \langle\mathbf{u}(\mathbf{x},t)\rangle \tag{2.43}$$

and the root-mean-square of the velocity fluctuation

$$u' = \sqrt{\langle u_x''^2\rangle} = \sqrt{\langle u_y''^2\rangle} = \sqrt{\langle u_z''^2\rangle}, \tag{2.44}$$

which is the typical velocity of the large eddies [57].

The velocity correlation function $Q_{ij}(\mathbf{r},\mathbf{x},t)$ is defined as

$$Q_{ij} = \langle u_i(\mathbf{x})u_j(\mathbf{x}+\mathbf{r})\rangle \tag{2.45}$$

and is a measure of the degree to which the velocity components at different points are correlated to each other. For example, if $Q_{ij} = Q_{xx}$, then two positions of distance $\mathbf{r}$ have the velocity fluctuation of the x-components velocity correlated, i.e.

$$Q_{xx} = \langle(u_x)_x(u_x)_{x+r}\rangle. \tag{2.46}$$

From Equation (2.45) and following the assumption of HIT where statistics are independent of position (i.e. $\mathbf{x}$) longitudinal and lateral velocity correlation functions can be defined as

$$Q_{xx}(r\mathbf{e}_x) = u^2 f(r), \tag{2.47}$$

$$Q_{yy}(r\mathbf{e}_x) = u^2 g(r). \tag{2.48}$$

This allows for another important turbulent quantity to be defined, the integral length scale (ℓ_{I})

$$\ell_{\text{I}} = \int_0^\infty f(r)\mathrm{d}r. \tag{2.49}$$

This definition will be used to deine the integral length scale for the rest of the thesis. The integral length scale is a decent measure of the region over which velocities are correlated, which coincides with the size of the larger eddies. At $r = 0$, $f(r) = 1$, and as r tends to

infinity and $f(r)$ tends to zero as very large eddies occur less frequently than smaller eddies. As u represents the turnover velocity of the larger eddies (around integral length scale) the turbulent turnover time can be defined as

$$\tau_{\mathrm{I}} = \frac{\ell_{\mathrm{I}}}{u'}. \tag{2.50}$$

2.2.2 The Energy Cascade

Richardson's Energy Cascade

Richardson [144] proposed that turbulence has a range of turbulent eddies of different sizes, where an 'eddy' is a turbulent motion, localised within a region of a given size ℓ_{R} [139], where a region of larger eddies can also have smaller eddies inside the same region. Eddies of size r also have a characteristic velocity of $u(\ell_{\mathrm{R}})$ and a turnover time of $\tau(\ell_{\mathrm{R}}) = \ell_{\mathrm{R}}/u(\ell_{\mathrm{R}})$. Richardson's proposal of the energy cascade is that eddies are unstable, and are inclined to break up; where their energy is transferred into progressively smaller and smaller eddies. Therefore, the turbulent kinetic energy injected into the system ($E_{k,\mathrm{in}}$) at the large scales is progressively cascaded into progressively smaller and smaller scales involving a "*hierarchy of vortices*" [57] until the molecular viscosity is effective in dissipating the kinetic energy. The Reynolds number (Re, conceptualised by Stokes [158] and implemented by Reynolds [143]), is a dimensionless quantity that measures the ratio of the inertial and viscous forces in a fluid flow. It is defined as

$$\mathrm{Re}(\ell_{\mathrm{R}}) = u(\ell_{\mathrm{R}})\ell_{\mathrm{R}}/\nu, \tag{2.51}$$

where $u(\ell_{\mathrm{R}})$ is the fluid velocity at a length ℓ_{R}, and ν is the kinematic viscosity. It can be seen from Equation (2.51) that as the length scale decreases, the Reynolds number is decreased and the effect of viscosity is increased. Therefore as the Reynolds number is sufficiently low (which will occur at the smaller length scales) the viscous forces will be effective at dissipating the kinetic energy. Alternatively, a sufficiently higher Reynolds number will occur at the larger length scales, say the integral scales (u', ℓ_{I}), which will be discussed in more detail below) for example

$$\mathrm{Re} = u'\ell_{\mathrm{I}}/\nu, \tag{2.52}$$

the turbulent flow at the larger scales are independent of viscosity. The rate of energy dissipation ε describes the rate of which energy is dissipated from the large scales to the small scales; Richardson predicts that the rate of energy dissipation from the large scales to the small scales and ultimately the rate energy is dissipated due to viscosity and is independent of ℓ thus at a given time ε is constant. The energy cascade can then be described as

$$E_{k,\text{in}} = \Pi_A = \Pi_B = \Pi_C = \varepsilon, \tag{2.53}$$

where ε can also be described as the energy dissipation due to viscosity and Π is the energy cascade at scale $\ell = A$ to $\ell = B$ and so-on.

Kolmogorov's Hypotheses

Kolmogorov in 1941 published two landmark papers [92, 93] (English translation [94]) which among others provided, a mathematical description of Richardson's cascade and proposed three hypotheses [139]:

1. Local Isotropy Hypothesis:
    - In every turbulent flow at sufficiently high Reynolds number, the statistics of the small-scale motions of size ℓ_{R} are statistically isotropic if $\ell_{\text{R}} \ll \ell_{\text{I}}$.
2. First Similarity Hypothesis:
    - In every turbulent flow at sufficiently high Reynolds number, the statistics of the small-scale motions ($\ell_{\text{R}} < \ell_{\text{EI}}$, where $\ell_{\text{EI}} \approx \frac{1}{6}\ell_{\text{I}}$) have a universal form that is determined uniquely by the rate of energy dissipation (ε) and the viscosity (ν).
3. Second Similarity Hypothesis:
    - In every turbulent flow at sufficiently high Reynolds number, the statistics of the small-scale motions of scale are ℓ_{R} larger than the Kolmogorov length scale (η) and smaller than the integral length scale (ℓ_{I}), i.e. $\eta \ll \ell_{\text{R}} \ll \ell_{\text{I}}$ have a universal form determined only by energy dissipation (ε) and independent of viscosity (ν).

The local isotropy hypothesis is based on the idea that the large eddies are isotropic and therefore influenced by the boundary conditions and mean flow. Kolmogorov proposed that the

information is lost as the energy is cascaded to smaller scales due to the chaotic "scale-reduction process". Thus at sufficiently high Reynolds number, the small-scale turbulent motions of size ℓ_{R} are statistically isotropic if $\ell_{\mathrm{R}} \ll \ell_{\mathrm{I}}$.

Naturally this leads to the first similarity hypothesis where Kolmogorov argued that the small-scale motions are the same in all high Reynolds number turbulent flows (statistically universal state [139]). It can then be asked, at what scale does this state occur? By defining a length scale ℓ_{EI} which represents a length that is too small for to have information of the mean flow and boundary conditions. When $\ell_{\mathrm{R}} < \ell_{\mathrm{EI}}$ there are logically two primary processes; the continuation of the transfer of energy to progressively smaller scales and the dissipation of energy into heat from viscosity (viscous dissipation), where the key parameters are the rate of which small-scales receive energy from the large scales (Π_{EI}), and the kinematic viscosity. Assuming that the field is statistically steady the rate of energy dissipation from viscosity ε must equal the energy entering the smaller scales from the larger scales, thus $\varepsilon = \Pi_{\mathrm{EI}}$, which is identical to equation (2.53) at the smaller scales. Thus in every turbulent flow at sufficiently high Reynolds number, the statistics of the small-scale motions ($\ell_{\mathrm{R}} < \ell_{\mathrm{EI}}$, where $\ell_{\mathrm{EI}} \approx \frac{1}{6}\ell_{\mathrm{I}}$) have a universal form that is determined uniquely by the rate of energy dissipation (ε) and the kinematic viscosity (ν).

The length-scale range of $\ell_{\mathrm{R}} < \ell_{\mathrm{EI}}$ is known as the universal equilibrium range, where the timescales at this size are small compared with the larger scales (i.e. $\tau(\ell_{\mathrm{R}}) \ll \tau(\ell_{\mathrm{I}})$). Therefore, in this range the turbulent eddies adapt quickly to changes in the flow field which maintains the "dynamic equilibrium" [139] thus always has the energy transfer rate of Π_{EI}. Kolmogorov then proposed three scales (length, velocity and time) from only the energy dissipation rate and kinematic viscosity, which will be referred to as the Kolmogorov length, velocity and time.

$$\eta = \left(\frac{\nu^3}{\varepsilon}\right)^{1/4}, \tag{2.54}$$

$$u_\eta = (\varepsilon\nu)^{1/4}, \tag{2.55}$$

$$\tau_\eta = \left(\frac{\nu}{\varepsilon}\right)^{1/2}. \tag{2.56}$$

The definitions indicate that the Kolmogorov scales characterise the small dissipative eddies. It

can be seen that the Kolmogorov scale ($\ell_{\text{R}} = \eta$) and the Reynolds number tends to unity

$$\text{Re}(\eta) = \frac{\eta u_\eta}{\nu} = 1. \tag{2.57}$$

It can be seen that in flows which are more inviscid, the scales at which viscosity is effective at dissipating energy (i.e. the Kolmogorov length scale) are smaller. The opposite is true in energy dissipation rate where the larger the energy dissipation rate the smaller the Kolmogorov length scale. The energy dissipation rate is given by

$$\varepsilon = \nu \left(\frac{u_\eta}{\eta} \right)^2. \tag{2.58}$$

To illustrate the consequences of the hypothesis, assuming a high Reynolds number at a fixed point in time at ($\mathbf{x}_0$), by normalising the coordinates by Kolmogorov length and the velocity field by Kolmogorov velocity, two dimensionless parameters can be formed. However, it is not possible to form a non-dimensional parameter for energy dissipation rate and kinematic viscosity; thus the non-dimensional field cannot depend on energy dissipation rate or kinematic viscosity. As a consequence, at the small scales (specifically $|\mathbf{x} - \mathbf{x}_o| < \ell_{\text{EI}}$) all points are statistically identical, thus "*on the small scales, all high-Reynolds-number turbulent velocity fields are statistically similar; that is, they are statistically identical when they are scaled by the Kolmogorov scales*" [94, 139]. Using the assumption that the rate of energy dissipation is controlled by the larger scales (i.e. Equation 2.53) and viscosity only controls the scales of which energy dissipation occurs, the energy dissipation is

$$\varepsilon \sim \frac{(u')^3}{\ell_{\text{I}}}, \tag{2.59}$$

which then allows for the following relations;

$$\frac{\eta}{\ell_{\text{I}}} \sim \text{Re}^{-3/4}, \tag{2.60}$$

$$\frac{u_\eta}{u'} \sim \text{Re}^{-1/4}, \tag{2.61}$$

$$\frac{\tau_\eta}{\tau_{\text{I}}} \sim \text{Re}^{-1/2}. \tag{2.62}$$

It can now be seen why sufficiently high Reynolds number is essential, because if the ratio of the dissipative length scale and the large turbulent scales is too small, then dissipation can happen at the larger scales. Assuming that the Reynolds number is sufficiently high, the ratio

of the dissipative scales are very small compared to the large scales. There is a large range of scales between these, i.e. $\eta \ll \ell_{\text{R}} \ll \ell_{\text{I}}$, where the Reynolds number at these length scales is sufficiently large that there is little effect from viscosity, thus the flow is independent of viscosity. This leads to the second similarity hypothesis: In every turbulent flow at sufficiently high Reynolds number, the statistics of the small-scale motions of scale ℓ_{R} larger than the Kolmogorov length scale (η) and smaller than the integral length scale (ℓ_{I}) i.e. $\eta \ll \ell_{\text{R}} \ll \ell_{\text{I}}$ have a universal form determined only by energy dissipation (ε) and independent of viscosity (ν).

The energy cascade can be split into the following length scale ranges (see Figure 2.2 showing the schematic diagram of the different turbulent length scales).

- Energy-containing range;
  - the largest scales where the large amount of kinetic energy resides and where kinetic energy is added to the system.
- Inertial sub-range;
  - where energy is cascaded from the larger scales to the smaller scales, but the Reynolds number ($\text{Re}(\ell_{\text{R}})$) is sufficiently high that the effect of viscosity is negligible.
- Dissipation range;
  - the smallest scales where Reynolds number is low and the viscosity is effective at dissipating the kinetic energy.

Next it is required to know how the turbulent kinetic energy is distributed at the different length scales. By considering Fourier transform of the two point correlation (Equation 2.45) using the spatial Fourier mode

$$e^{-i\boldsymbol{\kappa}\cdot\boldsymbol{r}} = \cos(\boldsymbol{\kappa}\cdot\boldsymbol{r}) + i\sin(\boldsymbol{\kappa}\cdot\boldsymbol{r}), \tag{2.63}$$

which is constant in the planes normal to the wave number vector ($\boldsymbol{\kappa}$) and varies sinusoidally with wavelengths $\ell_{\text{R}} = 2\pi/|\boldsymbol{\kappa}|$ in the direction of $\boldsymbol{\kappa}$. The velocity spectrum tensor ($\Phi_{i,j}(\boldsymbol{\kappa}, t)$)

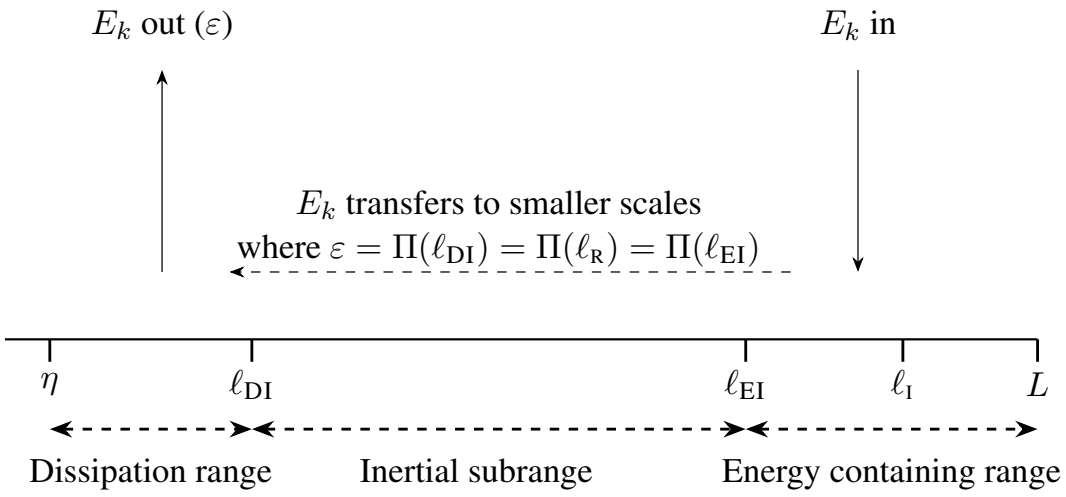

Figure 2.2: Schematic diagram of the energy cascade at a sufficiently high Reynolds number, inferred from Figure 6.2 in Pope [139].

is

$$\Phi_{i,j}(\boldsymbol{\kappa}, t) = \frac{1}{(2\pi)^3} \iiint_{-\infty}^{\infty} = e^{-\mathrm{i}\boldsymbol{\kappa}\cdot\boldsymbol{r}} Q_{i,j}(\boldsymbol{r}, t)\, \mathrm{d}\boldsymbol{r}, \tag{2.64}$$

where $\mathrm{i}^2 = -1$, with the inverse transform of

$$Q_{i,j}(\boldsymbol{r}, t) = \iiint_{-\infty}^{\infty} \Phi_{i,j}(\boldsymbol{\kappa}, t)\, \mathrm{d}\boldsymbol{r}, \tag{2.65}$$

The energy wave number spectrum function can then be defined as

$$E(\kappa, t) = \iiint_{-\infty}^{\infty} \frac{1}{2} \boldsymbol{\Phi}_{ii}(\boldsymbol{\kappa}, t) \delta(|\boldsymbol{\kappa}| - \kappa)\, \mathrm{d}\boldsymbol{\kappa}. \tag{2.66}$$

By defining a range of spherical region of wave numbers which has a radius of $\kappa = |\boldsymbol{\kappa}|$, integrating over all wave numbers gives the total fluctuation kinetic energy

$$\int_0^{\infty} E(\kappa, t)\, \mathrm{d}\kappa = \frac{1}{2} \langle u_i u_j \rangle. \tag{2.67}$$

Therefore, $E(\kappa, t)$ shows the contribution all modes $|\boldsymbol{\kappa}|$ in the range $\kappa \leq |\boldsymbol{\kappa}| \leq \kappa + \mathrm{d}\kappa$ have to the turbulent kinetic energy $\frac{1}{2}\langle u_i u_j \rangle$. Given a range of wavenumbers (κ_a, κ_b) the total fluctuation kinetic energy is

$$\int_{\kappa_a}^{\kappa_b} E(\kappa, t)\, \mathrm{d}\kappa. \tag{2.68}$$

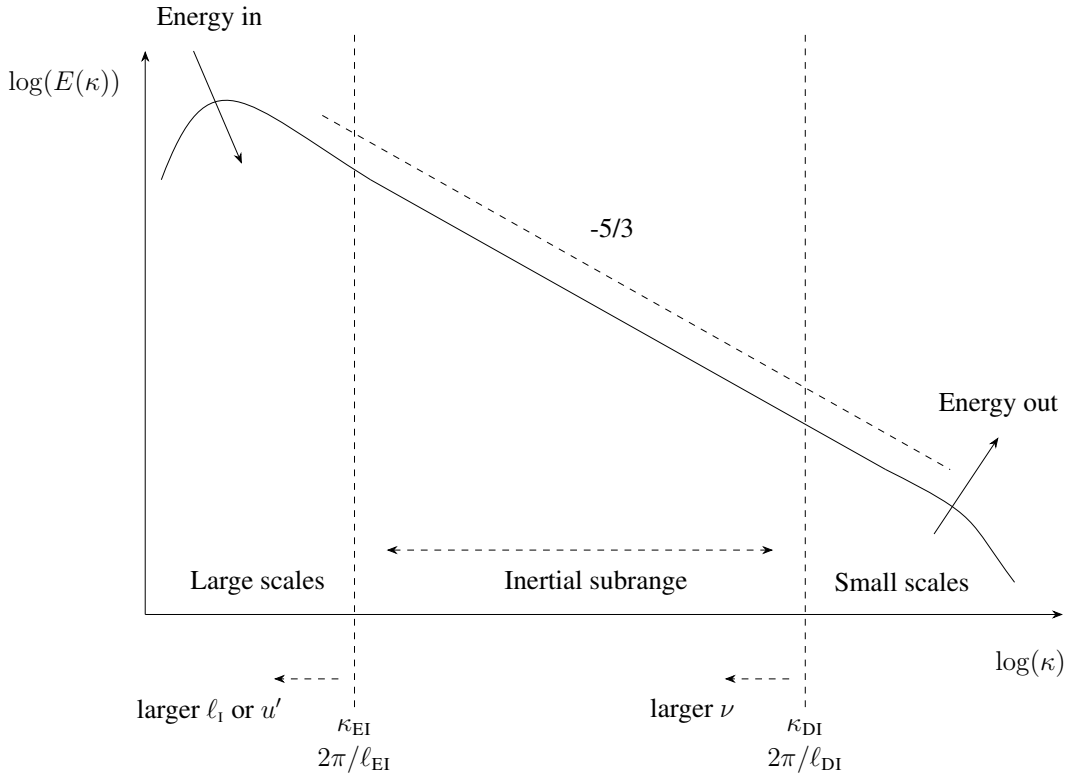

Figure 2.3: Energy cascade in wavenumber space.

The dissipation rate from turbulent motions in the range of (κ_a, κ_b) is

$$\varepsilon_{(\kappa_a,\kappa_b)} = \int_{\kappa_a}^{\kappa_b} 2\nu\kappa^2 E(\kappa)\,\mathrm{d}\kappa. \tag{2.69}$$

From Kolmogorov's first and second hypothesis in the inertial range, there is an independence from viscosity where the spectrum is defined as

$$E(\kappa) = C\varepsilon^{2/3}\kappa^{-5/3}, \tag{2.70}$$

which is Kolmogorov's minus five-thirds law. The works of Williams followed by Kolmogorov gives rise to the famous energy cascade shown in Figure 2.3.

2.3 Fundamentals of Unperturbed Laminar Premixed Flames

This section provides a quick overview on the fundamentals of an unperturbed unstretched premixed laminar flame. A description of a 1D unperturbed premixed laminar flame is where a 'deflagration wave' propagates through a mixture of fuel and oxidiser at a given speed which is

dependent on the properties of the fuel, the equivalence ratio, the chamber pressure and premixed fuel temperature. For convenience, the processes of the flame can be split into four zones: unburnt-mixture, preheat, reaction and burnt. The first theoretical description of the unperturbed premixed laminar flame was proposed by Zeldovich and Frank-Kamenetzki [179] and since has been described in many texts (Poinsot and Veynante [137], Law [100] and Lipatnikov [108] for example).

2.3.1 Flame Structure

To describe an unperturbed unstretched laminar flames it is easiest to use the example of a 1-dimensional flame with a fixed frame of reference (i.e. the flame position can be seen as stationary and thus as an unchanging x position). Imagining this flame in a 1-dimensional combustor with an inlet on the left, sufficiently far away from the flame so not to interrupt natural processes, provides a constant laminar flow of premixed fuel at a velocity u_u, temperature T_u and equivalence ratio ϕ. The equivalence ratio is defined as the ratio of the fuel (f) to oxidiser (o) for stoichiometric conditions,

$$\phi = \frac{m_{\mathrm{f}}/m_{\mathrm{o}}}{(m_{\mathrm{f}}/m_{\mathrm{o}})_{\mathrm{st}}}. \tag{2.71}$$

Therefore if the mixture is lean, stoichiometric or rich the equivalence ratio ϕ is < 1, $= 1$ and > 1, respectively. On the right (again, sufficiently far away from the flame so not to disturb the flame's processes) there is an outlet which allows the combustion products to flow unrestricted out of the domain at a velocity u_b and temperature T_{ad} also known as the adiabatic flame temperature. A diagram of this configuration is shown in Figure 2.4A. For the flame to remain stationary, the flame speed, normal to the flame which in the case of a steady, unperturbed, unstrained, laminar flame is referred to as the laminar flame speed s_{L} and must equal the unburnt fluid velocity, thus ($u_u = s_{\mathrm{L}}$). As the fluid flows through the flame, the temperature is increased, due to a net exothermic reaction (from reactants to products) the burnt temperature is referred to as the adiabatic flame temperature T_{ad}. Additionally, as a result of the increase in temperature, the density of the fluid is decreased, thus from the continuity Equation (equation (2.9)),

$$u_b = u_u \frac{\rho_u}{\rho_b} \propto u_u \frac{T_{\mathrm{ad}}}{T_u}, \tag{2.72}$$

the burnt velocity u_b must be greater than the unburnt velocity, where the ratio of the burnt and unburnt density is referred to as the density ratio

$$\sigma = \frac{\rho_u}{\rho_b}. \tag{2.73}$$

Figure 2.4B, shows the flame sheet of a typical lean premixed flame showing the profiles of temperature, fuel, reaction rate $\dot{\omega}$ characteristic thicknesses, and the diffusion directions. Starting from the left at the unburnt mixture, as the fluid approaches the flame it is gradually warmed by heat that is conducted out of the reaction zone (high $\dot{\omega}$) until reactants are hot enough to start reactions. This zone is known as the pre-heat zone. Transport in this zone is dominated by convection and diffusion where reactants can diffuse into the reaction zone. The reaction zone (which is much smaller than the preheat zone) is where the bulk of the reactions occur, where the fuel oxidises until fully consumed. These reactions have a net heat release, which heats the nearby fluid through thermal diffusion. In this zone the balance is controlled almost entirely by diffusive transport where diffusion of combustion products and heat are diffused into the unburnt mixture.

As the progress of the consumption of fuel mass fraction or oxidiser mass fraction or temperature is a monotonically increasing or decreasing value, a progress variable c can be constructed to describe the current progress of the combustion at any given position in the domain from 0 to 1,

$$c = \frac{\theta - \theta_u}{\theta_b - \theta_u}, \tag{2.74}$$

where θ is a variable that monotonically increases or decreases (usually temperature or fuel mass fraction). A progress variable value can be given to represent the surface of a flame, which can define normals to the surface as

$$\boldsymbol{n} = \frac{\nabla c}{|\nabla c|}. \tag{2.75}$$

A more complete review on the choice of isosurface and progress variable will be given later in Section 3.

2.3.2 Flame Speed and Thickness

The laminar unstretched thermal thickness ℓ_{L} is a common value used to characterise the flame thickness, which then in-turn is used to characterise non-dimensionalised parameters such as

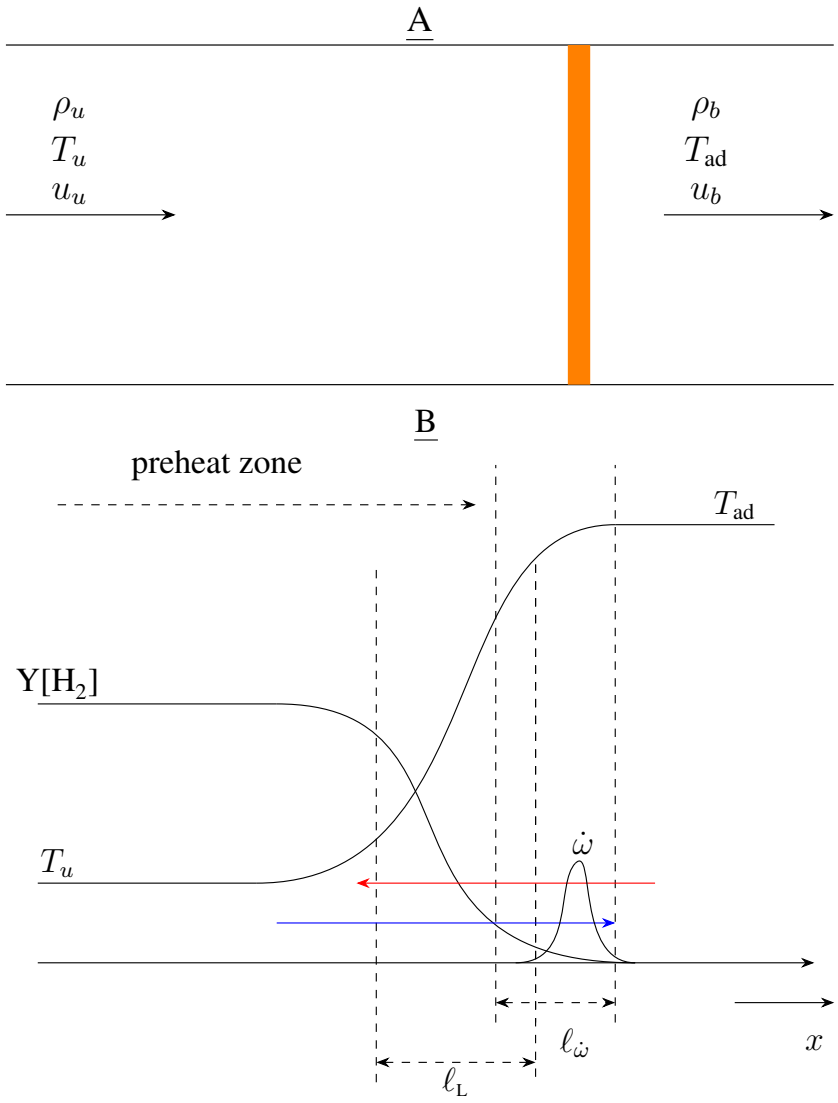

Figure 2.4: A) Basic diagram showing inflow outflow conditions for a flame with a fixed frame of reference. Orange shows the flame position. B) Example diagram of a 1-dimensional flame profile, showing the changes in fuel, temperature as-well as the thermal and reaction zone thicknesses and the directions of diffusion. The red arrow indicates the diffusion of products and heat into the preheat zone and the blue arrow indicates the diffusion of reactants into the reaction zone (ℓ_ω).

Karlovitz number and Damköhler number (to be discussed later). The flame thickness is classically defined as the ratio of the thermal diffusivity D_{th} and the flame speed [137]

$$\ell_{\text{L}}^{m} = \frac{D_{\text{th}}}{s_{\text{L}}} = \frac{\lambda}{\rho_u c_p s_{\text{L}}}, \tag{2.76}$$

where λ is the thermal conductivity and c_p is the coefficient of heat. The thermal thickness is is estimated as the length between the unburnt temperature and the adiabatic temperature if the gradient between the two temperatures was a constant at the peak value, i.e.

$$\ell_{\text{L}} = \frac{T_{\text{ad}} - T_u}{\max |\nabla T|}. \tag{2.77}$$

The flame speed can be calculated by integrating the species transportation equation over the entire domain for the fuel F, thus Equation (2.33) becomes

$$\int_{-\infty}^{\infty} \frac{\partial \rho Y_F u}{\partial \zeta} \, \mathrm{d}\zeta = \int_{-\infty}^{\infty} \left(\frac{\partial F_F}{\partial \zeta} + \rho \dot{\omega}_F \right) \, \mathrm{d}\zeta. \tag{2.78}$$

At $-\infty$ the conditions will be unburnt and at ∞ the conditions will be burnt. By substituting the unburnt velocity u_u for the flame speed s_{L}, Equation (2.78) becomes

$$\rho_b Y_{F,b} u_b - \rho_u Y_{F,u} s_{\text{L}} = F_{F,b} - F_{F,u} + \int_{-\infty}^{\infty} \rho \dot{\omega}_F \, \mathrm{d}\zeta. \tag{2.79}$$

The diffusive fluxes are zero; far away from the flame and from the continuity equation $\rho_b u_b = \rho_u s_{\text{L}}$, therefore the consumption based laminar flame speed is

$$s_{\text{L}} = -\frac{1}{\rho_u \left(Y_{F,u} - Y_{F,b} \right)} \int_{-\infty}^{\infty} \rho \dot{\omega}_F \, \mathrm{d}\zeta. \tag{2.80}$$

2.4 Freely-Propagating Premixed Laminar Flames

In the context of this project a laminar freely-propagating flame is a premixed flame that can propagate naturally, unrestricted by combustor geometry, external fluid velocity, turbulence and any external forcing. Any changes in the flame speed or behaviour will be the direct result of chemistry and the fluid response to the flame. Freely-propagating flames are rare in real world combustors, especially RICE, however as will be shown throughout this project, for lean hydrogen flames understanding the freely-propagating behaviour is a prerequisite to the successful study and modelling of TD-unstable flames. Many multidimensional freely propagating flames have complex behaviour where flame structures can naturally form and

variation in stretch can result in varying flame speed along the flame surface. This is especially true for lean hydrogen flames. This section introduces the key concepts of a freely-propagating flame relevant to lean hydrogen flames and the effects of intrinsic flame instabilities on the flame speed.

2.4.1 Intrinsic Flame Instability

An intrinsic instability is an instability caused by the flame itself without the influence of external factors. There are two intrinsic premixed flame instabilities; the Darrieus-Landau (DL) instability [56, 96] and the thermodiffusive (TD) instability. The DL instability results from the interaction between the high density of the premixed fuel and the lower density of the hot burnt gasses. This density jump increases the fluid velocity in regions of negative curvature and decreases the fluid velocity in regions of positive curvature.

The TD instability results from a disparity in the diffusion of heat and the diffusion of fuel. This ratio of thermal diffusion to fuel diffusion is expressed as the Lewis number. The Lewis number can be defined as

$$\mathrm{Le}_k = \frac{D_t}{D_k}. \tag{2.81}$$

Where D_t is the thermal diffusion and D_k is the diffusion of species k. A common measure of a premixed mixtures Lewis number is the effective Lewis number, which is given as [118]

$$\mathrm{Le}_{\text{eff}} = \begin{cases} \dfrac{\mathrm{Le}_{\mathrm{O}} + \mathcal{A}\mathrm{Le}_{\mathrm{F}}}{1+\mathcal{A}}, & \mathcal{A} = 1 + \beta\left(\phi^{-1} - 1\right) \quad \text{if lean mixture } \phi < 1, \\ \dfrac{\mathrm{Le}_{\mathrm{F}} + \mathcal{A}\mathrm{Le}_{\mathrm{O}}}{1+\mathcal{A}}, & \mathcal{A} = 1 + \beta\left(\phi - 1\right) \quad \text{if rich mixture } \phi > 1, \\ \dfrac{\mathrm{Le}_{\mathrm{F}} + \mathrm{Le}_{\mathrm{O}}}{2}, & \text{if stoichiometric mixture } \phi = 1, \end{cases} \tag{2.82}$$

where Le_{F} and Le_{O} is the Lewis number of the fuel and oxidiser, β is the Zeldovich number and ϕ is the equivalence ratio of the air-fuel mixture (which will be defined later in section 2.3). It will be shown that the effective Lewis number is a very useful quantity for predicting flame behaviour. In low Lewis number flames ($\mathrm{Le} < 1$), in regions of positive curvature, the fuel diffuses into the region quicker than the heat, resulting in a focusing of heat and fuel (for more details see books [137, 97]). The focusing results in an increase in fuel consumption rate and therefore an increase in local fuel consumption based flame speed. The opposite is true for

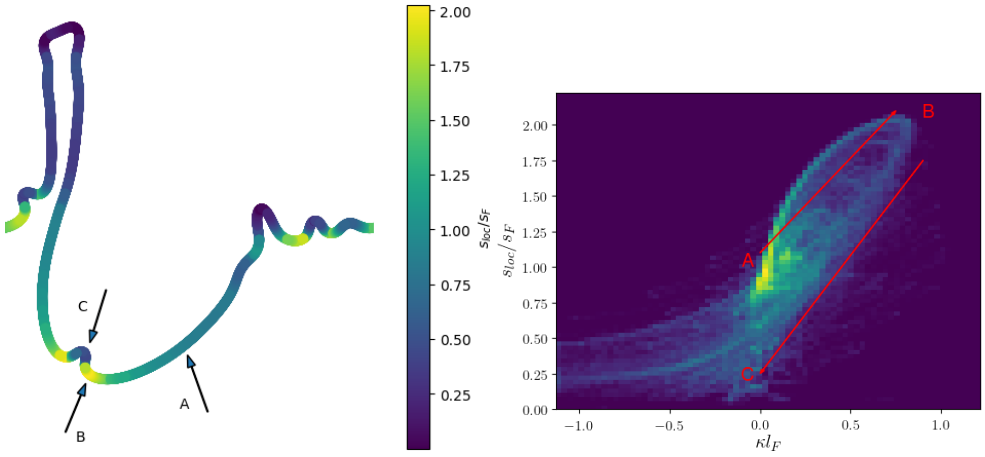

Figure 2.5: LHS shows the flame surface of a typical laminar 2-dimensional TD unstable flame (a flame finger) with the surface coloured by the local fuel consumption based flame speed. (A) shows a low positively curved region with near to slightly enhanced flame speed, (B) shows a strongly positively curved region resulting in greatly enhanced flame speed and (C) which points to a region of strongly negative curvature and therefore low speed. RHS shows the same points illustrated on a JPDF of surface flame speed as a function of curvature [80].

regions of negative curvature resulting in regions of reduced local flame speed. Figure 2.5 from [80] shows an example of this affect by Howarth and Aspden [80]. The variation of flame speed along the surface then results in flame structures forming, increasing the flame surface area and the global fuel consumption rate. An example of this effect is illustrated in 2D by Berger *et al.* [36]. In the context of lean hydrogen flames the TD-instability is considerably the leading order instability and therefore will be the focus of this background.

Local Flame Speed

Markstein [115], using experimental evidence, proposed a dependence of the local burning velocity on the local flame front curvature. Additional later works [119, 130, 54] found that the local flame speed depended on both local curvature and hydrodynamic strain, leading to a prediction of the local flame speed of

$$s_{\text{loc}} = s_{\text{L}} - \mathcal{L}\mathbb{K} = s_{\text{L}} - \mathcal{L}\left(s_{\text{L}}\kappa + E\right), \tag{2.83}$$

where $\mathcal{L}$ is a characteristic length (now referred to as the Markstein length), κ is the local flame curvature, $\mathbb{K}$ is the flame stretch rate and $E = -\boldsymbol{n}\cdot\boldsymbol{S}_{i,j}\cdot\boldsymbol{n}$ is the flame strain (and $S_{i,j}$ is the

strain rate tensor). This is often referred to as stretch which is the fractional rate of change of a flame surface area, [86, 172, 116] for example. The analysis was originally used to describe the stabilising effects of perturbed stable flames, where a positively curved flame fronts burn slower than un-stretched regions and trailing negatively regions burn faster, stabilising the flame. This behaviour is typical of a negative Markstein length, which is typical for traditional carbon based fuels. However, explained above lean hydrogen flames often accelerate with positive curvature, typical of positive Markstein lengths ([77, 148, 164, 29, 30] for example). Numerical work has observed that for lean hydrogen flames the mean local flame speed increases above the laminar unstretched value [36]. The increase in the mean local flame speed is often referred to in the literature as stretch factor (I_o) [42],

$$I_0 = \frac{s_\mathrm{T}}{s_\mathrm{L}} \frac{A}{A_\mathrm{T}} = \frac{\overline{s_\mathrm{loc}}}{s_\mathrm{L}}, \tag{2.84}$$

where $\overline{s_\mathrm{loc}}$ is the mean local consumption based flame speed.

Global Flame Speed and Structure

Laminar flame structure has been extensively studied for DL-instabilities [78, 118, 117, 68] for example, TD-unstable structures has seen less attention, especially numerically in 3D with complex chemistry. In 2D, TD-unstable structures commonly form flame fingers (shown in Figure 2.5), these have been observed numerically by [6, 7, 5, 36, 80] for example. These flame fingers have strongly positively curved tips, with significantly enhanced local flame speeds, local thinning and super adiabatic temperatures. Additionally, the size of the structures appears to depend on the reactant conditions, as pressure increases the flame fingers become thinner, faster and hotter and lead to the formation of new flame fingers. 3D freely-propagating flames exhibit a different structure, and the flame fingers in 2D are represented by bulb-like structures, with strong leading points and edges with trailing extinction channels and points as shown in [59, 32] for example. It is currently unclear, how this difference in flame structure will affect the local flame statistics and global flame structure will vary over a large range of conditions. This question will be one of the primary focuses of Chapter 4.

2.4.2 Linear Stability Analysis and Flame Characteristics

In the context of premixed laminar flames, linear stability analysis is a method used to anticipate the growth rate of a perturbed flame based on the reactant conditions and wave number. By considering a flame surface of the form $F(x,t) = Ae^{\omega t + ikx}$, Matalon *et al.* [118] formulated a dispersion relationship for the growth rate of an instability based off the thermal, molecular and viscous diffusion contributions

$$\omega = \underbrace{\frac{1}{\sigma+1}\left(\sqrt{\sigma^3+\sigma^2-\sigma}-\sigma\right)}_{\omega_{\mathrm{DL}}} s_{\mathrm{L}}k \underbrace{-\left[B_1+\beta B_2\left(\mathrm{Le}_{\mathrm{eff}}-1\right)+\mathrm{Pr}B_3\right]}_{\omega_2}\ell_{\mathrm{L}}s_{\mathrm{L}}k^2+\ldots, \quad (2.85)$$

where ω_{DL} is the DL contribution, k is the wave number, $\sigma = \rho_{\mathrm{u}}/\rho_{\mathrm{b}}$ is the density ratio arising from the thermodynamic expansion from the heat released from combustion, Pr is the Prandtl number, β is the Zeldovich number of the reaction and the $\mathrm{Le}_{\mathrm{eff}}$ is the effective Lewis number. The values B_1, B_2 and B_3 are positive values that represent the thermal, molecular and viscous diffusion respectively on flame stability. As noted by Matalon [117] the thermal and viscous diffusion has a stabilising effect on the flame. The molecular diffusion can have a stabilising (when $\mathrm{Le}_{\mathrm{eff}} > 1$) or destabilising ($\mathrm{Le}_{\mathrm{eff}} < 1$). If ω_2 is positive the flame will be TD-unstable.

Howarth and Aspden [80] showed that for 2D lean hydrogen flames, the mean local flame speed increases linearly with an instability parameter ω_2 in the high pressure regime and exponentially in the low pressure regime. The inverse is true for the mean local thermal thickness

$$\overline{s_{\mathrm{loc}}} \approx \begin{cases} \exp\left(0.057\omega_2\right) & \text{if low pressure regime,} \\ 1+0.22\omega_2 & \text{if high pressure regime,} \end{cases} \quad (2.86)$$

$$\overline{\ell_{\mathrm{loc}}} \approx \begin{cases} \exp\left(-0.045\omega_2\right) & \text{if low pressure regime,} \\ \left(1+0.13\omega_2\right)^{-1} & \text{if high pressure regime.} \end{cases} \quad (2.87)$$

It was noted that from Equation 2.85 that the Zeldovich number has a strong effect on the value of ω_2. Figure 2.6 shows a contour plot of ω_2 for different values of equivalence ratio and pressure at temperatures 300K and 700K. At a given temperature there are three distinct regions; stable, low pressure unstable and high pressure unstable with the most unstable surface (ridge) separating the high and low pressure regime. To separate the low pressure and

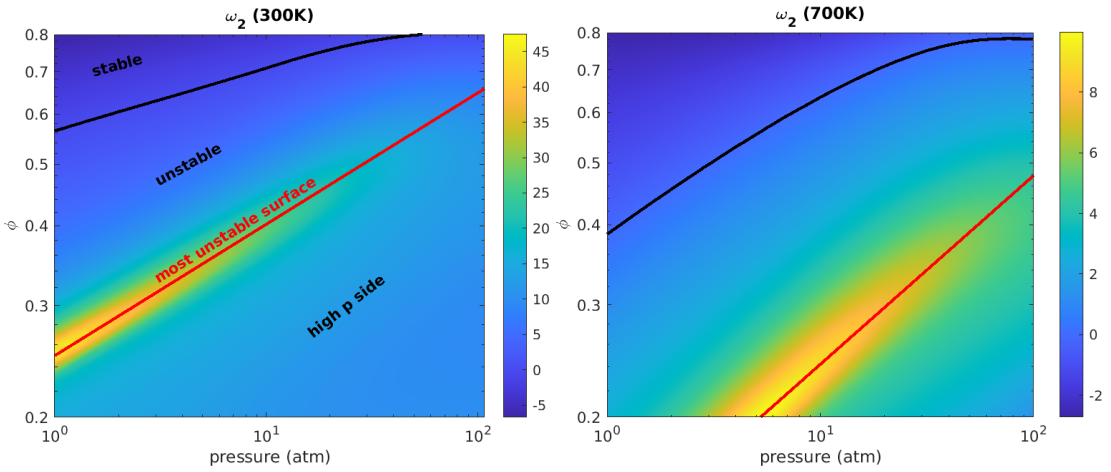

Figure 2.6: Contour of ω_2 over a range of equivalence ratios and pressures for temperatures 300K and 700K with different regimes labelled.

high pressure regime a critical pressure is calculated,

$$p_c = p_{\text{ref}} \left(\frac{20\phi}{7 - 2\frac{T}{T_{\text{ref}}}} \right)^{150/\left(21+10\frac{T}{T_{\text{ref}}}\right)}, \tag{2.88}$$

where $T_{\text{ref}} = 300\text{K}$ and $p_{\text{ref}} = 1\text{atm}$ and if

$$\begin{cases} p < p_c \text{ and } \omega_2 \leq 0 & \text{TD stable regime,} \\ p < p_c \text{ and } \omega_2 > 0 & \text{TD unstable low pressure regime,} \\ p > p_c & \text{TD unstable high pressure regime.} \end{cases} \tag{2.89}$$

It remains unanswered in the literature as to what effect different zones have on the 3D laminar and turbulent flames and how it effects the local and global flame statistics as well as the flame structure. These unknowns will be researched in Chapters 4, 5 and 6.

2.5 Turbulent Flames

Most combustors inducing RICE are turbulent, where the flame experiences rapid, chaotic fluctuations of the velocity field, which can manipulate the flame, both altering the local burning rates and increase the flame surface area which can then enhance the turbulent flame speed. The turbulent flame speed is the staple for the majority of device scale reacting simulation codes such as Vectis. The turbulent flame speed defines how much fuel is being

consumed; the resulting burning velocity burns normal to the flame brush and is interchangeable with “burning velocity” and “consumption based turbulent flame speed”; not to be confused with displacement speed. As typical flames, such as kernels, continually grow and therefore change size, it is useful to define global flame statistics relative to the cross-sectional area.

2.5.1 Damköhler 1940

As described in Damköhler’s landmark paper [55] and later explained by Peters [134, 135], who presented the theoretical expression of the turbulent flame speed, two primary burning regimes to describe the interaction between turbulence and flame surface area were presented. These are the small-scale and large-scale turbulence.

Large-Scale Limit (Damköhler’s First Hypothesis)

At the large-scale it was assumed that the interaction between turbulence and the flame front is purely kinematic. Given a mass flux $\dot{m}$ with a laminar flame speed s_{L} and a flame surface area A_T, the mass flux though a cross-sectional area A_x with a turbulent flame speed s_{T} gives

$$\dot{m} = \rho_u s_{\mathrm{L}} A_T = \rho_u s_{\mathrm{T}} A_x, \tag{2.90}$$

This configuration is presented as an example of a flame kernel in Figure 2.7A which shows an example for a typical flame kernel burning outwards. This example is valid for other types of burners such as a bunsen flame, where a flame surface is wrinkled by the turbulence which in-turn increases the flame surface area. The flame surface then burns at the local consumption based flame speed s_{loc} (assumed as s_{L} in most texts) normal to the flame surface. The flame burns at the turbulent flame speed s_{T} normal to the mean line of the flame surface (dotted line), which for the kernel example would be radially outwards. From Damköhler’s definition, this means that the turbulent flame speed must be the flame surface wrinkling multiplied by the averaged local flame speed (assumed as s_{L})

$$s_{\mathrm{T}} = s_{\mathrm{L}} \Psi_{\mathrm{T}}, \tag{2.91}$$

Where Ψ_{T} is the flame surface wrinkling

$$\Psi_{\mathrm{T}} = \frac{A_T}{A_x}. \tag{2.92}$$

An alternative visual example for a steady premixed flame in a duct is shown in Figure 2.21 in Peters' book [135]. Following a geometrical analogy with a bunsen flame, it was then shown by Damköhler that the increase in the flame surface area, relative to the cross-sectional area is proportional to the r.m.s. velocity u' over the laminar flame speed

$$\frac{s_{\mathrm{T}}}{s_{\mathrm{L}}} \sim 1 + \frac{u'}{s_{\mathrm{L}}}. \tag{2.93}$$

For large values of u' applied to the laminar flame speed Equation (2.93) becomes the large-scale limit

$$s_{\mathrm{T}} \sim u'. \tag{2.94}$$

Equation (2.93) has proven to be remarkably robust ([109] for example).

Small-Scale Limit (Damköhler's Second Hypothesis)

For small-scale turbulence, it was argued that turbulence modifies the transport between the reaction zone and the unburnt gas [55, 135]. Given the scaling relation for the laminar flame speed

$$s_{\mathrm{L}} \sim \sqrt{\frac{D_{\mathrm{L}}}{\tau}}, \tag{2.95}$$

where D_{L} is the laminar diffusivity and τ the chemical time scale. By using a theoretical turbulent diffusivity D_{T} Equation (2.95) becomes

$$s_{\mathrm{T}} \sim \sqrt{\frac{D_{\mathrm{T}}}{\tau}}, \tag{2.96}$$

where τ remains unchanged. By combining Equation (2.95) and (2.96)

$$s_{\mathrm{T}} \sim s_{\mathrm{L}} \sqrt{\frac{D_{\mathrm{T}}}{D_{\mathrm{L}}}}. \tag{2.97}$$

Given that D_{T} is proportional to $u'\ell_{\mathrm{I}}$ and D_{L} is proportional to $s_{\mathrm{L}}\ell_{\mathrm{L}}$ then

$$s_{\mathrm{T}} \sim s_{\mathrm{L}} \sqrt{\frac{u'}{s_{\mathrm{L}}} \frac{\ell_{\mathrm{I}}}{\ell_{\mathrm{L}}}}, \tag{2.98}$$

by using the dimensionless quantities $\Upsilon_{\mathrm{L}} = u'/s_{\mathrm{L}}$ and $\Lambda_{\mathrm{L}} = \ell_{\mathrm{I}}/\ell_{\mathrm{L}}$ equation (2.98) becomes

$$s_{\mathrm{T}} \sim s_{\mathrm{L}} \sqrt{\Upsilon_{\mathrm{L}} \Lambda_{\mathrm{L}}}. \tag{2.99}$$

Ultimately this shows that for small-scale turbulence the turbulent flame speed ratio ($s_{\mathrm{T}}/s_{\mathrm{L}}$) depends both on the relative turbulent fluctuation u' and the relative turbulent length scale ℓ_{I}.

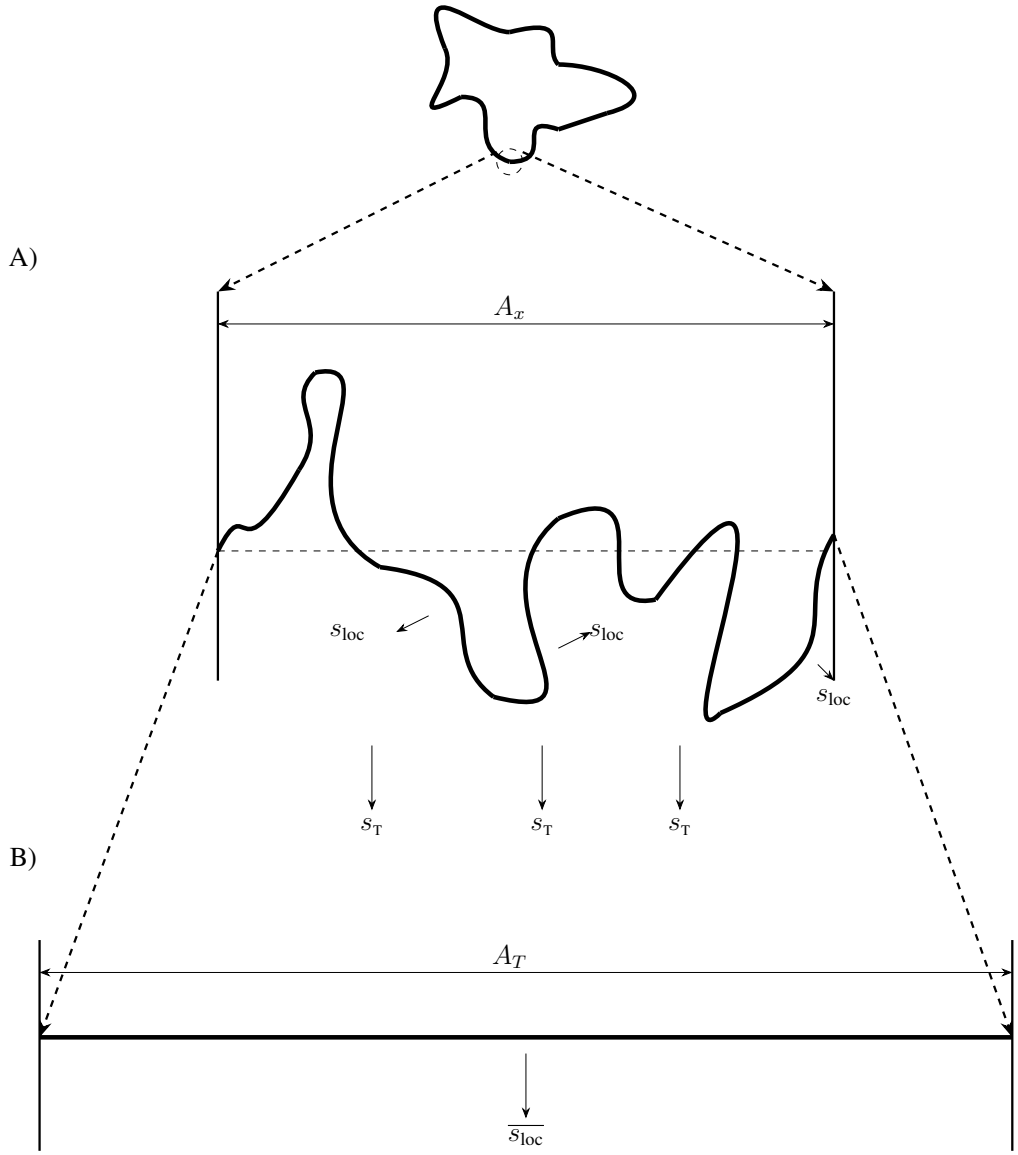

Figure 2.7: Neglecting thermal expansion for simplicity. **A)**. 2-dimensional diagram showing the magnification of a turbulent flame kernel presented as a turbulent flame surface (bold curves) within a given control volume of width A_x, with local consumption based flame speed s_{loc} propagating normal to the flame surface. From Damköhler's 1st [55, 135], the global consumption based flame speed s_{C} is then the ratio of the flame surface area A_T to cross-sectional area of the control volume width A_x ($\Psi_{\text{T}} = A_T/A_x$) multiplied by the averaged local global consumption based flame speed s_{loc}. **B)**. Diagram of the same flame as in A, but with the flame stretched flat so that it has a length of A_T and propagates normal to the new flame image at s_{loc}.

At a fixed integral lengthscale, as the turbulent regime transitions from small-scale turbulence to large-scale turbulence, this causes a bending from the large-scale gradient ($s_{\mathrm{T}} \propto u'$) to the small-scale gradient ($s_{\mathrm{T}} \propto \sqrt{u'}$), which is often referred to as the bending effect. For an in-depth numerical study of the bending effect a highly recommended text is the thesis of Nivarti [125]. An example of the proposed regime is shown in Figure 2.8A, where the Damköhler number Da_{L} and Reynold's number will be discussed later.

However, if $\overline{s_{\mathrm{loc}}} \neq s_{\mathrm{L}}$ (for example in non-unity Lewis number flames) then an adjustment is required and the turbulent flame speed can be defined as

$$s_{\mathrm{T}} = \overline{s_{\mathrm{loc}}}\Psi_{\mathrm{T}}, \tag{2.100}$$

or using the stretch factor notation

$$s_{\mathrm{T}} = I_0 s_{\mathrm{L}}\Psi_{\mathrm{T}}. \tag{2.101}$$

A key point is that, regardless of the turbulent regimes (large-scale or small-scale), the turbulent flame speed is increased with increasing r.m.s velocity and if in the small-scale turbulence also increases with integral length scale. Note that Damköhler's analysis assumes a laminar flame speed which is independent of the turbulence, thus is only evaluating the effects of turbulence on the flame surface area and therefore the large-scale limit is

$$\Psi_{\mathrm{T}} = s_{\mathrm{L}} + u', \tag{2.102}$$

and the small-scale limit is

$$\Psi_{\mathrm{T}} \sim \sqrt{\Upsilon_{\mathrm{L}}\Lambda_{\mathrm{L}}}. \tag{2.103}$$

2.5.2 Turbulent Combustion Regimes

As in Section 2.2, turbulence represents a range of eddies ranging in size (ℓ_{R}) from the integral scales $\ell_{\mathrm{R}} = \ell_{\mathrm{I}}$ to the Kolmogorov scales $\ell_{\mathrm{R}} = \eta$ with a turnover time of

$$\tau(\ell_{\mathrm{R}}) = \frac{\ell_{\mathrm{R}}}{u'(\ell_{\mathrm{R}})} = \frac{\ell_{\mathrm{R}}^{2/3}}{\varepsilon^{1/3}}, \tag{2.104}$$

where ε is the kinetic energy dissipation rate. The Damköhler number (Da) is a dimensionless quantity representing the ratio of the turbulent timescale (eddy turnover time) at scale ℓ_{R}

($\tau_t(\ell_{\mathrm{R}})$) to the flame to the chemical time scale (τ_c). By defining the chemical time scale as the time it takes for a flame to burn through one thermal thickness ($\tau_c = \ell_{\mathrm{L}}/s_{\mathrm{L}}$) then

$$\mathrm{Da}(\ell_{\mathrm{R}}) = \frac{\tau_t(\ell_{\mathrm{R}})}{\tau_c} = \frac{\ell_{\mathrm{R}} s_{\mathrm{L}}}{u'(\ell_{\mathrm{R}})\ell_{\mathrm{L}}}. \tag{2.105}$$

It can be seen that as the eddy size decreases from the large scales to the smallest scale the $\mathrm{Da}(\ell_{\mathrm{R}})$ is decreased as the chemical timescale becomes larger than the turbulent time scale. As a result at the smaller scales, the flame has influence on the turbulent scales and therefore Damköhler is not well-defined at these scales. Damköhler is typically used to describe the large scales, where the turbulent time is much larger than the chemical time, thus the integral scales are used ($\ell_{\mathrm{R}} = \ell_{\mathrm{I}}$ and $u'(\ell_{\mathrm{R}}) = u'$) therefore Damköhler number will be defined as

$$\boxed{\mathrm{Da}_{\mathrm{L}} = \frac{s_{\mathrm{L}}\ell_{\mathrm{I}}}{u'\ell_{\mathrm{L}}} = \frac{\Lambda_{\mathrm{L}}}{\Upsilon_{\mathrm{L}}},} \tag{2.106}$$

again where the dimensionless quantities are $\Upsilon_{\mathrm{L}} = u'/s_{\mathrm{L}}$ and $\Lambda_{\mathrm{L}} = \ell_{\mathrm{I}}/\ell_{\mathrm{L}}$. Following from Damköhler's work, if $\mathrm{Da}_{\mathrm{L}} \gg 1$ the turbulent flame is in the large-scale limit and if $\mathrm{Da}_{\mathrm{L}} \ll 1$ the turbulent flame is in the small-scale limit (shown in Figure 2.8A).

A second dimensionless number, the Karlovitz number, is used to characterise the interaction between the smallest scales and describes the ratio of the turbulent time at the Kolmogorov scale to the chemical timescale, thus

$$\mathrm{Ka}_{\mathrm{L}} = \mathrm{Da}(\eta)^{-1} = \frac{\tau_c}{\tau_t(\eta)} = \frac{u'(\eta)\ell_{\mathrm{L}}}{\eta s_{\mathrm{L}}}. \tag{2.107}$$

Using Equation (2.54), (2.59) and (2.76) Karlovitz number can be defined as

$$\mathrm{Ka}_{\mathrm{L}} = \frac{\sqrt{\varepsilon/\nu}}{s_{\mathrm{L}}/\ell_{\mathrm{L}}}, \tag{2.108}$$

where ν is the kinematic viscosity of the unburnt gas.

Kolmogorov similarity hypotheses applied to turbulent premixed flames

It was discussed in [22] that from the classical Richardson/Kolmogorov turbulent cascade, if it is assumed that the turbulent intensity is sufficient for the turbulent inertial sub-range to extend to the flame scale (i.e. the thin reaction zone, discussed below), dilatation modifies the turbulent structure at the flame scale, disrupting the classical dissipation sub-range. It is

discussed at length in Towery *et al.* [162] that the energy is still dissipated by viscosity at the small scales, but not in the traditional Kolmogorov length scale as in the constant-density non-reacting flow. For this reason, Aspden *et al.* [22] argued if the Karlovitz number is defined as the characteristic of turbulence-flame interaction at the flame scale then it would be illogical to define the Karlovitz number in terms of Kolmogorov scales. The energy dissipation rate is constant through the inertial sub-range, therefore can be written in terms of integral length. A general length r between the integral length and flame thickness and the flame thickness

$$\varepsilon = \frac{u'^3}{\ell_{\mathrm{I}}} = \frac{u'^3_r}{r} = \frac{u'^3_{\ell_{\mathrm{L}}}}{\ell_{\mathrm{L}}}, \tag{2.109}$$

where the latter represents the energy dissipation rate at the flame scale, which is inside the inertial sub-range. By normalising the turbulent velocity at the flame scale $u'_{\ell_{\mathrm{L}}}$ by the flame speed gives

$$\frac{u'_{\ell_{\mathrm{L}}}}{s_{\mathrm{L}}} = \frac{u'}{s_{\mathrm{L}}}\left(\frac{\ell_{\mathrm{L}}}{\ell_{\mathrm{I}}}\right)^{1/3} = \mathrm{Ka}_{\mathrm{L}}^{2/3}, \tag{2.110}$$

thus the Karlovitz number is defined as

$$\boxed{\mathrm{Ka}_{\mathrm{L}} = \sqrt{\frac{u'^3}{s_{\mathrm{L}}^3}\frac{\ell_{\mathrm{L}}}{\ell_{\mathrm{I}}}} = \sqrt{\frac{\Upsilon_{\mathrm{L}}^3}{\Lambda_{\mathrm{L}}}},} \tag{2.111}$$

which is the preferred approach in this thesis. Later in Chapter 6, this approach is supported by having the same turbulent-flame interactions independently from length scale. Note that this definition is identical to that explained in Peters [135] under different assumptions.

Using the same assumptions, the turbulent Reynolds number defined in Equation (2.51) becomes

$$\boxed{\mathrm{Re}_{\mathrm{L}} = \frac{u'\ell_{\mathrm{I}}}{s_{\mathrm{L}}\ell_{\mathrm{L}}} = \Upsilon_{\mathrm{L}}\Lambda_{\mathrm{L}}.} \tag{2.112}$$

Using the dimensionless quantities of Damköhler Da_{L} and Karlovitz Ka_{L} numbers three different burning regimes can be identified (referred to as the classical burning regimes, see [40]) which can be shown graphically in Figure 2.8A and is referred to as the classic regime diagram. The regimes identified were separated by Damköhler's small and large-scale limit and the Klimov-Williams criterion (which defines the point where turbulence at the Kolmogorov length can enter the flame $\mathrm{Ka}_{\mathrm{L}} = 1 =$ and $\eta = \ell_{\mathrm{L}}$):

- $\mathrm{Ka}_{\mathrm{L}} < 1$, the chemical time scale is shorter than the turbulent time and the flame thickness is smaller than the Kolmogorov length scale (i.e. $\ell_{\mathrm{L}} < \eta$). When this is the case, the turbulence cannot penetrate the flame and the flame profile closely resembles a laminar flame profile, therefore the turbulence can only wrinkle the flame surface. This regime is referred to as the flamelet regime. The flamelet regime can be further divided into the corrugated ($\Upsilon_{\mathrm{L}} > s_{\mathrm{L}}$) and the wrinkled ($\Upsilon_{\mathrm{L}} < s_{\mathrm{L}}$) flamelets. If $\Upsilon_{\mathrm{L}} < s_{\mathrm{L}}$, then it is argued that the turbulent motions are too slow to wrinkle the flame, thus the flame structure.

- $\mathrm{Ka}_{\mathrm{L}} > 1$ and $\mathrm{Da}_{\mathrm{L}} > 1$, the chemical time is still smaller than the turbulent time, but Kolmogorov turbulent scales are smaller than the flame thickness and therefore can penetrate the flame and modify the internal flame structure and the flame internal structure can no longer resemble a flamelet. This regime is call the distributed reaction zone.

- $\mathrm{Da} < 1$, the chemical time is larger than the turbulent time, therefore the mixing is fast between the products and the reactants and is referred to as the well stirred reactor regime.

For more details on the history of the turbulent regimes see [38, 173, 133].

Most modern papers and texts referring to the turbulent regime diagram often are referring to the Peters' regime diagram of which its final form was presented in [134] shown in Figure 2.8B. In this approach the regimes are solely based off the Karlovitz number and the velocity ratio (u'/s_{L}). Firstly the flamelet regime is the same in Peter's proposal. Peters then defines a new regime based of the mixing length (also called the Zimont scale [186, 183]) which is the size of an eddy within the inertial sub-range that has a turnover time equal to the time needed to diffuse heat over the flame thermal thickness

$$\ell_{\mathrm{Z}} = \sqrt{\varepsilon \left(\frac{\ell_{\mathrm{L}}^2}{D}\right)^3}. \tag{2.113}$$

The physical effects of this is that an eddy of a size of the Zimont length ($\ell_{\mathrm{R}} = \ell_{\mathrm{Z}}$) will be able to transport preheated fluid within a region the size of the Zimont length. Peters explains that smaller eddies would also do this, but the contribution would be small compared to the larger

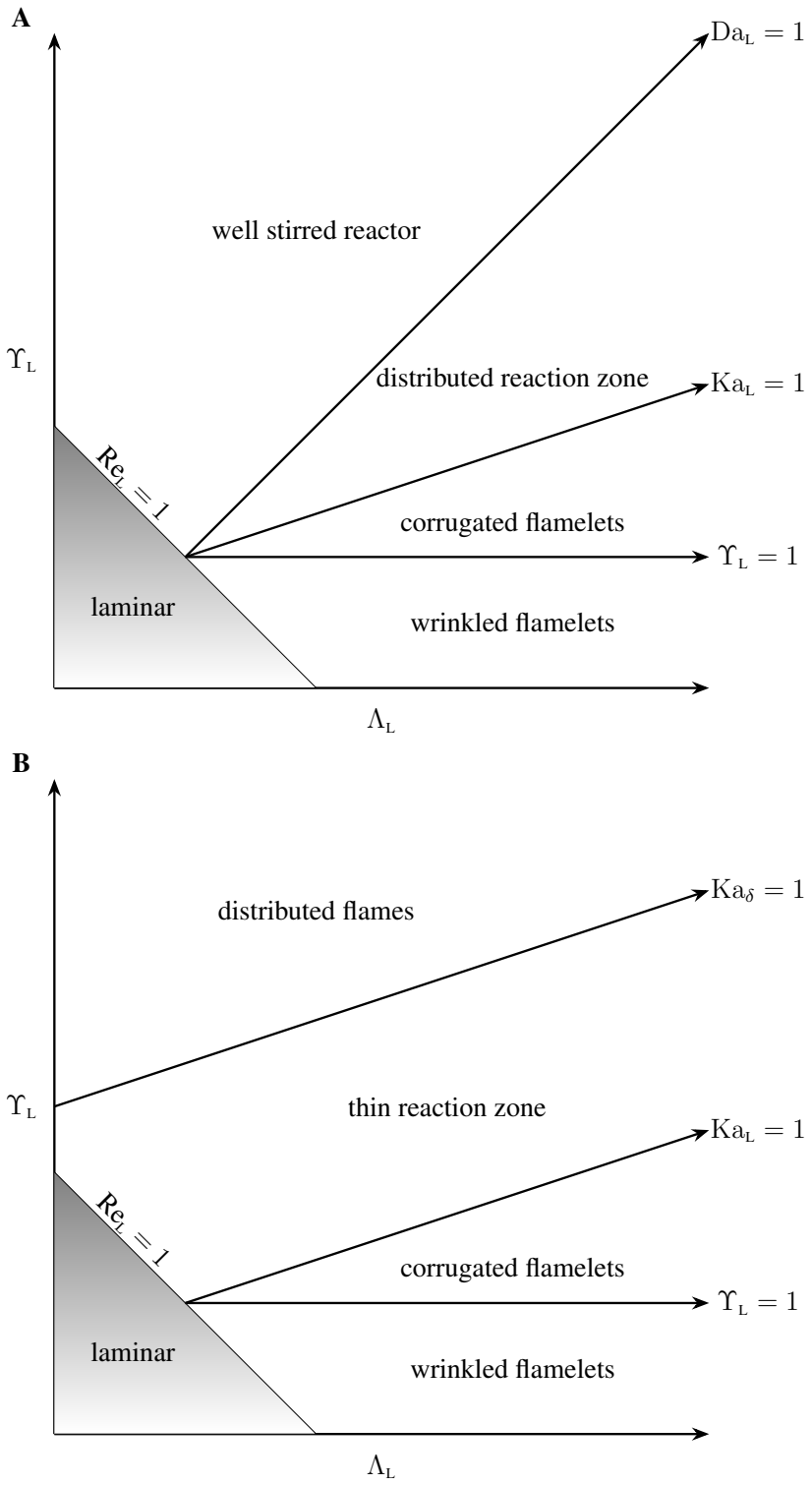

Figure 2.8: **A)**. Classical regimes [137]. **B)**. The modern regime diagram as proposed by Peters [134].

eddies. For eddies larger than the Zimont length the turnover time will be longer and thus would only be able to transport larger structures which have a larger timescale. Thus the Zimont length has been interpreted by Peters [134, 135] as the maximum length preheated fluid can be transported ahead of the flame, thus broadening the preheat zone. This zone is referred to as the thin reaction zone and can only occur when the Kolmogorov length scale is smaller than the flame thickness (i.e. $\ell_{\mathrm{Z}} > \ell_{\mathrm{L}}$). The upper limit of this regime is when the Kolmogorov length scale reaches a critical value ℓ_δ where the turbulent eddies can penetrate the flame reaction zone, this region is called the broken reaction zone or the distributed burning regime. Typically, distribution occurs at $\mathrm{Ka}_{\mathrm{L}} > 100$, although this is dependent on reactant conditions, for more details see [20].

2.6 Turbulent Flame Modelling

2.6.1 Direct Numerical Simulation

Utilising DNS to simulate turbulent flows, all the scale of turbulence need to be resolved, including the smallest Kolmogorov length scales; therefore the numerical cell size required to resolve the smallest scales is

$$\Delta x \sim \mathcal{C}_{\Delta x}\eta, \tag{2.114}$$

where $\mathcal{C}_N$ is a constant (Yeung and Pope [176] suggest $\mathcal{C}_N = 2$ for example). Given that the size of the integral lengthscale is typically related to the size of the combustor or numerical domain and a cube domain of size L_x then the relation $\eta/\ell_{\mathrm{I}} \sim \mathrm{Re}^{-3/4}$ becomes

$$L_x \sim \ell_{\mathrm{I}} \sim \mathrm{Re}^{3/4}\eta, \tag{2.115}$$

therefore the number of computational cells N_{cells} in the domain is given as

$$N_{\text{cells}} \sim \left(\frac{L_x}{\Delta x}\right)^3 \sim \frac{L_x^3}{\mathcal{C}_N^3\eta^3} \sim \frac{\mathrm{Re}^{9/4}}{\mathcal{C}_N^3}, \tag{2.116}$$

which according to [176], yields

$$N_{\text{cells}} \geq \frac{1}{8}\mathrm{Re}^{9/4}. \tag{2.117}$$

Given that in an explicit time-stepping numerical scheme, to maintain stability of the scheme a time stepping constraint is required and is given as

$$\Delta t = \mathcal{C}_{\mathrm{CFL}}\Delta x/u, \tag{2.118}$$

where $\mathcal{C}_{\text{CFL}}$ is a constant relating to the numerical stability (referred to as the CFL number and is dependent on the numerical methods used). Given Equation (2.114) then

$$\Delta t = \mathcal{C}_{\text{CFL}}\mathcal{C}_{\Delta x}\frac{\eta}{u} \tag{2.119}$$

Given that the computation cost for a simulation is proportional to the number of time steps and the number of cells then

$$\text{Cost} \sim \text{Re}^3. \tag{2.120}$$

DNS is a tool only suited to investigate the small-scales, thus turbulence and combustion modelling of the physics is required for practical combustor sizes. There are two primary simulation approaches practical for multi-dimensional, transient reacting flows, Large Eddy Simulation (LES) and Unsteady Reynolds Averaged Navier Stokes (URANS). URANS models all scales of turbulence and the flame and the computational grid is used to compute mean flow. LES is a hybrid of DNS and RANS, where the large energy containing eddies are computed and the smaller scales are modelled using a turbulence model where the scales modelled vs computed are separated via a filter cutoff wavelength (κ_c). This method does require a finer computational grid (dependent on the cutoff length), but often does yield more accurate results but can significantly increase the computational cost of the simulation. An additional modelling approach with the aim to reduce the computational cost of DNS is an implicit LES (ILES) method. ILES under-resolves the smallest scales and allows the numerical scheme to naturally dissipate the energy at the grid scale; consistent with the energy cascade, see [75] for a more detailed description of ILES. This approach will be discussed in more detail in Section 3.1.4. Figure 2.9 shows a diagram of the turbulent energy kinetic spectrum as modelled or computed by the different simulation approaches.

2.6.2 Averaging the Balance Equations

Given a quantity f which contains mean $\overline{f}$ and a fluctuating f'' components

$$f = \overline{f} + f''. \tag{2.121}$$

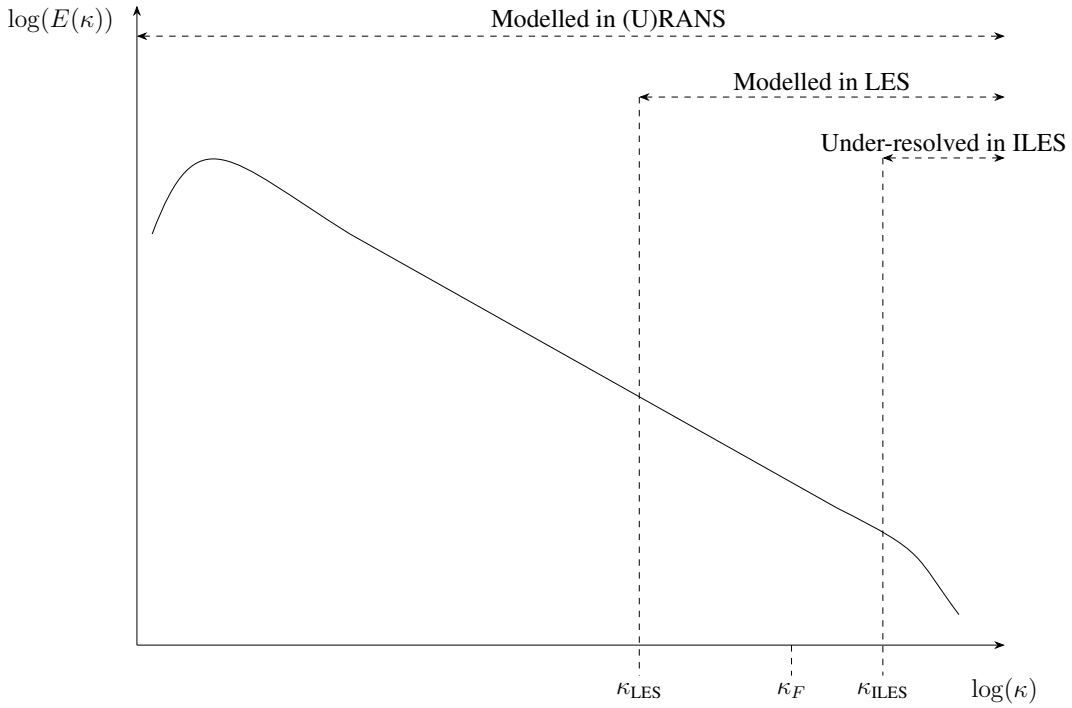

Figure 2.9: Energy cascade in wavenumber space with the different scales at with modelling approaches compute or model. κ_{LES} is the filter cutoff wavenumber and κ_F is the size of the flame thickness in wavenumber space.

By applying a mass-weighted average (also known as Favre average [67, 137]) of quantity f then

$$\tilde{f} = \frac{\overline{\rho f}}{\overline{\rho}}, \tag{2.122}$$

where the favre average of the fluctuating component is zero (i.e. $\tilde{f''} = 0$), then the Favre average of the balance equations (2.9), (2.13), (2.33) and (2.29) is given as:

$$\frac{\partial \overline{\rho}}{\partial t} + \nabla \cdot (\overline{\rho}\widetilde{\boldsymbol{u}}) = 0, \tag{2.123}$$

$$\frac{\partial \overline{\rho}\widetilde{\boldsymbol{u}}}{\partial t} = -\nabla \cdot \overline{\boldsymbol{\sigma}} + \overline{\boldsymbol{\mathcal{F}}} - \nabla \cdot \overline{\rho}\widetilde{\boldsymbol{u}}\widetilde{\boldsymbol{u}} - \nabla \cdot \left(\widetilde{\overline{\rho}\boldsymbol{u''}\boldsymbol{u''}}\right), \tag{2.124}$$

$$\frac{\partial \overline{\rho}\widetilde{Y}_k}{\partial t} = \overline{\rho}\widetilde{\dot{\omega}_k} - \nabla \cdot \overline{\boldsymbol{F}_k} - \nabla \cdot \left(\overline{\rho}\widetilde{Y}_k\widetilde{\boldsymbol{u}}\right) - \nabla \cdot \left(\widetilde{\overline{\rho}Y_k\boldsymbol{u''}}\right). \tag{2.125}$$

$$\frac{\partial \overline{\rho}\widetilde{h}}{\partial t} + \nabla \cdot \widetilde{\mathcal{Q}} + \nabla \cdot \left(\overline{\rho}\widetilde{h}\widetilde{\boldsymbol{u}}\right) + \nabla \cdot \left(\widetilde{\overline{\rho}h''\boldsymbol{u''}}\right) = 0. \tag{2.126}$$

This leaves some unclosed-terms, namely the Reynolds stress ($\widetilde{\boldsymbol{u''}\boldsymbol{u''}}$), turbulent transport of species ($\widetilde{Y''\boldsymbol{u''}}$), the enthalpy ($\widetilde{h''\boldsymbol{u''}}$) and ($\widetilde{\dot{\omega}_k}$). A traditional approach to modelling the terms

in the form $\widetilde{\mathcal{V}''\boldsymbol{u}''}$ is using an eddy-viscosity-based model approach; for example for the Reynolds stress

$$\widetilde{\boldsymbol{u}''\boldsymbol{u}''} = -\nu_T \nabla \tilde{\boldsymbol{u}}, \tag{2.127}$$

where ν_T is the eddy viscosity which can be seen as the product of some velocity scale u_T and length scale ℓ_T,

$$\nu_T = u_T \ell_T. \tag{2.128}$$

The popular turbulence model $k - \varepsilon$ model [140] which is used in Vectis and many device scale engine simulation tools is defined as

$$\nu_T = C\frac{k^2}{\varepsilon}, \tag{2.129}$$

where C is some constant. Turbulence modelling is a vast subject and many other popular models exist and is beyond the scope of this project, thus for a comprehensive summary see [171]. For a summary of models for the reacting closure terms in the form of $\widetilde{\mathcal{V}''\boldsymbol{u}''}$ see [137].

Closing $\widetilde{\dot{\omega}_k}$ is a challenging and ongoing problem in combustion research, which has been made more challenging for TD-unstable flames. There are many approaches, some brief examples (not intended to be a comprehensive list) include [137]:

- Arrhenius approach, which relates the reaction rate to the mean values of density and reduced temperature. This model is better known as the no-model and contains no sub-grid modelling, thus is only really appropriate in low turbulence where $\mathrm{Da_L} \ll 1$, thus is not typically used to model real world combustors such as internal combustion engines.

- Eddy Break Up [157] assumes high turbulence where $\mathrm{Re_L} \gg 1$ and $\mathrm{Da_L} \gg 1$ and assumes turbulent motions, namely the turbulent time controls the reaction rate, not the chemistry [137].

- Flame surface density models divide the reaction rate into the mean local flame speed (typically s_L) and a flame surface area (typically worded as the consumption rate per available unit of flame area). However, the transport equation for the flame surface area requires additional closures and sub-grid modelling, see [137] for more details.

- Probability density function PDF [138] determines the mean reaction rate though a function that measures the probability of a variable namely temperature takes a particular value and the corresponding reaction rate at that value, naturally the PDF approach has difficulties if the chemical reaction is determined by more than one progress variable [137].

- Bray Moss Libby [44, 43] assuming high turbulence where $\mathrm{Re}_{\mathrm{L}} \gg 1$ and $\mathrm{Da}_{\mathrm{L}} \gg 1$ assumes a one-step irreversible chemical reaction between the fresh gasses and the products, uses a statistical approach using a probability density function combined with physical analysis.

- Level set method [134], describes the flame propagation using the level set G-equation model where the flame can be tracked following the level set G which ranges from unburnt to burnt with an infinity thin interface. This is the approach adopted in Vectis (see [2]).

2.6.3 Turbulent Flame Speed Modelling

The turbulent flame speed s_{T} is an essential parameter in some sub-grid $\widetilde{\dot{\omega}_k}$ closure models. The approach that will be adopted in this project is modelling s_{T} through turbulent flame speed correlations with DNS data. An example of this is Damköhler's small and large scale limits (Equation (2.99) and (2.94)). Burke *et al.* [45] presents a good overview of turbulent flame speed correlations. A summary of popular models is presented in Table 2.1. The way these correlations are currently organised can make comparing models challenging. By rearranging the models in terms of the dimensionless quantities $\Lambda_{\mathrm{L}} = \ell_{\mathrm{I}}/\ell_{\mathrm{L}}$, $\Upsilon_{\mathrm{L}} = u'/s_{\mathrm{L}}$, Da_{L} and categorising the models into four categories; the Damköhler's small scale limit, Damköhler's large scale limit, the geometric mean of both Damköhler's small and large-scale limits and other, the small scale limit is written as:

$$s_{\mathrm{T}} = s_{\mathrm{R}} \left(1 + \mathcal{A}\Upsilon_{\mathrm{L}}\mathrm{Da}_{\mathrm{L}}^{0.5}\right), \tag{2.130}$$

the large-scale limit

$$s_{\mathrm{T}} = s_{\mathrm{R}} \left(1 + \mathcal{A}\Upsilon_{\mathrm{L}}\right), \tag{2.131}$$

and the geometric mean

$$s_{\mathrm{T}} = s_{\mathrm{R}} \left(1 + \mathcal{A}\Upsilon_{\mathrm{L}}\mathrm{Da}_{\mathrm{L}}^{0.25}\right). \tag{2.132}$$

The rearranged and categorised versions of the correlations shown in [45] are presented in Table 2.2. It can be seen that many of the presented models fall within the small-scale, large-scale and geometric mean limits. The "other" models are more difficult to evaluate. By plotting the other models as contour plots in $\Lambda - \Upsilon_{\mathrm{L}}$ space it can be more clearly seen how they relate to the small and large scale limits, these contours are presented in Figure 2.10. It can be seen that the KPP, Gouldin and Peters models are different attempts at a blended function between the small and large scale limits. Gouldin appears to have the slowest blend, with KPP as the quickest. Due to the difficulties with experimentation (both physically and numerically) over these large ranges of Λ_{L} and Υ_{L} it is still unclear what blending function is most effective, and how these functions depend on the type of fuel and reactant conditions. For more details on turbulent flame speed modelling see the review by Lipatnikov and Chomiak [109] and Burke *et al.* [45].

Table 2.1: Turbulent flame speed correlations from various authors as presented by Burke *et al.* [45]. For values of the constants shown see table)Table 3 in [45].

Correlation and Author	Equation
Zimont [184]	$s_{\mathrm{T}} = Cu/\mathrm{Da}_{\mathrm{L}}^{0.25}$
KPP [178]	$\frac{s_{\mathrm{T}}}{s_{\mathrm{L}}} = 1 + C\left(\frac{u'}{s_{\mathrm{L}}}\left(1 + \mathrm{Da}_{\mathrm{L}}^{-2}\right)^{-0.25}\right)$
Klimov [90]	$s_{\mathrm{T}} = Cu'^{0.7}\, s_{\mathrm{L}}^{0.3}$
Mantel & Borghi [114]	$s_{\mathrm{T}} = Cu/\mathrm{Re}_{\mathrm{L}}^{0.25}\left(1 + \frac{D_2 \mathrm{Re}_{\mathrm{L}}^{0.5}}{(1+D_1\frac{s_{\mathrm{L}}}{u'})^{D_3}}\right)^{-0.5}$
Anand & Pope [9]	$\frac{s_{\mathrm{T}}}{s_{\mathrm{L}}} = C\frac{u'}{s_{\mathrm{L}}}$
Gülder [76]	$\frac{s_{\mathrm{T}}}{s_{\mathrm{L}}} = 1 + C\left(\frac{u'}{s_{\mathrm{L}}}\right)^{0.5}\mathrm{Re}_{\mathrm{L}}^{0.25}$
Kobayashi [91]	$\frac{s_{\mathrm{T}}}{s_{\mathrm{L}}} = C\frac{u'}{s_{\mathrm{L}}}^{0.38}\left(\frac{P}{0.1\,\mathrm{MPa}}\right)^{0.38}$
Muppala [124]	$\frac{s_{\mathrm{T}}}{s_{\mathrm{L}}} = 1 + \frac{C}{\mathrm{Le}}\mathrm{Re}_{\mathrm{L}}^{0.25}\left(\frac{u'}{s_{\mathrm{L}}}\right)^{0.3}\left(\frac{P}{0.1\,\mathrm{MPa}}\right)^{0.2}$
Ronney [146]	$\frac{s_{\mathrm{T}}-s_{\mathrm{L}}}{s_{\mathrm{L}}} = C\mathrm{Da}_{\mathrm{L}}^{0.5}$
Cant [47]	$s_{\mathrm{T}} = Cu/\mathrm{Re}_{\mathrm{L}}^{0.25}$
Liu [110]	$\frac{s_{\mathrm{T}}-s_{\mathrm{L}}}{s_{\mathrm{L}}} = C\mathrm{Da}_{\mathrm{L}}^{0.47}$
Gouldin [74]	$\frac{s_{\mathrm{T}}}{s_{\mathrm{L}}} = C\left(\left(\left[1-\left(1-A_t^{0.25}\mathrm{Re}_{\mathrm{L}}^{-0.75}\right)\exp\left(-\left(\frac{A_t}{\mathrm{Re}_{\mathrm{L}}}\right)^{0.25}\frac{u'}{s_{\mathrm{L}}}\right)\right]A_t^{0.25}\mathrm{Re}_{\mathrm{L}}^{0.75}\right)^{D-2}\right)$
Abdel-Gayed & Bradley [3]	$\frac{s_{\mathrm{T}}}{s_{\mathrm{L}}} = C\left(\mathrm{Re}_{\mathrm{L}}^{0.47}\frac{u'}{s_{\mathrm{L}}}\left(1-\exp\left(-3.178\mathrm{Re}_{\mathrm{L}}^{0.5}\frac{u'}{s_{\mathrm{L}}}\right)\right) + 8.13\mathrm{Re}_{\mathrm{L}}^{0.22}\frac{u'}{s_{\mathrm{L}}}\left(1-\exp\left(-0.391\mathrm{Re}_{\mathrm{L}}^{-0.25}\frac{u'}{s_{\mathrm{L}}}\right)\right)\right)^{0.25}$
Peters [134]	$s_{\mathrm{T}} = s_{\mathrm{L}} - s_{\mathrm{L}}\frac{a_4 b_3^2}{2b_1}\frac{\ell_l}{\ell_{\mathrm{L}}} + \left(\left(\frac{a_4 b_3^2}{2b_1}\frac{\ell_l}{\ell_{\mathrm{L}}}\right)^2 + a_4 b_3^2\frac{u'\ell_l}{s_{\mathrm{L}}\ell_{\mathrm{L}}}\right)^{0.5}$

Table 2.2: Turbulent flame speed correlations (same as table)Table 2.1). Written in terms of dimensionless quantites Λ_{L}, Υ_{L} and Da_{L}.

Correlation and Author	Equation
	Small Scale Limit
Liu [110]	$s_{\mathrm{T}} = s_{\mathrm{L}}\left(1 + C\Upsilon_{\mathrm{L}}\mathrm{Da}_{\mathrm{L}}^{0.47}\right)$
Ronney [146]	$s_{\mathrm{T}} = s_{\mathrm{L}}\left(1 + C\Upsilon_{\mathrm{L}}\mathrm{Da}_{\mathrm{L}}^{0.5}\right)$
	Large Scale Limit
Klimov [90]	$s_{\mathrm{T}} = s_{\mathrm{L}}\left(1 + C\Upsilon_{\mathrm{L}}^{0.7}\right)$
Anand & Pope [9]	$s_{\mathrm{T}} = s_{\mathrm{L}}\left(1 + C\Upsilon_{\mathrm{L}}\right)$
Kobayashi [91]	$s_{\mathrm{T}} = s_{\mathrm{L}}\left(1 + C\Upsilon_{\mathrm{L}}^{0.38}\left(\frac{P}{100000}\right)^{0.38}\right)$
	Geometric Mean
Zimont [184]	$s_{\mathrm{T}} = s_{\mathrm{L}}\left(1 + C\Upsilon_{\mathrm{L}}\mathrm{Da}_{\mathrm{L}}^{0.25}\right)$
Gülder [76]	$s_{\mathrm{T}} = s_{\mathrm{L}}\left(1 + C\Upsilon_{\mathrm{L}}\mathrm{Da}_{\mathrm{L}}^{0.25}\right)$
Muppala [124]	$s_{\mathrm{T}} = s_{\mathrm{L}}\left(1 + \frac{C}{Le}\Upsilon_{\mathrm{L}}^{0.8}\mathrm{Da}_{\mathrm{L}}^{0.25}\left(\frac{P}{100000}\right)^{0.25}\right)$
Cant [48]	$s_{\mathrm{T}} = s_{\mathrm{L}}\left(1 + C\Upsilon_{\mathrm{L}}^{1.5}\mathrm{Da}_{\mathrm{L}}^{0.25}\right)$
	Other
KPP [178]	$s_{\mathrm{T}} = s_{\mathrm{L}}\left(1 + C\left(\Upsilon_{\mathrm{L}}\left(1 + \mathrm{Da}_{\mathrm{L}}^{-2}\right)^{-0.25}\right)\right)$
Mantel & Borghi [114]	$s_{\mathrm{T}} = s_{\mathrm{L}}\left(1 + C\Upsilon_{\mathrm{L}}^{0.5}\mathrm{Da}_{\mathrm{L}}^{0.25}\left(1 + \left(\frac{D_2\Upsilon_{\mathrm{L}}\mathrm{Da}_{\mathrm{L}}^{0.5}}{\left(1+D_1\Upsilon_{\mathrm{L}}^{-1}\right)^{D3}}\right)\right)^{-0.5}\right)$
Gouldin [74]	$s_{\mathrm{T}} = s_{\mathrm{L}}\left(1 + C\left(\left(1 - \left(1 - B^{-0.25}\Upsilon_{\mathrm{L}}^{-1.5}\mathrm{Da}_{\mathrm{L}}^{-0.75}\right)\exp\left(-\Upsilon_{\mathrm{L}}^{0.5}\left(\frac{B}{\mathrm{Da}_{\mathrm{L}}}\right)^{0.25}\right)\right)B^{0.25}\Upsilon_{\mathrm{L}}^{1.5}\mathrm{Da}_{\mathrm{L}}^{0.75}\right)^{D-2}\right)\right)$
Abdel-Gayed & Bradley [3]	$s_{\mathrm{T}} = s_{\mathrm{L}}\left(1 + C\left(\Upsilon_{\mathrm{L}}^{1.94}\mathrm{Da}_{\mathrm{L}}^{0.47}\left(1 - \exp\left(-3.178\Upsilon_{\mathrm{L}}^{0.2}\mathrm{Da}_{\mathrm{L}}^{0.5}\right)\right) + 8.13\Upsilon_{\mathrm{L}}^{1.44}\mathrm{Da}_{\mathrm{L}}^{0.22}\left(1 - \exp\left(-0.391\Upsilon_{\mathrm{L}}^{0.5}\mathrm{Da}_{\mathrm{L}}^{-0.25}\right)\right)\right)^{0.25}\right)$
Peters [134]	$s_{\mathrm{T}} = s_{\mathrm{L}}\left(1 + 2\alpha\Upsilon_{\mathrm{L}}\frac{\mathrm{Da}_{\mathrm{L}}}{\beta}\left(\left(1 + \frac{\beta}{\mathrm{Da}_{\mathrm{L}}}\right)^{0.5} - 1\right)\right)$

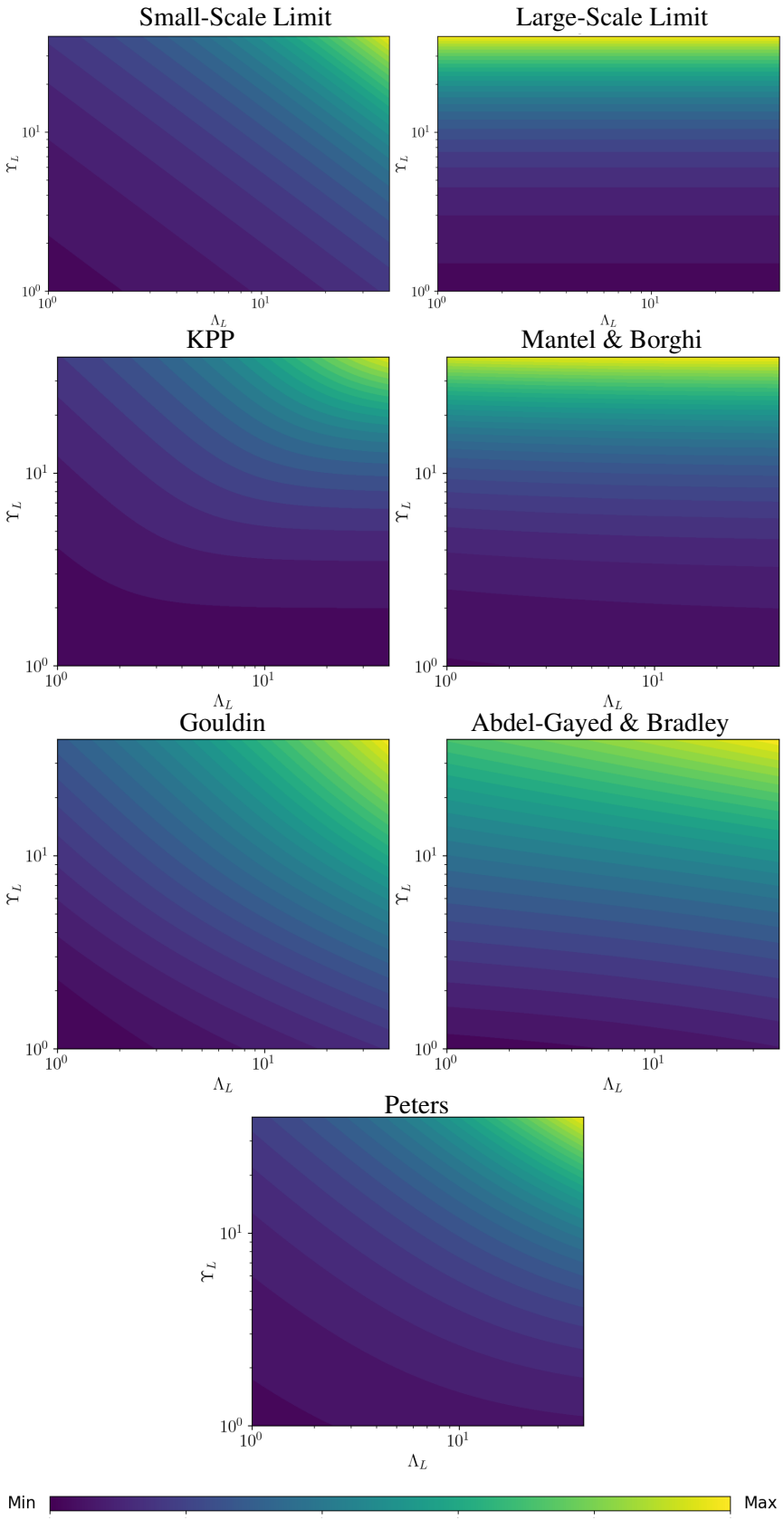

Figure 2.10: Contour plots in $\Lambda_L - \Upsilon_L$ space showing how the different "other" models compare to Damköhler's limits. The colour bar shows relative turbulent flamespeed for each model.

Chapter 3. Methods

This chapter focuses on the methods used throughout this thesis, with details of the codes used, the methodology for using the codes to run accurate DNS simulations and the post-processing strategy.

The simulation strategy for this thesis is to use the conical flame-in-a-box, where the flame is contained in a high aspect ratio domain with periodic walls where the domain is as thick as it is wide (i.e. $L_x = L_z$). The top of the domain has an outlet and the bottom is either an inlet (for freely-propagating flames) or a slip adiabatic wall (for turbulent flames). The idea behind this simple approach is to gather statistically stationary flame statistics to learn about the underlying flame or turbulent-flame behaviour with minimal influences from geometry or domain configuration.

3.1 The Code (PeleLM)

For the multi-dimensional direct numerical simulations of reacting flows used throughout this thesis, PeleLM has been used. PeleLM has been chosen due to its:

- Low Mach number implementation which allows for a significant increase in time step duration.
- Well implemented adaptive mesh refinement (AMR) for the reduction of total number of computational cells required for a well resolved simulation.
- Highly efficient scalability with multi CPU machines such as ARCHER2 (a 28 PFlop/s Cray EX supercomputer).
- Has a rich history of successful use in previous published works for example; 2D H_2, 3D freely-propagation H_2 and 3D turbulent.

PeleLM is an open-source, multidimensional, adaptive-mesh, low Mach number, hydrodynamics code used for the direct numerical simulation of reacting flows available at:

https://github.com/AMReX-Combustion/PeleLM

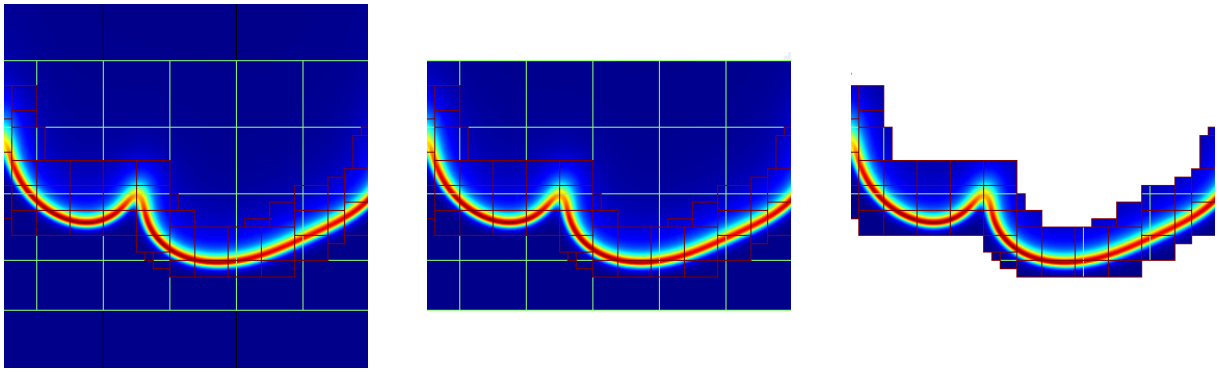

(a) All levels (levels 0,1 and 2) (b) Level 1 and 2 (c) Level 2

Figure 3.1: A 2D flame example coloured by the AMR criteria, showing the 3 levels of AMR.

Lead by M. Day and J. Bell, PeleLM was developed in 2000 at the Centre for Computational Sciences and Engineering at Lawrence Berkeley National Laboratory under the name LMC. Since its conception, PeleLM has seen enhancements supported by the US Department of Energy (ASCR) and is now supported by the Exascale Computing Project under the Pele Project. PeleLM depends upon and utilises the AMReX framework (formerly known as boxlib) for the data structures and tools to allow them to be run on massively parallel machines. PeleLM builds on from IAMR, a variable-density in-compressible Navier-Stokes equations with AMR integration.

3.1.1 AMReX

AMReX is a software framework that provides functionality to write massively parallel, block-structured adaptive mesh refinement (AMR) codes [180]. The AMR algorithm uses a hierarchical grid structure of uniform grids. Level 0 (the coarsest level) covers the entire domain which is referred to as the base grid. Higher levels can be dynamically allocated and de-allocated based on a user defined criteria (for example a specific temperature). The higher levels have a reduced cell size divided by a refinement ratio (for this project the refinement ratio is 2), for a 2D example of AMR see Figure 3.1. The full details of AMReX and the associated algorithms are beyond the scope of this PhD, therefore the reader is referred to [181] [131].

3.1.2 The PeleLM Model

PeleLM solves the reacting Navier-Stokes flow equations in the low Mach number regime detailed in [58]. PeleLM follows the model for low Mach number combustion as introduced and derived in [142, 113] thus assuming there are no spatial gradients in thermodynamic pressure. PeleLM uses the mixture-average model for species diffusion [168, 89] ignoring Soret, Dufort, body forces and radiative heat transfer effects and that bulk viscosity is small compared to shear viscosity. For full details on the equations, algorithm and multilevel approach used see papers [131, 4, 58, 126, 127].

Equation Set

This section follows the equation set used in PeleLM following the paper [58] and the documentation [1]. PeleLM solves the equations conservation of mass, momentum, species, energy (written as enthalpy), an equation of state and a system closure.

$$\frac{\partial \rho}{\partial t} + \nabla \cdot (\rho \boldsymbol{u}) = 0, \tag{3.1}$$

$$\frac{\partial \rho \boldsymbol{u}}{\partial t} + \nabla \cdot (\rho \boldsymbol{u}\boldsymbol{u} + \tau) = -\nabla \pi + \rho \boldsymbol{F}, \tag{3.2}$$

$$\frac{\partial \rho Y_m}{\partial t} + \nabla \cdot (\rho Y_m \boldsymbol{u} + \boldsymbol{\mathcal{F}}_m) = \rho \dot{\omega}_m, \tag{3.3}$$

$$\frac{\partial \rho h}{\partial t} + \nabla \cdot (\rho h \boldsymbol{u} + \boldsymbol{\mathcal{Q}}) = 0, \tag{3.4}$$

$$p_0 = \rho \mathcal{R} T \sum \frac{Y_m}{W_m}, \tag{3.5}$$

$$h = \sum_m Y_m H_m, \tag{3.6}$$

where ρ is the density, $\boldsymbol{u}$ is the velocity, τ is the stress tensor, π is a dynamic pressure, $\boldsymbol{F}$ is an external forcing term, Y_m is the mass fraction of species m, $\boldsymbol{\mathcal{F}}_m$ is the species diffusion fluxes, $\dot{\omega}_m$ is the molar production rate of species species m, h is the mass-weighted enthalpy, $\boldsymbol{\mathcal{Q}}$ is the heat flux, p_0 is the thermodynamic pressure, W_m is the species m molecular weight, $\mathcal{R}$ is the specific gas constant, T is the temperature and H_m is the standard-state molar enthalpy (which incorporates the heat of formation for each species). Under the stated assumptions, the stress tensor is approximated as

$$\tau_{i,j} = \mu \left(\frac{2}{3} \delta_{i,j} \frac{\partial u_k}{\partial x_k} - \left(\frac{\partial u_i}{\partial x_j} + \frac{\partial u_j}{\partial x_i} \right) \right) \tag{3.7}$$

where μ is the shear viscosity and $\delta_{i,j}$ is the Kronecker delta function. The heat flux is approximated as

$$\boldsymbol{\mathcal{Q}} = \sum_m h_m \boldsymbol{\mathcal{F}}_m - \lambda' \nabla T, \tag{3.8}$$

where λ' is the partial thermal conductivity and the species diffusion flux is approximated as

$$\boldsymbol{\mathcal{F}}_m = -\rho \sum_k Y_m D_{m,k} \nabla X_m, \tag{3.9}$$

where ∇X_m is the gradient of the molar concentration and $D_{m,k}$ is the diffusion matrix.

To solve these equations, a constraint is required, following the low Mach number assumption, the thermodynamic pressure can be assumed constant giving

$$\frac{\mathrm{D}p_0}{\mathrm{D}t} = 0, \tag{3.10}$$

which leads to

$$\nabla \cdot \boldsymbol{u} = \frac{1}{T}\frac{\mathrm{D}T}{\mathrm{D}t} + W \sum_m \frac{1}{W_m}\frac{\mathrm{D}Y_m}{\mathrm{D}t} = S. \tag{3.11}$$

where W is the the mean molecular weight. $\mathrm{D}T/\mathrm{D}t$ can be evaluated as

$$\frac{\mathrm{D}T}{\mathrm{D}t} = \frac{1}{\rho c_p}\left(\nabla \cdot \lambda \nabla T + \sum_m \left(h_m \nabla \cdot \boldsymbol{\mathcal{F}}_m - \nabla \cdot h_m \boldsymbol{\mathcal{F}}_m - h_m \rho \dot{\omega}_m\right)\right), \tag{3.12}$$

where λ is the thermal conductivity and c_p is the specific heat capacity.

Chemical Kinetics

Given N_s species interacting through M_r reactions are expressed as

$$\sum_{m=s}^{N_s} v'_{m,j} X_m \rightleftharpoons \sum_{m=s}^{N_s} v''_{m,j} X_m, \qquad \text{for } \; j \in [1, M_r], \tag{3.13}$$

where $v'_{m,j}$ and $v''_{m,j}$ are the stoichiometric coefficients for the reactant and product side respectively and X_m is the molar concentration of species m. The rate of reaction j (represented by R_j) is expressed as

$$R_j = k_{f,j} \prod_{m=1}^{N_s} X_m^{v'_{m,j}} - k_{r,j} \prod_{m=1}^{N_s} X_m^{v''_{m,j}}, \tag{3.14}$$

where $k_{f,j}$ and $k_{r,j}$ represent the forward and backward reaction rate coefficients respectively. The forward reaction rate coefficient is given from the Arrhenius equation

$$k_f = AT^{\beta} \exp\left(\frac{-E_a}{RT}\right), \tag{3.15}$$

where A is a pre-exponential factor, β is the temperature exponent and E_a is the activation energy. The backward reaction rate coefficient is given by

$$k_{r,j} = \frac{k_{f,j}}{\exp\left(\frac{\Delta S_j^0}{R} - \frac{\Delta H_j^0}{RT}\right)\left(\frac{p_0}{RT}\right)^{\sum_{k=1}^{N_s}\left(v''_{k,j} - v'_{k,j}\right)}}, \tag{3.16}$$

where ΔS_j^0 is the change in entropy of the reaction j and ΔH_j^0 is the change in enthalpy of the reaction j. Note that the low Mach number assumption allows for the denominator to be a function only of temperature, the products of reaction j and the thermodynamic properties of the reactants. The net production rate is then defined as the sum of the creation and destruction of species m over all reactions

$$\dot{\omega}_m = \sum_{j=1}^{M_R} R_j \left(v''_{m,j} - v'_{m,j}\right). \tag{3.17}$$

Thermodynamic Properties

Following the assumption of a mixture of ideal gas, the species m enthalpies H_m and entropies S_m are functions of only temperature and are given from [73] by polynomial fits of the species molar heat capacities ($C_{p,m}$)

$$C_{p,m} = \mathcal{R}\left(a_{m,1} + \frac{a_{m,2}}{2}T + \frac{a_{m,3}}{3}T^2 + \frac{a_{m,4}}{4}T^3 + \frac{a_{m,5}}{5}T^4\right) \tag{3.18}$$

molar enthalpy of species m is approximated as

$$H_m = \mathcal{R}\left(a_{m,1}T + \frac{a_{m,2}}{2}T^2 + \frac{a_{m,3}}{3}T^3 + \frac{a_{m,4}}{4}T^4 + \frac{a_{m,5}}{5}T^5 + a_{6,m}\right) \tag{3.19}$$

molar entropy of species m

$$S_{p,m} = \mathcal{R}\left(a_{m,1}\ln(T) + a_{m,2}T + \frac{a_{m,3}}{2}T^2 + \frac{a_{m,4}}{3}T^3 + \frac{a_{m,5}}{4}T^4 + a_{m,7}\right) \tag{3.20}$$

where $a_{k,m}$ are model constants.

PeleLM Algorithm

The numerical implementation of the PeleLM is behond the scope of this thesis, the full details of the algorithm please see [58], therfore a breife)therefore a brief summary is given here as described in [65].

PeleLM uses a finite volume approach on a Cartesian grid with discrete spacing. The variables $u, \rho, \rho h, \rho Y_m$ and T are the cell averages and the pressure field π is defined at the nodes. The momentum equation is solved using a predictor/corrector method shown in [4, 131]. The transport terms are computed using a spectral deferred correction time advancement scheme [127] which is used to ensure the tight coupling of the fast diffusion and reaction to the slow advection, while enforcing the low Mach number constraint [65]. The advection terms are computed using a second-order Godunov scheme, the diffusion terms are computed with a Crank-Nicholson scheme and the reaction terms are solved using the CVODE integrator detailed in [25]. AMReX's native geometric multi-grid solver computes the solution of the linear system arising from the implicit diffusion and velocity projections.

3.1.3 Turbulent Forcing

A flame-in-a-box at the scales simulated in this project does not have the natural large scale energy injection that would be present in real world systems. If the turbulence is initialised without a maintained source term appropriately, injecting turbulent kinetic energy then the turbulent field would decay too quickly to attain statistically stationary flame statistics. Maintaining a realistic homogeneous isotropic turbulent (HIT) field at DNS scale is a challenging topic with many different approaches.

A popular approach is to have a turbulent inflow, where turbulent kinetic energy is injected into the domain via a turbulent inflow and the turbulence is allowed to freely decay throughout the domain ([123, 34] for example). A major advantage of this method is that the turbulence is allowed to decay naturally and there is no risk of artificial forcing near the flame. A disadvantage of this approach is that the turbulence decays and the turbulent kinetic energy decreases as distance from the inlet increases which will result is distance dependent turbulence properties. Thus a flame position closer to the inlet will experience a different

turbulent intensity than a different part of the flame.

Another possible approach is the turbulent kinetic energy ahead of the flame is maintained and as the turbulent forcing stops just ahead of the flame, to ensure no interference with the natural flame response. An advantage of this method is that the turbulence experienced by the flame is not dependent on the flame location relative to the inlet, which in theory makes the turbulence experienced by the flame at all locations similar. A disadvantage to this is that there is still some variation of the turbulence experienced by the flame, especially when comparing the leading part of the flame to the trailing parts.

The method used throughout this project is to maintain the turbulent field using a forcing term in the Navier-Stokes moment equation denoted $\boldsymbol{F}$ in Equation 3.2. A zero-mean time-dependent low-wave number forcing term was implemented by Aspden *et al.* [23]

$$F(x,t) = \sum_{\kappa|\in[0,4\sqrt{3}]} a_{i,j,k} \cos\left(f_{i,j,k}t + \mathcal{A}_{i,j,k}\right) \cos\left(2\pi\kappa_i x + \mathcal{B}_{i,j,k}\right) \cos\left(2\pi\kappa_j y + \mathcal{C}_{i,j,k}\right) \cos\left(2\pi\kappa_k z + \mathcal{D}_{i,j,k}\right), \tag{3.21}$$

where there are random amplitudes $a_{i,j,k} \in [0,1]$, frequencies $f_{i,j,k}$ and phases $\mathcal{A}_{i,j,k}$, $\mathcal{B}_{i,j,k}$, $\mathcal{C}_{i,j,k}$ and $\mathcal{D}_{i,j,k} \in [0, 2\pi]$. For full details on the implementation and analysis see [23]. This approach maintains the turbulence within the domain resulting in a statistically-steady turbulent field over time. The key benefit of this approach is that turbulent intensity has a statistically-steady mean value, allowing for the extraction of statistically stationary flame statistics ([19, 20] for example). The key advantage of this method, and the reason this method was chosen over the others, is the turbulence experienced by the flame will be the same regardless of its location, which erases many of the data extraction difficulties. However, a major criticism of this method is that the flame could, in theory, be artificially forced by the turbulent kinetic energy injects which could suppress or enhance the natural flame response to turbulence. [13] considered turning the forcing off when close to the flame and did not see a notable difference. Note that throughout the project, there are some cases with a small $\mathrm{Ka_F}$. The Reynolds number of these cases are small, where the Reynolds number can be as small as $\mathrm{Re} \sim 10$. It could therefore be argued that Kolmogorov's hypotheses discussed previously are not valid.

3.1.4 Resolution Requirements

For DNS of turbulent reacting flows, the smallest scales must be resolved. For turbulent flames there are two independent scales that must be resolved; the smallest Kolmogorov scales and the flame scales. If the turbulence is sufficiently small $\mathrm{Ka_L} < 1$ when $\eta > \ell_\mathrm{F}$ and so if the resolution is adequate to resolve the flame scales then it must be adequate for the turbulent scales. Note ℓ_F which represents the flame thermal thickness for a freely-propagating flame instead of the 1-dimensional unstretched flame thickness because ℓ_F accounts for any flame thinning due to TD-instabilities.

Turbulence

PeleLM is capable of ILES, and in the case with PeleLM could be viewed as under-resolved DNS. The performance of under-resolved DNS was considered by Aspden *et al.* [23]. Aspden *et al.* demonstrated an ILES approach to simulate detailed turbulent behaviour. An effective viscosity was established which allowed the numerical scheme to appropriately dissipate turbulent kinetic energy below the grid-scale. To evaluate this method, Aspden *et al.* performed three distinct simulations (of which many turbulent intensities were evaluated): fully-resolved DNS at all turbulent scales, inviscid ILES where the viscosity was set to zero and ILES with true viscosity set (i.e. under-resolved DNS). It was found that given an underresolved viscosity (ν_u) at for example Δx, the effecitive visocisty (ν_e) of a simulation at that resolution and therfore the effective Kolmogorov length (η_e) can be derived. Figure 7 from [23] shows the dimensionless comparison of the effective viscosity ν_e to the set viscosity in the under-resolved DNS simulations ν_u.

Flame

The resolution of the chemistry of the flame and the flame structure is of paramount importance to ensure high fidelity DNS simulations. To define to the appropriate resolution requirements three approaches were taken:

- Evaluate the temperature profile and select species at varying resolutions in a laminar effective 1-dimensional PeleLM simulation.

- Look at the flame structure of lean H_2 flames at varying resolutions.
- Look at published works that use PeleLM for lean H_2 for the authors' resolution requirement.

A short convergence study was conducted to evaluate how well the species and fuel consumption rate profiles are captured. The case evaluated was simulated using an effective 1-dimensional simulation with a small width and with a large aspect ratio. The domain dimensions are $\ell_{\mathrm{L}} x 128 \ell_{\mathrm{L}}$ and the flame conditions have a pressure of 1 atm, a temperature of 300K and an equivalence ratio of 0.4 and using the Burke *et al.* kinetic model [46].
Figure 3.2 shows the profile for fuel consumption rate and intermediate species HO_2, where $N_{\mathrm{T}} = \ell_{\mathrm{L}}/\mathrm{d}x$ and case $N_{\mathrm{T}} = 128$ is used for comparison as the target profile due to it being an unquestionably fully resolved resolution. It can be seen that both profiles produce similar profiles and values at all resolutions, despite $N_{\mathrm{T}} = 2$ being clearly under-resolved this still has reasonable similarities with the target profile. However although all other cases show slight deviation from the target profile, there is only small improvements with increasing resolution. All resolutions $N_{\mathrm{T}} = 8, 12$ and 16 appear to adequately resolve the profiles. Figure 3.3 shows the measured laminar flame speed and laminar thermal thickness with increasing resolution. It can be seen that $N_{\mathrm{T}} = 2$ and 4 are under-resolved where $N_{\mathrm{T}} = 4$ has a significantly slower flame speed and thicker thermal thickness. Once $N_{\mathrm{T}} = 12$, then the difference is small $(2 - 3\%)$ and even as low as $N_{\mathrm{T}} = 8$ has small errors $(3 - 4\%)$, refinement above $N_{\mathrm{T}} = 12$ is arguably comfortably in the region of diminishing returns. Howarth and Aspden [80], using PeleLM, simulated 2-dimensional freely-propagating lean H_2 flames. As part of their investigation they evaluated the effect resolution had on both the flame structure and local flame statistics using the Burke *et al.* kinetic model [46]. Figure 3.4 shows the temperature field of a 2-dimensional freely-propagating flame at varying resolutions studied in [80]. The example flame has a very high level of TD-instability and provides a good example of what can happen in extreme cases of lean hydrogen flames. The findings showed that, at coarse resolution, the flame structure was changed, where true TD-unstable behaviours became absent or reduced such as fully formed flame fingers and reduced chaotic lateral movement. As the resolution increased to $\ell_{\mathrm{F}}/\mathrm{d}x = 9$ the flame structure returned to its typical state. It was also shown in the study by Howarth and Aspden that local flame statistics, provided the resolution

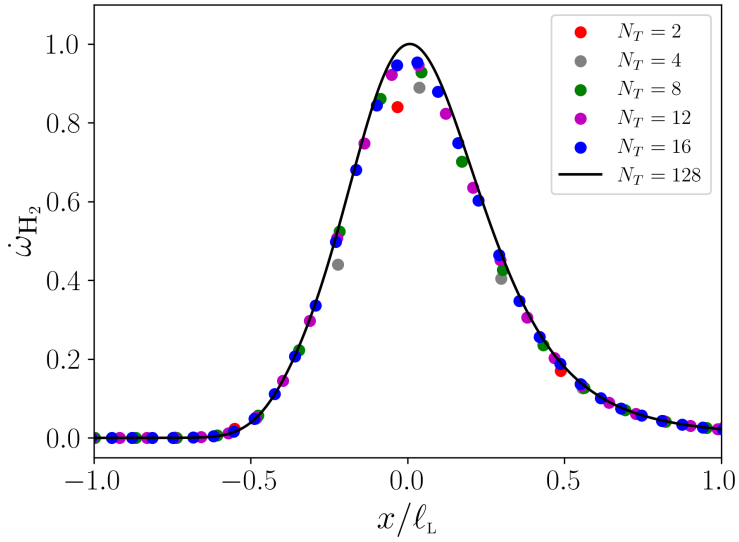

(a) $\dot{\omega}_{H_2}$

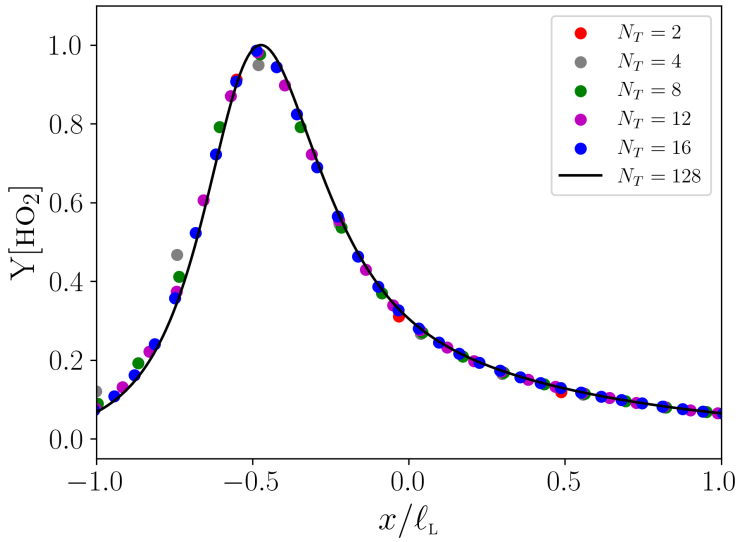

(b) HO_2

Figure 3.2: Fuel consumption rate and species HO_2 profiles at different simulation resolutions.

was enough to produce flame fingers, was independent of resolution. In other published work, using PeleLM for lean H_2 flames used various resolution requirements of as low as $\ell_F/dx = 7$ in [19] to as high as $\ell_F/dx = 20$ for distributed flames [22].

From these observations a good conservative minimum resolution for the flame is $\ell_F/\Delta x = 12$. This ensures that the flame surface and chemistry is sufficiently well-resolved but also allows room for additional thinning in highly turbulent flames. AMR will be used to resolve the flame while reducing the total number of computational cells, provided the turbulence can be

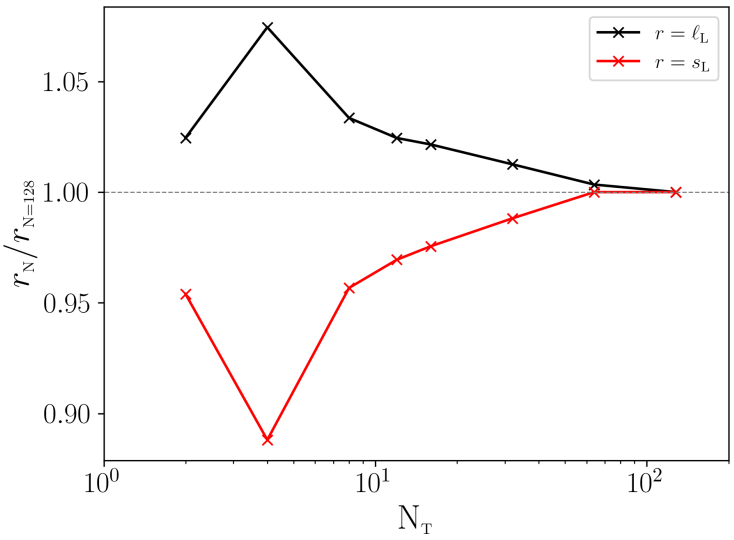

Figure 3.3: Measured laminar flame speed and laminar thermal thickness with increasing number of cells across the thermal thickness (N_T).

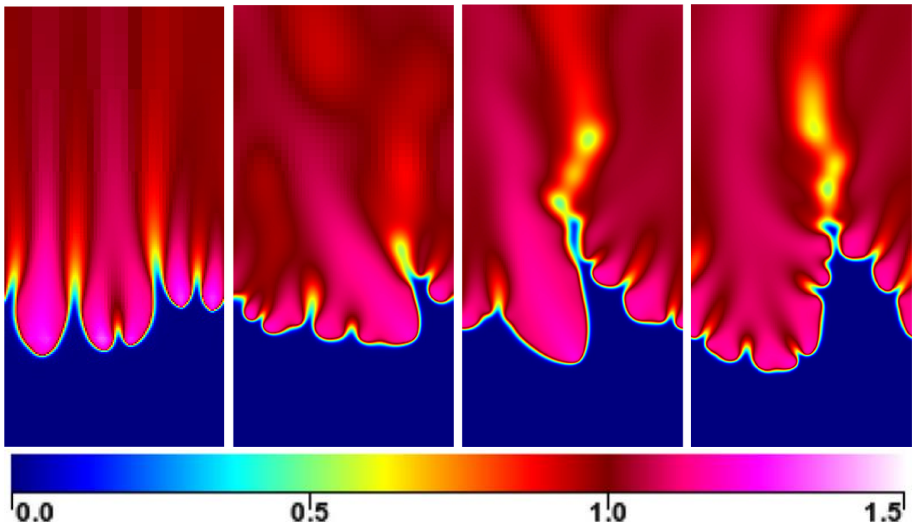

Figure 3.4: Temperature field for a 2-dimensional freely-propagating flame at the same conditions for different resolutions ($\ell_F/\mathrm{d}x = 3, 6, 9, 12$) by Howarth and Aspden [80]. *Reprinted from [80] under license CC BY 4.0.*

adequately resolved as discussed above.

3.1.5 Supporting Codes - Cantera

Cantera is an open-source suite of tools used for solving problems related to chemical kinetics, thermodynamics, and transport [72]. For this project Cantera was used to quickly and

accurately calculate the 1-dimensional freely propagating flame properties; notably the laminar flame speed and thickness s_{L}, ℓ_{L}, the adiabatic temperature T_{ad} and other flame properties (such as ω_2 [117]).

3.1.6 A Comment on Soret Effects

Soret effects have been shown to impact lean hydrogen flames, see [182, 152] for example. However, Soret effects have been excluded throughout this thesis. Soret effects were recently shown by Howarth *et al.* [81] not to disturb trends but can change exact values (usually minimally). It is expected these effects will be reduced with increasing turbulent intensities. It will likely be the case that the exact values of the simulations i.e. the flame speed, will differ from what they would be if Soret effects were considered. However, the focus of this project has been on trends, rather than exact values, thus the findings throughout this thesis should be consistent with those if Soret effects were included.

3.2 Extracting Simulation Data

The following subsections focus on the methods used for extracting simulation data from PeleLM simulations.

3.2.1 The Isosurface

The flame surface is a key parameter used in the analysis and modelling of the flame. The flame in detailed chemistry is not infinitely thin, meaning there is a gradient of species, fuel consumption rate and temperature through the flame. Therefore, a good choice of progress variable and isovalue that best represents the flames surface is of importance. An ideal isosurface would closely follow the peak fuel consumption rate which is commonly the sum of the mass fractions of major combustion products [136, 66]. For TD-unstable flames the surface defined by temperature is highly sensitive to the progress value c and has a tendency to overestimate the flame surface, this was shown in detail by Howarth & Aspden [80] and can be seen from Figure 3.5. It can be seen however, that using the fuel mass fraction as the progress variable yields a surface similar to the desired peak fuel consumption rate. Therefore for this

project the isosurface will be based on a progress variable of fuel mass fraction:

$$c = 1 - \frac{Y[\mathrm{F}]}{Y[\mathrm{F}]_u} \tag{3.22}$$

where $Y[\mathrm{F}]$ is the fuel mass fraction and $Y[\mathrm{F}]_u$ is the unburnt fuel mass fraction. This project will also use the isovalue of $c = 0.9$ proposed by Howarth & Aspden [80], which can be seen in Figure 3.5, and closely follows the fuel consumption rate. Other works studying lean hydrogen flames also use a similar approach ([34] for example). It should be noted that there is no perfect answer for what progress variable is most appropriate; Day *et al.* [59] compared multiple isosurfaces and did not find any variable is a perfect fit for a "true" isosurface.

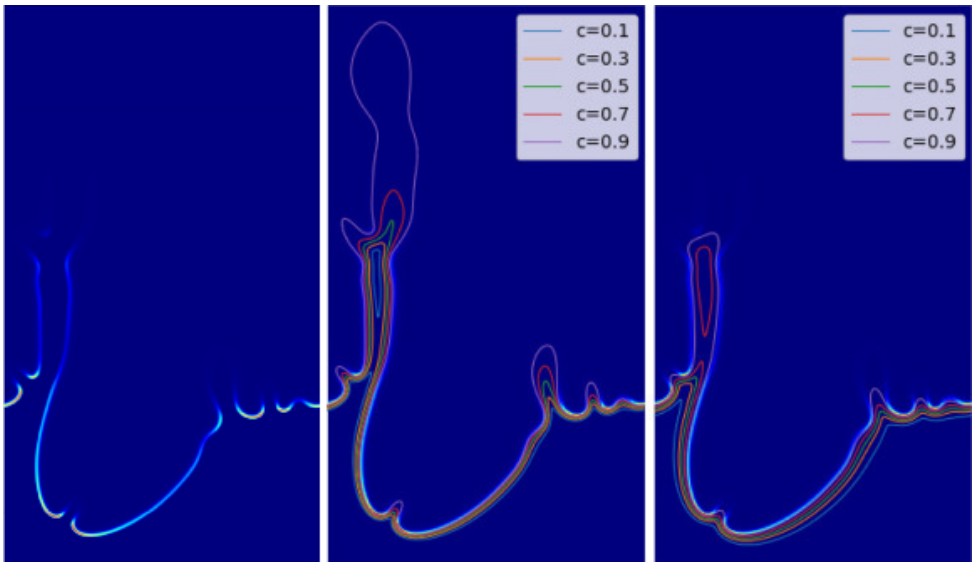

Figure 3.5: Fuel consumption rate $\dot{\omega}_{\mathrm{H_2}}$ (left) and isosurfaces based on temperature (centre) and fuel mass fraction $Y[\mathrm{H_2}]$ (right) for varying progress variable values c from Howarth & Aspden [80]. *Reprinted from [80] under license CC BY 4.0.*

3.2.2 Flame statistics

From Equation (2.80), the fuel consumption based global speed s_c is calculated as:

$$s_\mathrm{c} = -\frac{1}{\rho_u Y\left[\mathrm{H_2}\right]_u A} \int_V \rho \dot{\omega}_{\mathrm{H_2}} \mathrm{d}V \tag{3.23}$$

where $A = L_x L_y$ is the domain cross sectional area and V is the domain volume, suffix b and u denotes the burnt and unburnt states respectively (note as the simulations are all lean then $Y\left[\mathrm{H_2}\right]_u - Y\left[\mathrm{H_2}\right]_b \equiv Y\left[\mathrm{H_2}\right]_u$).

Throughout the project, flame surface data is required to gather an understanding of the flame behaviour. This method follows the approach by Bell *et al.* [33] [30] and Day *et al.* [59] with some modifications proposed by Howarth & Aspden [80]. A local coordinate system is constructed based on the fuel progress variable field near the flame. Using the flame surface as an origin, a fourth-order Runge-Kutta scheme is used to construct paths normal to the surface following gradients of the fuel progress variable C from the upstream reactants ($C = 1$) through the surface to the products ($C = 0$). The streamlines can then be used to construct N number with a localised prism-shaped (triangular) volumes Ω with element area at the surface A, referred to as stream-tubes (see Figure 7 in [59]). Within the stream-tubes a local consumption based flame speed and local thermal thickness can be calculated as a 1-dimensional flame along the path:

$$s_{\text{loc},i} = -\frac{1}{\rho_u Y \left[\text{H}_2\right]_u A_i} \int_{\Omega_i} \rho \dot{\omega}_{\text{H}_2} \text{d}\Omega_i, \tag{3.24}$$

$$\ell_{\text{loc},i} = \frac{T_b - T_u}{\max_{\Omega_i} |\nabla T|}, \tag{3.25}$$

where i is the ith tube along the surface, Ω_i is the volume of the ith tube and A_i is the area of the surface element through which the ith tube passes. The mean local flame speed or thickness (represented by $\mathcal{P}$) can then be calculated by averaging the local values spatially over the entire flame surface for all tubes i and temporally over a statistically stationary region from the start of the region t_s to the end of the region t_e with number of time points t_N

$$\overline{\mathcal{P}_{\text{loc}}} = \frac{1}{t_N \left(\sum_{t=t_s}^{t_e} \sum_{i=0}^{N} A_{i,t} \right)} \sum_{t=t_s}^{t_e} \sum_{i=0}^{N} \mathcal{P}_{i,t} A_{i,t}. \tag{3.26}$$

This method desensitises the choice of isovalue as neither speed nor thickness are measured at the surface, which gives an appropriate estimation of the mean local statistics.

3.2.3 Calculating Zeldovich Number

To calculate ω_2, the Zeldovich number β needs to be computed from Cantera's 1-dimensional free-flame. The Zeldovich number is defined as

$$\beta = \frac{E_a \left(T_b - T_u\right)}{R T_b^2}, \tag{3.27}$$

where E_a is the activation energy and R is the ideal gas constant. The activation energy calculation for detailed chemistry is computed following from Law and Sung [101], who suggest that

$$E_a = -2R\frac{\mathrm{d}\log(\rho_u s_\mathrm{L})}{\mathrm{d}T_b^{-1}}. \tag{3.28}$$

It can be seen that varying the adiabatic flame temperature without changing the fundamental conditions can be difficult. It is suggested in [101] that the nitrogen should be varied with another inert gas (i.e. argon) which can change the burning flux ($\rho_u s_\mathrm{L}$) and the adiabatic flame temperature without modifying the underlying conditions. Therefore, a small amount of argon was added to the premixed mixture and varied by a small amount over multiple simulations (usually 5 to give a line of best fit between $\log(\rho_u s_\mathrm{L})$ and T_b^{-1}), which allowed for the activation energy and Zelodvich number to be calculated.

3.3 Defining Flame Characteristics

Throughout this thesis, different reference values for speed, thickness and turbulent quantities will be discussed, each with a distinct meaning. This section exists as a reference point for the reader regarding what flame quantity is being referred too.

Mean Local Flame Properties

Throughout this thesis all flame speeds are consumption based. The local statistics with subscript (loc) refers to the local value attained using the stream-tubes method discussed above (i.e. Equation (3.24) and (3.25). The mean local value denoted by an overline ($\overline{\mathcal{P}}$) refers to the local values averaged spatially over all tubes on the flame and over a statistically stationary region, as shown in Equation (3.26).

Laminar Flame Properties

The laminar flame speed and thickness denoted by subscript L (ie s_L and ℓ_L) represents the unstretched 1-dimensional flame speed and thickness. This value is easily attained from a Cantera free flame simulation. Note that if a simulation is flat and unstrained (effectively 1-dimensional) then the mean local flame speed and thickness is equal to the laminar flame speed and thickness; for example

$$\overline{\mathcal{P}_\mathrm{loc}} = \mathcal{P}_\mathrm{loc} = \mathcal{P}_\mathrm{L}. \tag{3.29}$$

Freely-Propagating Flame Properties

The freely-propagating speed and thickness denoted by subscript F (i.e. s_{F} and ℓ_{F}) represents the mean local flame speed and thickness for a 3-dimensional freely-propagating flame

$$\overline{\mathcal{P}_{\mathrm{loc}}} = \mathcal{P}_{\mathrm{F}}, \tag{3.30}$$

where for TD-unstable flames $s_{\mathrm{F}} > s_{\mathrm{L}}$ and $\ell_{\mathrm{F}} < \ell_{\mathrm{L}}$.

Turbulent Flame Properties

The mean local flame speed and thickness for turbulent flames are denoted by subscript S (i.e. s_{S} and ℓ_{S}) and are the mean local flame speed and thickness for a 3-dimensional turbulent flame

$$\overline{\mathcal{P}_{\mathrm{loc}}} = \mathcal{P}_{\mathrm{S}}, \tag{3.31}$$

where typically (for example, provided turbulence it not close to distributed) for a TD-unstable turbulent flame $s_{\mathrm{S}} > s_{\mathrm{F}} > s_{\mathrm{L}}$ and $\ell_{\mathrm{S}} < \ell_{\mathrm{F}} < \ell_{\mathrm{L}}$. The turbulent flame speed is measured as the total fuel consumption per unit area from Equation (3.23) and is denoted by s_{C}. The flame surface wrinkling is defined as the ratio of the flame surface area A_T to the cross-sectional area of the domain A

$$\Psi_{\mathrm{C}} = \frac{A_T}{A}. \tag{3.32}$$

Based on Damköhler 1940 [55, 135], the following must be true

$$s_{\mathrm{C}} = \overline{s_{\mathrm{loc}}}\Psi_{\mathrm{C}}. \tag{3.33}$$

Chapter 4. Freely-Propagating Laminar Flames

TD-unstable freely-propagating lean premixed hydrogen flames are investigated over a wide range of reactant conditions with varying temperature, pressure and equivalence ratio to evaluate the thermodiffusive response for freely-propagating flames. Reactant conditions are characterised using an instability parameter ω_2 [118], which was recently shown in [80] in 2-dimensions to categorise freely-propagating well. Freely-propagating flame speeds and thickness are found to correlate with using the same functional form found in 2-dimensions but with larger model constant with different correlations either side of the most-unstable surface in ω_2-space, both are used to propose an empirical scaling model. Joint-probability density functions are used to correlate local consumption-based flame speed with curvature, strain-rate and stretch with single and independent Markstein numbers. A simple curvature-based model coupled with the empirical flame speed model is found to yield reasonable results. Flame surface structure is studied and principal curvature zones are used to partition the flame into six classifications (leading point, leading edge, flat, saddle point, trailing edge, trailing point) which are used for conditional analysis in different parts of the flame surface. Fractional contributions show that the bulk of the fuel consumption occurs in flat regions and leading edges, shifting from the former to the latter with increasing instability. Furthermore, the flat flame regions experience speeds in excess of the reference value (s_F) despite the lack of focussing of fuel by preferential diffusion in these regions, contrary to the conventional expectations of thermodiffusive instability. A thermal leading point interpretation is proposed: Where as expected, strong positive curvature in the leading points/edges result in diffusive focusing of fuel, increasing the reaction rates, resulting in super-adiabatic temperatures; these high temperatures left behind the leading points/edges then support higher-than-expected reaction rates in regions where the flame surface is relatively-flat.

The current chapter's work is published under the title *Thermodiffusively-unstable lean premixed hydrogen flames: phenomenology, empirical modelling, and thermal leading points* published in the journal *Combustion and Flame* in July 2023. This work was produced in collaboration with Dr. Thomas Howarth who was the joint first author.

4.1 Introduction

As discussed in Section 2.4, lean hydrogen flames often burn hotter, faster and thinner than their stable counterparts. It has been shown by Aspden *et al.* [18] that using the laminar flame speed and thickness (s_{L} and ℓ_{L}) is inadequate for appropriately categorising turbulent properties of low Lewis number flames. It was suggested that using freely-propagating flame speeds and thickness was required for appropriate turbulence (this will be shown in detail in Section 5). Lean TD-unstable flames have complex responses to turbulence, with flame folding enhancing the flame speeds locally in positively curved regions. This chapter aims to build a strong fundamental understanding of TD-unstable flames in the absence of turbulence, which will then inform the analysis and modelling of turbulent flames which will be studied in later chapters.

Continuing from Section 2.4 early numerical works on TD-unstable premixed flames used simple chemistry with turbulence as considered by [163]. Detailed chemistry with turbulent flow in 2-dimensions was considered by Baum *et al.* [28], Chen and Im [52, 83] for example. More recent works in 2-dimensions include the groups in Zurich [6, 7, 5, 70] and Aachen [36, 34, 35] who considered growth rate and dispersion relations in the linear regime in addition to pattern formation in the non-linear regime. The Darmstadt group [170] considered kernel configurations and Kadowaki *et al.* [85] considered pattern formation, for example.

Recent work by Berger *et al.* [36] studied 2-dimensional freely-propagating flames with complex chemistry in a large domain ($800\ell_{\mathrm{L}}$) for TD-unstable lean hydrogen flames. Strong flame surface wrinkling, enhanced flame speeds and super-adiabatic temperatures are observed. A particularly interesting observation was the domain size dependency of the flame to the domain size, and the flame surface wrinkling seemed somewhat linked to the theoretical wave length. It was shown that once the domain size is sufficiently large the flame surface wrinkling becomes constant. Recent work by Howarth and Aspden [80] also performed numerical studies on 2-dimensional freely-propagating flames with complex chemistry. Howarth studied the effect domain size had on the formation of flame instabilities and the effect domain size had on the formation of TD-unstable structures, specifically its link to stretch factor (I_0). [36, 80] also found a link between domain size and I_0, namely once the

domain size was large enough for TD-structures to form, the local flame statistics (such as speed and thickness) were independent of domain size. However, flame surface wrinkling was not evaluated.

Berger *et al.* [36] presented clear observations and formations of flame fingers, later [80] observed that flame finger formation and intensity was closely related to the instability parameter ω_2. Aspden *et al.* [18] showed briefly the formation of TD-unstable structures in 3-dimensions with complex chemistry. It was shown that different structures form to that observed in 2-dimensions, and more bulb-like structures form. More recent work by Wen *et al.* [169] (published after this was work conducted and published) showed a similar behaviour to Aspden *et al.* [18]. An especially relevant observation for conformation of this project is that in 3-dimensions, local flame speed is independent of domain size (like [80] in 2-dimensions) provided the domain size is large enough to support the instabilities.

Interestingly Joint probability density functions (JPDFs) of flame speed and curvature presented in [80], show elevated flame speeds at zero curvature which would be unexpected according to the conventional understanding of TD-instabilities. A similar phenomenon was observed recently in 3-dimensions for turbulent flames by Berger *et al.* [34]. In this paper it was theorised that the enhancement of flame speed at zero curvature is the result of strain rate, [34] utilising a counterflow flame observed enhanced reaction rates despite the zero curvature. Similar observations from turbulent low Lewis number flames have found similar correlations of strain-rate to flame speed ([51] for example).

Building upon the observations of [18, 36, 80] and utilising the instability coefficient ω_2 from [118, 117], this chapter starts by simulating 3-dimensional freely-propagating flames over a wide range of conditions (a total of 17 different reactant conditions). Firstly the bulk features are studied using isosurfaces of fuel mass fraction (Section 4.3). Measurements of freely-propagating flame speed and thickness are used to infer a 3-dimensional empirical model for freely-propagating flame speed and thickness attainable from 1-dimensional simulations. Comparisons are then made with 2-dimensional simulations from [80] (Section 4.4). JPDFs are then studied to evaluate how the flame speed responds to the flame stretch (both from curvature, strain and stretch) for both single and multiple Markstein numbers

(Section 4.4.2). A decomposition and classification of the flame surface is proposed using principle curvature zones, including characterisation though fractional consumption and scalar profiles conditioned on principal curvature zone. Lastly an explanation of thermal leading points are made to explain the existence of zero curvature flame speed enhancement (Section 4.5).

4.2 Numerical Configuration and Simulation Conditions

Freely-propagating flame sheets have been simulated in a high aspect ratio domain with a laterally-periodic inflow-outflow configuration. The domain size was configured as $28\ell_{\mathrm{F}} \times 28\ell_{\mathrm{F}} \times 112\ell_{\mathrm{F}}$. It has since been shown that the domain size chosen does provide sufficient space to allow for an instability to develop [35]. The domain size is unlikely to be sufficiently large for accurately attaining a flame surface wrinkling and global flame speed without domain dependence as shown by Burger *et al.* [36], but as shown by [22, 80], this domain size is sufficient for local flame quantities. The flame was initialised with a statistically-planar flame surface using a one-dimensional profile from Cantera at the desired conditions. The base grid was $96 \times 96 \times 384$ with two levels of AMR to give an effective resolution of $384 \times 384 \times 1536$ providing around 14 cells across the freely-propagating thermal thickness. The flame statistics are measured over a statistically-stationary period. The flame position is maintained using an inflow where the inlet velocity is variable depending on the fuel mass fraction in the domain (details on the active-control algorithm can be found in [31]).

A broad range of reactant conditions have been simulated with a specific focus on lean, TD-unstable conditions. The conditions span a wide range of pressure, temperature and the subsequent ω_2 values. The conditions studied are shown in Table 4.1 and are broken down into four distinct sets:

- P300. Is a pressure trajectory (increasing pressure from 1atm to 40 atm) with fixed temperature (300 K) and equivalence ratio (0.4). As shown from Figure 4.1 increasing the pressure, increases ω_2 up until the most unstable surface (at an estimated 10atm) then ω_2 decreases.

- P700. Has the same approach as P300, but at a higher fixed temperature of 700 K.

- R. Specifically varies pressure and equivalence ratio to follow the most unstable surface (as predicted by ω_2) at both 300 K and 700 K.

Some specific cases have been named and will be referred to throughout the study:

- A. Is a sensible control case, which has low temperature (300 K), pressure (1 atm) and equivalence ratio (0.4).
- B. Intended to be representative of RICE conditions as suggested by Realis, it has high pressure (40 atm), temperature (700 K) and is lean (0.4).
- C. An engine relevant condition intended to be representative of a micro-mix combustor as suggested by Reaction Engines, and is high pressure (20 atm), high temperature (700 K) and is very lean (0.2).
- I. An intermediate case between B and C to isolate the effect of equivalence ratio, independent of pressure and temperature.
- D. The case with the highest ω_2 so is estimated to be the most unstable of all the studied cases.
- Z. Has an ω_2 of zero, which could be an interesting case between the stable and unstable region in ω_2 space.

4.3 Flame Surfaces

Flame surfaces are considered first to paint a general picture of TD-unstable flame evolution. Figure 4.2 shows example isosurfaces (coloured by the normalised local flame speed) at incrementally increasing pressure from $P_0 = 3.5$ to 40 atm at fixed equivalence ratio $\phi = 0.4$ and two inlet temperatures $T_0 = 300$ and 700 K. Starting with $T_0 = 300$ K and $P_0 = 3.5$ atm, the flame is TD-unstable, with a large variation of flame speed across the surface. Flame acceleration ($s_{\text{loc}} > s_{\text{F}} > s_{\text{L}}$) is in the positively curved regions (denoted by the light blue / white colour), with large flat regions, tending to the mean local flame speed (s_{F}) and flame deceleration in negatively curved regions forming (dark blue) extinction channels. It can be seen that 3D structures do differ from 2D flame fingers, where the typical 2D flame fingers

Table 4.1: Reactant conditions for all freely-propagating simulations, coloured by the regime; black and red for the low and high pressure regimes, respectively, and magenta for cases near the most-unstable surface. Freely-propagating values are measured values from the three-dimensional simulations.

Set	Case	p (atm)	T (K)	ϕ	ω_2	s_L (cm/s)	ℓ_L (μm)	s_F (cm/s)	ℓ_F (μm)
	(A)	1			5.45	20.7	665	34.4	526
		1.7			7.39	15.2	465	29.8	329
		3.5			12.9	8.11	361	23.6	189
P300		6	300	0.4	20.7	3.83	408	18.3	140
		10			27.3	1.57	590	13.2	114
		20			17.1	0.78	609	7.00	120
		40			13.6	0.51	466	4.30	90.9
		1			-0.15	3.80	502	3.73	498
		3.5			1.30	2.24	111	2.49	108
P700		10	700	0.4	2.71	1.05	44.5	1.53	38.8
	(I)	20			4.22	53.6	32.6	106	25.4
	(B)	40			5.58	24.9	30.4	56.5	18.7
	(C)	20	700	0.2	2.82	1.08	1120	3.33	484
	(D)	1	300	0.25	48.2	0.140	49700	4.1	3200
R		3.5	300	0.32	36.8	0.551	4160	9.09	434
		20	700	0.28	7.44	6.14	204	24.3	75.5
Z	(Z)	1	300	0.565	0	75.2	390	85.3	382

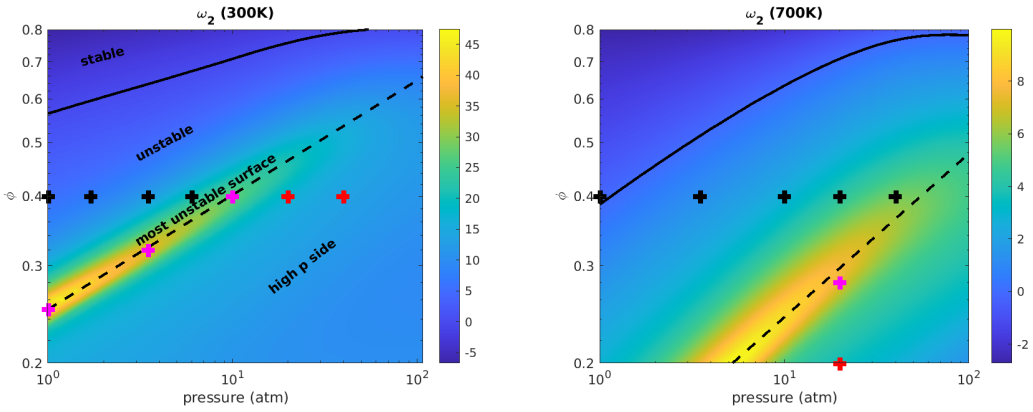

Figure 4.1: Contours of instability parameter showing dependence on pressure and equivalence ratio at 300K and 700K; markers denote conditions simulated in this chapter.

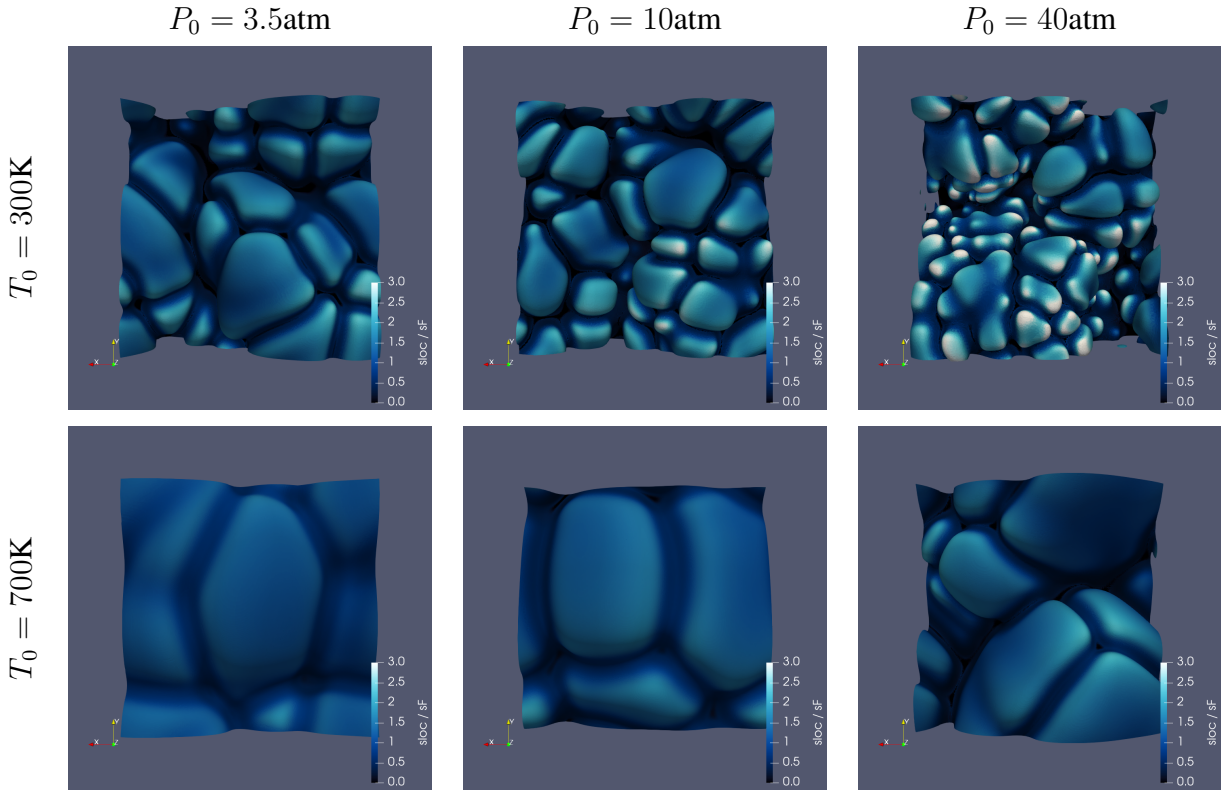

Figure 4.2: Isosurfaces of fuel mass fraction coloured by normalised local flame speed for increasing pressure at fixed equivalence ratio $\phi = 0.4$ and inlet temperature $T_0 = 300$ and 700K. The direction of flame propagation is moving directly out of the page.

with the w-shape pair have been replaced with far less stable structures with multiple neighbouring positively-curved structures. From Figure 4.2 for the $T_0 = 300$ K cases, it can be seen that increasing pressure decreases the size of the flame structure, even though the domain size has been normalised to account for flame thinning by normalising by ℓ_{F} instead of ℓ_{L}. Additionally, it can be seen that the positively curved regions get smaller and more bulbous with less of the structure being "flat" where the local flame acceleration is greater relative to the mean local flame speed than at lower pressure. Interestingly this trend continues across to the high pressure regime ($P_0 = 40$ atm, $T_0 = 300$ K), where the flame structure looks more unstable at a lower ω_2 than the most unstable surface case ($P_0 = 10$ atm, $T_0 = 300$ K). From Figure 4.2 it can be clearly seen that temperature at the same equivalence ratio and pressure has a stabilising effects, as shown by [118, 117, 80] for example. As with the $T_0 = 300$ K cases, as pressure increases the extent of the instability also increases.

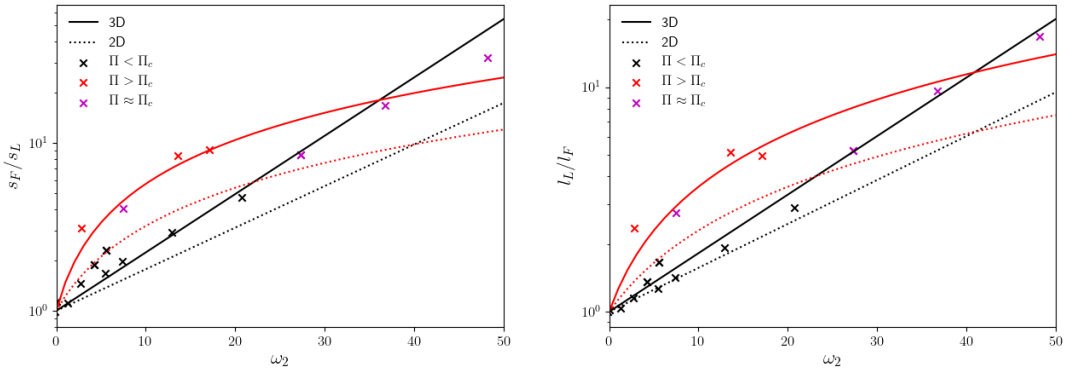

Figure 4.3: Normalised freely-propagating characteristic flame speed and (inverse) thickness as functions of instability parameter ω_2 . Solid lines denote the 3D empirical model; dotted lines show 2D model from [80] for comparison. Black denotes the low-pressure regime, red denotes the high-pressure regime, and magenta denotes conditions close to the most-unstable-surface. Each simulated case is denoted by the red and black crosses.

4.4 Characteristic Values

4.4.1 Mean Local Flame Speed and Thickness

As discussed previously (Section 3.2.2), the freely-propagating flame speed s_F and thermal thickness ℓ_F are defined as the temporal- and surface-average of the local values for both speed s_loc and thermal thickness ℓ_loc averaged a statistically stationary period. Figure 4.3 presents the freely-propagating values of speed and thermal thickness normalised by the unstretched laminar values as a function of the instability factor ω_2. The solid curves denote the 3D model proposed from this data shown in Equation (4.1) and (4.2). The dotted curves are that proposed by Howarth and Aspden [80] for 2D.

It can be seen from Figure 4.3 that the response is similar to that observed in 2-dimensions with TD-effects being stronger in 3-dimensions. This can be explained by having fuel focusing in more directions than in 2-dimensions. At typical engine relevant conditions, the mean local flame speed acceleration ($\overline{s_\mathrm{loc}}/s_\mathrm{L}$) was seen to be in the range of 2 to 4. The most extreme instabilities had a value of 29 as seen for case D. It also is observed that as the instability factor ω_2 increases, so does the extent of flame acceleration and thinning, consistent with the observation from [80]. As with 2-dimensions, there are two observable regimes, the low and

high pressure regimes, where the behaviour appears to change. It can be seen that for the cases studied in this project, the high-pressure regime has notably weaker local flame acceleration and thinning at the same comparable ω_2 values in the low-pressure regime. Additionally, the most unstable surface cases (coloured as magenta) appear to cross between both regimes with the lowest ω_2 case adhering to the low pressure regime model, and higher ω_2 cases adhering to the high pressure regime model from Equation 4.1 4.2,

$$\overline{s_{\text{loc}}} \approx s_{\text{M}} = \begin{cases} \exp\left(0.08\omega_2\right) & \text{if low pressure regime,} \\ 1 + 0.47\omega_2 & \text{if high pressure regime,} \end{cases} \tag{4.1}$$

$$\overline{\ell_{\text{loc}}} \approx \ell_{\text{M}} = \begin{cases} \exp\left(-0.06\omega_2\right) & \text{if low pressure regime,} \\ \left(1 + 0.26\omega_2\right)^{-1} & \text{if high pressure regime.} \end{cases} \tag{4.2}$$

Interestingly case Z, which has $\omega_2 = 0$ and is TD "neutral" has a slightly increased mean local flame speed above the unstretched laminar value of $\overline{s_{\text{loc}}}/s_{\text{L}} = 1.13$.

4.4.2 JPDFs of Local Flame Speed

Joint probability density functions (JPDFs) of local flame speed with different measures are instructive for quantifying the local flame behaviour and potential modelling approaches, such as a well-resolved G-Equation for example. It is also informative as to how the fundamental flame behaviour responds to different reactant conditions and TD-behaviour. Traditionally the JPDF would show the probability of the speed at the curvature as a fraction of flame surface area. For the JPDFs in this project the first moment, with respect to flame speed, is used to reduce the influence of the local extinction regions. The integrated JPDF gives the total fuel consumption rate which shows the locations where the flame is burning, not just where the flame surface is. Additionally, this reduces the importance of the exact value of progress variable used.

Following the approach from [80]; four different measures were evaluated against the local flame speed normalised by the freely-propagating flame speed (ie $\overline{s_{\text{loc}}} = s_{\text{F}}$); curvature

$$\frac{s_{\text{loc}}}{s_{\text{F}}} = \mathcal{M}_\kappa \kappa \ell_{\text{F}}, \tag{4.3}$$

strain, stretch with a single Markstein number

$$\frac{s_{\text{loc}}}{s_{\text{F}}} = \mathcal{M}\left(\kappa\ell_{\text{F}} + \left(E - \overline{E}\right)\tau_{\text{F}}\right), \tag{4.4}$$

and stretch with independent Markstein numbers for an independent weighting of curvature and strain components

$$\frac{s_{\text{loc}}}{s_{\text{F}}} = \mathcal{M}_1\kappa\ell_{\text{F}} - \mathcal{M}_2\left(E - \overline{E}\right)\tau_{\text{F}}, \tag{4.5}$$

where τ_{F} is the freely-propagating flame time $\tau_{\text{F}} = \ell_{\text{F}}/s_{\text{F}}$, E is the strain-rate, $\overline{E}$ is the mean strain-rate, and κ is the curvature. As the strain-rate is evaluated on the surface, it is somewhat sensitive to the progress variable. Howarth and Aspden [80] suggested that accounting for a non-zero mean strain, the strain-rate can be seen as the strain rate fluctuation from the mean $(E - \overline{E})$ hence the inclusion of a mean strain-rate in Equation (4.4). This approach is used for both single and independent Markstein numbers (as suggested in [53, 80]).

The results of all simulation cases (except the A/1.7 atm case so that the figure can fit on the page) are shown in four figures; Figure 4.5 for curvature, Figure 4.6 for strain, Figure 4.7 for stretch with a single Markstein number and Figure 4.8 for stretch with independent Markstein numbers. The JPDFs for curvature and stretch show dashed and dotted magenta lines which denote the freely-propagating and laminar flame speeds of the reactant conditions; a solid white line for the line of best fit using orthogonal distance regression and the dashed white line represents a proposed curvature-only model ($s_{\text{loc}} = s_{\text{F}}\left(1 - \mathcal{M}_\kappa\kappa\ell_{\text{F}}\right)$, where $\mathcal{M}_\kappa = -2.5$). The proposed model will be discussed in more detail below.

Starting with curvature only (Figure 4.5), for all $\omega_2 > 1$, i.e. theoretically TD-unstable [80], there is a clear positive correlation with local flame speed and local flame curvature, which is in agreement with the literature ([30] for example). For a fixed temperature and equivalence ratio with an increasing pressure (see P300 trajectory) it can be seen that increasing the pressure in-turn increases both the range of the flame curvature but also the peak local flame speed, indicative of a more unstable flame. The solid white line represents a line of-best fit and the dotted line is given by the model

$$s_{\text{loc}} = s_{\text{F}}\left(1 - \mathcal{M}_\kappa\kappa\ell_{\text{F}}\right) \quad \text{with } \mathcal{M}_\kappa = -2.5. \tag{4.6}$$

For the clearly unstable cases, the model has good agreement with the line-of-best fit; which indicates that, provided the flame is sufficiently TD-unstable, the curvature only Markstein number is somewhat independent of reactant conditions. Interestingly (looking at the P300 trajectory), even when ω_2 begins to reduce with pressure (crosses the ridge after 20 atm) the trend of increasing curvature ranges continues which is somewhat supported in Figure 4.2. This suggests that the flame behaviour is sensitive to the regime in ω_2 space as-well as the value of ω_2. It also is suggestive of an underlying pressure effect to flame structure and TD-response that is somewhat independent of ω_2.

The local flame speed against strain-rate JPDF is presented in Figure 4.6 (the colour scale applies to all following JPDFs.). It can be seen that for the TD-unstable cases there is a positive correlation between the local flame speed and the strain-rate. As pressure increases (see the P300 trajectory) the range of strain-rate increases. Additionally, as pressure increases the gradient of the local flame speed to strain decreases. Interestingly as ω_2 increases (which for the P300 cases peaks at $p = 20$ atm) the peak local flame speed stops increasing, but the range of strain-rate values continues to increase. As for curvature, for the TD-neutral case the range of local flame speeds is minimal, cluster around $s_{\mathrm{F}} = 1$ (ie $\overline{s_{\mathrm{loc}}} \approx s_{\mathrm{F}} \approx s_{\mathrm{L}}$) and there is no clear relationship between strain and local flame speed.

The local flame speed correlation with stretch, both with single (Figure 4.7) and independent (Figure 4.8) Markstein numbers, collapses well for all TD-unstable cases with a clear positive correlation with local flame speed and stretch. As expected and observed in both the individual curvature and strain JPDFs, as pressure increases the range and magnitude of local flame speed and stretch values are increased. It can be seen that there is a slight improvement using independent Markstein numbers, most notably for the cases of the most-unstable surface cases, which is different to the 2-dimensional observations in [80], which yielded little improvement.

Case Z ($\phi = 0.565, T_0 = 300$ K and $p = 1$ atm) which has an ω_0 of unity, shows a negative Markstein number, despite theoretically, being TD-neutral. It is theorised that the flame is not TD-unstable, but the small Darrious Landau instability slightly perturbs the flame, which in-turn results in a small amount of fuel focusing causing the small range of flame speed variation. This has some interesting implications in turbulent flames so will be revisited in

Chapter 5.

The predictive models presented by Equation 4.4 and 4.5 require expressions for the mean strain-rate and for single or multiple Markstein numbers. The curvature only model from Equation 4.6 requires a single Markstein number $\mathcal{M}_\kappa$. Figure 4.4 presents the lines of best fit for these quantities. It can be seen that there is significant scatter in the data for the single and double Markstein numbers, far more than in 2D [80]; which infers a model is therefore not satisfactory. The curvature only model does provide much less scatter, and therefore is preferred over the stretch models.

4.5 Principal Curvatures and Thermal Leading Points

To evaluate the flame structure and the contribution of different regions to the flame speed, the flame surface has been divided into principle curvature zones. The usage of principal curvatures for evaluating hydrogen-air flames has been done by Shim *et al.* [154] and Uranakara *et al.* [165].

4.5.1 Principal Curvatures

Principal curvature $\kappa_1 > \kappa_2$ can be calculated by the Gaussian curvature (κ_g) from Goldman [71] and the mean curvature (κ_m)

$$\kappa_g = -\frac{\begin{vmatrix} F_{xx} & F_{xy} & F_{xz} & F_x \\ F_{xy} & F_{yy} & F_{yz} & F_{xy} \\ F_{xz} & F_{yz} & F_{zz} & F_{xz} \\ F_x & F_y & F_z & 0 \end{vmatrix}}{|\nabla F|^4} \tag{4.7}$$

given that it is known that

$$\kappa_m = \frac{\kappa_1 + \kappa_2}{2}, \tag{4.8}$$

$$\kappa_g = \kappa_1 \kappa_2, \tag{4.9}$$

the principle curvature zones can be given as

$$\kappa_1 = \kappa_m + \sqrt{\kappa_m^2 - \kappa_g}, \tag{4.10}$$

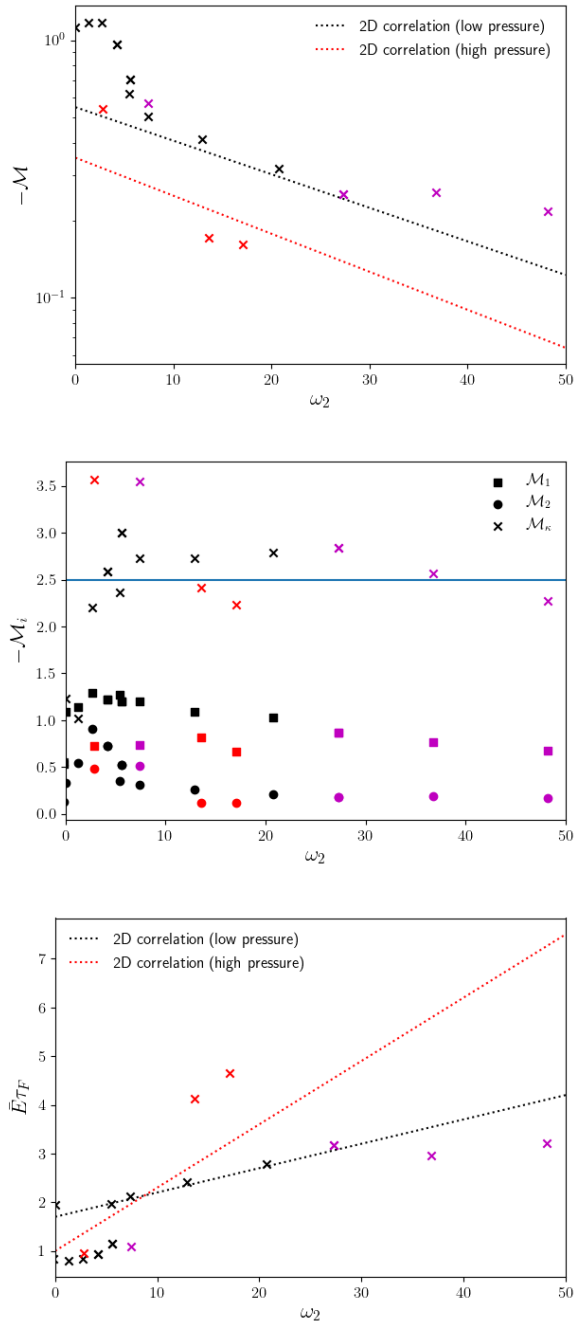

Figure 4.4: Single Markstein number (left), independent Markstein numbers (right) and mean strain-rate (bottom) as a function of the instability parameter ω_2, with the added model lines from the 2D model from [80]. For the data presented, there is significant scatter, preventing a modified empirical model. The curvature-based approach with $\mathcal{M}_\kappa = -2.5$, appears to work well and appears largely independent of ω_2.

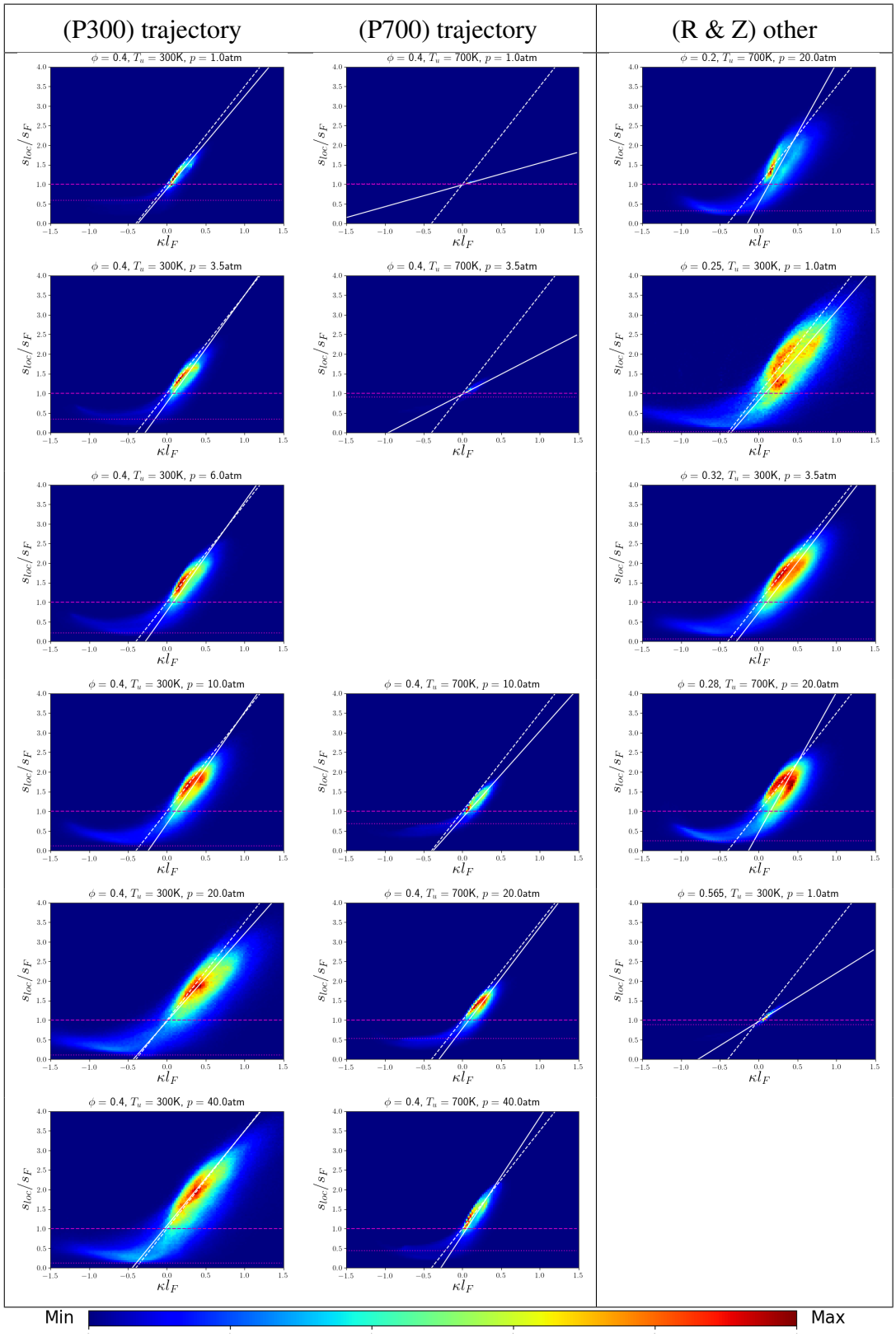

Figure 4.5: JPDFs of normalised s_{loc} and κ. The dashed white line represents a constant gradient of 2.2, the solid white line represents the gradient of each individual case, the dashed red line represents $s_{\text{loc}}/s_{\text{F}} = 1$ and the dotted fine red line represents $s_{\text{L}}/s_{\text{F}}$.

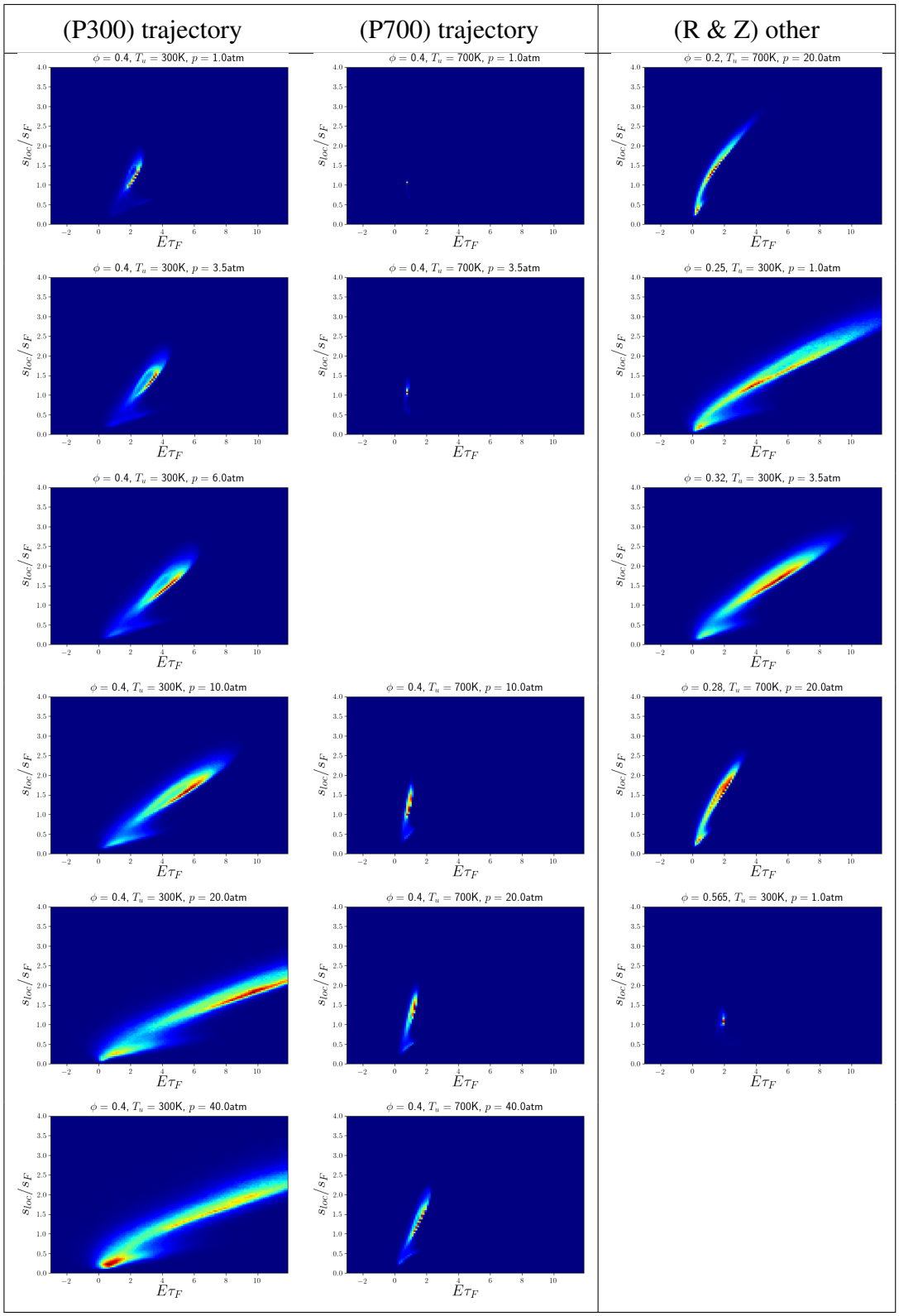

Figure 4.6: JPDFs of normalised s_{loc} and strain-rate.

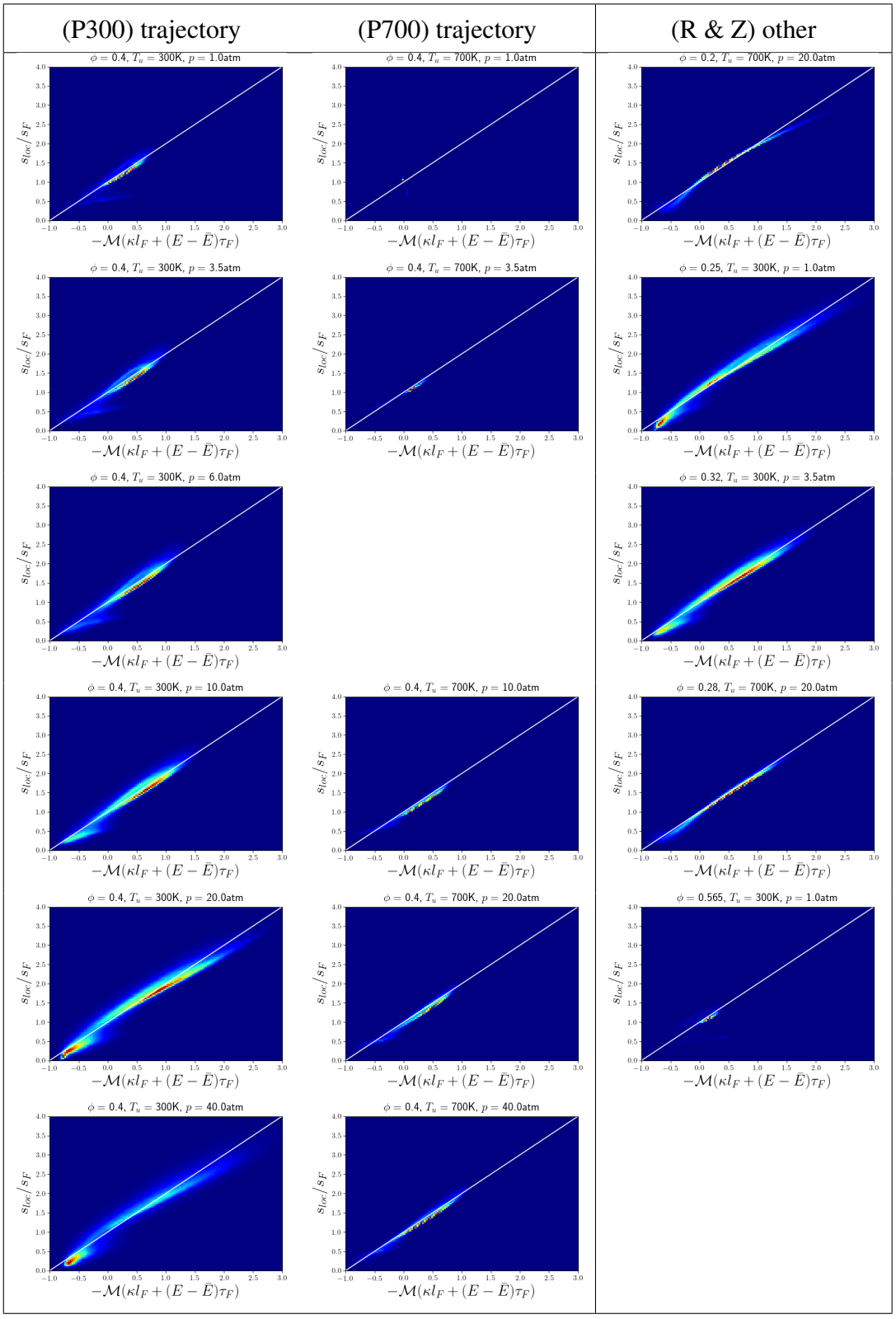

Figure 4.7: JPDFs of normalised s_{loc} and stretch. The solid white line represents the gradient of each individual case.

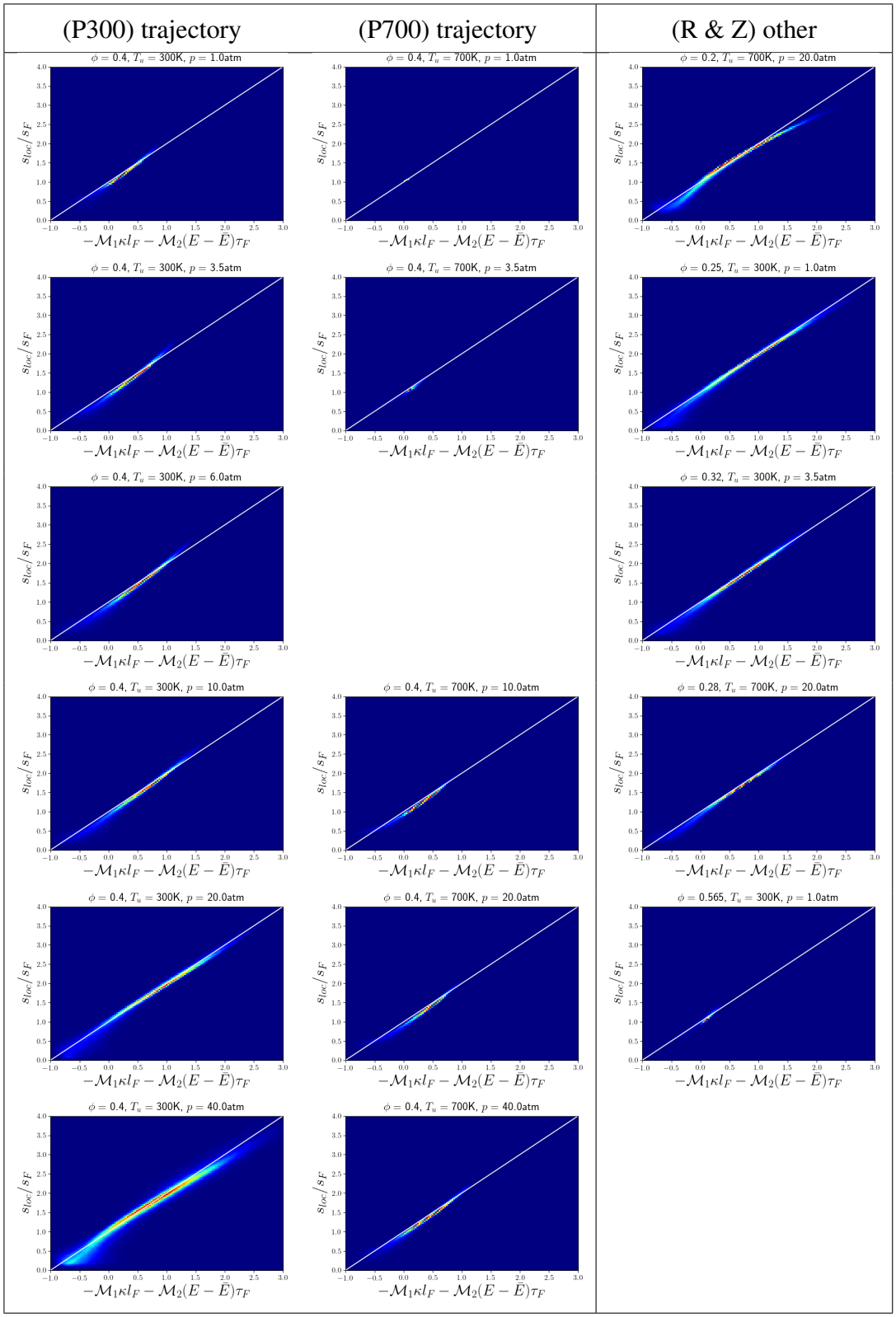

Figure 4.8: JPDFs of normalised s_{loc} and stretch with independent Markstein numbers. The solid white line represents the gradient of each individual case.

$$\kappa_2 = \kappa_m - \sqrt{\kappa_m^2 - \kappa_g}, \tag{4.11}$$

has been used to partition the flame surface into six classifications. These are flat flame (FF), leading point (LP), leading edge (LE), saddle point (SP), trailing edge (TE) and trailing point (TP). These are defined by principle curvature zones:

$$\begin{aligned}
&\text{FF} && \text{if } \sqrt{\kappa_1^2 + \kappa_2^2} > \frac{1}{2}\ell_{\text{F}}, \text{ otherwise:} \\
&\text{LP} && \text{if } \kappa_2 > \frac{\kappa_1}{2}, \\
&\text{LE} && \text{if } \left|\frac{\kappa_2}{\kappa_1}\right| \leq \frac{1}{2}, \\
&\text{SP} && \text{if } -2\kappa_1 < \kappa_2 < -\frac{\kappa_1}{2}, \\
&\text{TE} && \text{if } \left|\frac{\kappa_1}{\kappa_2}\right| \leq \frac{1}{2} \text{ and} \\
&\text{TP} && \text{if } \kappa_1 > \frac{\kappa_2}{2}.
\end{aligned} \tag{4.12}$$

A schematic of these zones is shown in Figure 4.9. Zones categorised as "points" can be interpreted as being spherically curved, while "edges" as cylindrically curved, where "leading" and "trailing" refer to the positive and negative mean curvature, respectively. The threshold values used are somewhat arbitrary, and the values chosen could be modified. The purpose of the values provided are not to predict the unique distribution of curvature zones, but to investigate the trends, which are anticipated to be largely independent of the specific zone values. The values chosen however were judged to be appropriate by inspection of the isosurface in conjunction with JPDFs (shown below in Figure 4.11).

Figure 4.10 shows example isosurfaces coloured by the principle curvature zones at incrementally increasing pressure from $P_0 = 3.5$ to 40atm at fixed equivalence ratio $\phi = 0.4$ and inlet temperature $T_0 = 300\,\text{K}$. The change in the structure as a result of pressure is clear; the flame structure transitions from a flame with large flat flame regions to leading edges and trailing edges. The low pressure cases have long leading edges and extinction channels separating large flat regions with relatively few leading points forming the w-shaped flame structure as discussed above. The higher pressure cases have a structure dominated by more extreme curvatures where the majority of the flame is governed by leading edges and extinction channels with an increased number of leading points.

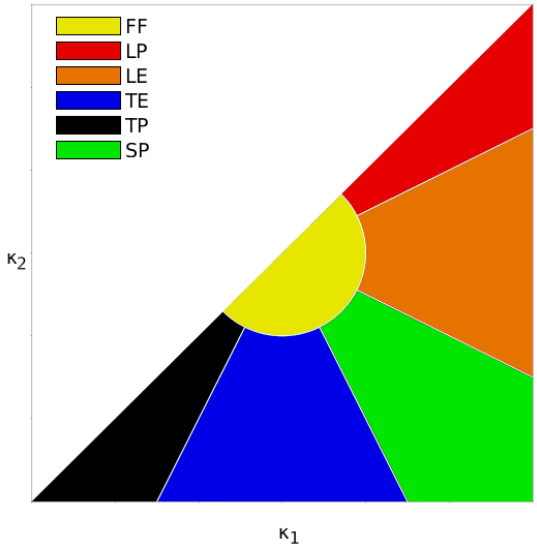

Figure 4.9: Schematic of principal curvature zones classification. FF: flat flame; LP: leading points; LE: leading edges; TE: trailing edges; TP: trailing points; SP: saddle points. Points are spherically curved; edges are cylindrically curved.

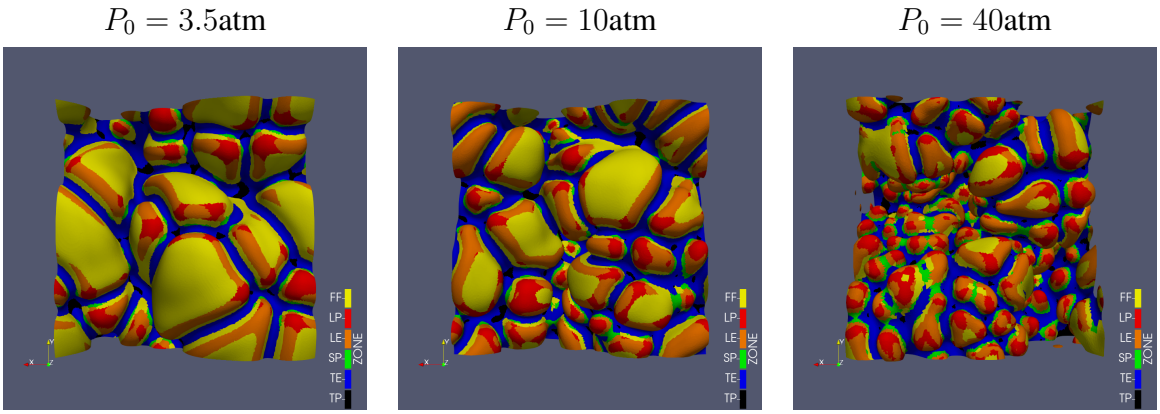

Figure 4.10: Isosurfaces coloured by principal curvature zone for $p_0 = 3.5, 10$ and 40atm at $T_0 = 300$K and $\phi = 0.4$

Figure 4.11 shows JPDFs of principal curvatures weighted by flame speed (top), and local flame speed conditionally-averaged on principal curvatures (bottom) for increasing pressure (left-to-right and top-to-bottom) for the P300 pressure trajectory.

Starting with the principal curvatures weighted by flame speed (top of Figure 4.11), for the low pressure case (Case A), it can be seen that there is little range of principal curvatures; almost

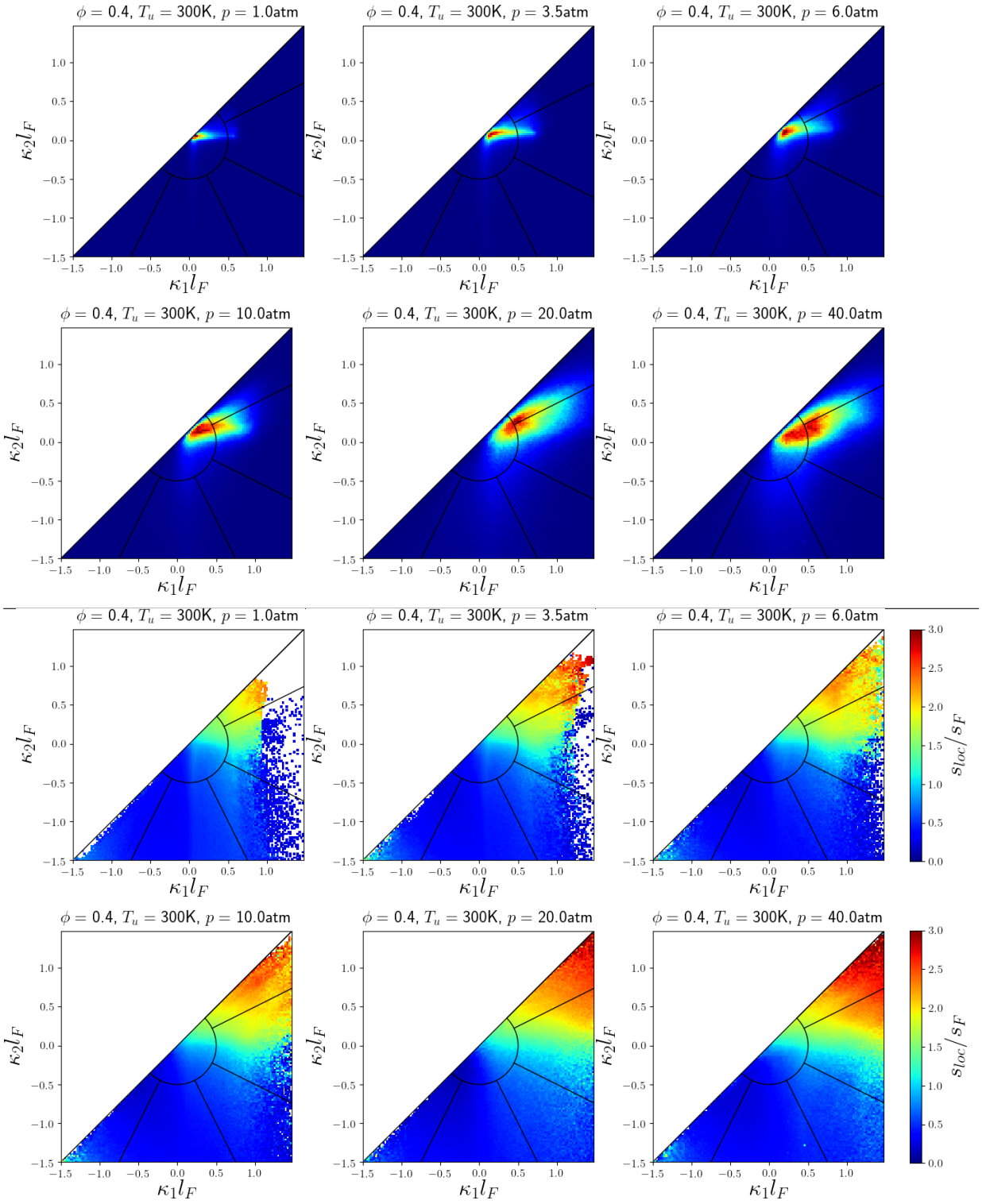

Figure 4.11: JPDF of principal curvatures weighted by flame speed (top), and local flame speed conditionally-averaged on principal curvatures (bottom) for increasing pressure (left-to-right and top-to-bottom).

all burning occurs within the flat flame region. It can be see that as pressure increases, like with the flame speed curvature JPDFs in Figure 4.5, the range of principle curvatures increases. The majority change with the burning is that the burning transitions from near κ_1 and $\kappa_2 = 0$ to increasingly positive principle curvatures.

Looking at the local flame speed conditionally-averaged on principal curvatures (bottom of Figure 4.11) as indicated by the flame speed curvature JPDFs (Figure 4.5) and the principal curvatures weighted by flame speed (top of Figure 4.11,) there are more regions with stronger positive curvature with increasing pressure. This is shown by more data points JPDFs (less white space) with increasing pressure. Additionally, the stronger the positive principle curvature the faster the normalised local flame speed. Note that the normalised local flame speed is normalised by the freely-propagating flame speed thus has already accounted for the increased mean flame speed due to TD-instabilities. As expected, the peak value of local flame speed occurs at the highest value of $\kappa_1\kappa_2$. It does appear that for flame speed principle curvatures κ_1 and κ_2 have a similar contribution the increased local flame speed. This suggests that the increase in local flame speed above the freely-propagated flame speed is dominated by fuel focusing, not the other zero-curvature flame speed enhancement discussed previously.

To perform a more detailed analysis of the affect flame instability has on flame structure; fractional contributions to overall burning of each principle curvature zone has been constructed. The fractional contributions were calculated by integrating the fuel consumption conditioned by each zone relative to the total fuel consumption. The contributions where then averaged temporally over the statistically stationary region. Figure 4.12 presents the fractional contributions with increasing pressure for the P300 cases. As implied by the isosurfaces, it can be seen that as pressure increases the fractional contribution transitions from flat flame to leading edges and leading points. It can be seen that for the low pressure cases (Case A for example), the bulk of the flame is consumed at the flat flame region. Combining this with the curvature JPDFs (Figure 4.5), at zero curvature the flame burns hotter and faster than its unstretched 1-dimensional flame. This observation is somewhat contradictory to the classical description of TD-unstable flames [137, 97] because there is no fuel focusing in flat flame regions. This observation begs the question as to the origins of this phenomena and will be the

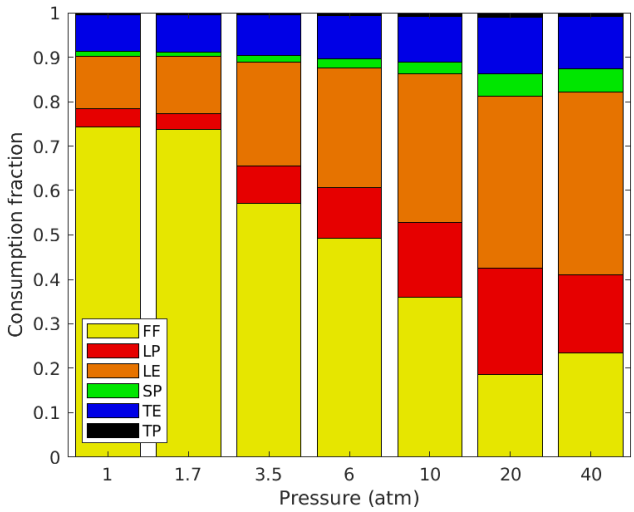

Figure 4.12: Fractional contribution to fuel consumption rate by principal curvature zone against pressure at $T_0 = 300$K and $\phi = 0.4$.

subject of the next section (4.5.2).

4.5.2 Surface Normals and Thermal Leading Points

The local flame speed curvature JPDFs presented in Figure 4.5 clearly show a local flame speed enhancement of above the laminar flame speed even at zero curvature. In turbulent flames this has been attributed to both curvature and strain-rate [34] for example, however in freely-propagating flames there should be zero strain from the fluid acting on the flame without the flame generating that strain to begin with. Additionally, at zero curvature there should not be any focusing of fuel into the region. Using a traditional description of a TD-unstable flame the flame speed at zero curvature in a freely-propagating flame should be the laminar flame speed s_{L}. This section aims to propose and evidence an explanation for this phenomena which is dubbed the thermal leading point concept. The argument that will be proposed is that leading points and edges from the TD-instability have strong positive curvature which results in preferential diffusion of heat and fuel into these positively curved regions (as described by the literature [137] for example). These regions then burn faster and hotter than the laminar flame. These super-adiabatic regions can be described as thermal leading points. The thermal leading points leave a wake of super-adiabatic temperatures, that can then diffuse into regions of flat flame, which typically trail the leading points / edges. Flat flame regions now experience hotter

temperatures than would occur in a 1-dimensional flame, which results in increased burning and thus and increased flame speed, even in the absence of any fuel focusing.

To support this claim, profiles along paths normal to the flame surface have been constructed. The stream-tube approach described in Section 3.2.2 which was utilised for local flame speed and local thermal thickness has been used to construct profiles along paths normal to the flame surface. The paths have been conditionally-averaged according to the intersecting surface principle curvature zone. This allows for profiles of temperature, equivalence ratio and fuel consumption rate to be plotted as a function of arc length ζ along the paths, which are then normalised by the local thermal thickness (ℓ_{loc}) of the paths corresponding to that principle curvature zone. Figure 4.13 presents the normals at increasing pressure; $P_0 = 3.5, 10$ and 40atm at a fixed $T_0 = 300$K and $\phi = 0.4$. An additional TD-stable case is presented with reactant conditions; $P_0 = 1$atm, $T_0 = 700$K and $\phi = 0.4$. All plots have an unstretched 1D laminar flame profile for reference, indicated by the dashed black line. Firstly, by focusing on the $P_0 = 3.5$ case, as expected, leading points are the hottest, richest and most reactive of the zones, followed by leading edges, flat flame then the saddle point, trailing edges and trailing points. The leading points and edges behave as expected, with preferential diffusion increasing the temperature and reaction rates above the 1-dimensional laminar profile. Interestingly, the flat flame regions are different to the 1-dimensional laminar profile, which as explained above should not occur at near zero curvature. A natural explanation as to why the flame is hotter and more reactive, is that there must be an external source of heating diffusing into the flat flame region. This is further supported when the pressure is increased. As previously shown, increasing the pressure increases the strength of the leading points where there is stronger curvature, resulting in even hotter regions, which in-turn should diffuse more heat into the flat flame regions increasing the reaction rate of the flat flame region. This is exactly what is observed in Figure 4.13. For reference, a TD-stable case is provided where there is an absence of leading points and edges. This means there are no strong super-adiabatic leading points, thus there is not the increased temperature at the flat flame region, thus the flat flame region does not experience enhanced burning rates and closely resembles the 1-dimensional laminar profile.

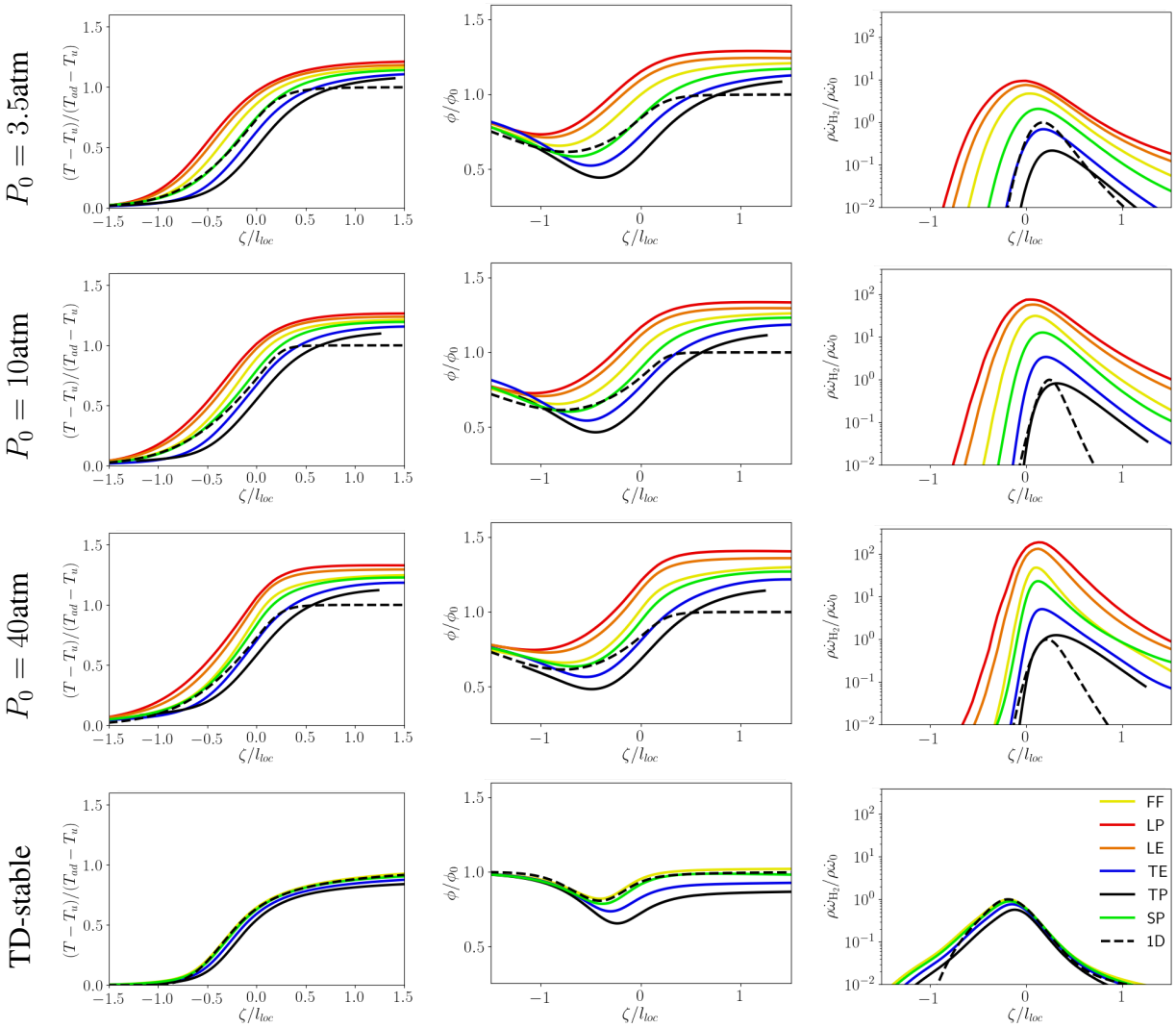

Figure 4.13: Normalised temperature, equivalence ratio and fuel consumption rate against normalised distance from the flame surface, all conditionally-averaged by principal curvature zone. For incrementally increasing pressure; $P_0 = 3.5, 10$ and 40atm at a fixed $T_0 = 300$K and $\phi = 0.4$. The TD-stable case is $P_0 = 1$atm, $T_0 = 700$K and $\phi = 0.4$. The dashed black line denotes the one-dimensional unstretched laminar flame profile.

4.6 Conclusions

This chapter studied TD-unstable, 3-dimensional, freely-propagating flames over a wide range of reactant conditions to explore the effect of reactant conditions on the TD-response of lean hydrogen flames. There has been a specific focus on how local flame speed and thickness correlate with an instability factor ω_2 proposed by [118, 117] which arises from classical stability analysis and has been shown to work well in 2-dimensions by [80].

The TD-behaviour was found to be largely consistent with the findings from [80], most notably that the TD-response scales well with decreasing ω_2. It was found that the response differed depending on which side of the most unstable (low and high pressure regime) the reactant conditions were on. It was observed that 3D flames had a stronger TD-response when compared to 2-dimensions, with faster flame speeds and thinner flame thermal thicknesses. It was also found that the TD-flame structures were different in 3-dimensions than in 2-dimensions, consistent with the observations from [18]. The flame experienced more bulbous shaped leading points and formed distinct channels of leading edges and extinction regions. The flame structures with high positive curvature, which were more unstable and often disturbed by neighbouring flame structures, were compared to the very stable flame fingers observed in 2-dimensions with less extreme positive curvature.

Two models proposed in [80] were shown to work well in 3-dimensions with larger constants to account for the additional diffusion direction. The models have been presented to predict the mean local flame speed acceleration and mean local flame thinning based on ω_2, and has good predictive capabilities:

$$\overline{s_{\text{loc}}} \approx \begin{cases} \exp\left(0.08\omega_2\right) & \text{if low pressure regime,} \\ 1 + 0.47\omega_2 & \text{if high pressure regime,} \end{cases}$$

$$\overline{\ell_{\text{loc}}} \approx \begin{cases} \exp\left(-0.06\omega_2\right) & \text{if low pressure regime,} \\ \left(1 + 0.26\omega_2\right)^{-1} & \text{if high pressure regime.} \end{cases}$$

It will be shown in later chapters that these models are essential for appropriately categorising flame turbulent conditions, as suggested in [18]. These models will also be shown to be a vital component in accounting for TD-effects for turbulent flame speed models.

Interestingly a small TD-effect was observed for the $\omega_2 = 0$ (Z) case, which has been attributed to DL instability inducing curvature, provoking a TD-response. It will be shown in later chapters that this effect is more prominent in turbulent flames.

To evaluate the relationship between local flame speed and local flame quantities, joint probability density functions (JPDFs) of local consumption based flame speed and mean curvature, strain-rate and stretch based of single and multiple Markstein numbers were constructed. It was found that local flame speed has a positive correlation with local flame curvature with a gradient (Markstein number) of -2.5, where the Markstein number was found to be largely independent of reactant conditions. It was found that local flame speed also had a positive correlation with strain-rate. Unlike curvature only, the strain-rate correlation was dependent on reactant conditions, where it was found that in the low pressure regime, the dependence on strain rate grows faster than linear, is linear at the most unstable surface, and is slower than linear in the high pressure regime. Using a single Markstein number to correlate local flame speed with stretch was found to collapse well (when accounting for mean strain-rate). Following [80] independent Markstein numbers were considered for independent turning of curvature and strain dependence. However unlike in 2D, independent Markstein numbers yielded minimal improvement. It was found that both the single Markstein, and independent Markstein numbers had no obvious scaling with reactant conditions due to large scatter in the measured Markstein numbers. It was concluded that the most appropriate model was the curvature only model with a constant Markstein number of -2.5 and is independent of reactant conditions, provided the flame is TD-unstable.

Secondly, the structure of the flame surface has been evaluated, by deconstructing the flame curvature into six principle curvature zones (flat flame, leading point, leading edge, saddle point, trailing edge and trailing point). It was found that increasing pressure transitioned the flame structure from a majority flat flame, to being dominated by leading points and edges. By evaluating surface normals conditionally-averaged by principle curvature zone, it was found that leading points experienced the highest temperatures, equivalence ratios and reaction rates, followed by leading edges. This effect was attributed to the focusing of fuel into positively curved regions (see [137, 97] for example). It was observed throughout, that flat flame regions

experienced flame speeds above the 1-dimensional profiles which is surprising considering flat flame regions should not experience preferential diffusion. This observation is consistent with other works ([18] for example), who did not comment on the effect. It was then proposed that this phenomena is the result of thermal leading points, where positively curved regions focus fuel and heat which then can diffuse into flat flame regions, accelerating the regions above the expected 1-dimensional flame speed.

Chapter 5. Turbulent Flames Part 1: Fixed Length Scale

TD-unstable turbulent lean premixed hydrogen flames are investigated over a wide range of reactant and turbulent conditions with varying temperature, pressure, equivalence ratio and Karlovitz number to evaluate the thermodiffusive response to both reactant and turbulent conditions. Continuing from Chapter 4, flames are characterised using the flame instability parameter ω_2 [118] and the turbulence characterised by the freely-propagating Karlovitz number $\mathrm{Ka_F}$ at a fixed normalised integral length scale. The Karlovitz number has been varied to induce different TD-responses. Turbulence was found to enhance the local flame speed and flame thermal thickness thinning above the freely-propagating vales. It was found that the rate of the increase in speed and thinning strongly correlated to $\sqrt{\mathrm{Ka_F}}$, with a weak dependence on ω_2, provided the TD-response from reactant conditions in freely-propagating flames had been accounted for. An empirical scaling model combining the effects of the TD-response to reactant and turbulent conditions is then proposed. This chapter follows a similar approach to the previous chapter where joint probability density functions are used to correlate local consumption-based flame speed with curvature, strain-rate and stretch with single and independent Markstein numbers. It was found that there was weak correlation for strain-rate based models, even with single and multiple Markstein numbers, therefore a simple curvature-based model was again proposed which was found to yield reasonable results. Flame surface structure is again studied using principle curvature zones. It was found that turbulence dominated the flame surface structure, even at low $\mathrm{Ka_F}$. Finally, the thermal leading point concept is then evaluated again in the context of turbulent flames.

As in Chapter 4, the current chapter's work is published under the title *Thermodiffusively-unstable lean premixed hydrogen flames: phenomenology, empirical modelling, and thermal leading points* published in the journal *Combustion and Flame* in July 2023. This work was produced in collaboration with Dr. Thomas Howarth who was the joint first author.

5.1 Introduction

Following on from Chapter 4, the majority of combustion engines are turbulent, thus an understanding of the interaction between turbulence and the TD-instability is required. Early numerical work on turbulent lean hydrogen flames using the canonical turbulent flame-in-a-box configuration were conducted by the Berkeley group [30, 59, 18, 21, 13, 22] for example and further analysed by [149] and [8]. Other works on the effect of Lewis number on fundamental turbulent flame behaviour include that from Chakraborty *et al.* [49, 50, 87] for example. Recent works include that from Lu and Yang [111] and Lee *et al.* [103, 104, 105, 106, 107, 102] for example, who have provided numerical support to the leading point concept. There are also more realistic combustor configurations [167, 32, 61, 34, 123] for example.

Day *et al.* [59] simulated a TD-unstable lean hydrogen flame at increasing levels of turbulence, it was shown that turbulence enhanced the TD-response and local flame speeds were increased with increasing turbulence. The positive correlation with local flame speed and curvature, as observed in Chapter 4, was still clearly present. It was later shown by Aspden *et al.* [22] that even at high turbulence ($\mathrm{Ka_F} = 108$) TD-structures still existed, and local flame acceleration was still present. However, at extreme levels of turbulence ($\mathrm{Ka_F} \geq 974$) these structures disappeared. These levels of turbulence are unlikely to exist in real-world combustors, but is an interesting observation as to how persistent TD-effects can be. In agreement with the flame-in-a-box configurations from the Berkeley group, it was found that for the low Lewis number, local flame speed was increased above the laminar flame speed, while the unity Lewis number case did not. Recent work by Mohan *et al.* [123] also shows that Lewis number in turbulent flames increases the local flame acceleration in a bunsen flame. Its is suggested that local flame acceleration is well approximated by $I_0 = \mathrm{Le}^{-1}$. This is shown to provide good approximations for large variations in Lewis number.

It was shown in [18] that as a consequence of the TD-instability, characteristic values for flame speed and thickness cannot be taken from simple 1-dimensional flames; it is more appropriate to take freely-propagating values obtained from multidimensional numerical simulations to use for nondimensionalisation purposes such as classifying the turbulent burning regime.

Throughout the literature there is ample evidence that for low-to-moderate turbulence the TD-response is enhanced by turbulence. However the studies conducted provide a limited number of conditions, thus the potential for extracting appropriate models and trends that are viable over a large range of conditions are unclear.

5.2 Numerical Configuration and Simulation Conditions

A broad range of reactant and turbulent conditions have been considered. Following [21], flames are considered in the thin-reaction zone of the premixed regime diagram, with freely-propagating Karlovitz numbers of $1, 4, 12$ and 36 with a fixed integral length scale of $\ell_{\mathrm{I}}/\ell_{\mathrm{F}} = 1.6$. Following [20], the freely propagating values determined in Chapter 4 have been used to determine the appropriate turbulent parameters. As in Chapter 4 set P300 is a trajectory of incrementally increasing pressure at fixed temperature $T_{\mathrm{in}} = 300\,\mathrm{K}$ and equivalence ratio $\phi = 0.4$ at two Karlovitz numbers $\mathrm{Ka}_{\mathrm{F}} = 4$ and 36. Cases A, B, C, D and Z from Chapter 4 are now sets of incrementally increasing Karlovitz numbers $\mathrm{Ka}_{\mathrm{F}} = 1, 4, 12$ and 32. Some additional cases along the most unstable surface R have been evaluated at a fixed Karlovitz number of $\mathrm{Ka}_{\mathrm{F}} = 4$. An additional case I which is the intermediate between sets B and C and has been added at a fixed Karlovitz number of $\mathrm{Ka}_{\mathrm{F}} = 4$. For full details of simulation conditions see Table 5.1. As described in Chapter 3, and similar to Chapter 4, the turbulent flame sheets have been simulated in a high aspect ratio domain with a laterally-periodic slip wall-outflow configuration, where the the flame starts near the top of the domain and burns towards the bottom where homogeneous isotropic turbulence is maintained throughout the domain. The domain size is fixed at $16\ell_{\mathrm{F}}$ x $16\ell_{\mathrm{F}}$ x $64\ell_{\mathrm{F}}$.

5.3 Effect of Pressure at a Fixed Karlovitz Number

This section focuses on the set P300/04, which is where the equivalence ratio, inlet temperature and Karlovitz number are fixed at 4 and the pressure is increased.

Table 5.1: Turbulent flame simulation conditions. For all cases, the domain size is $\mathrm{L}_x = \mathrm{L}_y = 16\ell_\mathrm{F} = 10\ell_\mathrm{I}$, with $L_z = 4\mathrm{L}_x$.

Set	Case	p (atm)	T_in (K)	ϕ	ω_2	s_F (cm/s)	ℓ_F (μm)	$\mathrm{Ka_F}$	$\mathrm{Da_F}$
P300/04	(A/04)	1	300	0.4	5.45	34.4	526	4	0.55
		1.7			7.39	29.8	329		
		3.5			12.9	23.6	189		
		6			20.7	18.3	140		
		10			27.3	13.2	114		
		20			17.1	7.00	120		
		40			13.6	4.30	90.9		
P300/36	(A/36)	1	300	0.4	5.45	34.4	526	36	0.13
		3.5			12.9	23.6	189		
		10			27.3	13.2	114		
		40			13.6	4.30	90.9		
A	(A/01)	1	300	0.4	5.45	34.4	526	1	1.37
	(A/04)							4	0.55
	(A/12)							12	0.26
	(A/36)							36	0.13
B	(B/01)	40	700	0.4	5.58	56.5	18.7	1	1.37
	(B/04)							4	0.55
	(B/12)							12	0.26
	(B/36)							36	0.13
C	(C/01)	20	700	0.2	2.28	3.33	484	1	1.37
	(C/04)							4	0.55
	(C/12)							12	0.26
	(C/36)							36	0.13
D	(D/01)	1	300	0.25	48.2	4.10	3200	1	1.37
	(D/04)							4	0.55
	(D/12)							12	0.26
	(D/36)							36	0.13
Z	(Z/01)	1	300	0.565	0	85.3	382	1	1.37
	(Z/04)							4	0.55
	(Z/12)							12	0.26
	(Z/36)							36	0.13
R/04	(D/04)	1	300	0.25	48.2	4.10	3200	4	0.55
		3.5	300	0.32	36.8	9.09	434		
		20	700	0.28	7.44	24.3	75.5		
I/04		20	700	0.4	4.22	106	25.4	4	0.55

5.3.1 Flame Surfaces

Figure 5.1 presents two surfaces for each case ($p = 3.5$,10 and 40 atm at fixed $T_{\text{in}} = 300$ K and $\phi = 0.4$) at a fixed $\text{Ka}_{\text{F}} = 4$; showing the isosurfaces of fuel mass fraction ($c = 0.9$) coloured by the local flame speed normalised by the freely propagating flame speed and the principle curvature zones discussed in Chapter 4. The principal curvature zone has been normalised using the mean local surface average thermal thickness ℓ_{S} rather than the larger freely propagating thermal thickness ℓ_{F}, and as a result classifies relatively more of the surface as flat but leaves the other zones unchanged. Most notably from Figure 5.1, the surfaces look very similar to each-other. This is in stark contrast to the freely propagating observations in Figure 4.2 even when normalised by s_{F} and ℓ_{F}. This observation implies that even at a relatively low turbulent intensity, turbulence dominates the small-scale flame surface structure and speed provided the freely propagating flame characteristic values have been accounted for. The similarities between the surfaces, regardless of reactant conditions, indicated that using the freely propagating values are ideal for determining the appropriate turbulent characteristics compared with traditional 1-dimensional laminar flame characteristics (i.e. s_{L} and ℓ_{L}). Another notable observation is that local flame speed appears to be greater than s_{F} even when the flame is flat and therefore is not a direct result of hydrogen diffusion. A visual comparison of flame structure through principal curvature zones are shown in Figure 5.1. It can also be seen that unlike in the freely propagating cases, the normalised peak local flame speed is faster than in the freely propagating cases. This is the result of turbulence folding the flame and thus generating stronger positive curvature than the TD-instability could generate naturally. This is also implied by the curvature zones (Figure 5.1 bottom), where a larger region flame surface is more dominated by leading ridge than observed for freely propagating.

To compare the difference between using the freely-propagating turbulent characteristics (as suggested by Aspden *et al.* [18]) to the 1D unstretched values traditionally used, three reactant conditions have been compared with pressures $0.35, 10$ and 40 atm at fixed temperature (300 K) and equivalence ratio (0.4), with fixed $\text{Ka}_{\text{F}} = 4$ compared to fixed $\text{Ka}_{\text{L}} = 4$. It can be seen clearly that, like in figure 5.2, the cases normalised by freely propagating values are similar, implying that the turbulence interacting with the flame is similar for all cases. The same cases normalised by 1-dimensional laminar values look very different, where the cases

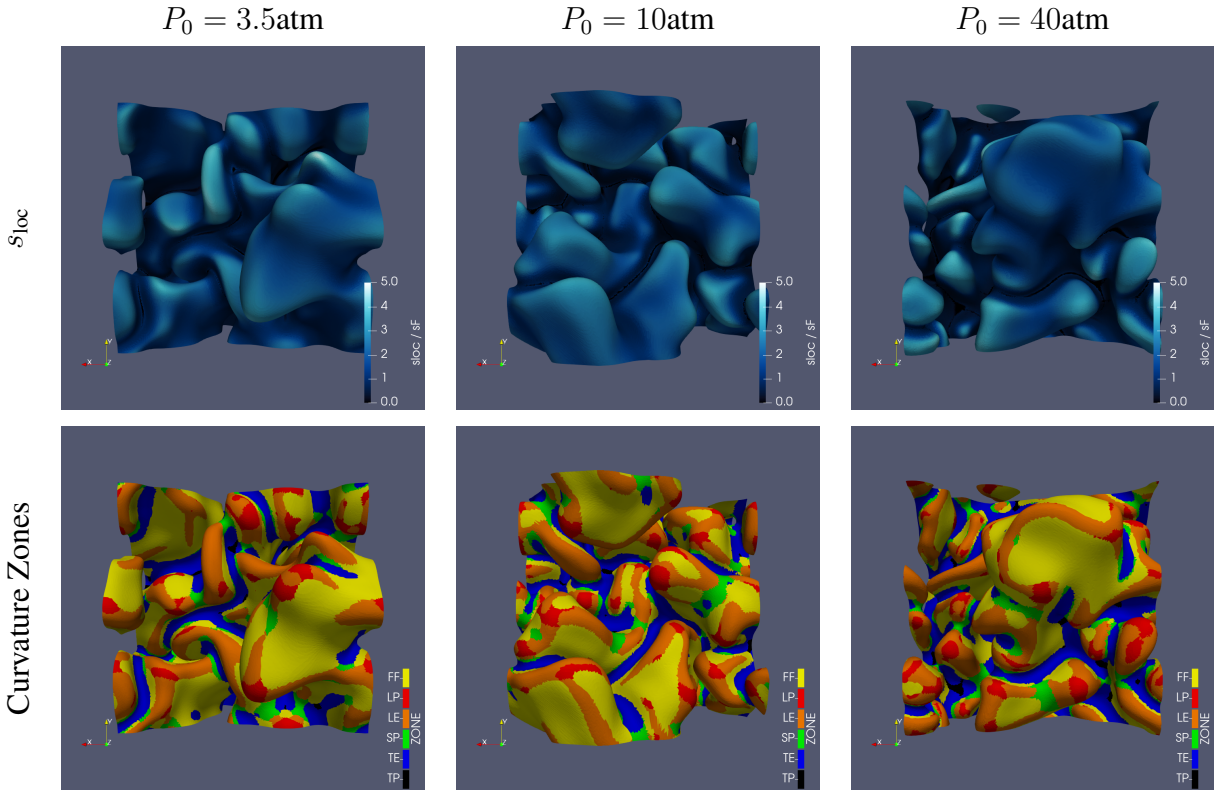

Figure 5.1: Isosurfaces of fuel mass fraction coloured by the normalised local flame speed (top) and coloured by principle curvature zone (bottom) for increasing pressure (left to right); the direction of flame propagation is out of the page toward the reader. Note how similar the flames appear.

with the higher levels of ω_2 (and thus expect a stronger freely propagating TD-response) do not look very turbulent with freely-propagating TD-unstable structures appearing, with very high local flame speeds. This presents a clear case that for local flame quantities the characteristic values must be attained by using the freely propagating values. It should be noted however that the effect of characteristic values has only been studied for local effects, although it is expected that the same observations will be observed for global effects (i.e. flame surface area), it is out the scope of this chapter and will be revisited in Chapter 6.

5.3.2 Principal Curvature Zones

The fractional contribution to fuel consumption for each principal curvature zone is presented in Figure 5.3 with incrementally increasing pressure (from left to right). It can be seen that the

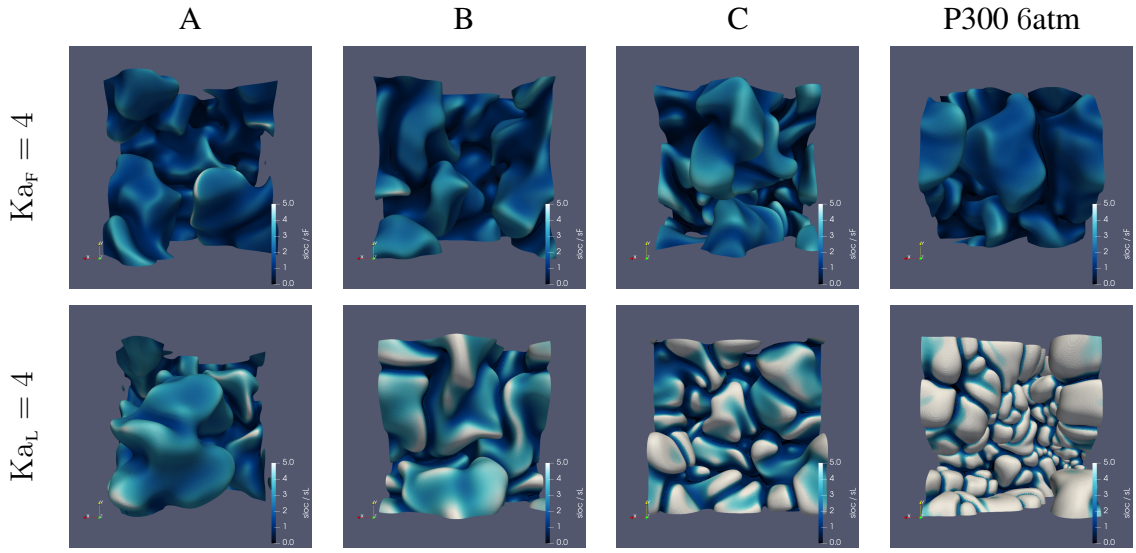

Figure 5.2: Isosurfaces comparing cases normalised by (top) freely-propagating values and (bottom) laminar 1D values; left-to-right, the reactant cases are A/04, B/04, C/04 and P300[6 atm]/04, respectively. Clearly, the freely propagating normalisation gives similar-looking flames with comparable normalised burning rates, whereas the 1-dimensional laminar values gives flames that look categorically different and have burning rates that do not fall in the same normalised range.

flat flame accounts for about $40 - 50\%$ of the fuel consumption, followed by leading edges, then trailing edges, with leading points and saddle points consisting of a small contribution and trailing points being very small for each case. Despite contribution between the cases being very similar, there is a small trajectory of larger contributions of leading edges and less flat flames as pressure increases. When compared to the freely-propagating flames (Figure 4.12) where the fractional contributions were quite different with increasing pressure, the turbulent cases are very similar. This suggests that despite a TD-response to turbulence, the local flame surface structure is primarily determined by turbulence, not reactant conditions.

5.3.3 JPDFs and Local Flame Speed

Figure 5.4 are the JPDFs (as defined in the previous chapter) showing the normalised local consumption speed (s_{loc}) against normalised local curvature (κ) for the P300 $\mathrm{Ka_F} = 4$ set (where the pressure increases top-to-bottom (left)) and the other $\mathrm{Ka_F} = 4$ cases (B, C, D,

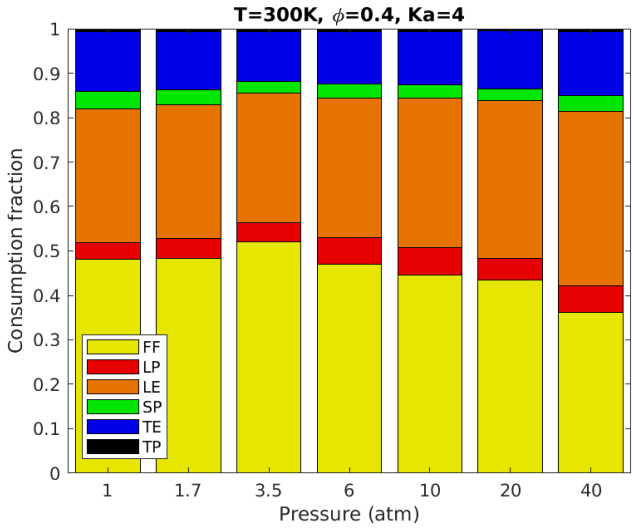

Figure 5.3: Fractional contribution to fuel consumption partitioned by principal curvature zone for simulation set P300/04 which have the same reactant conditions as in Figure 4.12 but at $\mathrm{Ka_F} = 4$. Again, note how similar the cases are, unlike the corresponding freely-propagating cases in Figure 4.12

R(3.5), R(20) and I) top-to-bottom respectively (right). The colour scale used for the JPDFs applies to all following JPDFs. The plot has solid, dashed and dotted magenta lines to denote the mean local flame speed, (s_S), freely-propagating flame speed (s_F) and laminar flame speed (s_L) for each case respectively. The solid white line represents the line of best fit (by orthogonal distance regression) and the dashed white line represents a curvature only model ($s_\mathrm{loc} = s_\mathrm{S}\left(1 - \mathcal{M}_\kappa \kappa \ell_\mathrm{S}\right)$ to be discussed later). Figure 5.5 are the JPDFs showing the normalised local consumption speed (s_loc) against strain-rate, stretch with single and independent Markstein numbers, left-to-right respectively for $\mathrm{Ka_F} = 4$ set where the pressure increases top-to-bottom. The strain-rate has been normalised by the appropriate surface-averaged time-scale (τ_S) to bring the data into a comparable range. The solid white line represents line of best fit (by orthogonal distance regression). Figure 5.6 is the same as 5.5 but considered the other $\mathrm{Ka_F} = 4$ cases (B, C, D, R(3.5), R(20) and I) top-to-bottom respectively.

Starting with figure 5.4 for the P300 set, at a fixed $\mathrm{Ka_F} = 4$ the local flame speed response looks very similar with increasing pressure, much more than in the freely-propagating cases. Even when comparing with the highest ω_2 case (case D, a ridge case in ω_2 space) all the cases

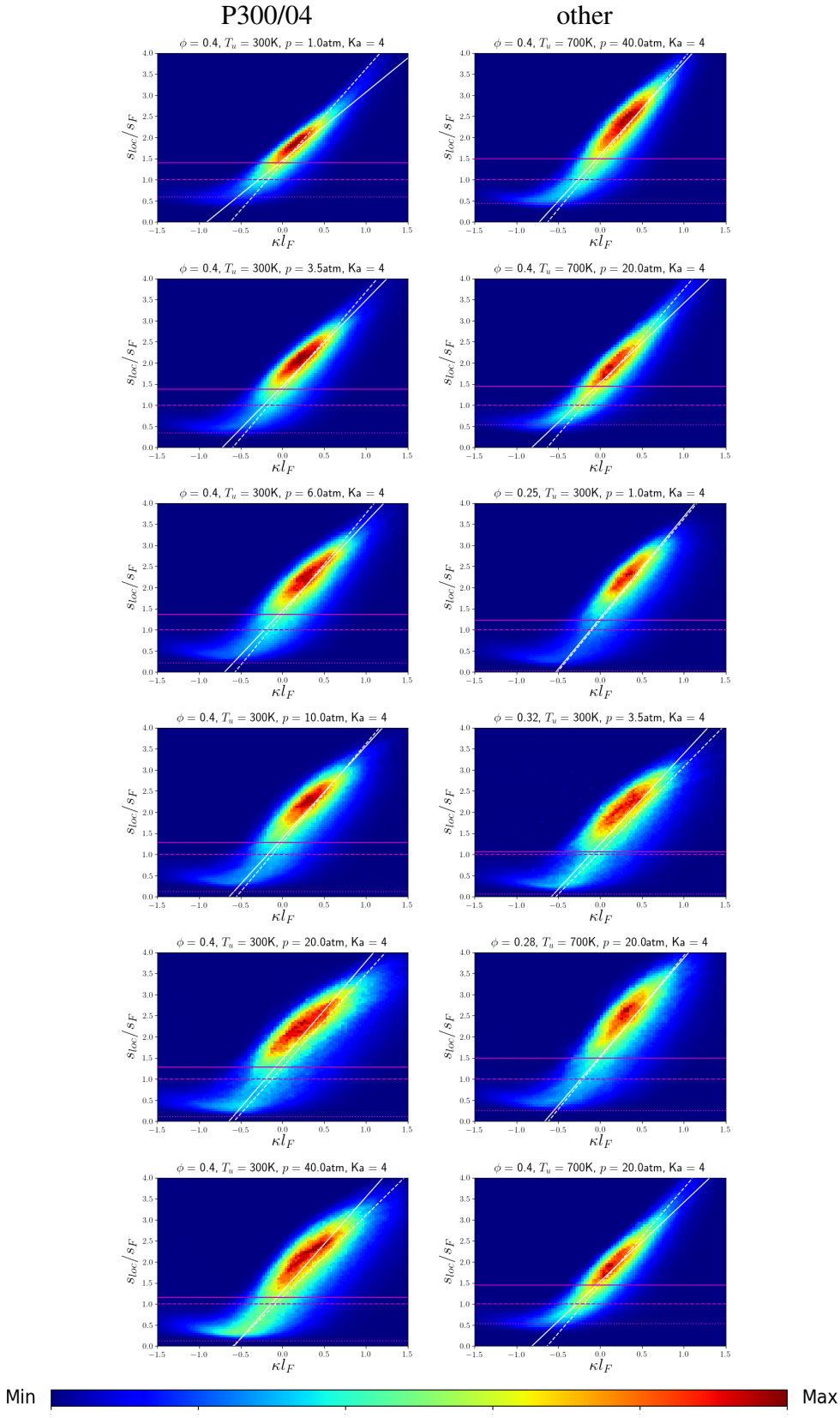

Figure 5.4: JPDFs of local flame speed and curvature for the P300/04 (left) set (pressure increasing top-to-bottom) and cases B, C, D, R(3.5), R(20), I/04 (right) top-to-bottom respectively.

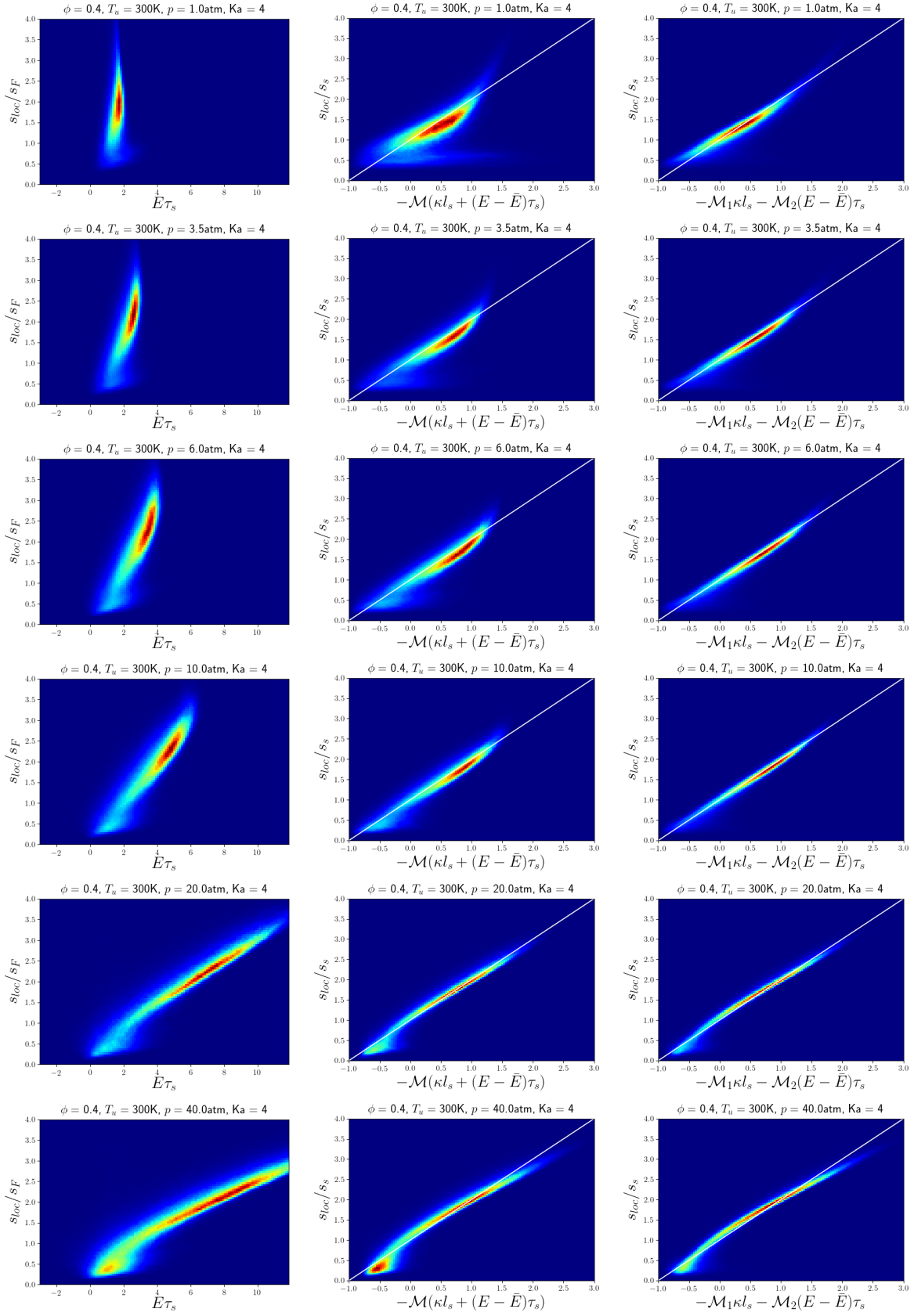

Figure 5.5: JPDFs of local flame speed and three quantities (strain-rate, and stretch with single and independent Markstein numbers) from left-to-right respectively for the P300/04 set.

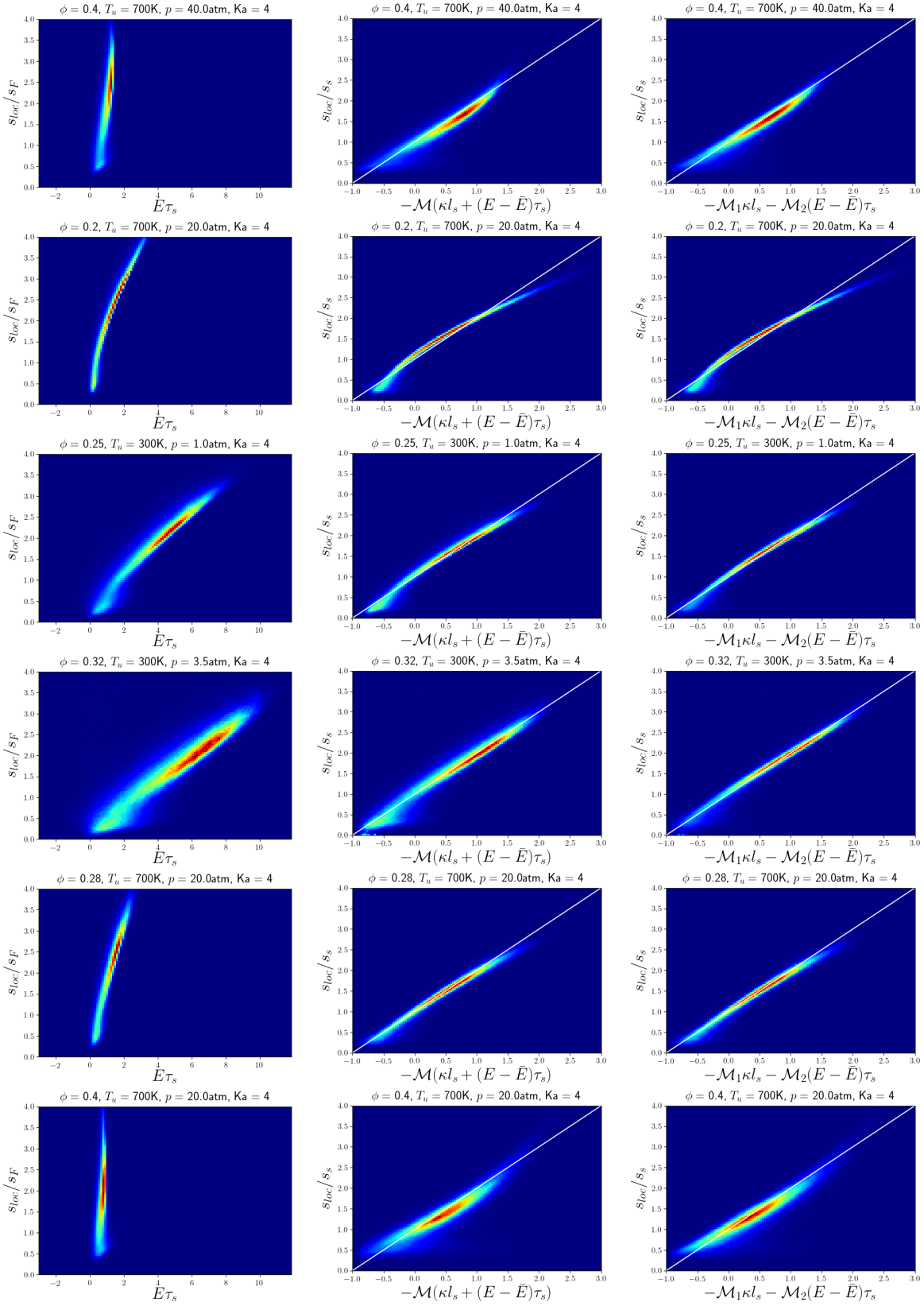

Figure 5.6: JPDFs of local flame speed and three quantities (strain-rate, and stretch with single and independent Markstein numbers) from left-to-right and cases B, C, D, R(3.5), R(20), I/04 top-to-bottom respectively.

still look very similar. It can be seen that the gradient (represented by the solid white line of best fit) varies slightly between cases and the proposed model (which will be discussed in more detail later in the chapter) with a Markstein number $\mathcal{M}_\kappa = -2.2$ does a good job at predicting the local flame speed response, independently of reactant conditions. This is surprising as it is suggesting that the flame speed response at a fixed curvature when turbulent is somewhat independent of the expected level of TD-response (i.e. ω_2 or pressure). It can be noted that despite these similarities, there is some variation with increasing pressure, where despite the gradient remaining similar the range of curvatures increases as does the scatter around the line of best fit. The same is true when comparing two cases; set P300/04 case $p = 3.5$ and case D/04, which both have the same pressure but different ω_2 values. It can be seen that, as with increasing pressure there is a larger range of curvatures and scatter around the line of bet fit, indicating the effect may be driven by the instability (i.e. ω_2) rather than a pressure effect. It will be evaluated later how turbulent intensity effects these observations.

In the local flame speed response to strain-rate and stretch with single and independent Markstein numbers shown in Figure 5.5 for the P300/04 cases and Figure 5.6 for the other cases, it can be seen that at low pressure there is no obvious correlation with strain-rate and flame speed (left). As pressure increases a correlation with strain-rate does occur at higher pressures, where the gradient of local flame speed with strain-rate progressively decreases with increased pressure. Evaluating the stretch with a single Markstein number yields improved collapse, more so at higher pressure, provided the Markstein number is evaluated for each individual case. Independent Markstein numbers yield an even better collapse, even at the lower pressure, again provided the Markstein numbers are evaluated for each individual case.

5.4 Increasing Karlovitz Number

5.4.1 Flame Surfaces

Isosurfaces from simulation sets A, B, C and D at increasing turbulent intensity $\mathrm{Ka_F} = 1, 4, 12$ and 36 are coloured by normalised local flame speed in Figure 5.7 and principle curvature zone in Figure 5.8. Firstly, by looking at set A in Figure 5.7 (left-hand side), it can be seen that increasing the turbulence (top to bottom) significantly changes both the flame structure and the

local flame speed. At $\mathrm{Ka_F} = 1$ the flame structure is more similar to the TD-unstable freely propagating structures, with the characteristic bulb-like flame fingers with deep extinction channels. As turbulence increases the structure transitions quickly from a turbulence dominated flame structure ($\mathrm{Ka_F} = 4$) to a leading ridge type structure, with strong leading edges and high local flame speed with peak values about five times the freely-propagating mean local flame speed. As turbulence continues to increase the flame structures reduce in size resulting in more flame surface experiencing positive and negative curvature. It can also be seen that the peak local flame speed continues to increase. As turbulence increases it can be seen that the curvature at the ridges increases making a "sharper" more defined edge than the lower turbulence's more cylindrical ridges. It can also be seen as ω_2 increases at high turbulence, the flat flame regions also experience higher relative local flame speeds relative to the lower ω_2 cases, denoted by the overall lighter colouration of the flame surface.

Figure 5.9 shows the fractional contribution to the fuel consumption partitioned by principle curvature zone for simulation sets A, B, C and D with incrementally increasing $\mathrm{Ka_F} = 1, 4, 12, 36$ (left-to-right); supporting the observations that turbulence transitions the flame structure from having more burning occurring from flat flame at lower turbulence to having a lower contribution of flat flame and more leading edge at high turbulence. Interestingly, as the flames TD-instability increases (most apparent in cases C and D), the flame does not transition from flat flame to leading edge where even at low turbulence levels the flame has significantly less flat flame than cases A and B. Some possible explanations for this phenomena are the TD-effects are strong even at low turbulence, therefore increasing the turbulence or further folding the flame does not result in additional instability and a transition of flame surface structure. It could also be the result of a "volume filling surface" which means there is limited volume in the flame-in-a-box, restricting the extent to which a flame surface can grow from a strong positively curved region, artificially limiting the flame surface. There is a lack of domain sizes studied in this chapter to properly evaluate this theory, thus will be explored in more detail in Chapter 6.

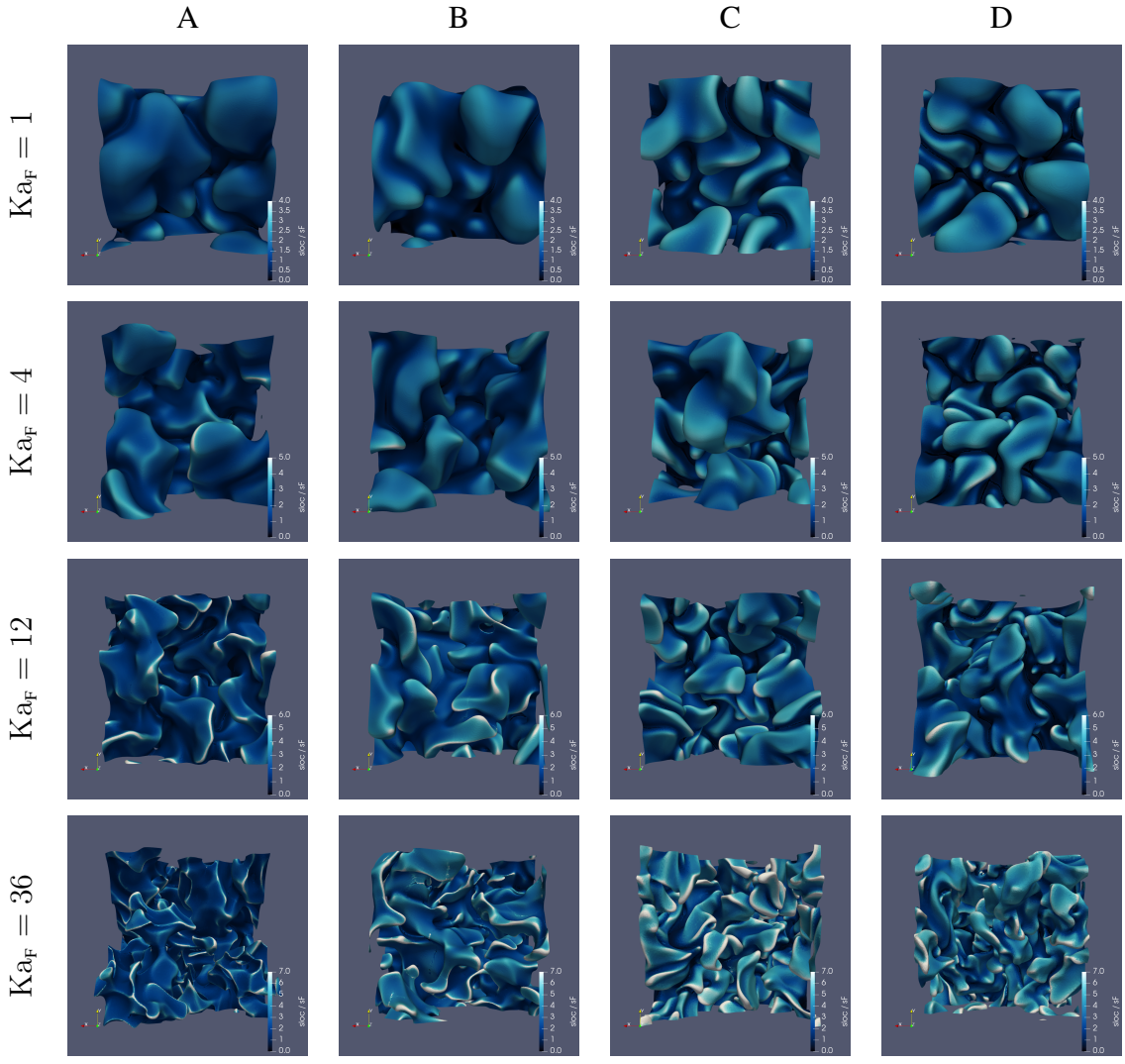

Figure 5.7: Isosurfaces of fuel mass fraction coloured by local consumption based flame speed for sets A, B, C and D (left-to-right) with increasing turbulent intensity from top-to-bottom ($\mathrm{Ka_F} = 1, 4, 12, 36$).

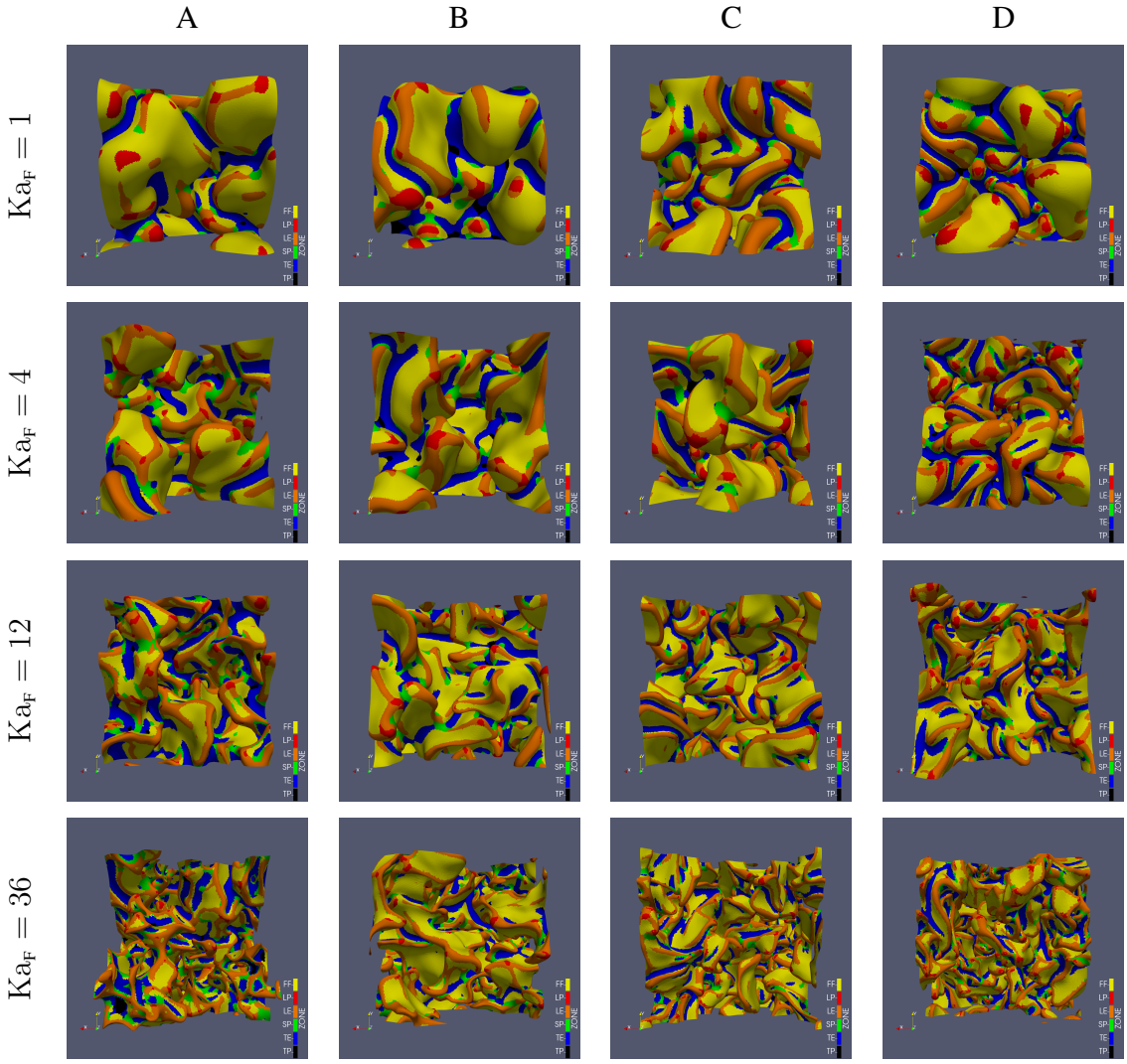

Figure 5.8: Isosurfaces of fuel mass fraction coloured by principle curvature zone for sets A, B, C and D (left-to-right) with increasing turbulent intensity from top-to-bottom ($\mathrm{Ka_F} = 1, 4, 12, 36$). Note as with Figure 5.1, the principal curvature zone has been normalised using the mean local surface average thermal thickness ℓ_s.

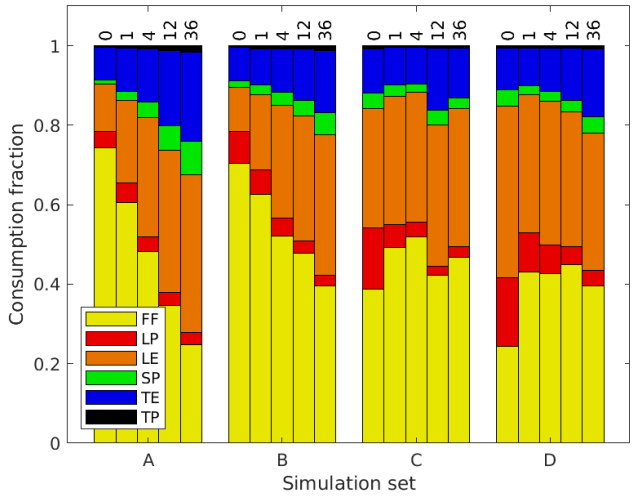

Figure 5.9: Fractional contribution to fuel consumption partitioned by principal curvature zone for simulation set A, B, C and D with incrementally increasing $\mathrm{Ka}_\mathrm{F} = 1, 4, 12, 36$ (left-to-right).

5.4.2 JPDFs

Figure 5.10 shows the JPDFs (as defined in the previous chapter) showing the normalised local consumption speed against normalised local curvature for increasing Ka_F (left-to-right) for cases from set P300 at pressures $p = 1, 3.5, 10, 40$ and sets B, C and D (top-to-bottom). As with the previous JPDFs, the plot has solid, dashed and dotted magenta lines to denote the mean local flame speed, freely-propagating flame speed and laminar flame speed for each case respectively. The solid white line represents the line of best fit and the dashed white line represents a curvature only model ($s_\mathrm{loc} = s_\mathrm{s}\left(1 - \mathcal{M}_\kappa \kappa \ell_\mathrm{s}\right)$ where $\mathcal{M}_\kappa = 2.2$). Figure 5.11 are the JPDFs showing the normalised local consumption speed against strain-rate, Figure 5.12 against stretch with a single Markstein number and Figure 5.13 against stretch with independent Markstein numbers. Again the solid white line represents line of best fit. Figure 5.14 shows the normalised local consumption speed against normalised local curvature for increasing Ka_F (left-to-right) for the TD-neutral case Z where the lines are the same as in Figure 5.10.

Starting with the curvature only JPDFs (Figure 5.10) at a fixed reactant conditions (i.e. case A labelled P300 $p = 1$, B, C or D) it can be seen that as Ka_F increases the range of curvatures and flame speeds increases, as does the scatter around the mean line. Interestingly it can be

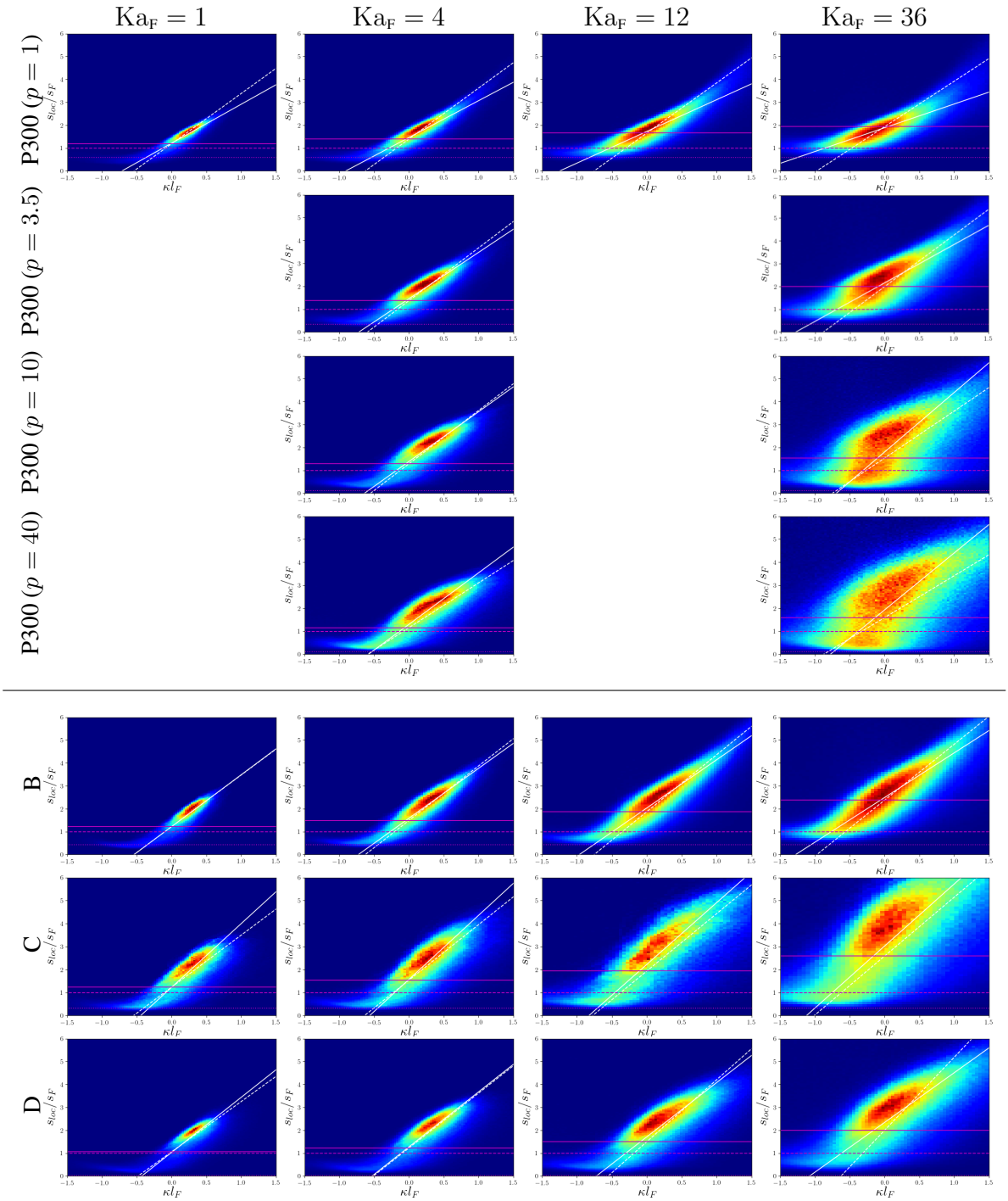

Figure 5.10: JPDFs of local flame speed and curvature for increasing $\mathrm{Ka_F}$ left-to-right for different reaction conditions P300 ($p = 1, 3.5, 10, 40$) and B, C, D top-to-bottom. The solid, dashed and dotted magenta lines to denote the mean local flame speed, freely-propagating flame speed and laminar flame speed for each case respectively. The solid white line represents the line of best fit and the dashed white line represents a curvature only model.

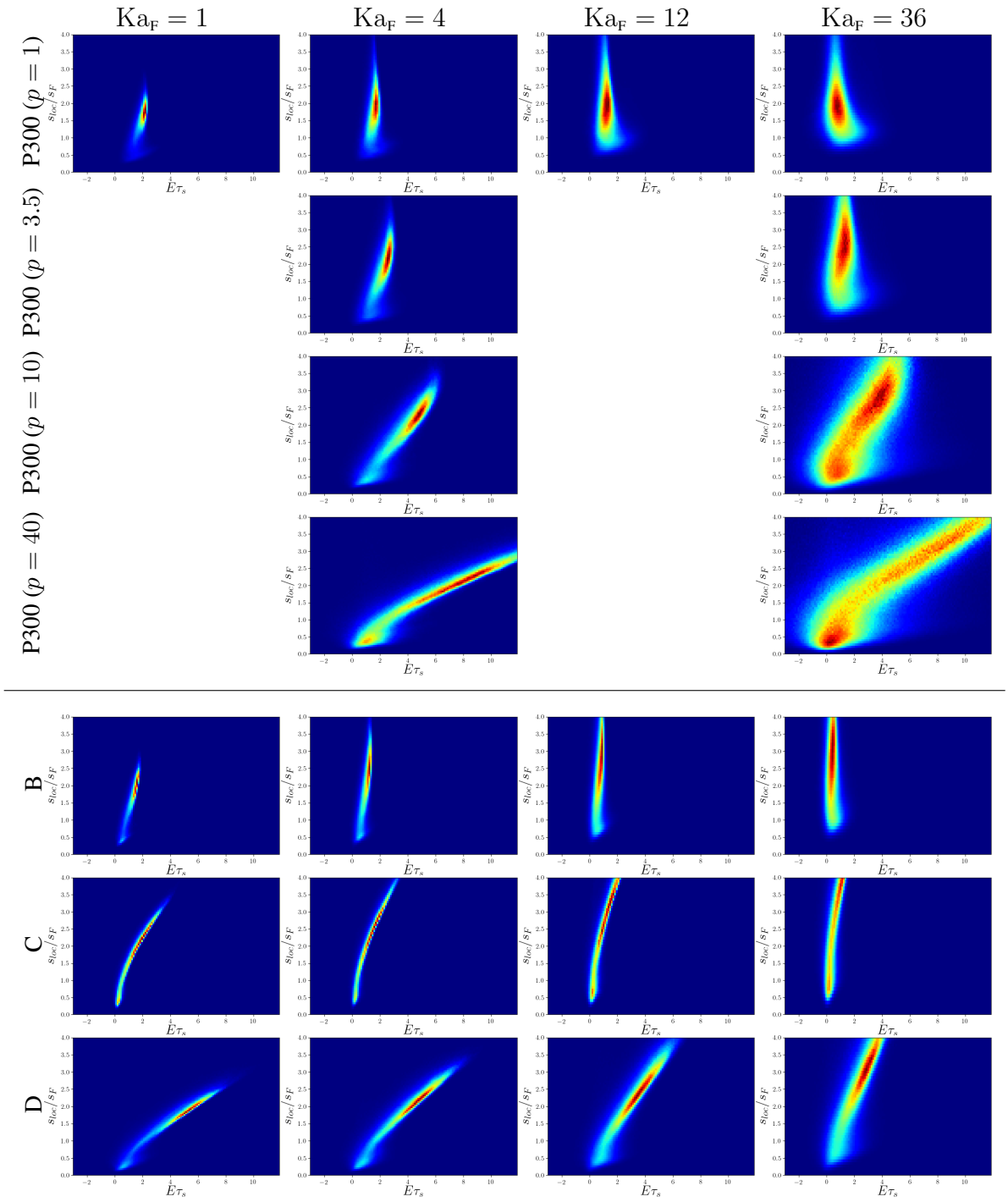

Figure 5.11: JPDFs of local flame speed and strain-rate for increasing $\mathrm{Ka_F}$ left-to-right for different reaction conditions P300 ($p = 1, 3.5, 10, 40$) and B, C, D top-to-bottom.

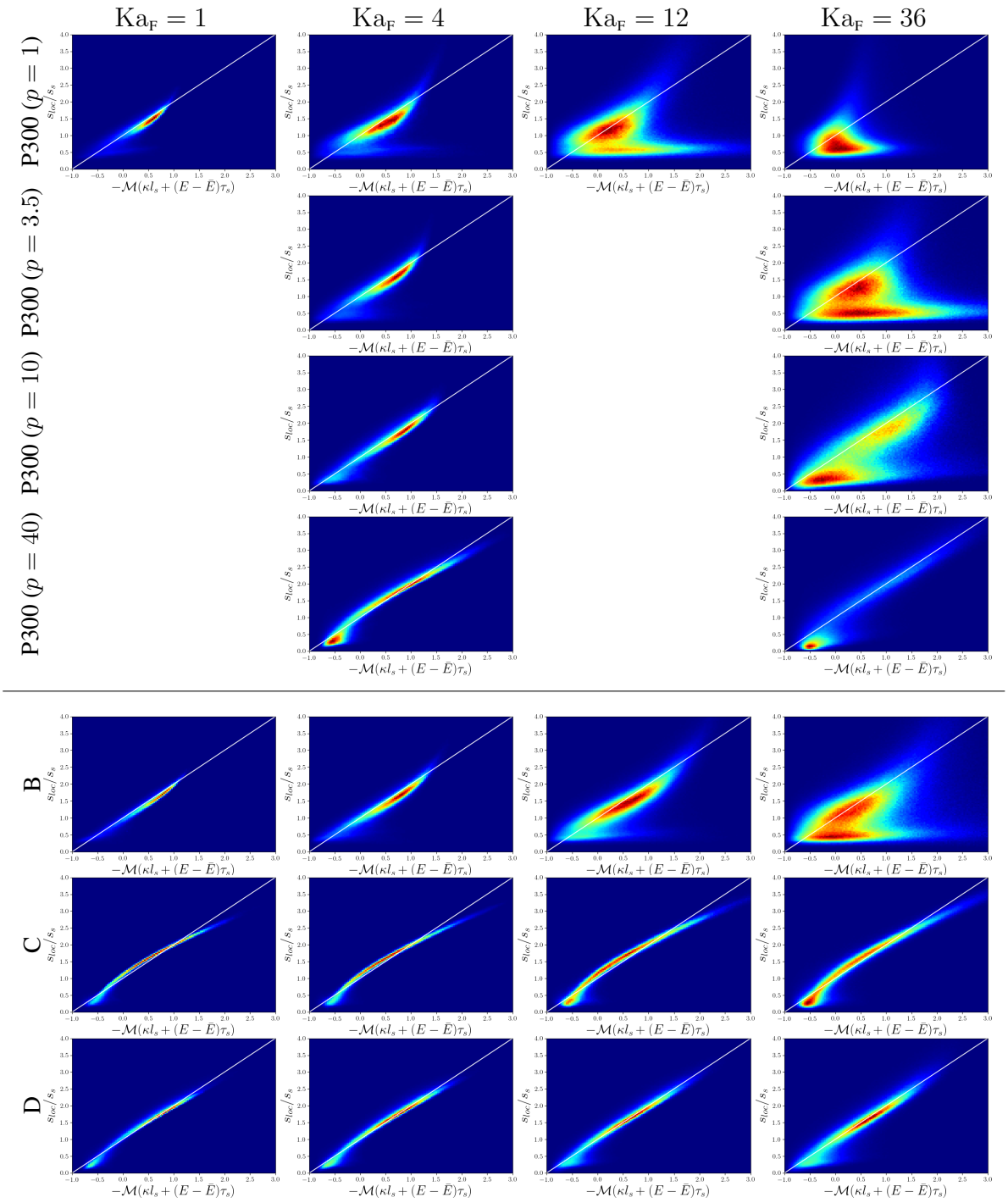

Figure 5.12: JPDFs of local flame speed and stretch with a single Markstein number for increasing $\mathrm{Ka_F}$ left-to-right for different reaction conditions P300 ($p = 1, 3.5, 10, 40$) and B, C, D top-to-bottom. The white line denotes the line of best fit.

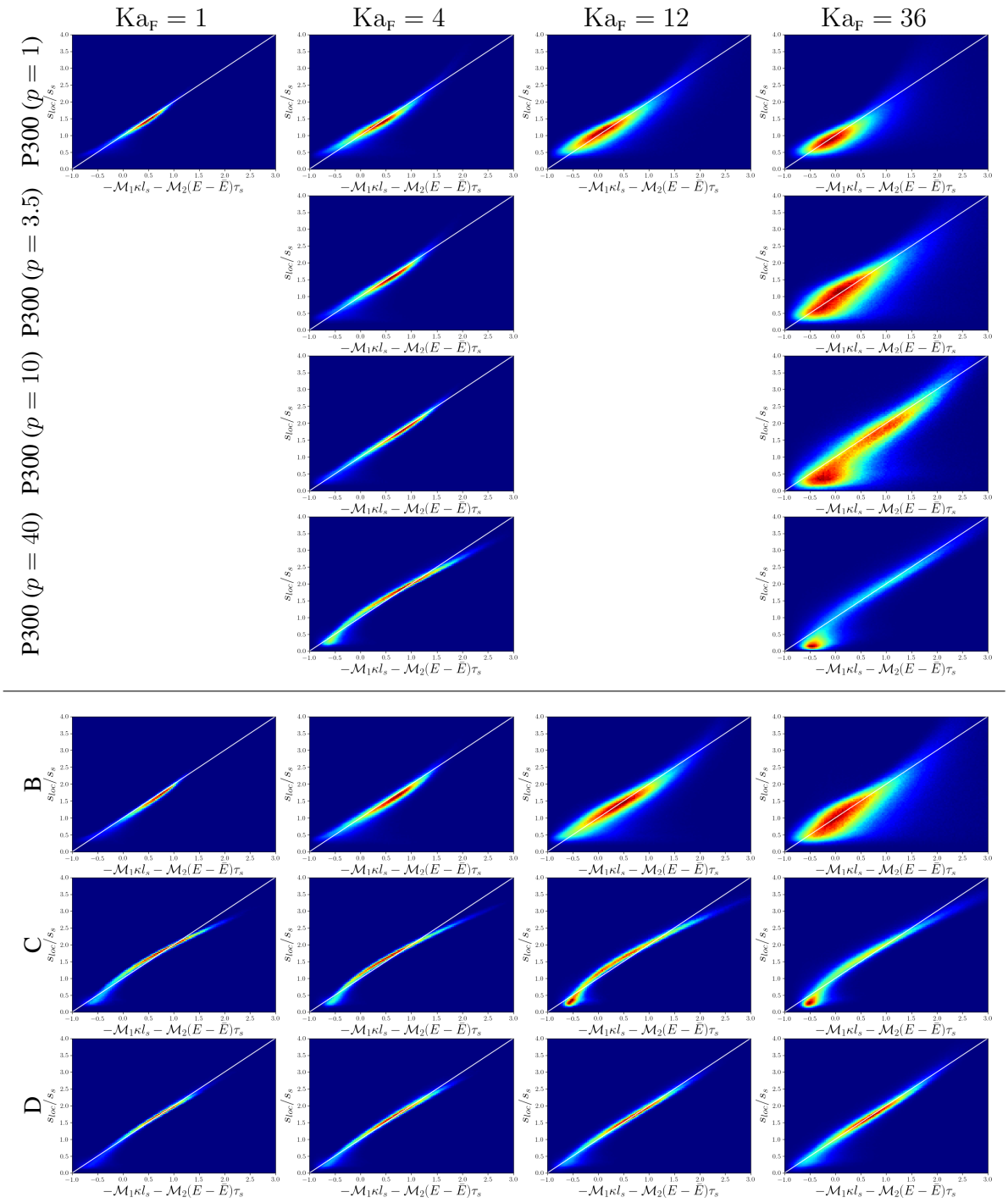

Figure 5.13: JPDFs of local flame speed and stretch with independent Markstein number for increasing $\mathrm{Ka_F}$ left-to-right for different reaction conditions P300 ($p = 1, 3.5, 10, 40$) and B, C, D top-to-bottom. The white line denotes the line of best fit.

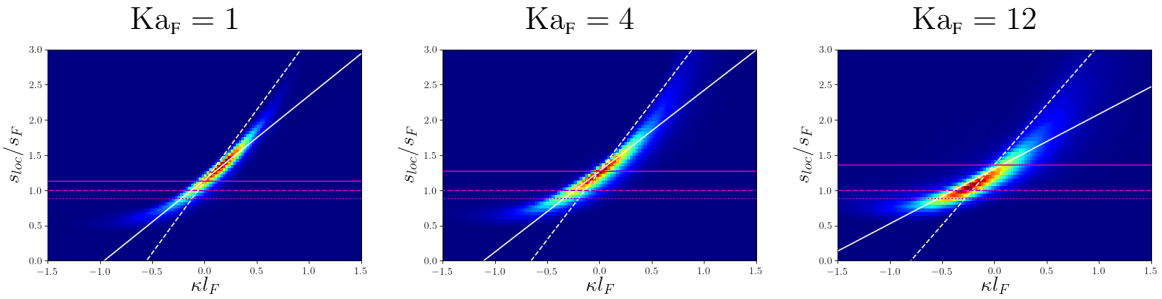

Figure 5.14: JPDFs of local flame speed and curvature for increasing $\mathrm{Ka_F}$ left-to-right for case Z. The solid, dashed and dotted megenter lines to denote the mean local flame speed, freely-propagating flame speed and laminar flame speed for each case respectively. The solid white line represents the line of best fit and the dashed white lin represents a curvaure only model.

seen that the mean-line itself is quite similar with increasing turbulence (note; set A is not as similar as other cases, for example B which has a similar ω_2 but at high pressure and temperature). It can also be seen that as turbulence increases, the region with the highest burning contribution occurs at successively lower curvature values starting from slightly positive to slightly negative. At a fixed $\mathrm{Ka_F}$, unlike the observations from Figure 5.4, at higher turbulence (i.e. $\mathrm{Ka_F} = 36$) it can be seen that as the reactant conditions move from lower pressure (lower ω_2) to higher pressure (higher ω_2) the JPDFs do not look similar. The range of curvatures, flame speeds and scatter around the mean line becomes increasingly large with increasing pressure, this trend appears to continue with increasing pressure ($p = 10$ to $p = 40$) even with a decreasing ω_2, which could be the result of a change of behaviour as the reactant conditions transition from the low-pressure to high-pressure regime in ω_2 space. In this study, there are not enough conditions to properly evaluate this effect.

The strain-rate only JPDFs (Figure 5.11) show little correlation with flame-speed and strain-rate. Where there is a large range of flame speeds that fall within a narrow range of strain-rates this prevents an adequate collapse of the data. This issue persists for the single Markstein number (Figure 5.12) with lower turbulence yielding better results; cases C and D do yield a good collapse of the data even at high $\mathrm{Ka_F}$. Independent Markstein numbers (Figure 5.13) present a much greater improvement even at higher $\mathrm{Ka_F}$, with still some scatter at the high $\mathrm{Ka_F}$ for the P300 cases.

The TD-neutral case Z (Figure 5.14), despite being TD-stable, still shows a positive gradient in local flame speed with increasing curvature and with an enhanced mean local flame speed. Again this, denoted by the solid magenta line, increases with turbulence as does the local flame speed scatter. Despite the natural TD-instability arising from classical stability analysis [118] being neutral (i.e. $\omega_2 = 0$), the effective Lewis number is still less than unity, which in theory can still result in preferential diffusion in positively curved regions. In the case for the turbulent flame, the turbulence folds the flame which can then result in the focusing of heat and fuel into the positively curved region, enhancing the reaction rates. This behaviour will be discussed further in Chapter 6.

Despite the decent collapse of the independent Markstein number JPDFs, each case requires re-calibration of the Markstein numbers. Figure 5.15 presents the calibrated Markstein numbers for the curvature only ($\mathcal{M}_\kappa$) and stretch with both single ($\mathcal{M}$) and independent ($\mathcal{M}_i$) Markstein numbers. It can be seen that for the single and independent Markstein numbers there is a large range of values. An empirical model that adequately captures the range of the constants involved remain elusive.

5.5 Surface-Normals and Thermal Leading Points

The same approach used for surface-normal shown in Figure 4.13 are presented for the turbulent cases. Figure 5.16 shows the surface-normal profiles for each zone from simulation set A, $\mathrm{Ka_F} = 36$. This specifically shows the normalised temperature, equivalence ratio and fuel consumption rate plotted against normalised distance along the surface streamline, following the progress variable conditionally-averaged according to the principle curvature zone and against the corresponding trajectories in T-Y space. The freely-propagating values are shown by the faint dotted line and are coloured by zone. It is clear that turbulence enhances the TD-behaviour observed in the freely propagating cases, where for the turbulent case the principal curvature zones have profiles that are hotter, richer and with higher reaction rates than the freely-propagating cases, which are in-turn hotter, richer and with a higher reaction rate than the 1-dimensional profiles. Following the same principle of the thermal leading point as discussed previously ((Section 4.5.2), now the turbulence folds the flame to present even stronger positively curved regions than what is possible from intrinsic instabilities. These

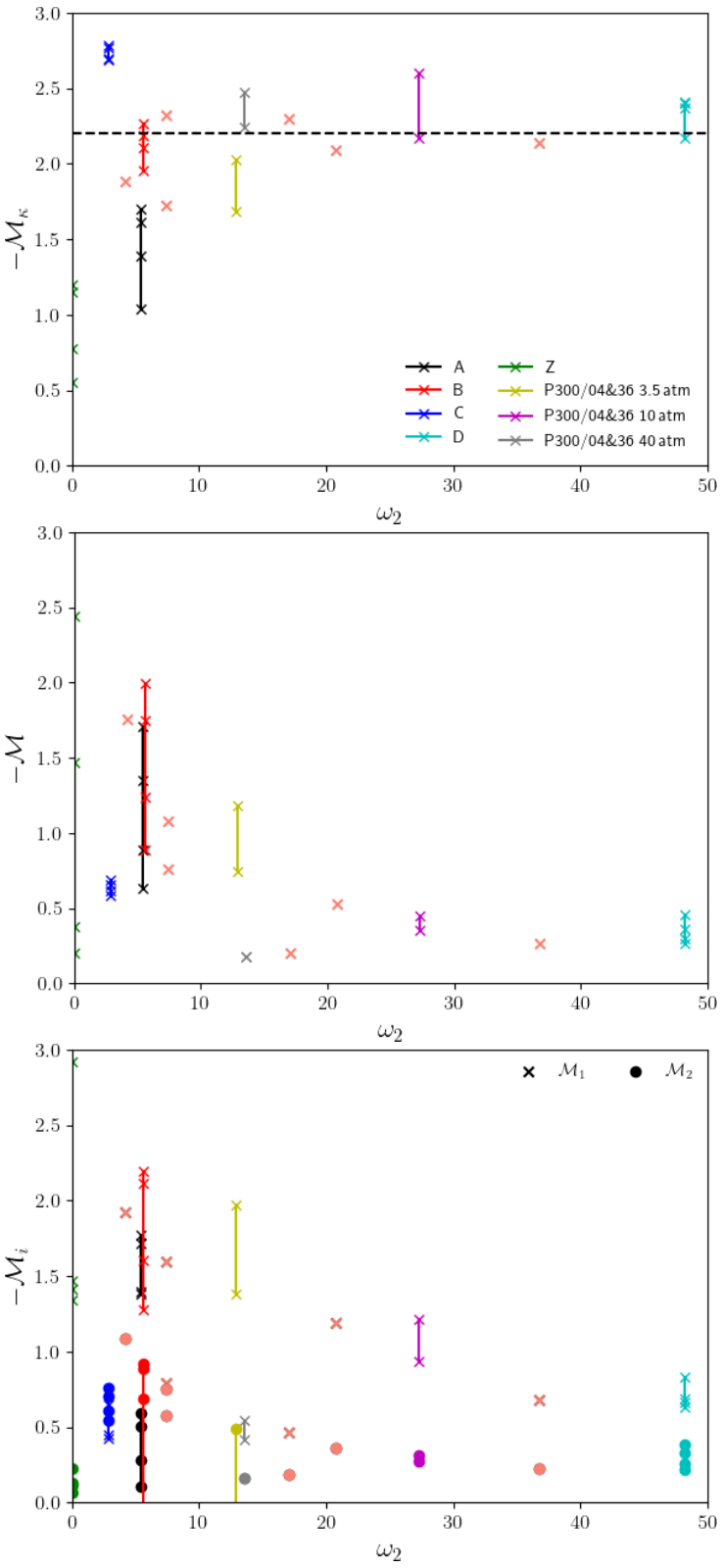

Figure 5.15: Curvature-only, single and independent Markstein numbers as a function of instability parameter ω_2 for all turbulent cases.

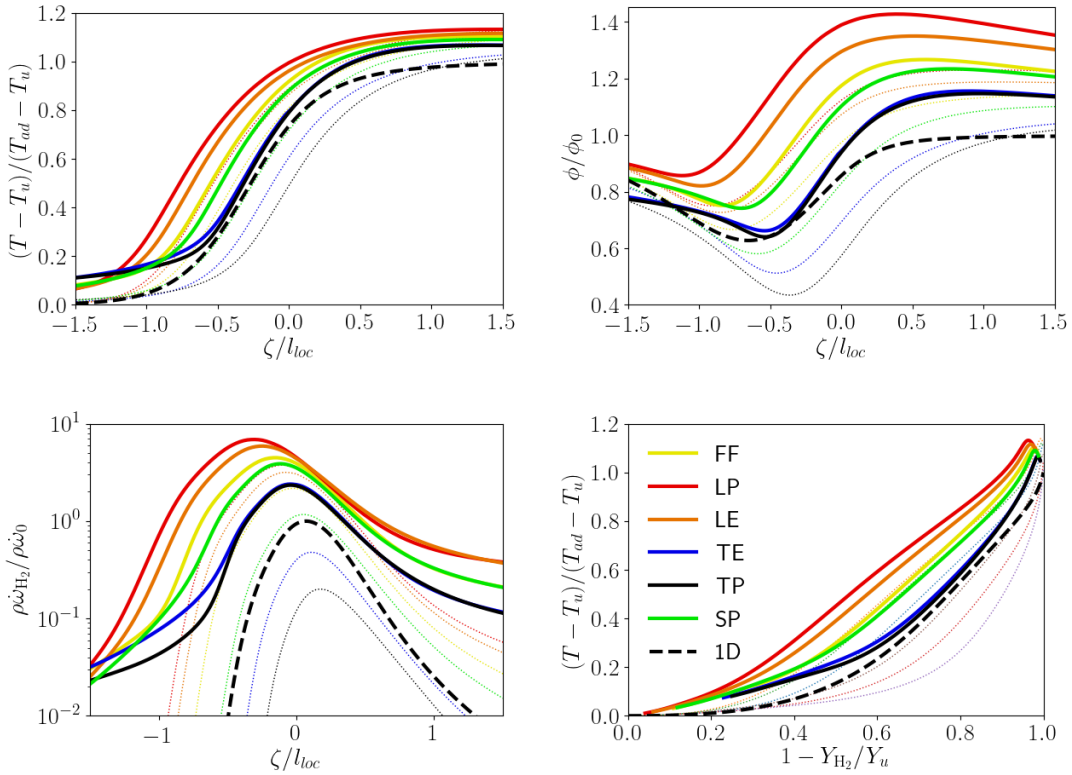

Figure 5.16: Case A, set $\mathrm{Ka_F} = 36$ of normalised temperature, equivalence ratio and fuel consumption rate against normalised distance from the flame surface along the streamline following progress variable, along with profiles in temperature-fuel progress variable space. All are conditionally-averaged by principal curvature zone. Where faint dotted lines are the corresponding freely-propagating profiles with the same zonal colouration.

stronger positively curved regions allow for even more fuel and heat focusing, which then can allow for even higher reaction rates in neighbouring regions, thus enhancing the flat flame regions further than observed in the freely-propagating cases.

As mentioned previously, Berger *et al.* [34] has attributed the enhancement of the mean local flame speed to both preferential diffusion from positive curvature and strain-rate, and presented a compelling argument using effectively 1-dimensional strained flames, which experienced an acceleration in the flame speed, similar to what has been observed in this work.

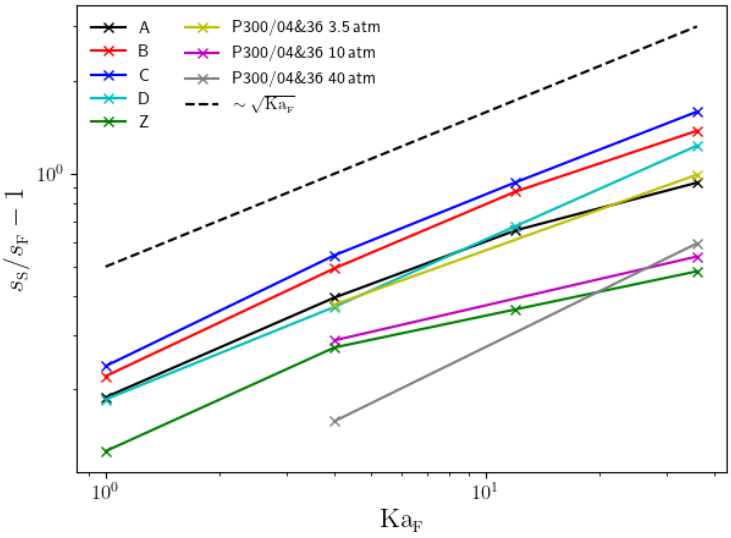

Figure 5.17: Surface-mean local flame speed s_S normalised by s_F plotted as a function of $\mathrm{Ka_F}$ showing a similar gradient to $\sqrt{\mathrm{Ka_F}}$ over the broad range of conditions.

5.6 Surface-mean Local Flame Properties

For each case, the local flame speed and thickness was surface and temporally-averaged using the method discussed in Chapter 3.2.2 to give the mean local flame speed s_S and the mean local thermal thickness ℓ_S. Figure 5.17 shows the mean local flame speed plotted as a function of $\mathrm{Ka_F}$ normalised by the corresponding set specific freely-propagating values.

From Figure 5.17 it can be seen that as $\mathrm{Ka_F}$ increases, the mean local flame speed also increases. By normalising the mean local flame speed by the freely-propagating flame speed, the leading order effects of the TD-instability can be accounted for, in principle, allowing for just the TD-response to turbulence to be studied somewhat independently. It can be seen that once the TD-instability has been accounted for the mean local flame speed scales well with $\sqrt{\mathrm{Ka_F}}$.

Taking the $\sqrt{\mathrm{Ka_F}}$ dependence as the basis for an empirical model and including a small dependence of ω_2, the mean local flame acceleration due to turbulence can be accounted for using the following model

$$\overline{s_{\mathrm{loc}}} \approx s_{K'} = s_F \left(1 + 0.26\exp\left(-0.038\omega_2\right)\sqrt{\mathrm{Ka_F}}\right), \tag{5.1}$$

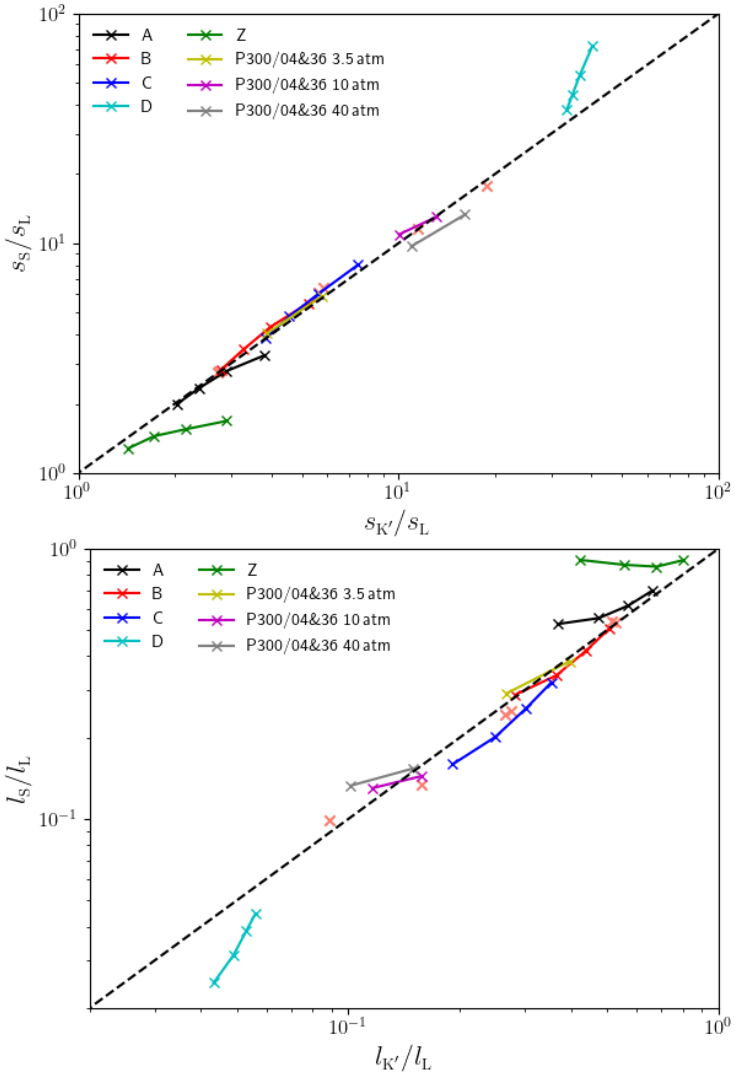

Figure 5.18: Surface-mean local flame speed s_S (left) and thermal thickness ℓ_S (right) normalised by s_L and ℓ_L respectively; plotted as a function of the proposed empirical model equation (5.1) and (5.2).

and

$$\overline{\ell_{loc}} \approx \ell_{K'} = \ell_F \left(1 + 0.22\exp\left(-0.026\omega_2\right)\sqrt{Ka_F}\right)^{-1}. \tag{5.2}$$

Figure 5.18 presents the measured surface-mean local flame speed (left) and thermal thickness (right) normalised by the laminar flame speed and thermal thickness plotted as a function of the proposed empirical model shown in Equation (5.1) and (5.2). It can be seen that there is remarkable agreement between the measured and the modelled flame speed and thickness, given the large range of laminar values presented. Set D does appear to be an outlier, noting

that this is an extreme case with very high values of ω_2. Case Z is also an outlier, this is somewhat expected as set Z is a TD-neutral case. Ideally an empirical model would have a smooth transition from the TD-unstable to neutral to stable, which would be of most use in industrial codes where conditions can range from rich-to-lean combustion. However there is a lack of conditions within the scope and budget of this project to cover these additional cases.

The empirical model proposed above contains the measured freely-propagating surface-mean local flame speed and thermal thickness (denoted by the subscript F i.e. s_{F} and ℓ_{F}). Therefore, for this model to be useful freely-propagating values must be attained. Attaining the freely-propagating values is computationally expensive and not practical for industrial codes such as Vectis. It would be more useful for industrial applications if the characteristic values could be attained from simple 1-dimensional simulations, therefore a combined empirical scaling model is proposed. The model combines both the empirical model accounting for the TD-instability (Equations (4.1) and (4.2) from Chapter 4) with the proposed model for the TD-response to turbulence (Equations (5.1) and (5.2). By attaining the modelled freely-propagating flame speed s_{M} and thermal thickness ℓ_{M} from Equations (4.1) and (4.2 and modelling the freely-propagating Karlovitz number Ka_{M} as

$$\text{Ka}_{\text{M}} = \sqrt{\frac{(u')^3 \ell_{\text{M}}}{s_{\text{M}}^3 \ell_{\text{I}}}}, \tag{5.3}$$

from Equations (5.1) and (5.2), the full compounded model (denoted by subscript K, ie s_{K} and ℓ_{K}) can then be written as

$$s_{\text{K}} = s_{\text{M}} \left(1 + 0.26\text{exp}\left(-0.038\omega_2\right)\sqrt{\text{Ka}_{\text{M}}}\right), \tag{5.4}$$

$$\ell_{\text{K}} = \ell_{\text{M}} \left(1 + 0.22\text{exp}\left(-0.026\omega_2\right)\sqrt{\text{Ka}_{\text{M}}}\right)^{-1}. \tag{5.5}$$

Similar to Figure 5.18, Figure 5.19 presents the measured surface-mean local flame speed (left) and thermal thickness (right) normalised by the laminar flame speed and thermal thickness plotted as a function of the proposed full compounded empirical model shown in equation (5.4) and (5.5). It can be seen that there is still good agreement over a large range of conditions, with a some scatter between the cases, showing that using the measured freely-propagating values does yield better results. It will be shown later in Chapter 6 that

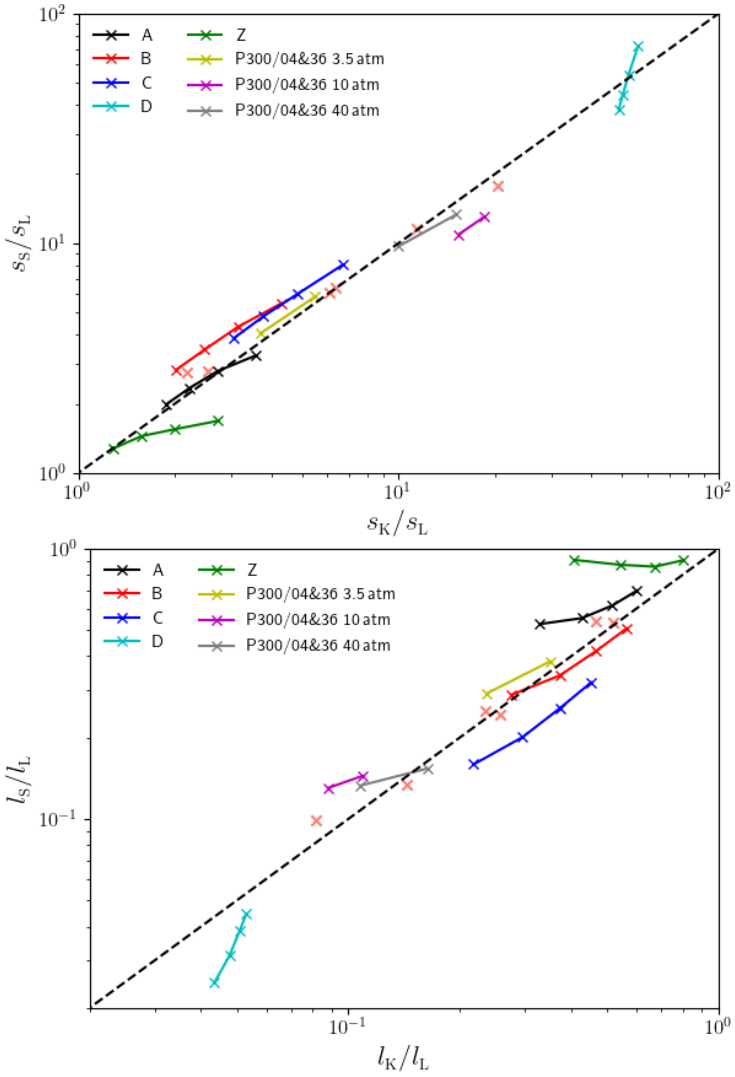

Figure 5.19: Surface-mean local flame speed s_S (left) and thermal thickness ℓ_S (right) normalised by s_L and ℓ_L respectively plotted as a function of the proposed full compounded empirical model Equation (5.4) and (5.5).

using the proposed full compounded empirical model is an essential component in the turbulent flame speed modelling of TD-unstable flames.

5.7 Conclusions

This chapter studied TD-unstable, three-dimensional, turbulent flames at a fixed length scale over a wide range of reactant and turbulent conditions to explore the TD-response to turbulence.

It was found that at a fixed $\mathrm{Ka_F} = 4$, the flames looked remarkably similar regardless of the reactant conditions (Figure 5.1); a stark difference to freely-propagating flames in Chapter 4. The JPDFs of local flame speed and curvature (Figure 5.4) and the fractional contributions of the principal curvature zones (Figure 5.3) were also similar. The local flame speed and strain-rate (Figure 5.5) however, did present some pressure-dependence similar to the freely-propagating flames. Additionally, the JPDFs did present a large range of flame speeds over a narrow band of strain-rate in the low-pressure regime.

The similarity of all the cases at the same $\mathrm{Ka_F}$ (Figure 5.2) reinforces the importance of using the freely-propagating characteristic flame speed and thickness to classify the turbulent burning regime for TD-unstable conditions as suggested in [18]. The corresponding $\mathrm{Ka_L}$ values at a fixed $\mathrm{Ka_F}$ span a large range from $\mathrm{Ka_L} = 10$ to $\mathrm{Ka_L} = 2500$. To address this point, four additional cases were considered where the characteristic values were given as the traditional 1-dimensional flame properties (subscript L). It was clearly demonstrated that the traditional 1-dimensional flame values do not characterise the turbulent flame well. Consequently, it is advocated to use the freely-propagating values for normalisation purposes.

Turbulence exaggerates the TD-response. Increasing turbulence increases the TD-response (Figure 5.7, see also [21, 22, 34]). Turbulence folds the flame surface, giving higher positive curvatures which experience stronger preferential diffusion, therefore burning richer, hotter, faster and thinner. Once accounting for the TD-instability for the freely-propagating flames, turbulence has a much stronger effect on the flame than the reactant conditions where $\mathrm{Ka_F}$ has the leading-order effect (note all simulations were conducted in the thin-reaction-zone). Note the similarity for each $\mathrm{Ka_F}$ case presented in Figure 5.7 despite the large difference in reactant conditions (and ω_2).

The broad range of local flame speeds over a narrow band of strain-rate (Figure 5.11) for turbulent flames in the low-pressure regime complicates a simple flame speed modelling approach using strain-rate (such as a stretch-based approach). Some improvement is offered by allowing independent Markstein numbers for curvature and strain-rate. Cases with high pressure appear not to suffer from the same issue, and correlate quite well with a stretch-based approach, albeit a non-linear relation.

Similar to the freely-propagating flames, a reasonable approximation can be obtained from the local flame speed response to curvature only given the model

$$s_{\mathrm{loc}} \approx s_{\mathrm{S}} \left(1 - \mathcal{M}_{\kappa} \kappa \ell_{\mathrm{S}}\right), \tag{5.6}$$

where $\mathcal{M}_{\kappa} = -2.2$. This is the same model as proposed in Chapter 4 but with a slightly smaller $\mathcal{M}_{\kappa}$. This model could be combined with the models in Equations (5.4) and (5.5) and used for a well-resolved (i.e. no sub-surface wrinkling model) G-equation approach. Such an approach could enable larger simulations for the study of large-scale effects for TD-unstable flames.

Principle curvature zone classification (Figures 5.8 and 5.9) shows the change in flame surface structure as a fraction of bulk fuel consumption, where turbulence transitions the flame from flat flame regions to leading edges. This trend is most apparent at the lower pressure (lower ω_2) cases, whereas at higher pressure (near the most unstable surface in ω_2 space) this trend is less apparent.

As with Chapter 4, surface-normal profiles (Figure 5.16) further shows that turbulence exaggerates the TD-effects, enhancing the temperature, equivalence ratio and reaction rates above both the 1-dimensional profiles and the freely-propagating profiles.

Unlike TD-stable flames which present largely uniform propagation speed over the flame surface, the local flame speed in the presented cases varies significantly. The mean-local flame speed was found to increase with turbulence and scale well with $\sqrt{\mathrm{Ka}_{\mathrm{F}}}$ (Figure 5.17), where the magnitude of the mean local flame speed is moderated by ω_2. Interestingly for cases where the TD-instability is strong in the freely-propagating case, the mean local flame speed in the turbulent case is not significantly higher than the freely-propagating flame speed. The turbulence brings about a similar flame response to the TD-instability in the freely-propagating flames, where increased turbulence leads to more highly-curved structures and a greater proportion of leading edges and leading points.

From the mean local flame speed properties a model was proposed where, given the freely-propagating flame speed and thickness, the flame acceleration due to turbulence can be

modelled via

$$\overline{s_{\text{loc}}} \approx s_{\text{K}'} = s_{\text{F}} \left(1 + 0.26\text{exp}\left(-0.038\omega_2\right)\sqrt{\text{Ka}_{\text{F}}}\right), \tag{5.7}$$

and

$$\overline{\ell_{\text{loc}}} \approx \ell_{\text{K}'} = \ell_{\text{F}} \left(1 + 0.22\text{exp}\left(-0.026\omega_2\right)\sqrt{\text{Ka}_{\text{F}}}\right)^{-1}. \tag{5.8}$$

which has been shown to have good agreement with the measured flame speed data (Figure 5.18). It was also shown by replacing the measured freely-propagating flame speed and thickness with the modelled values as proposed in Chapter 4. Good agreement with the measured data is still found (Figure 5.19).

The TD-neutral case (Z) where $\omega_2 = 0$, there is still a small TD-response to turbulence. This was shown in Figures 5.17 and 5.14, but the effective Lewis number is still less than one; thus the turbulence folds the flame surface, potentially strongly, inducing a TD-response making the flame locally hotter, faster and thinner. Further simulations will be required to understand the behaviour around the stability transition region and how to incorporate that into any model.

This chapter was conducted at a fixed length scale. It is currently unclear how the TD-response to turbulence changes with varying length scale. Additionally flame surface area, a key parameter in turbulent flame speed modelling, has not yet been studied. These questions will be studied in the next chapter.

Chapter 6. Turbulent Flames Part 2: Length Scale Effects

TD-unstable turbulent lean premixed hydrogen flames are investigated over a wide range of reactant (pressure, temperature, and equivalence ratio) and turbulent conditions (Karlovitz and Damköhler number). Following from Chapter 5, the effects of different turbulent length-scales are investigated on local and global flame response. Turbulent-flame interactions are confirmed to be independent of integral length scale (or Damköhler number) for a fixed Karlovitz number. Furthermore, the model proposed from Chapters 4 and 5 is demonstrated to be independent of integral length scale. This model thereby reduces turbulent flame speed modelling for TD-unstable cases to predicting the flame surface area enhancement. The flame surface area wrinkling is found to have good agreement with Damköhler's small-scale limit. There is scatter in the data, although this is comparable with similar experimental results. The subsequent turbulent flame speed predictions appear more sensitive to the freely-propagating flame properties than the flame surface area. It is demonstrated that domain size can have an effect on flame surface area even if the integral length scale remains unchanged; the larger volume into which flame surface area can develop results in a higher turbulent flame speed. To investigate the influence of the fuel Lewis number $\mathrm{Le_F}$*, an additional study is presented where* $\mathrm{Le_F}$ *(alone) is artificially modified to span a range from* 0.35 *to* 2*. The results demonstrate that more flame surface area is generated for smaller* $\mathrm{Le_F}$*, but the difference for* $\mathrm{Le_F} \leq 1$ *is much smaller than that observed for* $\mathrm{Le_F} > 1$*. A volume-filing-surface concept is used to argue that there is a limit to how much flame surface can develop in a given volume, and so there is only so much more flame surface that can be induced by the TD-response whereas the TD-response at high* $\mathrm{Le_F}$ *is to reduce the flame surface area. The agreement of the present data with Damköhler's small scale limit (even for low-to-moderate Karlovitz numbers) suggests that a distinction should be made between the small-scale limit and the distributed burning regime. Furthermore, it is argued that the distinction between large- and small-scale limits should be made based on Damköhler number. Consequently, it is argued that the flame-lets thin reaction and distributed regimes should be distinguished by Karlovitz number (as usual), but the two latter regimes both have separate large- and small-scale regimes. Finally, implications for the turbulent premixed regime diagram are discussed, and a modified regime diagram is proposed.*

6.1 Introduction

The key quantity of interest is the consumption based turbulent flame speed. As discussed in the Chapter 2, since Damköhler's landmark paper [55], the effect of turbulent intensity u' and turbulent integral length scale ℓ_{I} on the turbulent flame speed s_{T} has been a primary focus of many numerical and experimental studies, see review papers by Lipatnikov and Chomiak [109], Driscoll [62] or Burke *et al.* [45] for example.

The usual premise for turbulent flame speed models is to multiply some reference flame speed s_{R} (traditionally s_{L}) by the turbulent flame surface area wrinkling factor Ψ_{T} and can be written in the form

$$s_{\text{T}} = s_{\text{R}}\Psi_{\text{T}}. \tag{6.1}$$

Deviations of the local flame speed from the laminar value can be represented by a so-called stretch factor thus Equation (6.6) can be written as

$$s_{\text{T}} = I_0 s_{\text{L}}\Psi_{\text{T}}. \tag{6.2}$$

Damköhler's small- and large-scale limit (SSL and LLS) (as discussed in Section 2.5) can be written as

$$\Psi_{\text{T}} \sim \sqrt{\frac{u'\ell_{\text{I}}}{s_{\text{R}}\ell_{\text{R}}}} = \sqrt{\text{Re}_{\text{R}}}, \tag{6.3}$$

and

$$\Psi_{\text{T}} \sim \frac{u'}{s_{\text{R}}}, \tag{6.4}$$

respectively. The traditional laminar flame values have been replaced by characteristic reference values (subscript R). Lipatnikov and Chomiak [109] associated the SSL with a thick flame, distributed or well-stirred reactions, and suggest $\ell_{\text{I}} < \ell_{\text{L}}$ as a sufficient condition. Aspden *et al.* [15, 20] similarly assumed that distributed burning would be required for turbulent diffusion to be appropriate, and so associated the SSL with high Karlovitz numbers. However, agreement with SSL scaling laws have been observed in both hydrogen and methane flames in the thin reaction zone [22].

It is common for turbulent flame surface area models to start from an expression of the form,

$$\Psi_{\text{T}} = 1 + C\Upsilon_{\text{R}}^{n}, \tag{6.5}$$

which is referred to as the power-law model, for some power n and a factor C, which should be expected to depend on a length scale in some way but is often assumed constant [135]. The power-law model has seen wide adoption and study [90, 88, 9, 48] for example with the suggestion of constants depending on the experimental or simulation conditions. Length scale is seldom considered in detail, as it is challenging to study both numerically and experimentally due to the range of scales. Importantly, it is a dimensional necessity that the parameters space is two-dimensional (length and time); all relations can be written in terms of the length scale ratio $\Lambda_{\mathrm{R}} = \ell_{\mathrm{I}}/\ell_{\mathrm{R}}$ and the velocity ratio $\Upsilon_{\mathrm{R}} = u'/s_{\mathrm{R}}$, or combinations thereof (e.g. $\mathrm{Re}_{\mathrm{R}} = \Upsilon_{\mathrm{R}}\Lambda_{\mathrm{R}}$, $\mathrm{Da}_{\mathrm{R}} = \Lambda_{\mathrm{R}}/\Upsilon_{\mathrm{R}}$, $\mathrm{Ka}_{\mathrm{R}}^2 = \Upsilon_{\mathrm{L}}^3/\Lambda_{\mathrm{R}}$). The question is, which combination of parameters can best be used to distinguish burning regimes, and how are these affected by TD-effects?

Most algebraic turbulent flame speed models fall into broad categories, and can be written in the form

$$\Psi_{\mathrm{T}} = 1 + C\Upsilon_{\mathrm{R}}^n \mathrm{Da}_{\mathrm{R}}^m, \tag{6.6}$$

for some constants C, n and m. Small-scale limit models ($n = 1$;$m = 1/2$) include Ronny [146] and Liu [110] for example. Large-scale limit ($n = 1$; $m = 0$) include Anand and Pope [9] for example. More general power law models include Klimov [90] ($n = 0.7$; $m = 0$) and Cant [48] ($n = 3/2$; $m = 1/4$). Some models are a blend of the two limits, e.g. both Zimont [184] and Gülder [76] are effectively the geometric mean of the two limits ($n = 1$; $m = 1/4$). Other models have more complex expressions, e.g. Gouldin [74], Mantel and Borghi [114], and Abdel-Gayed and Bradley [3]. Naturally there are models that do not fit this simple classification; for example, Kobayashi [91], Muppala [124] and Lu [112] who include correction terms for pressure and/or Lewis number. See Tables 2.1 and 2.2 for more details and papers [134, 135, 109, 45, 112] for example, for details and discussion of turbulent flame models.

Two models of note transition between the small- and large-scale limits. Firstly, Peters [134] used a G-equation approach valid for both large and small regimes, and resulted in an

expression of the form

$$\Psi_{\mathrm{T}} = 1 - \frac{a_4 b_3^2}{2b_1}\frac{\ell_{\mathrm{I}}}{\ell_{\mathrm{R}}} + \left[\left(\frac{a_4 b_3^2}{2b_1}\frac{\ell_{\mathrm{I}}}{\ell_{\mathrm{R}}}\right)^2 + a_4 b_3^2 \frac{u'\ell_{\mathrm{I}}}{s_{\mathrm{R}}\ell_{\mathrm{R}}}\right]^{1/2}, \tag{6.7}$$

where a_i and b_i are model constants. Secondly, a model derived from the KPP approach [178, 153, 109], resulted in an expression that can be written as

$$\Psi_{\mathrm{T}} = 1 + \Upsilon_{\mathrm{R}}\left(1 + \mathrm{Da}_{\mathrm{R}}^{-2}\right)^{-1/4}. \tag{6.8}$$

It was noted in [135], that normalising equation 6.7 by the turbulent velocity u' results in a function of Damköhler number alone, which also applies to Equation 6.8. By defining $\alpha = b_1$, $\beta = (4b_1^2)\,/\,(a_4 b_3^2)$, and $\xi_{\mathrm{R}} = \mathrm{Da}_{\mathrm{R}}/\beta$ Equation 6.7 can be written as

$$\frac{\Psi_{\mathrm{T}} - 1}{2\alpha\Upsilon_{\mathrm{R}}} = \sqrt{\xi_{\mathrm{R}}^2 + \xi_{\mathrm{R}}} - \xi, \tag{6.9}$$

where the right-hand side is a function of Da_{R} alone. Similarly, Equation 6.8 can be written as

$$\frac{\Psi_{\mathrm{T}} - 1}{\Upsilon_{\mathrm{R}}} = \left(1 + \mathrm{Da}_{\mathrm{R}}^{-2}\right)^{-1/4}. \tag{6.10}$$

To separate expressions for small and large values of Damköhler numbers, Equation 6.9 can be written in two equivalent ways

$$\frac{\Psi_{\mathrm{T}} - 1}{2\alpha\Upsilon_{\mathrm{R}}} = \begin{cases} \xi_{\mathrm{R}}^{1/2}\left(1 + \xi_{\mathrm{R}}\right)^{1/2} - \xi_{\mathrm{R}}, \\ \xi_{\mathrm{R}}\left(1 + \frac{1}{\xi_{\mathrm{R}}}\right)^{1/2} - \xi_{\mathrm{R}}, \end{cases} \tag{6.11}$$

so they can be expanded (by Taylor series) in the small- and large-scale turbulence limits respectively,

$$\frac{\Psi_{\mathrm{T}} - 1}{2\alpha\Upsilon_{\mathrm{R}}} = \begin{cases} \xi_{\mathrm{R}}^{1/2}\left(1 + \frac{\xi_{\mathrm{R}}}{2} + \frac{\xi_{\mathrm{R}}^2}{8} + \ldots\right) - \xi_{\mathrm{R}} & \text{for } \xi_{\mathrm{R}} \ll 1, \\ \xi_{\mathrm{R}}\left(1 + \frac{1}{2\xi_{\mathrm{R}}} + \frac{1}{8\xi_{\mathrm{R}}^2} + \ldots\right) - \xi_{\mathrm{R}} & \text{for } \xi_{\mathrm{R}} \gg 1, \end{cases} \tag{6.12}$$

where the leading orders are

$$\frac{\Psi_{\mathrm{T}} - 1}{2\alpha\Upsilon_{\mathrm{R}}} = \begin{cases} \xi_{\mathrm{R}}^{1/2} & \text{for } \xi_{\mathrm{R}} \ll 1, \\ \frac{1}{2} & \text{for } \xi_{\mathrm{R}} \gg 1. \end{cases} \tag{6.13}$$

Therefore, the approximations are

$$\frac{\Psi_{\mathrm{T}} - 1}{\Upsilon_{\mathrm{R}}} = \begin{cases} \gamma \mathrm{Da}_{\mathrm{R}}^{1/2} & \text{for } \mathrm{Da}_{\mathrm{R}} \ll \beta, \\ \alpha & \text{for } \mathrm{Da}_{\mathrm{R}} \gg \beta, \end{cases} \tag{6.14}$$

where $\gamma = 2\alpha/\beta^{1/2}$; or in terms of turbulent flame speed,

$$\frac{s_{\mathrm{T}}}{s_{\mathrm{R}}} = \begin{cases} 1 + \gamma \mathrm{Re}_{\mathrm{R}}^{1/2} & \text{for } \mathrm{Da}_{\mathrm{R}} \ll \beta, \\ 1 + \alpha \Upsilon_{\mathrm{R}} & \text{for } \mathrm{Da}_{\mathrm{R}} \gg \beta. \end{cases} \tag{6.15}$$

The model expression can then be written as

$$s_{\mathrm{T}} = s_{\mathrm{R}} \left(1 - 2\alpha \Upsilon_{\mathrm{R}} \frac{\mathrm{Da}_{\mathrm{R}}}{\beta} + \left[\left(1 + \frac{\beta}{\mathrm{Da}_{\mathrm{R}}} \right)^{1/2} - 1 \right] \right), \tag{6.16}$$

and following Peters [135], $a_4 = 0.78$, $b_1 = 2$ and $b_3 = 1$, which gives $\alpha = 2$, $\beta = 20.5$ and $\gamma = 0.88$. While this observation was also noted in [109], here normalising by velocity u' means that no further conditions on velocity are required (although $\mathrm{Re}_{\mathrm{R}} > 1$ is implicit). Importantly these observations suggest that Damköhler number is the appropriate dimensionless parameter to distinguish between small- and large-scale limits.

While Damköhler number $\mathrm{Da}_{\mathrm{F}} = \Lambda_{\mathrm{F}}/\Upsilon_{\mathrm{F}}$ represents the ratio of turbulent time scale at the integral length scale to the flame time scale, as discussed in Chapter 2 the Karlovitz number $\mathrm{Ka}_{\mathrm{F}} = \Upsilon_{\mathrm{F}}^3/\Lambda_{\mathrm{F}}$ represents the ratio of the flame time scale to the turbulent time scale at the flame scale. When defined this way the Karlovitz number is invariant in the inertial sub-range of the turbulent cascade, therefore, for a fixed Ka_{F}, the turbulence-flame interaction at the flame scale is independent from the larger turbulent scales, i.e. the Damköhler number. Similar arguments have been made by [183, 109, 156, 174] and will be demonstrated with numerical evidence later in this chapter.

This chapter starts by focusing on the effect of turbulent integral length scale on the local flame response, primarily to evaluate the validity of the models proposed in Chapters 4 and 5 over a range of integral length scales. It is then evaluated as to how the effect of fixing Ka_{F} compared with turbulent intensity u'/s_{F} effects the local flame response, followed by the flame surface area's response to increasing turbulent intensity and length scale. The effect of domain size is then evaluated by comparing the flame surface area when the domain size is independently increased without an increase in integral length scale. A normalised measure of flame surface wrinkling is compared to Damköhler number for all of the turbulent simulations conducted throughout this thesis and compared to Peters model and Damköhler's small and large scale limits. Next the effects of fuel Lewis number on the local and global flame statistics are

evaluated where the Lewis number of the fuel is artificially changed and the flame response is quantified. Finally, recommendations for a turbulent flame speed modelling approach for TD-unstable flames is proposed and a modified premixed turbulent regime diagram is presented.

6.2 Numerical Configuration and Simulation Conditions

A two-dimensional parameter space has been explored whereby normalised integral length scale Λ_{F} and turbulent intensity Υ_{F} are varied in such a way as to explore the influence of length scale (equivalently Damköhler number Da_{F}) at a fixed Karlovitz number Ka_{F}. The premise is to ensure that the turbulence at the flame scale is unchanged as length scale is increased. Four reactant conditions have been considered, following on from Chapters 4 and 5; simulations sets A, B, P300 $p = 3.5$ atm (now called set P3.5), P300 $p = 10$ atm (now called set P10). See Table 6.1 for details. When considering detailed TD-response at the flame scale,

Table 6.1: Reactant and turbulence conditions. Freely-propagating values are measured values from the three-dimensional simulations. For additional simulations, see Table 5.1.

Set	p (atm)	T_0 (K)	ϕ	ω_2	s_{F} (m/s)	ℓ_{F} (μm)	Λ_{F}	Υ_{F}	Ka_{F}	Da_{F}
A	1	300	0.4	5.54	0.34	526	1.6	1.17	1	1.37
								2.95	4	0.54
								6.13	12	0.26
B	40	700	0.4	5.58	0.56	18.7	2.4	1.33	1	1.79
								3.37	4	0.71
								7.02	12	0.34
P3.5	3.5	300	0.4	12.88	0.24	189	3.2	1.47	1	2.17
								3.71	4	0.86
								7.72	12	0.41
P10	10	300	0.4	27.27	0.13	114	4.8	1.69	1	2.85
								4.25	4	1.13
								8.84	12	0.54

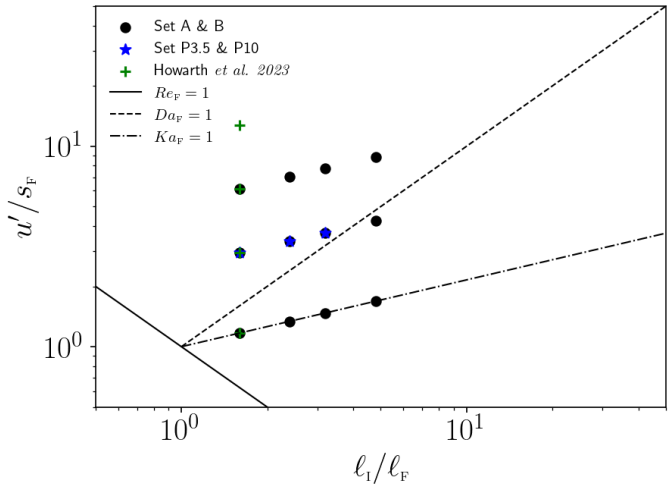

Figure 6.1: Turbulent burning regime diagram showing simulation conditions.

the focus has been on simulation set B (nominal conditions relevant for IC engines). Simulation set A was considered over the same turbulent parameter space as set B, but the focus was on flame speeds rather than detailed local turbulence-flame interaction. For simulation sets A and B, three Karlovitz numbers have been considered $\mathrm{Ka_F} = 1, 4$ and 12, and four length scales $\Lambda_\mathrm{F} = 1.6, 2.4, 3.2$ and 4.8. Two further reactant conditions have been considered, denoted by P3.5 and P10; these two sets were run at $\mathrm{Ka_F} = 4$ and length scales $\Lambda_\mathrm{F} = 1.6, 2.4$ and 3.2.

A property of the turbulent forcing strategy, is that the integral length scale ratio Ω is fixed, thus $\Omega = L/\ell_\mathrm{I}$ where L is the domain width and $\Omega \approx 10$. Consequently the smallest integral length scales also had the smallest domain size. The effect of this will also be evaluated in this chapter. All flames are in the thin reaction zone of the premixed regime diagram (based on the freely-propagating characteristic speed and thickness) and are shown in figure 6.1. For turbulent flame speed modelling, the turbulent flame speed conditions used in chapter 5 will also be included in the dataset.

6.3 Isosurfaces

Identically to previous sections and as detailed in Section 3.2.1, isosurfaces have been constructed using a fuel based mass fraction which closely resembled the location of the local

peak fuel-consumption-rate. Figure 6.2 presents the flame isosurfaces coloured by the consumption based flame speed for the twelve cases from simulation set B. It can be seen that as $\mathrm{Ka_F}$ increases, the flame becomes more wrinkled, with strong positively curved regions at the leading points (spherically-curved) and edges (cylindrically-curved). For details of flame structure see Section 4.5. As seen previously, these highly curved regions correlate with high flame speed, which can be seen to be in excess of five times the freely-propagating flame speed which in-turn is close to twice the unstretched laminar flame speed. As the domain and integral length scales are increased, there is more flame surface area, but there does not appear to be a discernible change in flame structure or local flame speed (from colour) at a fixed $\mathrm{Ka_F}$. This visually suggests that the flame structure and local flame speed is independent of domain / integral length scale. Despite the flame structure being visually similar between the different length scales, it would appear that global thickness of the flame (also referred to as a flame brush thickness) is larger. This indicates that the larger length scales, albeit integral length or domain size, do influence the flame structure at a global scale but not a smaller scale. Further analysis of these observations are provided below.

6.4 Length Scale Effects on Local Flame Speed

This section aims to focus on the local effects of turbulent integral length scale on the flame.

6.4.1 Mean Local Flame Speeds

Figure 6.3 presents the mean local flame speed s_S normalised by the freely-propagating flame speed as a function of freely-propagating Karlovitz number $\mathrm{Ka_F}$ for sets A and B (top). The mean local flame speed normalised by both the unstretched laminar flame speed and the modelled mean local flame speed (based off the $\sqrt{\mathrm{Ka_F}}$ dependence shown in Equation (5.1) from Chapter 5) by the turbulent integral length scale for all sets. The large values observed in Figure 6.3b when normalised by s_L demonstrate the acceleration due to thermodiffusive effects compounded by turbulent flame interactions. Note that case P10 does not fit within the range of the graph $s_\mathrm{S}/s_\mathrm{L} \approx 10$), but each case presents little variation with integral length scale. Importantly it can be seen that once TD-effects are accounted for by ω_2 and $\mathrm{Ka_F}$ the normalised mean local flame speeds collapse very close to unity, clearly demonstrating that the

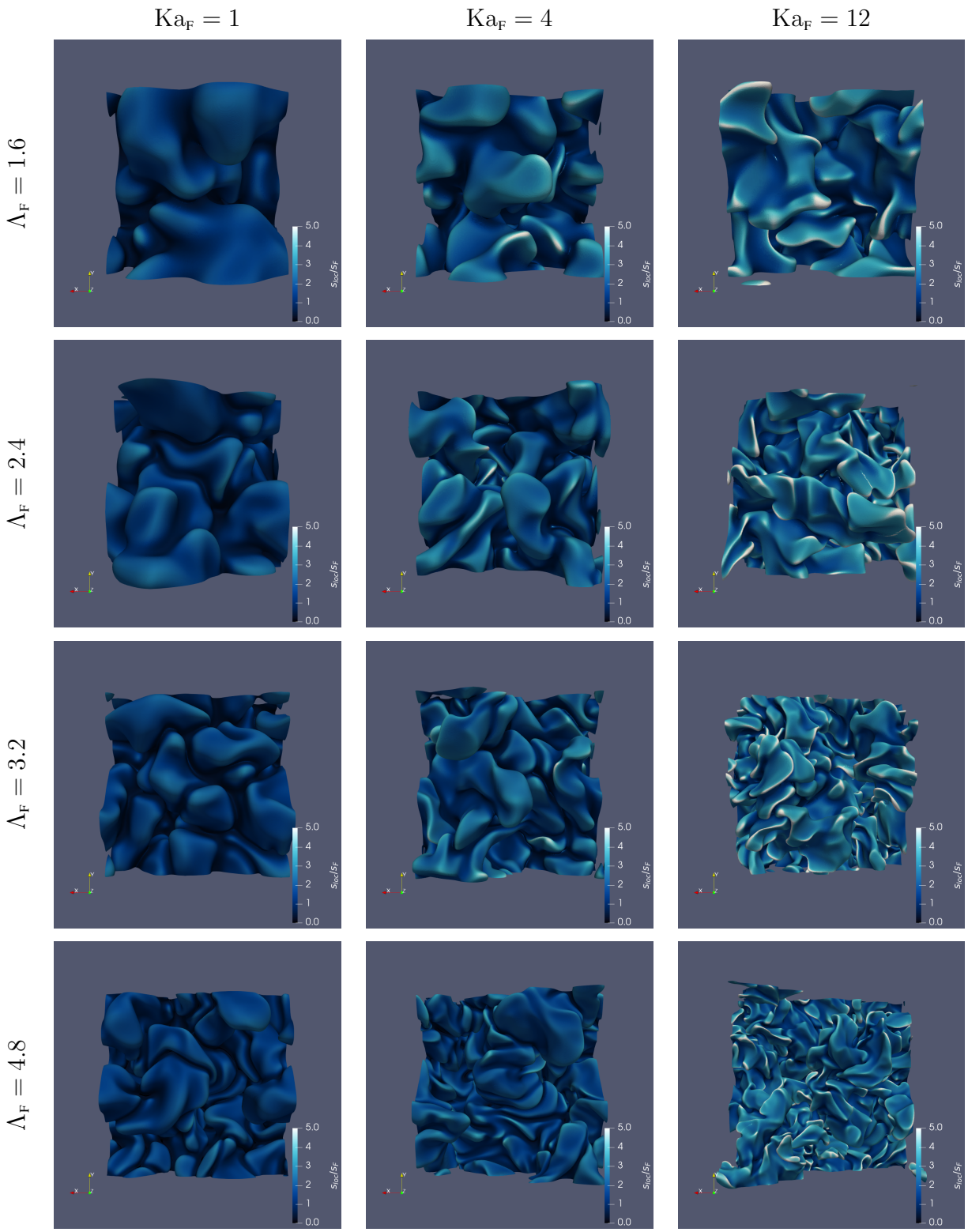

Figure 6.2: Flame surfaces for cases B coloured by local consumption-based flame speed at the different $\mathrm{Ka_F}$ and Λ_F. Naturally, the flame surface wrinkling increases with both $\mathrm{Ka_F}$ and Λ_F. The local flame speeds also increase with $\mathrm{Ka_F}$, but appear independent from Λ_F.

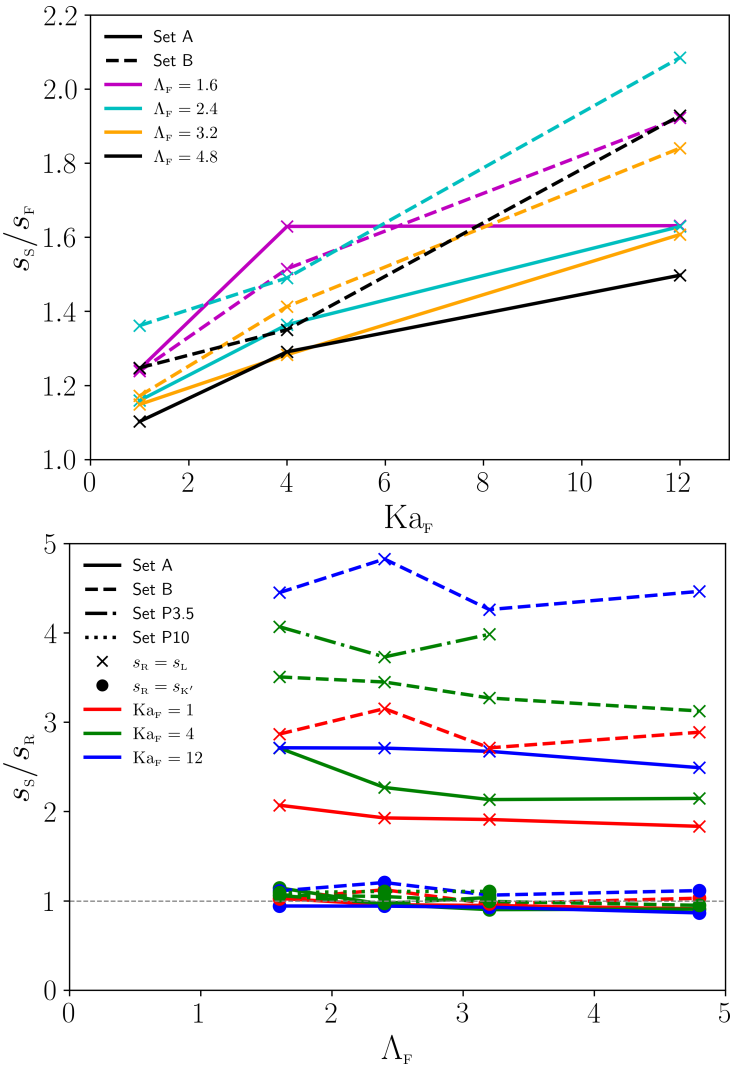

Figure 6.3: Normalised mean local flame speed as a function of (a, top) Karlovitz number Ka_F, and (b, bottom) normalised integral length scale Λ_F; the TD-response is exaggerated by turbulence, but appears to be independent from integral length scale.

mean local flame speed models proposed in the previous chapters are appropriate for variable integral length scale within the range of conditions presented here.

6.4.2 Joint Probability Density Functions

To further demonstrate that the local flame statistics are independent of integral length scale, JPDFs of local flame speed and flame surface curvature for set B over a range of Karlovitz (left-to-right) and length scale ratio (top-to-bottom) for set B are shown in Figure 6.4 (the colour scale applies to all following JPDFs.). The dotted reference line is the Markstein model

from Chapter 5 ($s_{\text{loc}} = s_{\text{K}'}(1 - \mathcal{M}_\kappa \kappa \ell_{\text{F}})$ for $\mathcal{M}_\kappa = -2.2$). As with previous chapters the JPDFs are temporally-averaged, and the first moment has been taken with respect to the local flame speed. At a fixed Ka_{F} it can be seen that the JPDFs (notwithstanding the improved statistical convergence with increased domain size due to the significantly higher number of data points) are very similar. Identically to Figure 5.4, there is a strong correlation between local flame speed and curvature (with a negative Markstein number) and the bulk of the burning occurring at approximately zero curvature (i.e. flat flame) with a higher than s_{F} flame speed. As Ka_{F} increases, the range of curvatures increases with the bulk of the burning occurring at a higher speed but still at zero curvature. This is all consistent with the observations in Section 5.4.2 and length scale does not change these observations, crucially confirming the argument that the integral length scale has little effect on the local flame statistics for a fixed Ka_{F}.

6.4.3 Comparison of Velocity and Karlovitz Number

To further emphasise that the important parameter that determines the local turbulence-flame interaction is Ka_{F} rather than Υ_{F}, a further case was considered where u' was matched to a reference condition at a larger length scale. The reference cases were taken at $\Lambda_{\text{F}} = 1.6$ and 4.8 from set B at $\text{Ka}_{\text{F}} = 12$, and an additional simulation was conducted with the same length scale as the former and turbulent intensity of the latter; specifically $\Lambda_{\text{F}} = 1.6$ and $\Upsilon_{\text{F}} = 8.84$ which corresponds to $\text{Ka}_{\text{F}} = 20.8$. While the two reference cases have almost identical local flame speed, the resulting mean local flame speed in the additional test case is approximately 20% higher; see Figure 6.5 (left). Similarly to 6.4, the additional case JPDF of local flame speed and curvature is shown in Figure 6.5 (right), with the same reference lines. When compared with the reference cases, the JPDF from the additional case clearly shows higher flame speeds (the JPDF is further from the reference line) despite the same u' (i.e. Υ_{F}), and also achieves more extreme values of both positive curvature and high flame speed. Clearly the flame is experiencing more turbulence at the flame scale. Therefore the length scale at which turbulent intensity is measured is crucial to turbulence-flame interaction at the flame scale. This means that for studying turbulence at the flame scale is imperative to define the Ka_{F} with the appropriate definition and flame characteristic values.

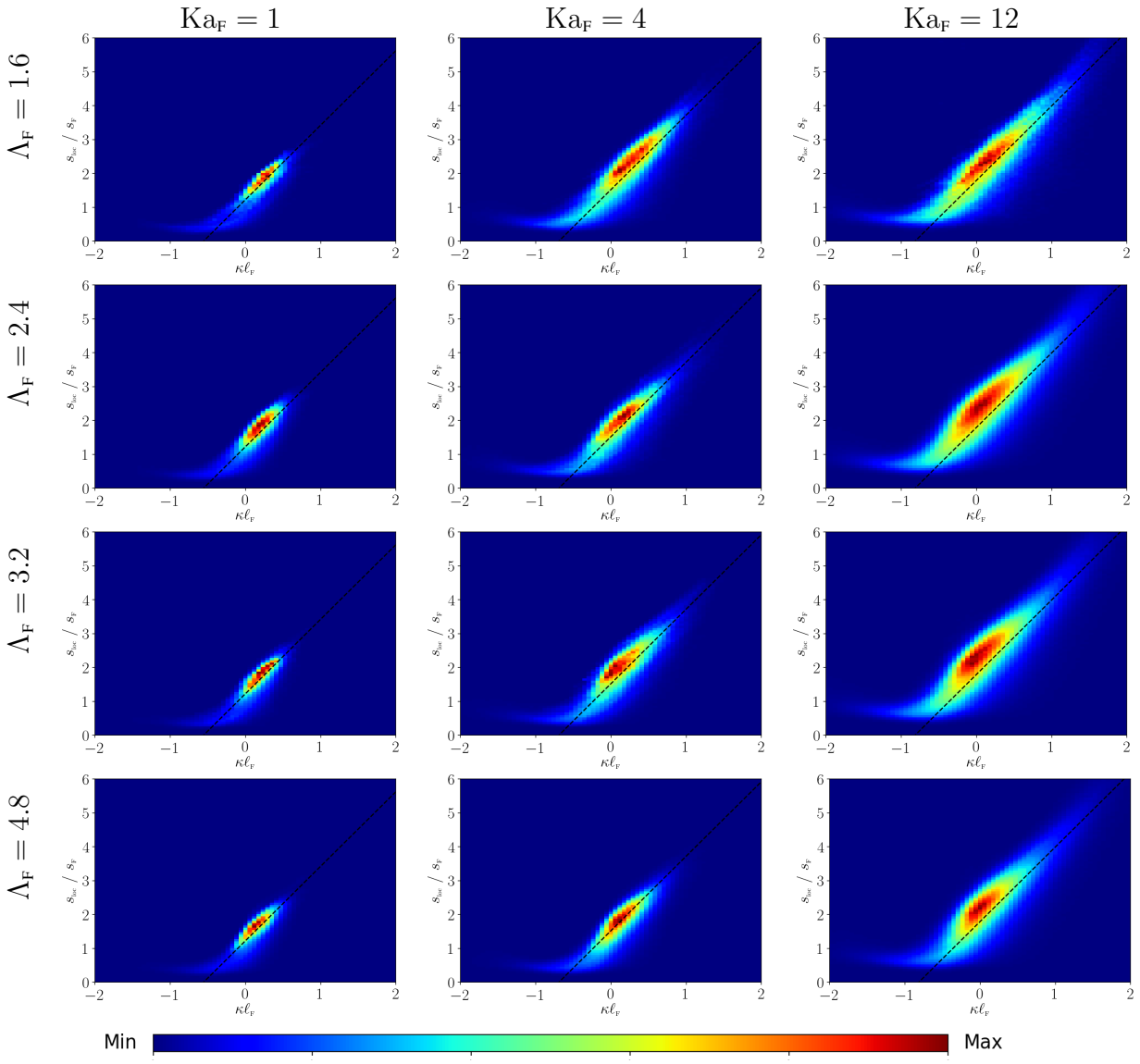

Figure 6.4: Joint probability density functions (JPDFs) of the normalised local consumption-based flame speed and normalised curvature for increasing length scale ratio Λ_F (top-to-bottom) at increasing Karlovitz numbers $\mathrm{Ka_F}$ (left-to-right) from simulation set B. The dotted reference line is the Markstein model from chapter 5 ($s_\mathrm{loc} = s_{\mathrm{K}'}(1 - \mathcal{M}_\kappa \kappa\ell_\mathrm{F})$ for $\mathcal{M}_\kappa = -2.2$).

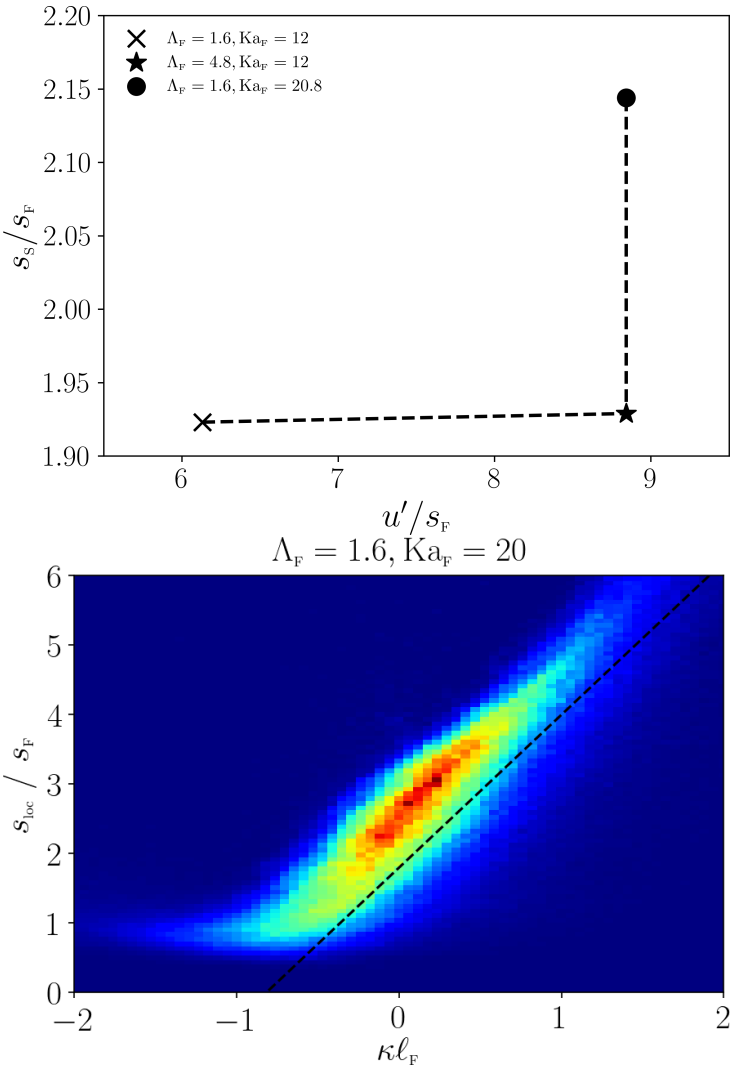

Figure 6.5: The mean local flame speed normalised by the modelled freely propagating flame speed for fixing u compared with fixing Ka_F (top). Note how the local flame speed in the test case (circle) is 20% higher than the reference case at the same turbulent intensity (star). And the JPDF of the area weighted first moment of the local flame speed against curvature for the fixed u' case $\Lambda_F = 1.6, \mathrm{Ka}_F = 20$ (bottom). The dotted reference line is the same as Figure 6.4.

6.5 Flame Surface Wrinkling

The previous section has demonstrated that variations across the surface of local statistics that are observed in TD-unstable lean premixed flames are independent of integral length scale for a fixed Ka_F. Therefore, predicting the turbulent flame speed can be reduced to the problem of predicting the flame surface wrinkling, which is the focus of this section. The premise is to use

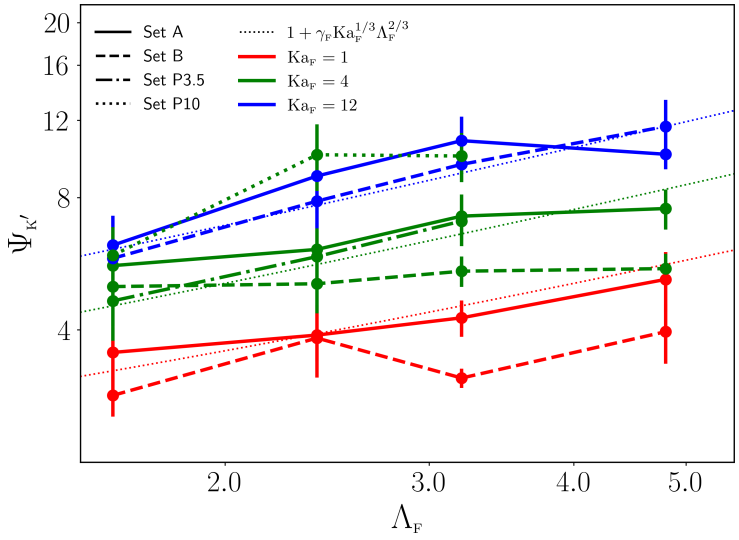

Figure 6.6: Measured flame surface wrinkling $\Psi_{K'}$ as a function length scale ratio Λ_F, compared with the SSL model surface wrinkling given by equation (6.19). Vertical lines denote standard deviation.

the model mean local flame speed $s_{K'}$ to write the turbulent flame speed (discussed in Section 6.1) as

$$s_T = s_{K'}\Psi_T. \tag{6.17}$$

There are two equivalent approaches that can be taken to measure the flame surface wrinkling, one is by direct measurement of the isosurface area Ψ_C, and the other is to evaluate the ratio of global consumption speed s_C to the mean local flame speed $s_{K'}$. The latter is consistent with the modelling approach and will be used to investigate how flame surface wrinkling is effected by turbulence. The TD-effects will be denoted by:

$$\Psi_{K'} = \frac{s_C}{s_{K'}}. \tag{6.18}$$

Figure 6.6 shows the measured wrinkling factor $\Psi_{K'}$ as a function of Λ_F for all simulation in sets A, B, P3.5 and P10 (indicated by line style) and the three different Karlovitz numbers (indicated by colour). Damköhler's turbulent small scale limit (SSL) scaling laws are denoted by dotted lines, i.e:

$$\Psi_T = 1 + \gamma_F \mathrm{Ka}_F^{1/3}\Lambda_F^{2/3}, \tag{6.19}$$

where the same constant γ_F is used for all three Karlovitz numbers. There are clear trends, the flame surface wrinkling increases with both Ka_F and Λ_F. The data is also in reasonable

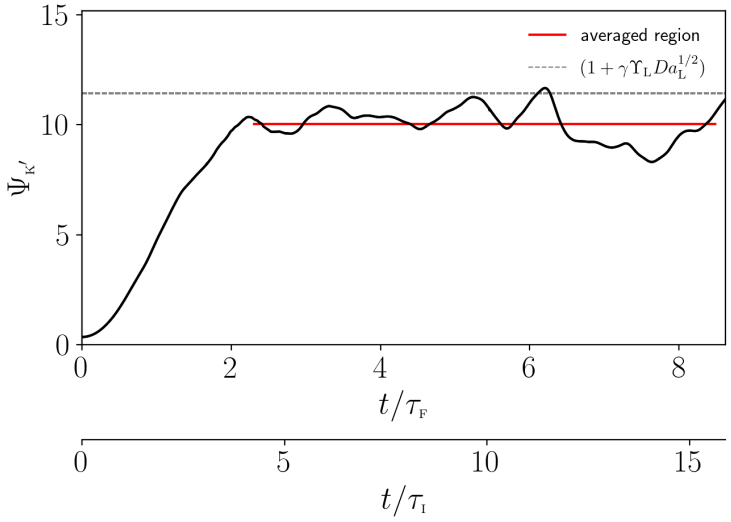

Figure 6.7: Time history of wrinkling factor as a function of time for case A, $\Lambda_{\mathrm{F}} = 4.8$, $\mathrm{Ka}_{\mathrm{F}} = 12$. The red line shows the region of which averaged statistics were taken.

agreement with the SSL model, but there is some scatter in the data which is comparable with experimental data (see Figure 2.24 in [135]). This could be a limitation of measuring global quantities from DNS which has a limited domain size. Even though the domain sizes are among some of the largest found in the literature, the cross-section extent is still limited to 48 freely-propagating flame thicknesses (in the large case). Although the turbulent flame speed has burned through a domain length of approximately 80 to 160 thermal thicknesses in all cases, the combination of both high flame speeds and large area enhancement means that the resulting turbulent flame speed is so rapid that the entire domain can be consumed within 10 freely-propagating flame times in the fastest case. See Figure 6.7 for an example time history showing the flame surface wrinkling over time for case A, $\Lambda_{\mathrm{F}} = 4.8$, $\mathrm{Ka}_{\mathrm{F}} = 12$. The beginning of the temporal averaging window is chosen by eye once the statistically-steady period has been reached. The simulations conducted have a large statistically stationary region; therefore the bounds of the statistically stationary region can adequately be done by eye. If shorter simulations are conducted (ie the simulations have smaller statistically stationary region) then a more sophisticated method should be used. Other factors that may affect these statistics could be that the reactant conditions (such as higher temperatures and pressures) are not completely accounted for by ω_2.

As discussed previously, Peters [135] notes that normalising by velocity gives an equation that is a function of Damköhler number alone. To examine this relation, Figure 6.8 presents the flame surface wrinkling normalised as $(\Psi_{K'} - 1)/\Upsilon_R$ as a function of Da_R where subscript R is a reference value of L, F and K′. The models from Section 6.1 are provided for comparison

$$\frac{\Psi_{K'} - 1}{\Upsilon_R} = \begin{cases} \gamma_R \mathrm{Da}_R^{1/2}, & \text{SSL}, \\ \alpha_R, & \text{LSL}, \\ 2\alpha_R \left(\sqrt{\xi_R^2 + \xi_R} - \xi_R \right), & \text{Peters}, \end{cases} \tag{6.20}$$

where $\xi_R = \mathrm{Da}_R/\beta_R$; the constant $\gamma_R = 1.32, 1.60$ and 1.65 for R = L, F and K′ respectively which has been established by the best fit to the data, with $\alpha_R = 2$ and $\beta_R = 4\alpha_R^2/\gamma_R$. The value of γ_L differs from the value of 0.88 quoted in [135]; whether this is a TD-effect or a consequence of how quantities are evaluated is considered later. Visually, the L-normalisation from Figure 6.8 presented is more compelling, but there is little difference in the relative error between the L and F normalisation. This is possibly due to the limited range of Damköhler numbers accessible to DNS, combined with the log scale. Nevertheless, the data are in reasonable agreement with the SSL, and the outliers are cases close to the most unstable surface in ω_2 space. Note that if the data in Figure 6.6 was plotted using Λ_L instead of Λ_F, then a different model line would be required for each reactant condition, which is not the case for Λ_F. The key difference between the different normalisations is the choice of flame timescale; $\tau_R = \ell_R/s_R$ and there is no clear choice between L, F or K′. It may be the case that there is a turbulent time scale $\tau_T = \ell_T/s_T$ (for some measure of turbulent flame speed and thickness) that could be more appropriate; this is discussed further later.

6.6 Domain Size Effects

It has already been determined from Howarth and Aspden [80] and Wen *et al.* [169] for freely-propagating flames and for turbulent flames in Section 6.4 that, provided the domain size is sufficiently large for TD-unstable structures to form, the mean local flame speed is independent of domain size. It has been observed in [36] and [169] that for TD-unstable freely-propagating laminar flames, domain size can effect the global consumption based flame speed. From the findings of [80] and [169] it was found this increase was driven by flame

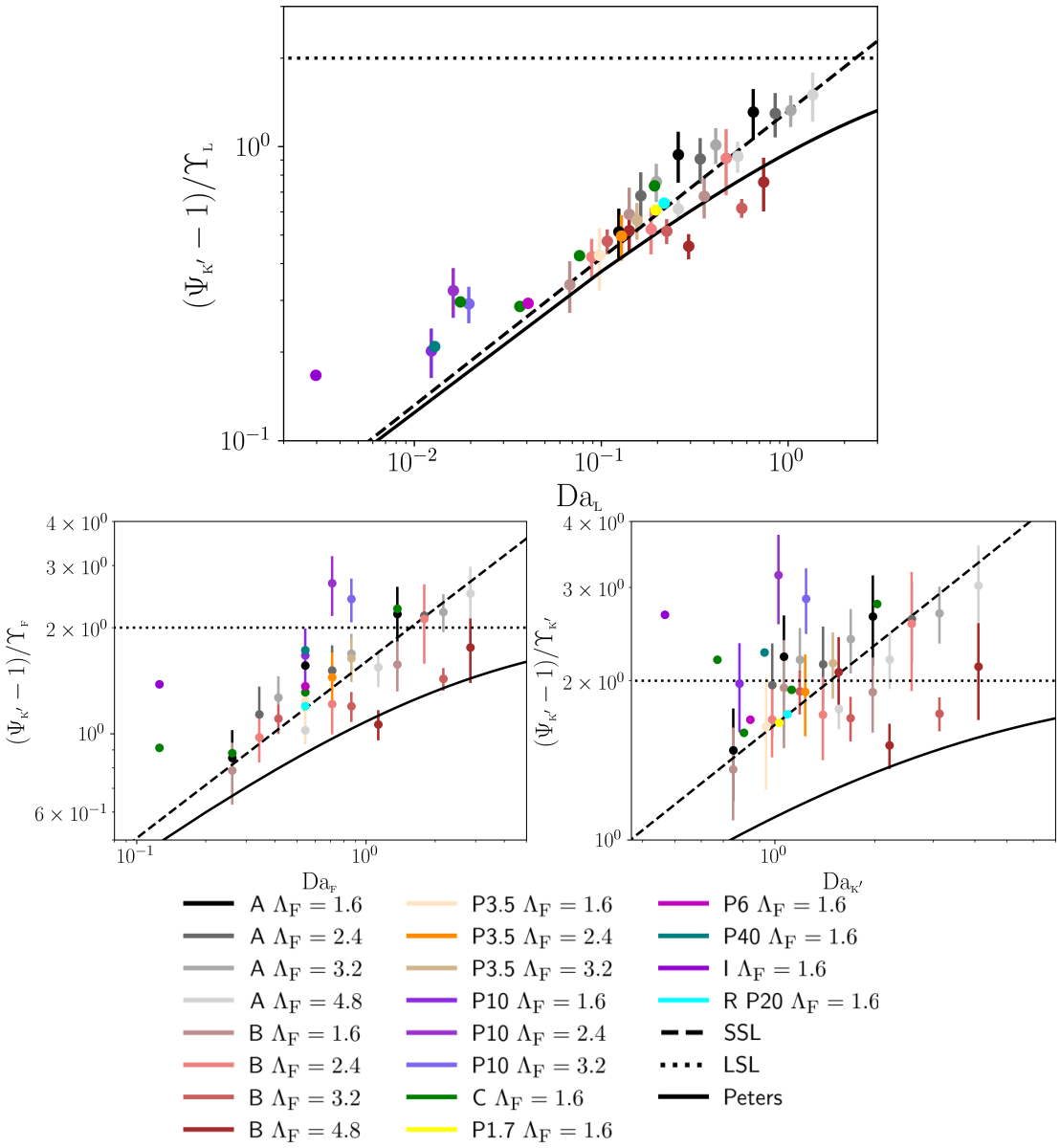

Figure 6.8: Normalised measured flame surface wrinkling $\Psi_{K'}$ against Damköhler numbers Da_R for L, F and K' normalisations for all simulation cases (including those from Chapter 5), and compared with the three models for flame surface wrinkling Ψ_T; SSL, LSL and Peters from 6.20.

surface wrinkling, not a change in mean local flame speed. It was speculated in Aspden *et al.* [22] that in highly turbulent flames the domain size could affect the turbulent flame speed also. As observed in the previous section, increasing the integral length scale increases flame surface wrinkling, however from the turbulence forcing method used (section 3.1.3, [23]) integral length scale is fixed to the domain size ($L_x = \Omega \ell_I$, where $\Omega = 10$), thus increasing the

integral length scale results in a proportionally larger domain size. Therefore, it is difficult to attribute the increase in flame surface wrinkling to the integral length scale alone. This section separates the domain size and integral length scale through an additional simulation case from simulation set B where the turbulence was set fixed at $\mathrm{Ka}_{\mathrm{F}} = 12$, but the domain size was doubled by the integral length scale which remained constant (i.e. $\Omega = 20$, $\Lambda_{\mathrm{F}} = 1.6$). By doubling the wave number in the momentum forcing term that maintains the turbulence, a periodic reproduction of the turbulence was obtained, resulting in a domain size being doubled without changing the integral length scale. Figure 6.9 shows an example 2-dimensional cross-section slice of the magnitude of vorticity from the $\Omega = 20$ case. Note the periodic reproduction mentioned above. Combining the additional case with existing cases, the following set (referred to as the Ω set) can be used to isolate domain size effects:

- Case 1, start with small domain size and integral length scale ($\Omega = 10, \Lambda_{\mathrm{F}} = 1.6$).
- Case 2, double the domain size, keep the integral length scale the same by doubling the forcing wave number ($\Omega = 20, \Lambda_{\mathrm{F}} = 1.6$).
- Case 3, keeping the domain size the same, double the integral length scale, i.e. has the same domain size as case 2 and double the integral length scale of case 1 and 2 ($\Omega = 10, \Lambda_{\mathrm{F}} = 3.2$).

Figure 6.10 shows the measured flame surface wrinkling factor $\Psi_{\mathrm{K}'}$ against length scale ratio Λ_{F} for the three cases, where the star represents Case 2. It can clearly be seen that by increasing domain size, even at a fixed integral length scale (Case 1, star) the flame surface wrinkling is increased. This would also mean the turbulent flame speed would increase as the mean local flame speed would remain the same. The two cases with a length scale ratio of $\Lambda_{\mathrm{F}} = 1.6$ have the same Ka_{F} and Da_{F} number (note as it is the same reactant conditions and flame scale turbulent intensity, the normalisation choice (L, F and K') makes no difference between Case 1, 2 and 3). Therefore, the turbulent models discussed above cannot distinguish between Case 1 and 2, thus predict the flame surface wrinkling. A potential cause of this behaviour could be explained using a volume-filling-surface argument; where the turbulence folds the flame increasing the local flame speed, thus the flame burns quickly, especially at the leading points and edges, increasing the flame surface wrinkling. However, in smaller domains

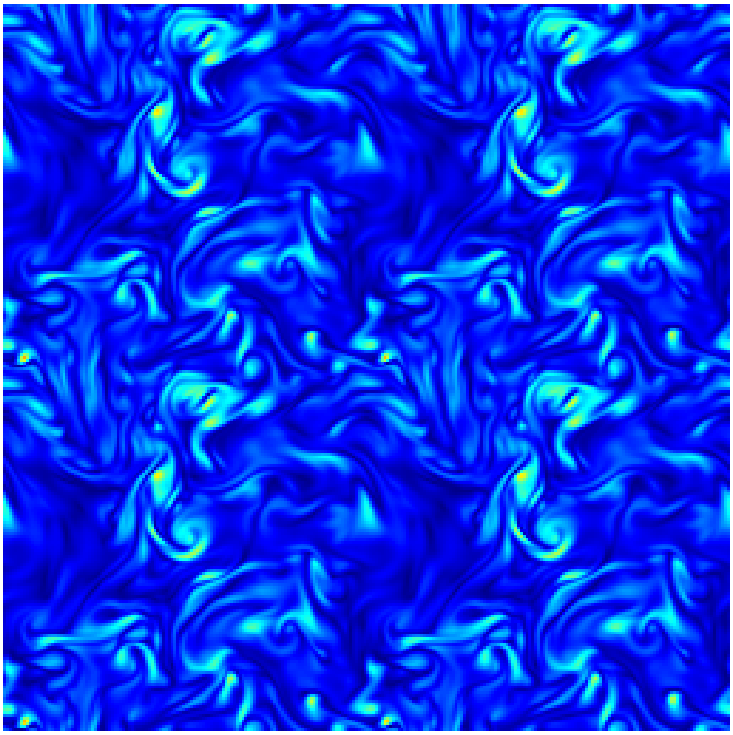

Figure 6.9: Example cross-section slice of vorticity magnitude showing the periodic reproduction from the $\Omega = 20$ case.

the available volume to the flame is reduced, thus the available volume to the flame is limited, artificially limiting the flame surface area. This phenomena is likely to be more pronounced at higher turbulent intensities. Despite this seemingly subtle observation, domain size constrainment does pose a potential issue to attributing the bending effect in DNS, with small domain sizes at high turbulence. It is still unclear if this phenomena is present in TD-neutral or stable flames. It can be speculated that as the flame instability decreases the effect of domain size will also diminish. The presented observations are only a single reactant case at a fixed $\mathrm{Ka_F}$ and is by no means meant to be an exhaustive study. However, this does present a potential limitation to DNS which is not often acknowledged in the literature.

6.7 Combined Model for Turbulent Flame Speed

Combining the mean local flame speed model with the SSL model for flame surface wrinkling, the turbulent flame speed can be predicted as

$$s_\mathrm{T} = s_\mathrm{P}\left(1 + \gamma_\mathrm{L}\Upsilon_\mathrm{L}\mathrm{Da}_\mathrm{L}^{1/2}\right), \tag{6.21}$$

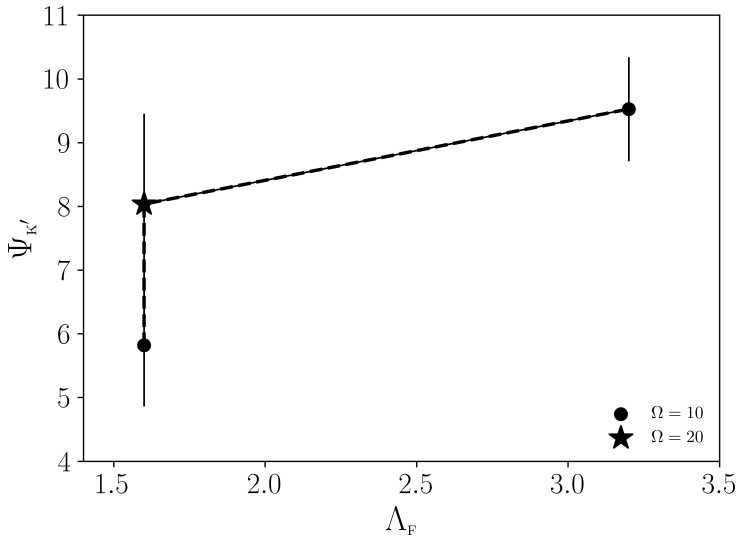

Figure 6.10: Measured flame surface wrinkling factor $\Psi_{K'}$ against length scale ratio Λ_F, comparing the effect of domain size for simulations in set B at $\mathrm{Ka}_F = 12$. Note how the wrinkling is higher in the larger domain even with the same equivalence ratio (star versus circle).

where the quantity of interest here is the prefactor s_P. The resulting predictions are compared with the measured value s_C in is Figure 6.11, where four prefactors are shown; specifically $s_P = s_L$ (red), s_F (magenta), s_K (blue, equation 5.4) and $s_{K'}$ (black, equation 5.1). It is clear that accounting for the TD-response though the prefactor (i.e. using $s_P = s_F$ in preference to s_L) is the leading order effect, and the prediction is improved further still by accounting for the increase in local flame speed with increasing Karlovitz number (i.e. using s_K in preference to s_F). As found in Chapter 5 using a measured value for the freely-propagating flame speed s_F (from a precursor DNS simulation) provides slightly improved predictions over the model value s_M (Equation 4.1) and therefore $s_{K'}$ provides a slight improvement over s_K. The latter still provides a satisfactory prediction and is a model that is far more appropriate for industrial CFD codes such as Vectis. Again, these observations may be a consequence of the limited range of turbulence conditions accessible to DNS, and at larger length scales different behaviours may be observed.

6.8 Fuel Lewis Number Effects

The model constants in Section 6.5 differ from those in the literature (e.g. [135]), and it is unclear if this difference is due to TD-effects in lean hydrogen or whether it is due to the way

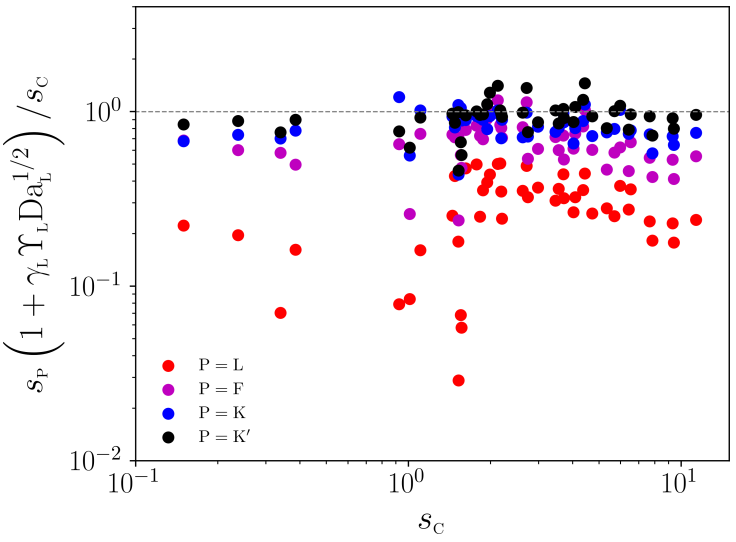

Figure 6.11: Modelled turbulent flame speed s_{T} using the small scale limit Equation 6.21, compared with the measured global consumption speed s_{C}. The wrinkling component $\Psi_{\mathrm{T}} = \gamma_{\mathrm{L}}\mathrm{Da}_{\mathrm{L}}^{1/2}$ and the prefactor s_{P} is compared for $\mathrm{P} = \mathrm{L}, \mathrm{F}$ and K'. Note the leading order effect is accounting for the TD-response in the prefactor, with a slight improvement using K' over K.

the contributing quantities have been evaluated (e.g. turbulent intensity, integral length scale etc.). Furthermore, despite having studied a large range of ω_2 conditions (5.58 to 27.27), the range of fuel Lewis numbers remains somewhat narrow (0.36 to 0.428). To evaluate the effect of Lewis number and establish whether the model constants are a hydrogen effect, a small number of additional cases have been simulated (Table 6.2). The Lewis number of the fuel has been artificially modified, while keeping the mechanism and all other aspects of the simulations unchanged; this approach means that any differences can be attributed to the Lewis number, rather than other fuel effects. Specifically, four values have been considered for the Lewis number of molecular hydrogen, $\mathrm{Le}_{\mathrm{F}} = 0.35, 0.7, 1$ and 2. The lowest value is representative of the realistic cases considered in the previous section. The freely-propagating flame speed and thermal thickness for all four Lewis numbers were obtained from precursor freely-propagating simulations (as conducted in Chapter 4). A single normalised domain size and integral length scale was considered ($\Lambda_{\mathrm{F}} = 2.4$), but the turbulent intensity was varied such that $\mathrm{Ka}_{\mathrm{F}} = 1, 4$ and 12, as above.

Table 6.2: Simulation conditions examining the effect of fuel Lewis numbers. Reactant conditions are $\phi = 0.4$, T =300 K, p=1 atm. Turbulence conditions are $\mathrm{Ka_F} = 1$, 4, 12 and $\Lambda_\mathrm{F} = 2.4$.

$\mathrm{Le_F}$	ω_2	s_L (m/s)	ℓ_L (μm)	s_F (m/s)	ℓ_F (μm)
0.35	8.17	0.225	587	0.368	512
0.7	−3.34	0.335	466	0.349	486
1	−11.4	0.392	430	0.392	455
2	−34.9	0.488	386	0.487	410

6.8.1 Local Flame Speed

Figure 6.12 shows the normalised mean local flame speed as a function of Karlovitz number for all four fuel Lewis numbers. The local flame speed in the low Lewis number case increases with turbulent intensity, as in Section 6.4. There is also a slight increase for the $\mathrm{Le_F} = 0.7$ case, despite being TD-stable (ω_2). It is suspected to be the same behaviour as the $\omega_2 = 0$ case (case Z) from Chapter 5 where the turbulence artificially folds the flame giving strong positive curvatures allowing for preferential diffusion, and as a result of the thermal leading point where the mean local flame speed is increased. Interestingly, this suggests that there is a Lewis number dependence for predicting the mean local flame speed at higher $\mathrm{Ka_F}$, which ω_2 cannot account for, when reactant conditions are TD-stable but experience preferential diffusion in positive curvature (i.e $\omega_2 \geq 0$ and $\mathrm{Le_{eff}} < 1$). Naturally, the unity Lewis number case does not experience a significant change in the mean local flame speed with turbulence. Finally, it can be seen that the high Lewis number flame sees a reduction in mean local flame speed with turbulence, which is consistent with previous simulations of high Lewis number fuels e.g. [163, 99, 98] for example.

This difference in flame speeds can be examined further by considering JPDFs of local flame speed and flame surface curvature; Figure 6.13 shows the JPDFs for all the modified fuel Lewis number cases. As fuel Lewis number increases from 0.35 to 2 the Markstein number increases from negative to positive, and is accompanied by a general decrease in the local flame speed. This is consistent with [77, 60, 150, 14]. Note that the Markstein number is slightly negative for the $\mathrm{Le_F} = 0.7$ case, despite being TD-stable ($\omega_2 < 0$). Again, the

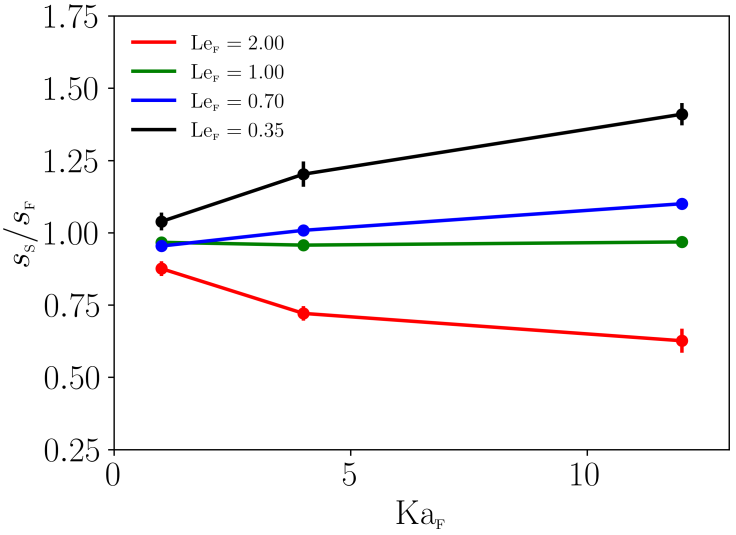

Figure 6.12: Normalised mean local flame speed as a function or Karlovitz number for the different fuel Lewis numbers. Whereas low fuel Lewis numbers result in an increase in mean local flame speed, high fuel Lewis numbers decrease.

TD-response is induced by turbulence folding the flame.

6.8.2 Flame Surface Winkling

The key question to be addressed by this artificial Lewis number study is whether flame surface wrinkling is affected by the Lewis number. Figure 6.14 shows the flame surface wrinkling with increasing $\mathrm{Ka_F}$ for the four $\mathrm{Le_F}$ cases (note that mean local flame speeds s_S have been used for normalisation as the Karlovitz-dependent models $s_{K'}$ have not been established for these cases). Consistent with the unmodified Lewis number cases, the flame surface wrinkling increases with turbulent intensity; also note the similarity with Figure 6.3. Importantly, it appears that flame surface does increase with decreasing Lewis number (at the same corresponding $\mathrm{Ka_F}$). However, the effect is relatively small for $\mathrm{Le_F} \lesssim 1$, and much more significant for the high Lewis number cases. This observation could further support the volume-filling surface argument. As a result of all the available space being filled by the flame, increasing the Lewis number cannot fill anymore volume. This argument would require additional simulations, and significantly larger domain sizes to appropriately evaluate, which was outside of the scope and budget of this project.

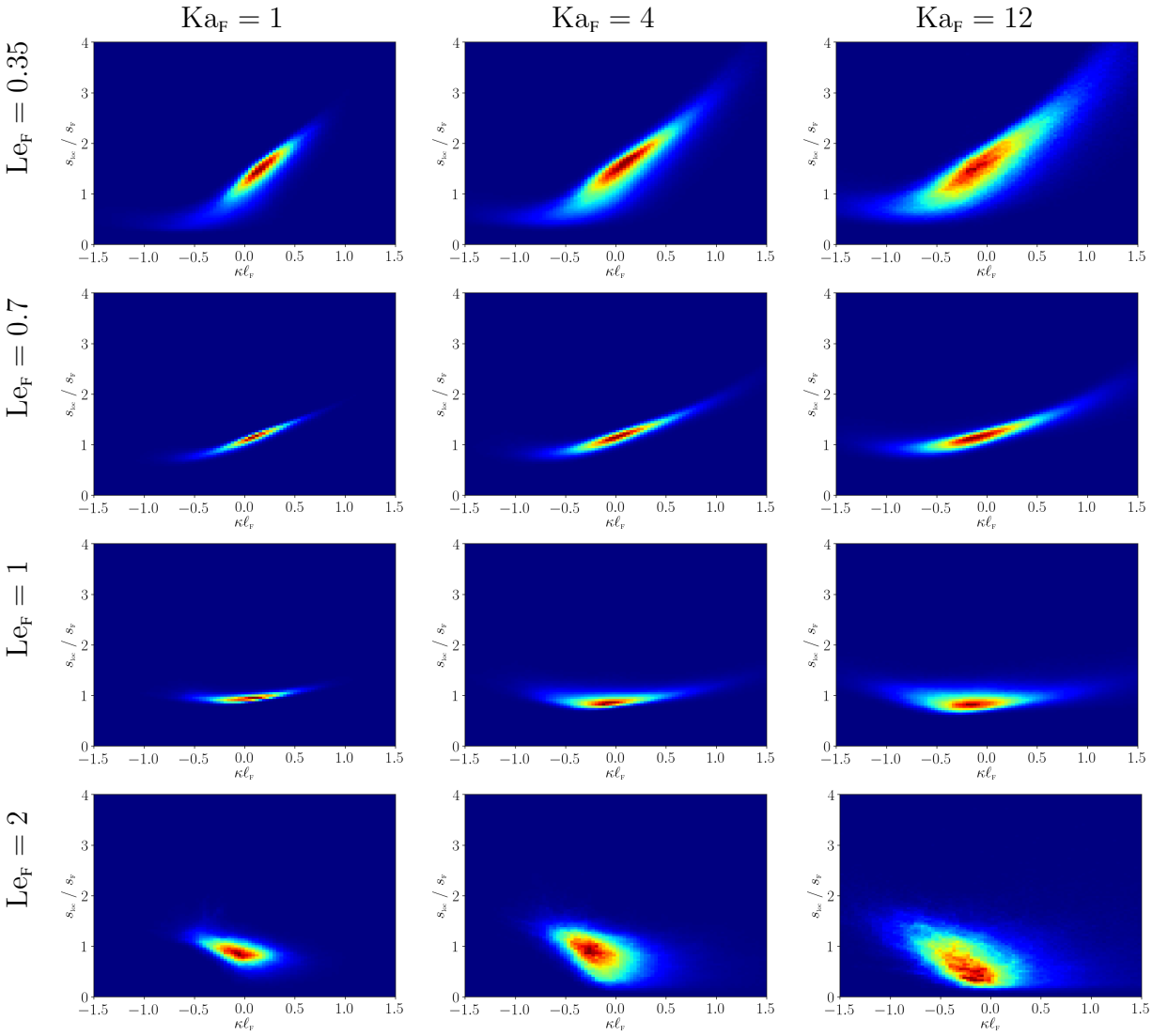

Figure 6.13: Joint probability density functions (JPDFs) of the normalised local consumption-based flame speed and normalised curvature for increasing fuel Lewis number $\mathrm{Le_F}$ (top-to-bottom) at increasing Karlovitz numbers $\mathrm{Ka_F}$ (left-to-right).

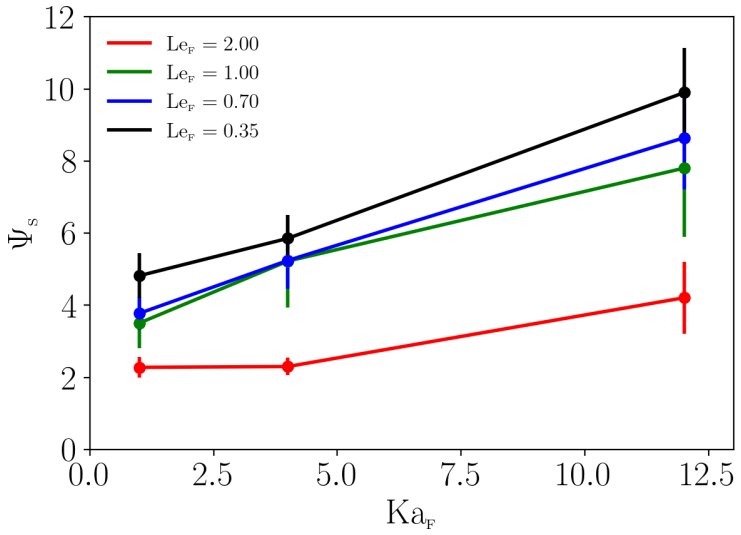

Figure 6.14: Flame surface wrinkling as a function of Karlovitz number for different fuel Lewis numbers. Low fuel Lewis numbers result in slightly enhanced flame surface area, but a significant reduction is observed at fuel high Lewis numbers.

To assess the impact on the model constants for flame surface wrinkling, Figure 6.15 presents the data in the same form as Figure 6.8. There is clearly a measurable difference between fuel Lewis numbers at around unity and below, but it is small compared with the difference observed in the high Lewis number case. In particular, since the difference between $\mathrm{Le_F}$ cases between 0.35 and 1 is small, then it suggests that differences between the model constants proposed and the literature (e.g. [135]) have more to do with how the dimensionless quantities are constructed than it being a low-Lewis number phenomenon, but that there is still an effect from fuel Lewis number.

6.9 The Premixed Regime Diagram Revisited

Attempts to classify turbulent premixed burning regimes have a long and rich history, from Ballal and Lefevre [24], Borghi [39] and Peters [133, 134], to more recent work by Skiba *et al.* [156]. In light of the observations from this work and previous works [17, 12, 22], a modification is proposed. A justification will be presented to characterise the regime diagram by Karlovitz and Damköhler numbers, which are essential for classifying the different regime. It is argued that the Karlovitz number is used to characterise the turbulent-flame interactions at the flame scale, which therefore is used to distinguish between the flame-let, thin reaction

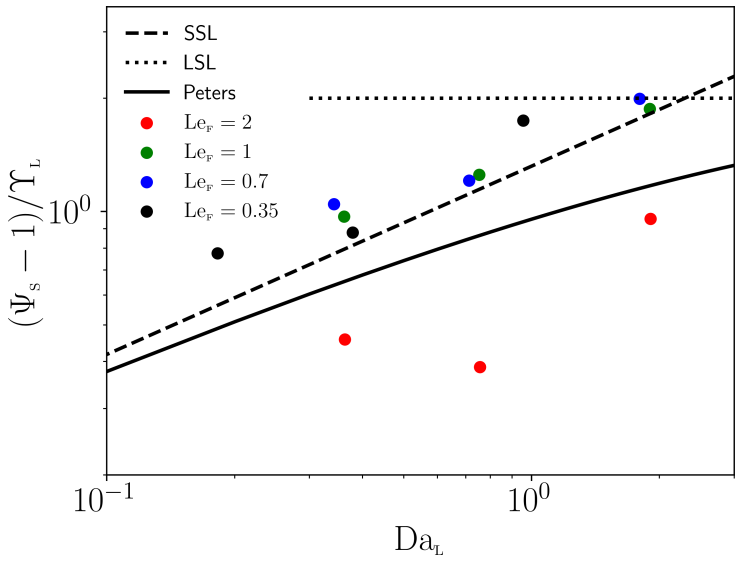

Figure 6.15: Normalised measured flame surface wrinkling Ψ_S against Damköhler number $\mathrm{Da_L}$ for all simulations with artificial fuel Lewis number, and compared with the three models for surface wrinkling Ψ_T (i.e. SSL, LSL and Peters) given by equation 6.20.

zones and distributed burning regimes. The Damköhler number is used to characterise the turbulent-flame interactions at the integral length scale, which therefore is used to distinguish between the large- and small-scale turbulence limits as identified by Damköhler [55].

6.9.1 Turbulent-Flame Interactions at the Flame Scale: The Karlovitz Number

In summary to the discussion in Chapter 2, Section 2.5.2, the Karlovitz number was defined by applying Kolmogorov's similarity hypothesis to turbulent premixed flames. It was argued following [162, 22] the energy cascade is terminated by dilatation at the flame scale, thus Karlovitz number is defined at the flame scale not the Kolmogorov lenght scale. As the energy dissipation rate is constant through the inertial sub-range, and both the integral length and flame scale (provided) exist inside the inertial sub-range, the following is true

$$\varepsilon = \frac{u'^3}{\ell_\mathrm{I}} = \frac{u'^3_r}{r} = \frac{u'^3_{\ell_\mathrm{F}}}{\ell_\mathrm{F}}, \tag{6.22}$$

where the latter represents the energy dissipation rate at the flame scale, which is inside the inertial sub-range. By normalising the turbulent velocity at the flame scale u'_{ℓ_L} by the flame speed gives

$$\frac{u'_{\ell_\mathrm{F}}}{s_\mathrm{F}} = \frac{u'}{s_\mathrm{F}} \left(\frac{\ell_\mathrm{F}}{\ell_\mathrm{I}} \right)^{1/3} = \mathrm{Ka}_\mathrm{F}^{2/3}, \tag{6.23}$$

thus the Karlovitz number is defined as

$$\mathrm{Ka_F} = \sqrt{\frac{u'^3}{s_\mathrm{F}^3}\frac{\ell_\mathrm{F}}{\ell_\mathrm{I}}} = \sqrt{\frac{\Upsilon_\mathrm{F}^3}{\Lambda_\mathrm{F}}}. \tag{6.24}$$

Please see Section 2.5.2 for a more complete description. Additionally the presented simulations (e.g. Figure 6.4) and the simulations presented in Chapter 5 support the argument that Karlovitz number defined this way characterises the turbulent-flame interactions at the flame scale well, independently from Damköhler number.

When defining Karlovitz this way it can be used to distinguish between the conventional burning regimes in the usual way ([134, 135] for example). For small Karlovitz number $\mathrm{Ka_F} < 1$, the Kolmogorov length scale is larger than the flame scale, so there can only be turbulent-flame interaction at the large-scale, called the flame-let regime. At $\mathrm{Ka_F} \approx 1$, the smallest turbulent scales are similar to the flame scale. As $\mathrm{Ka_F}$ gets larger, turbulence can begin to interact with the preheat zone, but not yet the reaction zone, called the thin reaction zone (TRZ). As $\mathrm{Ka_F}$ gets larger still, at some point $\mathrm{Ka_F}$ exceeds a critical value where turbulence becomes strong enough to penetrate the reaction zone, and mix the internal structure of the flame on a shorter time scale than burning, called the distributed burning regime (DRB). Note that this critical $\mathrm{Ka_F}$ value is higher than the often-quoted value of 100 [14, 22]. Figure 6.16[1] shows a conventional turbulent premixed regime diagram [134, 135] with illustrative turbulent spectra. Three Karlovitz numbers are presented are denoted by the three dotted black lines. Note how for each Karlovitz number the inertial sub-range coincide, and the turbulent-flame interactions at the flame scale are independent of Damköhler number. Different Reynolds numbers are denoted by different colours and demonstrate how each Reynolds number can appear in any regime, thus is not a useful tool for regime classification.

6.9.2 Turbulent-Flame Interactions at the Integral Scale: The Damköhler Number

In Damköhler's small-scale limit (SSL), it is argued that the diffusive transport is modified so that turbulent diffusion can be used as a substitute for molecular diffusion. The SSL has been previously associated with different turbulent conditions; Damköhler [55] suggested $\ell_\mu << \ell_\mathrm{L}$ where ℓ_μ is some mixing length, Peters [135] associated the SSL with the TRZ, Lipatnikov and

[1] Thanks to A. J. Aspden for making the figure.

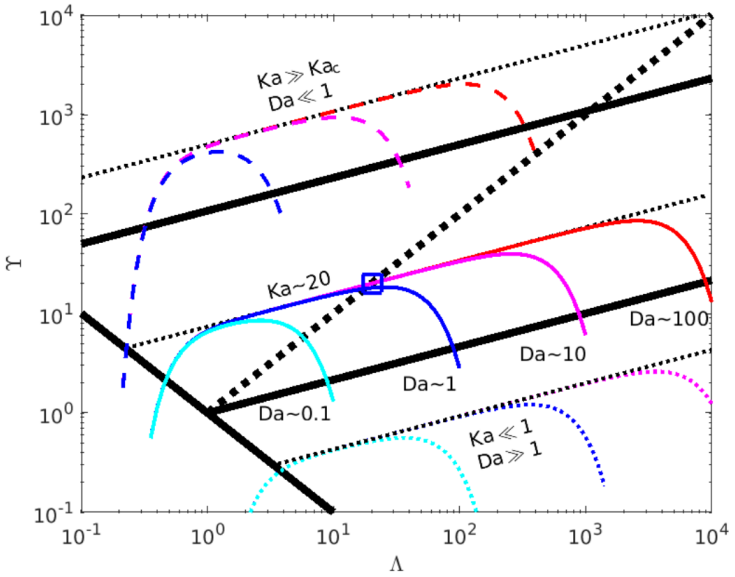

Figure 6.16: A conventional turbulent premixed regime diagram [134, 135], with illustrative turbulent spectra. The dotted black lines show constant Karlovitz numbers, and the colours denotes different Reynolds numbers.

Chomiak [109] and Aspden *et al.* [16, 20] considered the SSL to require high turbulent intensity (the DBR).

From the conditions provided in this thesis (Chapters 5 and 6) the simulations are comfortably in the TRZ, but are in the low turbulence end of the regime, and are not close to becoming distributed. The data is also consistent with the SSL. This was also seen in [22] (see Figure 4c) for both hydrogen and methane where the turbulent flame speed was found to grow at the rate $\mathrm{Ka}_\mathrm{F}^{1/3}$ (at a fixed Λ_F) even when flames were not in the DBR. Consequently, it seems important to make a distinction between the SSL and DBR, where a flame does not need to be experiencing distributed burning to present scaling consistent with the SSL. The SSL appears to correspond to the small Damköhler numbers and the DBR corresponds to the high Karlovitz numbers. It could be speculated that the presented simulations' consistency with the SSL scaling laws is a dimensional necessity, which results from turbulence driving the flame surface wrinkling. Additionally, as noted in [109] and observed from simulation data from [22] and more recently [174], there is a transition from the TRZ to the DBR. Specifically, the turbulent flame speed first increases with increasing Ka_F in the TRZ but appears to experience some transition where the turbulent flame speed drops significantly. It was found in [22] that

the turbulent flame speed then starts to increase again as $\mathrm{Ka_F}$ continues to increase. The transition from the TRZ to the DBR appears more subtle than described in the literature, which means determining the critical Karlovitz number for the DBR as discussed in [134, 135] remains an open question.

From the data provided in this work, the length scales were not large enough to observe a transition from SSL to LSL, however such a transition was observed in the DBR in [17], where the distributed flames presented in [16] were extended to large Damköhler numbers at a fixed Karlovitz number. Figure 6 in [17] presents the turbulent flame speed normalised by turbulent intensity as a function of Damköhler number. It was observed to follow the scaling for the SSL ($s_\mathrm{T}/u' \sim \mathrm{Da_T}^{1/2}$) up to a limit of $\mathrm{Da_T} \approx 1$, where the scaling followed the LSL ($s_\mathrm{T}/u' \approx 2$). Where $\mathrm{Da_T}$ is turbulent Damköhler number which is defined as the ratio of the turbulent eddy turnover time and the turbulent flame time scale (will be discussed below).

From the data presented in this work and the resulting distinction between the DBR and the SSL, the transition from SSL to LSL observed in [17], the observation that normalising the flame surface by the velocity results in a function of just Damköhler number and the consistency with the limits of the turbulent flame speed models, it can be argued that there exists a turbulent time scale τ_T such that a turbulent Damköhler number $\mathrm{Da_T}$ can be used to define the limit that separates the SSL from the LSL. Therefore, Damköhler numbers are a necessary condition to define the limit between the SSL and LSL despite the suggestion in [134] that the unity Damköhler number line has no significance for turbulent burning regimes. Following these observations and suggestions, the TRZ and DBR have separate regions in the both the SSL and LSL, which in turn are separated by the $\mathrm{Da_T} \approx 1$ line.

The turbulent flame time scale τ_T is key to the argument, which may be different to the 1-dimensional unstreached laminar flame timescale, which can depend on Karlovitz number and reactant conditions, but independent from integral length scale at a given Karlovitz number. Dimensionally, combing the time scale and the energy dissipation rate ε gives the velocity and length scales (see Equation (12) in [17])

$$s_\lambda \sim \sqrt{\varepsilon \tau_\mathrm{T}}, \tag{6.25}$$

$$\lambda \sim \sqrt{\varepsilon \tau_{\mathrm{T}}^3}. \tag{6.26}$$

This length scale was identified by Zimont and Sabelnikov [185, 183][2], which was interpreted as a mixing length by Peters [134] and named the Zimont scale. The Zimont approach was discussed in detail in Appendix D in [109]. The length scale λ is interpreted here as the size of the turbulent eddy with the same time scale as the turbulent flame time (note again that this is not likley to be the same as the 1-dimensional unstreached laminar flame timescale), which occurs at the intersection of the constant Karlovitz line with the line where the turbulent Damköhler number equals unity.

The SSL an LSL can now be identified by comparing the turbulent eddy turnover time with the turbulent flame time. For $\mathrm{Da}_{\mathrm{T}} < 1$, the turbulent eddies between the integral length scale ℓ_{I} and the flame thickness ℓ_{F} turnover faster than the turbulent flame time which results in an increase in flame surface wrinkling following the SSL. If $\mathrm{Da}_{\mathrm{T}} > 1$, the turbulent eddies between the integral length scale and the length scale λ turnover slower than the turbulent flame time where the turbulence foes not contribute to an increase in flame surface wrinkling, thus only follow the LSL. It should be noted that the turbulent eddies between the sizes λ and ℓ_{F} are still able to broaden the flame, which means that the SSL is embedded within the LSL. To explain this consider the $\mathrm{Ka}_{\mathrm{F}} \sim 20$ cases shown in Figure 6.16. The cyan and blue curved denote $\mathrm{Da}_{\mathrm{T}} \leq 1$ cases; these cases have the inertial subrange between the length λ and ℓ_{F} have increased the flame surface wrinkling as much as possible, whereas the larger scales (from ℓ_{I} to λ) are too slow to increase the wrinkling further. The large-scale regime is effectively a unity turbulent Karlovitz number flame, where the turbulent Karlovitz number is given by

$$\mathrm{Ka}_{\lambda}^2 = \left(\frac{u'}{s_{\lambda}}\right)^3 \frac{\ell_{\mathrm{I}}}{\lambda}. \tag{6.27}$$

At this scale the flame was referred to as a λ-flame in [17] where λ represents the limiting length scale of the SSL at the given Karlovitz number.

[2]Thanks to A. N. Lipatnikov for explaining that this length scale was previously identified in the paper with Sabelnikov.

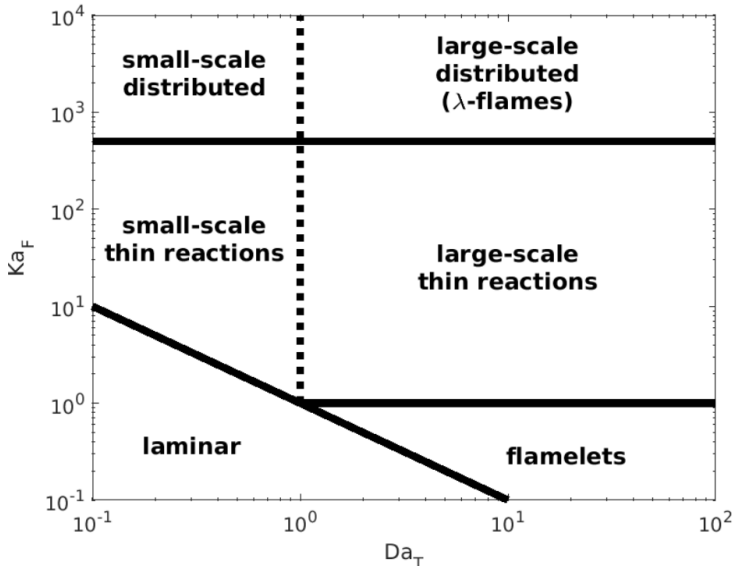

Figure 6.17: Turbulent burning regime diagram presented in terms of $\mathrm{Da_T}$ and $\mathrm{Ka_F}$. $\mathrm{Ka_F}$ characterises the turbulent-flame interactions at the flame scale (thus separating the flamelet regime from the thin reaction zone from the distributed burning regime). $\mathrm{Da_T}$ classifies turbulent-flame interactions at the integral scale (thus separating the large- and small-scale regimes).

6.9.3 A Modified Regime Diagram

Figure 6.17 presents a modified regime diagram, which collects all the findings and discussion above. The regime diagram is given as a 2-dimensional parameter space where the regimes are separated using Karlovitz and Damköhler number. This regime diagram is essentially a roatatrion of the conventional regime diagrams from [39, 135] with the addition of the $\mathrm{Da_T} = 1$ line. It could also be interpreted as a combination of the two predecessors; including the distributed burnin regime at high Karlovitz numbers as seen in [134, 135] while retaining the unity Damköhler line as seen in [39, 133]. Now the verticle lines represent variable Karlovitz at a fixed Damköhler number seperating the thin reactions from the distributed and the horizontal lines represent a fixed Karlovitz at a variable Damköhler number seperating the small-scale and large-scale limits.

How to define $\mathrm{Da_T}$ (i.e. the turbulent flame time scale τ_T is key and still to be determined. It would be determined by measuring the flame brush thickness and turbulent flame speed and thus demonstrating a similar invariance in the TRZ that was obereved in the DBR from [17];

the resulting flame time scale can be matched with the inertial subrange of the turbulence where λ can then be found. Such a study is extremely challenging to compute in DNS with detailed chemistry, but may be possible by using a well-resolved g-equation approach, for example, which is the focus of the next chapter.

6.10 Conclusions

Direct numerical simulations have been presented to explore the effect of reactant and turbulent conditions on TD-unstable lean premixed hydrogen flames, with a particular focus on the influence of the larger turbulent length scales. It is concluded that three parameters are important to characterise turbulence-flame interactions in such flames: an instability parameter ω_2, which represents the strength of the TD-response; Karlovitz number, which represents turbulence-flame interactions at the flame scale and a Damköhler number, which represents the turbulent-flame interactions at the large scales. The mean local flame speed was measured over a range of integral length scales and range of reactant conditions and turbulent intensities (Figure 6.3). As expected, the TD-response was stronger with increasing Karlovitz number, but crucially, the mean local flame speed was shown to be independent from integral length scale at a fixed $\mathrm{Ka_F}$ and that the model from chapter 5 (Equations 5.1, 5.2, 5.4 and 5.5) provides excellent predictions in terms of the instability parameter and Karlovitz number. It was further shown that turbulence-flame interactions as represented by JPDFs of local flame speeds and curvature (Figure 6.4) are similarly independent from integral length scale at a fixed $\mathrm{Ka_F}$. An additional simulation was conducted to emphasise that matching the turbulent intensity alone is insufficient (Figure 6.5). The length scale at which this intensity is measured is important, and the appropriate dimensionless parameter is the Karlovitz number; this was recently supported by observations from Yao and Blanquart [174]. Importantly, since the mean local flame speed can be well predicted by the existing models from Chapter 5, the key to constructing a turbulent flame speed model is reduced to predicting the flame surface area enhancement.

Naturally, flame surface wrinkling was found to increase with both Karlovitz number and integral length scale (figure 6.6) with good agreement with scaling laws predicted in Damköhler's small-scale limit [55, 134, 135], with some scatter in the data. Following Peters [135], normalising the flame surface area by turbulent intensity results in a function that is a

function of Damköhler number alone. Again, the data were in reasonable agreement (Figure 6.8), but with some scatter; note that experimental data has a similar scatter (for example, see Figure 2.24 in Peters' book [135]). Different normalisations were considered and while normalising by the laminar flame properties was visually more compelling, there was little difference in the relative error. It is possible that there is a turbulent timescale that would be more appropriate, which is yet to be identified.

Comparisons of turbulent flame speed models (Figure 6.11) demonstrated good agreement with the small-scale limit,

$$s_{\mathrm{T}} = s_{\mathrm{R}} \left(1 + \gamma \Upsilon_{\mathrm{R}} \mathrm{Da}_{\mathrm{R}}^{1/2}\right), \tag{6.28}$$

where $\gamma = 1.32$ which is larger than the value (0.88) given in [135]. This difference in the constant was attributed to the way the various other terms in the expression are evaluated, with a strong notion that a domain size constrainment effect (volume-filling surface) is present, as discussed further below. The mean local flame speed prefactor was observed to be a leading order effect, and it is emphasised that it needs to be taken into account for TD-unstable flames. Accounting for the local acceleration through s_{F} in preference to s_{L} has the largest effect and accounting for additional acceleration from turbulence with $s_{\mathrm{K}'}$ provides further improvement. Finally, $s_{\mathrm{K}'}$ shows a small improvement by removing the modelling error from s_{M} by using s_{F} instead. It was suggested in [22] that the domain size could have an effect on flame surface area, especially in small DNS-scale domains. To test this prediction, an additional simulation was performed where the domain size was doubled, but the integral length scale kept the same by ensuring the turbulence was a periodic reproduction (by modifying the maintaining source term in the momentum equation). Taking the starting point to be the case with the smaller domain (and integral length scale), it was found that the turbulent flame surface area could indeed increase in a larger domain without changing the integral length scale (Figure 6.10). The flame surface area increased again when the integral length scale was increased in the same sized domain. This effect is usually neglected and is not predicted by any conventional algebraic model for turbulent flame speed (i.e. there is no Ω term), and it is anticipated that it will not only be relevant for DNS but for experimental studies of limited physical extent.

The periodicity of the flame-in-a-box configuration can constrain the development of the flame

surface area, resulting in under-prediction of turbulent flame speed. This is anticipated to become increasingly problematic with increasing turbulent intensity, and may be more pronounced where the ratio of domain size to integral length scale is small. Consequently, there is a possibility that observing the so-called "bending effect" could result from an inadequately-sized domain. The present observations do not question the phenomenon, but serve as a warning that care is required to ensure that it is not an artefact of a domain or burner of insufficient size. Furthermore, there have been several observations of the turbulent flame speed dropping with increasing turbulent intensity (e.g [22, 174]).

To establish whether the different value observed for the SSL constant γ is due to a TD-effect or simply how the various quantities have been evaluated, a further study was performed considering different fuel Lewis numbers. Only the diffusion coefficient of molecular hydrogen was artificially modified; the same hydrogen mechanism was used and all other species were left unchanged. Naturally, fuel Lewis number was found to have a leading order effect on mean local flame speed (Figure 6.12), increasing for low Lewis number and decreasing for high Lewis number with he effect becoming more pronounced with increasing Karlovitz number. Similarly, a significant effect was observed in the JPDFs of flame speed and curvature (Figure 6.13), transitioning from negative to positive Markstein numbers with increasing fuel Lewis number. Furthermore, the flame speeds at zero curvature were observed to decrease with increasing fuel Lewis number, consistent with previous simulations of high Lewis number fuels (e.g. [77, 60, 150, 14]) which warrants further study.

The flame surface wrinkling was observed to be higher for the lower fuel Lewis number cases (Figure 6.14); the differences are significantly smaller for $\mathrm{Le}_{\mathrm{F}} \lesssim 1$ compared with $\mathrm{Le}_{\mathrm{F}} > 1$. A potential explanation for the behaviour observed is a simple volume-filling-surface concept. The TD-response for the low fuel Lewis number case is to exaggerate flame surface deformation, and increase the wrinkling. However, there is a limit to how much flame surface area can fit into a given volume. Therefore, for low fuel Lewis numbers there is only so-much more flame surface that can be created, and so the differences are small when compared with unity Lewis number. Turbulence can lead to a larger flame brush, and therefore a larger volume, but the wrinkling in that volume is already close to the limit at unity Lewis number.

Conversely, the TD-response of the high Lewis number flame is to flatten the flame, and so the observed wrinkling is much lower, and only increases with much higher turbulence. Again, this is consistent with [14] and a similar phenomena was reported in [16].

Lastly a modified regime diagram was proposed which separates the different burning regimes using a 2-dimensional parameter space, the Karlovitz and Damköhler number. The Karlovitz number is used to differentiate the thin-reaction-zone and the distributed reaction zone independently from Damköhler. The Damköhler number is then used to differentiate between the small-scale and large-scale limit, independently from Karlovitz number. The exact values of where these limits occur is the focus of furture work and significant challenges (namely the limitations of DNS with detailed chemistry) need to be considered.

Chapter 7. A DNS Level-Set Approach for Lean Hydrogen Flames

The direct numerical simulation of flames with complex chemistry is computationally expensive and these costs limit the size of the flame that can be studied. As shown in Chapter 6, global flame statistics can be influenced by the integral length scale, which is constrained by the relative domain size. To study flames at larger scales, larger simulations at a wide range of turbulent and reactant conditions are required, yet currently is too computationally expensive to be studied. The limiting factor for the computational cost is the equation set, resolution and corresponding time step to resolve the flame scale and chemistry. This chapter focuses on developing a DNS-style G Equation, influenced by Rastigejev and Matalon's paper [141], where the flame and subsequent chemistry can be modelled where the surface is fully represented by a level-set (G-equation). Using the findings from Chapters 4, 5 and 6 an appropriate model can be developed to replace the chemistry, significantly reducing the computational cost. The methods implemented have a specific focus on TD-unstable flames, which have yet to been successfully implemented into a DNS-style G-Equation which have historically been used to study Darrius-Landau instabilities for near unity Lewis number flames [141, 122].

This chapter introduces the level-set method and motivation in Section 7.1 then explains and discusses the numerical implementation of the level-set in Section 7.2, where the fundamental equations are introduced, discussed, important choices are highlighted and the algorithm is presented. Next, in Section 7.3, the simulation test conditions are introduced and in Section 7.4 the effective 1-dimensional simulations are conducted in both the level-set and in PeleLM. The results are compared over a small range of conditions. Next, 2-dimensional freely-propagating simulations are conducted and compared between the level-set and PeleLM for the same range of conditions in Section 7.5. Lastly computational costs between the level-set and PeleLM are compared in Section 7.6 to highlight the significant cost-saving advantages of using the method over PeleLM.

This section represents ongoing work and is not intended to be an exhaustive validation procedure. This chapter is designed to present a proof of concept, highlighting the method and

its potential applications.

7.1 Introduction

Level-sets typically use a single transport equation that can be used to track an interface, for example two-phase flow such as that studied in [160] or a flame position studied in [141]. A level-set is often a signed distance function, where the level-set field is divided into three distinct sections; negative, positive and zero, where zero represents the interface between the two states. Williams [173] introduced the concept of level-sets for combustion where the premise behind the level-set method is to track the flame position, often called a G-equation. The three distinct regions are constructed as the burnt region, the unburnt region and the interface between the two, which can be associated with the isosurface (see Osher for a more general introduction to level-set methods [129]). This approach is typically used to model flames in (U)RANS and LES simulations as discussed by Peters [134, 135] for example and has seen wide adoption in the combustion community, such as models used in Vectis and OpenFoam. These approaches do not resolve the smallest turbulent scales, thus adopt a model to account for sub-grid flame surface wrinkling, for example s_{T} as studied in Chapter 6. The approach being used in this chapter suggests that using a well-resolved G-equation where the surface is fully represented by the level-set, the turbulent scales are resolved, and the turbulent-surface interaction is tracked, no sub-grid modelling is required. The flame is then resolved at the small turbulent scales where chemistry is modelled using a Markstein model such as that proposed in Chapter 5. Rastigejev and Matalon [141] presented the capabilities of this approach by using a DNS style G-equation for 2-dimensional unity Lewis number flames experiencing Darrious-Landau instabilities. The approach used in [141] is not suitable for flame with negative Markstein numbers which will be discussed later.

This chapter uses IAMR (version 23.12) as a base for solving the in-compressible Navier-Stokes equations. The equation set and algorithms are then modified to add level-set functionality and will be detailed below. This work also borrows from AMReX-Hyrdro (version 23.12) which contains the hydrodynamic solver routines for low Mach number flows used in IAMR and AMReX (version 23.12) and the framework used for massively parallel, block-structured adaptive mesh refinement. These codes are all open-source and

freely-available at:

https://amrex-fluids.github.io/IAMR/

https://amrex-fluids.github.io/amrex-hydro/docs_html/

https://amrex-codes.github.io/amrex/docs_html/

7.2 Numerical Implementation

This section introduces the theory and numerical implementation of the level-set methods.

7.2.1 The IAMR Equation Set

IAMR solves the variable-density in-compressible Navier-Stokes equations though the following conservation equations (mass, momentum and velocity constraint):

$$\frac{\partial \rho}{\partial t} + \nabla \cdot \rho \boldsymbol{u} = 0. \tag{7.1}$$

$$\frac{\partial \rho \boldsymbol{u}}{\partial t} + \nabla \cdot \rho \boldsymbol{u}\boldsymbol{u} = -\nabla \cdot \boldsymbol{\sigma} + \boldsymbol{\mathcal{F}}, \tag{7.2}$$

$$\nabla \cdot \boldsymbol{u} = 0. \tag{7.3}$$

Firstly, introducing the level set by defining a scalar field G (will be referred to as the G-field), where

$$G \begin{cases} < 0 & \text{if unburnt,} \\ = 0 & \text{if flame surface,} \\ > 0 & \text{if burnt.} \end{cases} \tag{7.4}$$

By defining a position at the flame front (x_0), the propagation of the flame front at position x_0 can be defined as the sum of the flow velocity $\boldsymbol{u}$ and the burning velocity normal to the flame surface at speed s_{loc}

$$\frac{\mathrm{d}x_0}{\mathrm{d}t} = \boldsymbol{u} + \boldsymbol{n} s_{\text{loc}}, \tag{7.5}$$

where the normal is given as

$$\boldsymbol{n} = -\frac{\nabla G}{|\nabla G|}. \tag{7.6}$$

Note that the normal is negative so that the normal points towards the more negative regions. Then by differentiating the G-field with respect to time, the rate of change of G can be given as

$$\frac{\partial G}{\partial t} + \nabla G \cdot \frac{\mathrm{d}x_0}{\mathrm{d}t}, \tag{7.7}$$

which can be written as

$$\frac{\partial G}{\partial t} + \boldsymbol{u} \cdot \nabla G = s_{\mathrm{loc}} |\nabla G|, \tag{7.8}$$

where in three spacial dimensions

$$|\nabla G| = \sqrt{(\nabla_x G)^2 + (\nabla_y G)^2 + (\nabla_z G)^2}. \tag{7.9}$$

By using the G-field as a replacement for a real flame, neither species transport or temperature are required or calculated. In a real flame however, heat is released as a result of combustion, which reduces the density of the products. This process now must be modelled; [141] suggested that the density jump from combustion can be approximated with

$$\rho = \rho_u + \frac{1}{2}(\rho_b - \rho_u)\left(1 + \tanh\left(\frac{G}{h}\right)\right), \tag{7.10}$$

where ρ_u and ρ_b is the unburnt and burnt density and h is a thickness, where [122] suggests $2\mathrm{d}x$. It was found (validation is still ongoing) that for TD-unstable flames a more realistic thickness with $h \sim \ell_{\mathrm{F}}$ controls the extent to which strongly curved regions can form, which is a problem that was not likely to be encountered in the TD-stable flames from [141]. Equation (7.10) will now replace Equation (7.1) which is no-longer required.

Resulting from the modelled thermodynamic expansion the velocity constraint is no longer zero, and therefore must be modified, again using the recommendation from [141] where

$$\nabla \cdot \boldsymbol{u} = \rho_u s_{\mathrm{loc}} \frac{\partial}{\partial n}\left(\frac{1}{\rho}\right). \tag{7.11}$$

It should be noted that this formulation does not include a component from diffusion, which is often incorporated as part of a displacement speed, and so would not be an appropriate approach for a non-reacting case.

7.2.2 *Modelling s_{loc} and the Problem with TD-unstable Lean Hydrogen Flames*

Previous chapters have proposed a curvature only model for freely-propagating and turbulent TD-unstable lean hydrogen flames in the form

$$s_{\text{loc}} = \overline{s_{\text{loc}}} \left(1 - \mathcal{M}\kappa\overline{\ell_{\text{loc}}}\right), \tag{7.12}$$

where $\overline{s_{\text{loc}}}$ and $\overline{\ell_{\text{loc}}}$ is the mean local flame speed and thickness which can be modelled by Equations (4.1) and (4.2) for freely-propagating flames and Equations (5.4) and (5.5) for turbulent flames. κ is the curvature and $\mathcal{M}$ is the Markstein number. The resulting transport equation of G (Equation (7.13)) becomes

$$\frac{\partial G}{\partial t} + \boldsymbol{u} \cdot \nabla G = \overline{s_{\text{loc}}} \left(1 - \mathcal{M}\kappa\overline{\ell_{\text{loc}}}\right) |\nabla G|, \tag{7.13}$$

where curvature is defined as

$$\kappa = -\frac{\nabla^2 G - \boldsymbol{n} \cdot \nabla \left(\boldsymbol{n} \cdot \nabla G\right)}{|\nabla G|}. \tag{7.14}$$

As shown in chapters 4, 5 and 6, TD-unstable lean hydrogen flames have a negative Markstein number. This results in a focusing of G rather than a diffusion of G (like the methods implemented in [141]). Therefore regular re-initialisation of the G-field will be required. Achieving this efficiently can be challenging and potential numerical issues can result which will be highlighted as they are encountered.

7.2.3 *The Re-initialisation Equation*

As discussed previously, a re-initialisation equation is required, [141] used a fast marching method to avoid the computationally costly re-initialisation method. Thanks to the unstable nature of the transport equation of G for TD-unstable flames, re-initialisation is unavoidable. The approach used here will be at the first computational step, the signed distance function of G will be constructed where the surface at $G = 0$ will be user defined. Then the value of G will be proportional to the locations distance from the surface. To construct the initial G-field, the value of G is simply set as the horizontal distance from the surface

$$G = y - y_0, \tag{7.15}$$

where y_0 is the y-position of the flame.

The next step is to re-distance the G-field to get a smooth signed function of the distance from the flame surface. A simple construction of this is the equation

$$\frac{\partial G}{\partial \tau} - |\nabla G| = \begin{cases} 1 & \text{if } G > 0, \\ -1 & \text{if } G < 0, \end{cases} \tag{7.16}$$

where τ is an artificial time, the time step exists to re-distance G and does not progress in real time. Sussman *et al.* [160] defined the re-initialisation equation as

$$\frac{\partial G}{\partial \tau} + S\left(|\nabla G| - 1\right) = 0, \tag{7.17}$$

where S is a sign function which is used to keep the surface stationary during re-initialisation. At the beginning of each re-initialisation step, the S-field is initialised as [159]

$$S = 2\left(\mathcal{A} - \frac{1}{2}\right), \tag{7.18}$$

where

$$\mathcal{A} = \begin{cases} 0 & \text{if } G > -\varepsilon, \\ \frac{1}{2}\left(1 + \frac{G}{\varepsilon} + \frac{1}{\pi}\sin\left(\pi\frac{G}{\varepsilon}\right)\right) & \text{if } |G| \leq \varepsilon, \\ 1 & \text{if } G < \varepsilon, \end{cases} \tag{7.19}$$

where

$$\varepsilon = \mathcal{A}\,\mathrm{d}x, \tag{7.20}$$

with $\mathcal{A}$ being within the region of 2 (an exact value of 2 has been used for the current implementation). The S-field is evaluated at every artificial time step using the definition from [132]

$$S = \frac{G}{\sqrt{G^2 + |\nabla G|^2 + \mathrm{d}x^2}}. \tag{7.21}$$

Numerical Implementation of $|\nabla G|$

Re-initialising will be one of the most computationally expensive steps in the addition to the IAMR algorithm, as $|\nabla G|$ needs to be calculated for every real time step and artificial time step. The quicker $|\nabla G|$ reaches steady state the less artificial time steps are required, thus a balance between accuracy and compute speed needs to be found.

$|\nabla G|$ is spatially discretised using a second order ENO finite difference scheme adopted for two phase flow, as in [147, 121, 120] for example.

$$|\nabla G|_{i,j,k} \simeq \begin{cases} \sqrt{\max\left(\left(\mathcal{A}^-\right)^2, \left(\mathcal{B}^+\right)^2\right) + \max\left(\left(\mathcal{C}^-\right)^2, \left(\mathcal{D}^+\right)^2\right) + \max\left(\left(\mathcal{E}^-\right)^2, \left(\mathcal{F}^+\right)^2\right)} & \text{if } G \geq 0, \\ \sqrt{\max\left(\left(\mathcal{A}^+\right)^2, \left(\mathcal{B}^-\right)^2\right) + \max\left(\left(\mathcal{C}^+\right)^2, \left(\mathcal{D}^-\right)^2\right) + \max\left(\left(\mathcal{E}^+\right)^2, \left(\mathcal{F}^-\right)^2\right)} & \text{if } G < 0. \end{cases} \tag{7.22}$$

$\mathcal{A}^{\pm}, \mathcal{B}^{\pm}, \mathcal{C}^{\pm}, \mathcal{D}^{\pm}, \mathcal{E}^{\pm}$ and $\mathcal{F}^{\pm}$ are the one-sided ENO finite differences in the x, y and z directions respectively. Where

$$\mathcal{A}^+ = \frac{G_{i+2,j,k} - G_{i+1,j,k}}{\Delta x} - \frac{\Delta x}{2}\text{minmod}(D_{i+1,j,k}, D_{i+2,j,k}), \tag{7.23}$$

$$\mathcal{A}^- = \frac{G_{i+1,j,k} - G_{i,j,k}}{\Delta x} - \frac{\Delta x}{2}\text{minmod}(D_{i,j,k}, D_{i+1,j,k}), \tag{7.24}$$

$$\mathcal{B}^+ = \frac{G_{i,j,k} - G_{i-1,j,k}}{\Delta x} - \frac{\Delta x}{2}\text{minmod}(D_{i,j,k}, D_{i-1,j,k}), \tag{7.25}$$

$$\mathcal{B}^- = \frac{G_{i-1,j,k} - G_{i-2,j,k}}{\Delta x} - \frac{\Delta x}{2}\text{minmod}(D_{i-1,j,k}, D_{i-2,j,k}), \tag{7.26}$$

which is repeated for all spatial dimensions. The one-sided finite differences can then be approximated using a central difference approximation

$$D_{i,j,k} = \frac{G_{i-1,j,k} - 2G_{i,j,k} + G_{i+1}}{\Delta x^2}. \tag{7.27}$$

Note that the minmod function gives the smallest absolute value when both $D_{i,j,k}$ and $D_{i+1,j,k}$ have the same sign and zero when they have different signs. Again, this is repeated for the other values.

The re-initialisation equation (equation (7.17)) is temporally discretised using a first order forward time approach

$$G^{\tau}_{i,j,k} = G_{i,j,k} - \tau S_{i,j,k}\left(|\nabla G_{i,j,k}| - 1\right), \tag{7.28}$$

which is repeated until $|\nabla G_{i,j,k}| = 1$ is near the flame surface. This approach was used for its simplicity, however it is unlikely to be optimal. For example, other approaches suggest using a second order Runge-Kutta method ([120]).

Table 7.1: Simulation conditions with a fixed reactant reactant conditions are $\phi = 0.4$, T =300 K, p=1 atm, with a modified fuel Lewis numbers.

$\mathrm{Le_F}$	ω_2	s_L (m/s)	ℓ_L (μm)	s_F (m/s)	ℓ_F (μm)
0.35	8.17	0.225	587	0.368	512
0.7	−3.34	0.335	466	0.349	486
1	−11.4	0.392	430	0.392	455
2	−34.9	0.488	386	0.487	410

7.2.4 Algorithm

7.3 Test Simulation Conditions

To verify the feasibility of the proposed method and to verify the implementation of the algorithm into IAMR, test simulation cases have been conducted in both the new level-set simulation code and PeleLM. A range of reactant conditions will be conducted in PeleLM and compared directly with the results from the level-set. The test reactant conditions are the same as the fixed fuel Lewis number study from Chapter 6 and are presented in table 7.1. The pressure, temperature and equivalence ratio is fixed at 1 atm, 300 K and 0.4 respectively, and the fuel Lewis number ($\mathrm{Le_F}$) is artificially modified to $0.35, 0.7, 1$ and 2. Simulations will be conducted firstly as effective 1-dimensional flat flames, then 2-dimensional freely-propagating flames with an initial perturbation to produce both TD-instabilities and DL-instabilities. The resolution of PeleLM will be well resolved at 16 cells across the thermal thickness. The level-set will modify the s_loc model to represent the different cases.

7.4 Effective 1-dimensional Laminar Flames

Firstly, the results from an effective 1-dimensional flame simulated using PeleLM and the level-set are compared. The domain is set up similarly to the turbulent flames, where there is a wall at the bottom of the domain and an outlet at the top of the domain with periodic boundaries on the sides of the domain. The domain is filled with premixed fuel and the flame burns from near the top of the domain to the bottom. This configuration is simple and is used

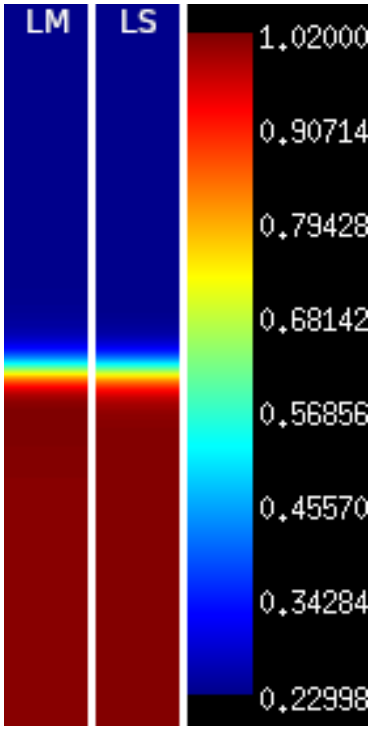

Figure 7.1: A slice of the domain, showing the density coloured by the colour bar (right) for the case $\mathrm{Le_F} = 0.35$. Left (LM) shows the simulation conducted by PeleLM and the center (LS) shows the simulation conducted by the level-set approach.

to compare the unstretched laminar flame speed (s_L) and the thermodynamic expansion between PeleLM and the level-set. For comparison, the domain size and resolution between the control simulations from PeleLM are the same for the level-set approach. Although the level-set method should be able to make good predictions at a lower resolution than PeleLM, at this stage evaluation of the approach is the priority rather than efficiency.

Figure 7.2 shows a slice of the domain displaying the density. The left slice shows the density as calculated by PeleLM, the center as calculated by the level-set and the right image displays the colour bar. It can be seen that the range of densities is indistinguishable. This is to be expected as the burnt and unburnt density are user provided parameters. The transition between the unburnt and burnt density shows that Equation (7.10) does a good job at smoothing the transition, and closely mimics the real flame. The effect of this specific function is currently unclear in perturbed and turbulent flames.

Figure 7.2 (top) compares the laminar flame speeds as calculated by PeleLM to the level-set

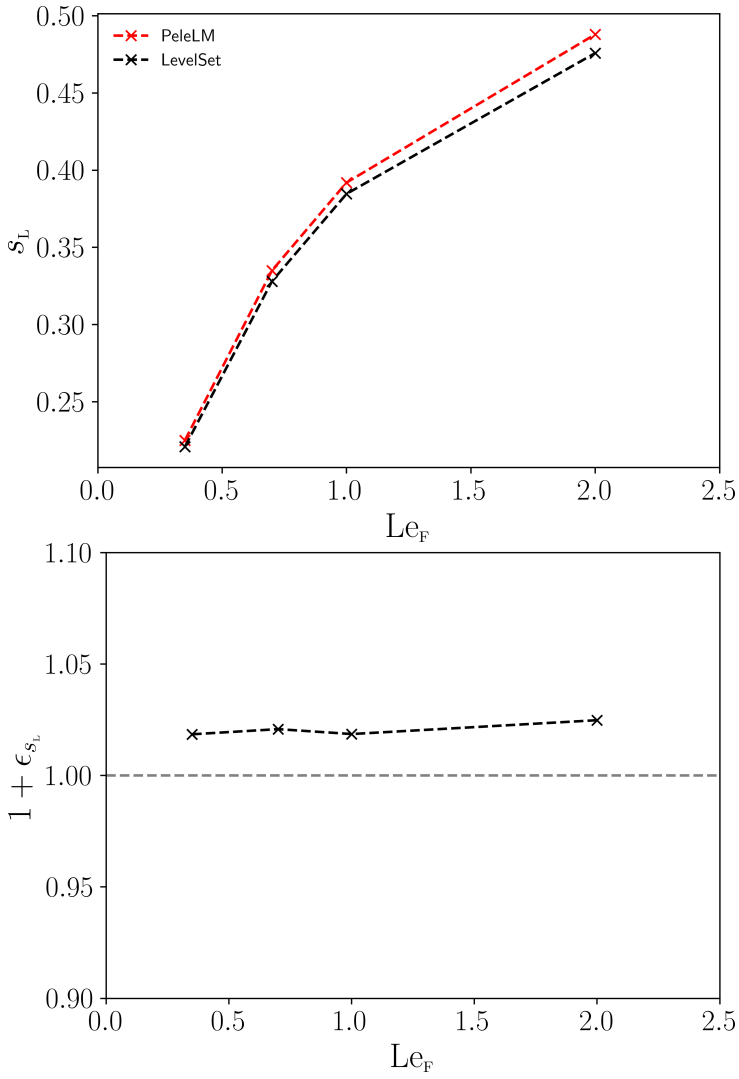

Figure 7.2: Top) A plot comparing the laminar flame speed (s_L) between the simulations conducted in PeleLM (red) to the level-set simulations (black) with for the different cases. Bottom) A plot of the error between the laminar flame speed computed in PeleLM to the laminar flame speed computed by the level-set.

for the different range of conditions. Figure 7.2 (bottom) presents the same data as an error ($\epsilon = ((s_L)_{LS} - s_L)/s_L$). It can be seen that the flame speeds are all similar with a small but constant error between the PeleLM and level set. This error is satisfactory and results from a large time step (or equivalently a large grid size). For multi-dimensional turbulent flames the time-step will be much smaller, thus this error is expected to become less significant. It should be noted that this issue is mitigated in level-set methods that use the fastmarching method, however as explained previously, is not appropriate for negative Markstein number flames.

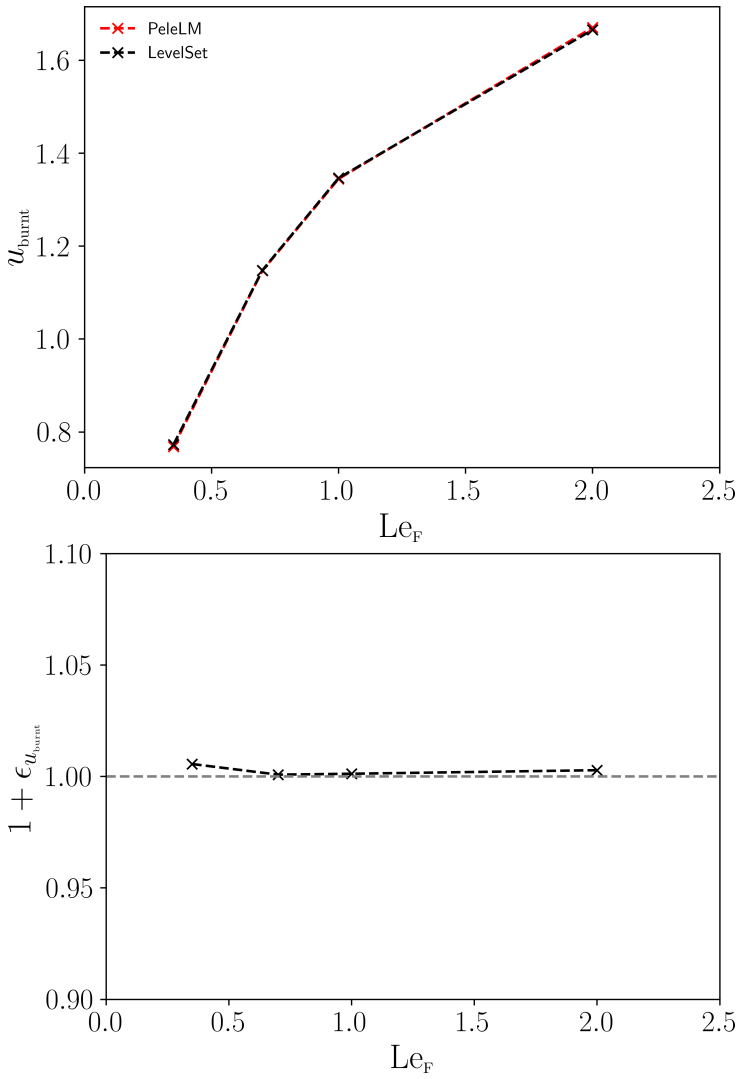

Figure 7.3: Top) A plot comparing the exhaust velocity between the simulations conducted in PeleLM (red) to the level-set simulations (black) for the different cases. (Bottom) A plot of the error between the exhaust velocity computed in PeleLM to the laminar exhaust velocity computed by the level-set.

Figure 7.3 (top) compares the exhaust velocity between the simulations conducted by PeleLM and the level-set. It can be seen that the results are very similar, indicating that the divergence of the velocity is being appropriately computed. Figure 7.3 (bottom) presents the results as an error, again, further demonstrating the similarity between the results.

7.5 2-Dimensional Freely Propagating Flames

Figure 7.4 presents 2-dimensional slices of the progress variable from the freely-propagating simulations conducted using PeleLM (top) and the level-set (bottom). For the PeleLM cases the fuel Lewis number is artificially modified to $\mathrm{Le}_{\mathrm{F}} = 0.35$ (left) and $\mathrm{Le}_{\mathrm{F}} = 1$ (right). The corresponding level-set simulations have an adjusted Markstein model to represent the expected flame behaviour from the corresponding fuel Lewis number. Note that the model used was an informed judgement to demonstrate feasibility, rather than to be proposed. Investigation into exact models for different cases is ongoing. Without turbulence, the fuel Lewis number cases of $0.7, 1$ and 2 are TD-stable and show only Darrious-Landau instabilities are present, so only $\mathrm{Le}_{\mathrm{F}} = 0.35$ and 1 are presented.

Starting with the TD-stable case, from PeleLM (top right) there is clearly a DL-instability resulting in a single perturbation. It can be seen that this behaviour is nicely reproduced by the level-set (bottom right), where there is also a DL-instability. The height of the perturbation is slightly higher which is likely the result of both the time the slice was taken (these perturbations are somewhat transient) and the exact Markstein number used (0.2). Figure 7.4 (right) demonstrates that the proposed method captures DL-instabilities well. Further investigations and validations into the behavior of the DL-instability, such as dispersion relations, will be the focus of future work.

For the TD-unstable case, from PeleLM (top left) there is a clear TD-instability with a typical flame finger like those observed in [36]; note the finger is quite constrained by the domain size. The level-set (bottom left) shows a similar flame structure, with a leading point with strong positive curvature and followed by a large trailing region and trailing point. Visually comparing PeleLM to the level-set, the global features are similar with leading and trailing regions formed with a similar visual height of the instability. However, there are still some key differences, namely the level-set does not produce the negatively curved regions separating in the leading points, as you see with PeleLM. This is likely the result of hydrogen being depleted in this region, which results in a drop in flame speed; there is no hydrogen in the level-set therefore species depletion cannot be replaced. Secondly, in the flat flame regions with only small positive curvatures, in PeleLM this region is smooth without any small perturbations, for

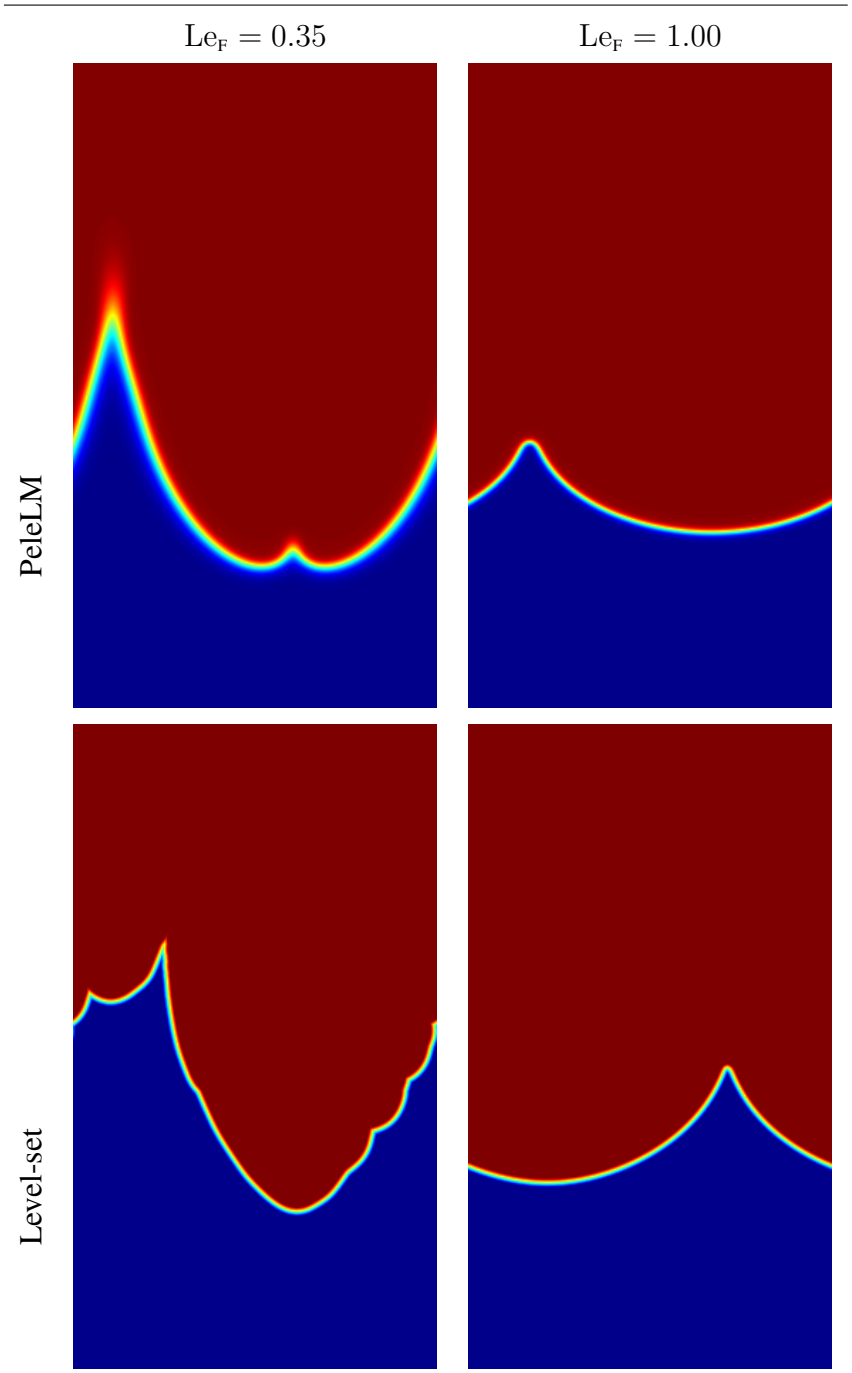

Figure 7.4: 2-dimensional slices of progress variable (H_2) from freely propagating simulations conducted by PeleLM (top) and 2-dimensional slices of progress variable (function of G) for the level-set (bottom). The fuel Lewis number is artificially modified to $\mathrm{Le_F} = 0.35$ (left) and $\mathrm{Le_F} = 1$ (right). For the level-set the Markstein model is adjusted to represent the change in fuel Lewis number. Note that without turbulence the fuel Lewis number cases of $0.7, 1$ and 2 are TD-stable and show only Darrious-Landau instabilities are present so only $\mathrm{Le_F} = 0.35$ and 1 are presented.

the level-set there are some small perturbations. It is currently unclear the origin of this behaviour and is currently under investigation. Please note that the Markstein model used for the level-set is only an approximation of the PeleLM flame, and will be improved upon in the future. The presented comparison exists only to demonstrate feasibility of the methods ability to simulate negative Markstein number flames rather than to get a precise reproduction of the PeleLM flame.

7.6 Computational Cost

The primary reason for proposing the level-set is for reducing computational cost. To compare the costs a benchmark simulation was made in PeleLM for a $\mathrm{Le}_{\mathrm{F}} = 1$ flame experiencing DL-instability for both 16 and 8 computational cells across the thermal thickness. The simulations were conducted on a local workstation with 16 MPI tasks. The computational cost was calculated as the ratio of the real world time to complete the simulation to the time simulated. The same simulation was then repeated using the level-set method for different resolutions ($16, 8, 4, 2$ and 1). All the level-set simulations were run for the same length of simulated time and domain size to ensure a fair comparison.

Figure 7.5 compares the relative computational cost from the level-set simulation. Each computational cost is normalised by the cost of the simulation from PeleLM. The dotted black line represents the cost to compute in PeleLM for 16 computational cells across the thermal thickness (such as those conducted in Chapter 4 and 5). The dotted grey line represents the cost to compute for PeleLM for 8 computational cells. The red dotted lines represent the computational cost for the same simulation using the level-set approach.

It can be seen that there is significant reduction in computational cost when using the level-set. At the same resolution, level-set is about 16 times faster. However unlike PeleLM, the level-set does not require the resolution to resolve the chemistry of the flame, just the surface, therefore the resolution is likely to be able to be significantly reduced. How far the resolution can be reduced is still under investigation, but preliminary results suggest 2 to 4 computational cells across a flame thickness should be sufficient thus could be 800 to 3000 times faster. This would allow for increased domain sizes of 30 to 60 times larger (assuming the domain height

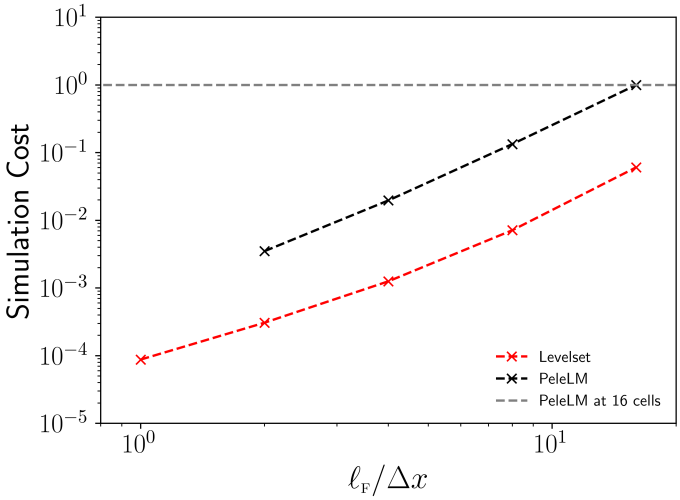

Figure 7.5: Relative computational cost to conduct a 2-dimensional freely propagating flame using the level-set approach when compared to PeleLM.

is unchanged).

As explained, this chapter is focused only on potential capabilities, thus significant further investigations into the methods used and the impact on the results, both for DT-stable and unstable flames which are both freely-propagating and turbulent, is required. Also the re-initialisation frequency and number of artificial steps have not been fully investigated and are likely to provide additional cost savings when optimised. Also it is likely that turbulence will be the limiting factor for the resolution of the level-set. It therefore may not be possible to lower the resolution to 2 to 4 computational cells across a flame thickness, especially in high turbulence.

7.7 Conclusions

The current chapter has proposed a DNS-style level-set approach which can be used for TD-stable, neutral and unstable flames, where the flame surface and turbulence are well resolved but the chemistry is modelled using a curvature based Markstein model. This approach yields similar flame responses but at a fraction of computational cost, allowing for larger simulations where large scale effects can be studied (a clear limitation in Chapters 4 5 and 6). The proposed method and algorithm is implemented into IAMR and a feasibility study

has been conducted. Using a variety of conditions with increasing fuel Lewis numbers, effective 1-dimensional and freely-propagating flames have been analysed.

Starting with the effective 1-dimensional simulations, it was found that both the flame speed and the velocity acceleration due to the modelled density jump has been well captured by the level-set, with exact values all very similar to a real DNS simulation using PeleLM. Next the expected behaviour of freely propagating flames was observed; the stable flames and neutral flames where Darrious-Landau instabilities were clearly visible and visually well represented. However a more detailed analysis and validation procedure is underway.

Throughout this chapter, important decisions have been made that will have measurable impacts of both computational complexity and cost, as well as simulation accuracy. This chapter has presented the required equation set and demonstrated the feasibility and capabilities of such an approach. However the numerical implementation requires review with respect to the optimal configuration, namely the re-initialisation equation. Decisions such as using a spatially second order and temporally first order scheme may not result in the optimal result. Other works have used higher order schemes ([151] for example). Additionally, the frequency of re-initialisation and number of artificial time steps are essential for optimal performance. The values chosen in this chapter were liberal to ensure the correct functioning of the algorithm at the expense of computational cost. The gradients calculated for density in Equation (7.11) and curvature were first order accurate for simplicity, but it is likely that higher order methods may yield better results (such as a the method used to calculated curvature in [63]). The thickness of the density transition is also likely to influence the range of curvatures that can be achieved by the flame. This is likely to become important for turbulent flames, therefore more work on the correct value is required. The current recommendation of $2\mathrm{d}x$ is unlikely to be sufficient.

This chapter has demonstrated that using a DNS-style level-set approach has the potential to be used for simulating TD-unstable hydrogen flames at significantly reduced computation cost with a limited reduction in simulation accuracy. This chapter has formed the foundation of ongoing and future work to further implement and optimise the algorithm to be used for TD-unstable turbulent hydrogen flames at larger scales.

Chapter 8. Conclusions

Hydrogen combustion is a promising substitute for carbon emitting traditional fuels for transport, heating and re-electrification [177]. This thesis makes a significant contribution to our understanding of the underlying physics of hydrogen and necessary modification of the models used to develop hydrogen combustors which will help to facilitate future global adoption [161].
This project utilised direct numerical simulations with detailed chemistry focused on the fundamental behaviour of lean thermodiffusively-unstable hydrogen flames with a specific emphasis on the turbulent flame speed, and modelling of the turbulent flame speed, for device scale internal combustion engines. The problem was divided into increasingly more complicated flames, starting with laminar freely-propagating flames, then turbulent flames with a fixed turbulent lenghtscale and finally turbulent flames at a varying turbulent lengthscale.

8.1 Freely-Propagating Flames

Following [80], as in 2-dimensions, it was found that an instability parameter ω_2 has good predictive capabilities for the expected TD-instability over a broad range of reactant conditions for 3-dimensional freely-propagating flames. An empirical scaling model (equations (4.1) and (4.2)) was proposed and shown to have good predictive capabilities to capture the freely-propagating flame speed and thermal thickness of the presented conditions. The model could be calculated cost-effectively from a 1-dimensional unstretched flame, eliminating the need for expensive 3-dimensional freely-propagating DNS. This model was shown later to be a key component to calculating both the mean local flame speed and thickness for turbulent flames and the turbulent flame speed model.

A curvature-based model was proposed to explore the local flame response to the TD-instability. It was found that a curvature-only model with a Markstein number of -2.5 captures the local flame speed response to curvature over a broad range of conditions, although the range of curvatures and local flame speeds observed were somewhat pressure dependence. It was found that using a stretch based model with both single and independent Markstein

numbers, did yield improvement over the curvature-based model, however no correlation between the Markstein numbers and reactant conditions were found.

The flame surface structure was also analysed and principle curvature zones were constructed to divide the TD-unstable structure into six zones; leading point, leading edge, flat flame, saddle point, trailing edge and trailing point. It was found that as the flame became more TD-unstable the flame structure transitions from a flat flame to more leading edge and point.

It was found that at zero curvature, the local flame speed was still higher than the unstretched laminar flame speed, which was unexpected when using the existing fuel and heat focusing argument. A thermal leading point concept was proposed where the leading point and edges of the flame have strong positive curvature thus experience preferential diffusion, resulting in super adiabatic temperatures. The higher temperatures then diffuse into flat flame regions enhancing the local flame speed without fuel focusing.

8.2 Turbulent Flames - Fixed Lengthscale

Turbulent flames were then studied, where a broad range of reactant and turbulent conditions at a fixed relative integral length scale were presented. The turbulence was characterised by the freely-propagating characteristic values which were shown to correctly characterise the flames (Figure 5.2).

It was found that turbulence exaggerates the TD-response, which increases the mean local flame speed above both unstretched laminar, and freely propagating speeds. It was shown that the mean local flame speed and thermal thickness was well characterised by $\sqrt{\mathrm{Ka_F}}$ for all TD-unstable turbulent and reactant conditions, provided the freely-propagating values have been accounted for. A model for mean local flame speed and thermal thickness was proposed (Equations (5.1) and (5.2)) which was shown to have good predictive capabilities over a wide range of conditions. This model required measured freely-propagating flame speed and thickness values, thus an additional model was presented (Equations (5.4) and (5.5)) which combined the proposed model with the freely-propagating model previously proposed. The combined model had good predictive capabilities over the broad range of conditions, but with

more scatter than the model with the measured characteristics.

A curvature-based model was proposed to explore the TD-response to turbulence for local flame speed. Similarly to the freely-propagating flames, the curvature-only model with a Markstein number of -2.2 captures the range of reactant and turbulent conditions well, provided the flame speed enhancement due to both reactant and turbulent conditions has been accounted for. It was found that turbulence enhances the TD-instability, resulting in a larger range of curvatures and flame speed, but the Markstein number remains largely unchanged. This was not found to be the case for strain-rate, where at lower pressure little correlation was found where there was a large range local flame speed, under a narrow band of strain-rate. Stretch with single and independent Markstein numbers was found to yield an improvement over curvature-only, however again no clear Markstein numbers captured the range of conditions well.

The flame surface structure was analysed again using principle curvature zones. It was found that turbulence transitioned the flame from a predominately flat flame to leading edges and points for low pressure cases. It was found that more TD-unstable flames that already had a high proportion of leading edges and points did not experience much of an increase in leading edges and points. This suggests that there is a limit to how much leading edges and points, and increasing turbulence, can yield more leading edges and points, possibly due to a domain size constrainment effect, which is revisited later.

Lastly it was shown that the local flame speed at zero curvature, was higher than both the unstretched laminar and freely-propagating flame speed. The thermal leading point concept was revisited where it was proposed that turbulence generates stronger leading points with a stronger curvature resulting in stronger preferential diffusion, and thus even higher temperatures diffusing into flat flame regions.

8.3 Turbulent Flames - Length Scale Effects

The turbulent study was then extended to a range of turbulent integral length scales. It was found that the mean local flame speed was unaffected by the integral length scale, concluding

that the previously proposed model for mean local flame speed was appropriate and independent of integral length scale effects. This reduces the turbulent flame speed model to a flame surface area.

This found that the local flame speed response to curvature was also independent of integral length scale, and dependent on the Karlovitz number. It was demonstrated that the local flame response scales with Karlovitz number independent of length scale and that using the root mean square of the velocity fluctuation is not appropriate for comparing the local effects in TD-unstable lean hydrogen flames.

The effect of turbulence on the flame surface wrinkling was studied. It was found that the flame surface area (presented as a wrinkling factor) increases with both turbulent intensity and integral length scale which adhered well to Damköhler's small scale limit. Peters model appeared to have good predictive capabilities for wrinkling factor for flames with Lewis numbers at and below 1. It was shown that it was important to account for the increase in mean local flame speed due to the TD-response to reactant conditions and turbulence by adjusting the prefactor in traditional turbulence flame speed models by using the model previously presented (Equations (5.4) and (5.5)).

8.4 Well Resolved G-equation

A limitation of DNS with chemistry is the significant limit to the size of the domain, and therefore limits to the range of Damköhler numbers that can be studied. To mitigate this, a well-resolved surface-tracking approach has been implemented and, by applying the local curvature based model proposed in Chapter 5, should be appropriate for laminar, freely-propagating and turbulent TD-unstable flames. The resulting method reduces computational expense by about three orders of magnitude. This could then be used to explore larger domains and Damköhler numbers. Preliminary results have been presented and show that the method is capable, although is the focus of ongoing work.

8.5 Vectis

Throughout this work, Realis Simulation have implemented these suggested models into Vectis, which has yielded promising results by comparing the presented models simulated at a device scale and real world internal combustion engines. The work conducted was published by Hernandez *et al.* [79].

8.6 Future Work and Concluding Remarks

The work undertaken throughout this thesis has revealed clear trends and behaviours of TD-unstable flames. Models with good predictive capabilities have been proposed and implemented into existing device scale simulation codes. Despite these findings, the project has also generated many more questions that require future study.

Thermal leading points have been proposed as an explanation for the zero curvature local flame speed enhancement, however the evidence supplied does not demonstrate causality. The relationship between local flame speed and stretch is still unclear. Recent works in pre-print from Im and Chaudhuri [82] continue to look for evidence.

ω_2 has proven to be a good parameter for predicting the expected level of instability, however other parameters appear to also have good predictive capabilities such as a Zeldovitch number and Peclet number ratio (see [145] for example). Further investigation into comparing other instability factors should be the focus of future work.

A clear limitation of DNS has been the small range of length scales which can be studied. As shown in Chapter 6, the turbulent flame speed (more specifically the flame surface wrinkling) is sensitive to the integral length scale. It is currently unclear at what scale the flame surface wrinkling becomes independent of integral length scale, therefore larger simulations are required. Planned future work will use the well-resolved G-equation approach to achieve these scales.

Lastly all of the conditions studied have been conducted using a flame-in-a-box approach. Future work could focus on real-world-combustor configurations, evaluate where the

limitations of the flame-in-a-box lie and what statistics can successfully be translated to real-world-combustors.

Chapter 9. Bibliography

[1] *PeleLM Documentation, Version 2018.10.* "https://amrex-combustion.github.io/PeleLM/manual/html/".

[2] *Realis Simulation VECTIS VSOLVE User Manual, Version 2022.3.*

[3] R Abdel-Gayed and D Bradley. A two-eddy theory of premixed turbulent flame propagation. *Philosophical transactions of the royal society of London. Series A, Mathematical and physical sciences*, 301(1457):1–25, 1981.

[4] A Almgren, J Bell, P Colella, L Howell, and M Welcome. A conservative adaptive projection method for the variable density incompressible navier–stokes equations. *Journal of Computational Physics*, 142(1):1–46, 1998.

[5] C Altantzis, C Frouzakis, A Tomboulides, and K Boulouchos. Direct numerical simulation of circular expanding premixed flames in a lean quiescent hydrogen-air mixture: Phenomenology and detailed flame front analysis. *Combustion and flame*, 162(2):331–344, 2015.

[6] C Altantzis, C Frouzakis, A Tomboulides, S Kerkemeier, and K Boulouchos. Detailed numerical simulations of intrinsically unstable two-dimensional planar lean premixed hydrogen/air flames. *Proceedings of the combustion institute*, 33(1):1261–1268, 2011.

[7] C Altantzis, C Frouzakis, A Tomboulides, M Matalon, and K Boulouchos. Hydrodynamic and thermodiffusive instability effects on the evolution of laminar planar lean premixed hydrogen flames. *Journal of fluid mechanics*, 700:329–361, 2012.

[8] A Amato, M Day, R Cheng, J Bell, and T Lieuwen. Leading edge statistics of turbulent, lean, h2–air flames. *Proceedings of the Combustion Institute*, 35(2):1313–1320, 2015.

[9] M Anand and S Pope. Calculations of premixed turbulent flames by pdf methods. *Combustion and Flame*, 67(2):127–142, 1987.

[10] J Anderson. *Fundamentals of Aerodynamics*. McGraw-Hill Education, 2016.

[11] N Armaroli and V Balzani. The legacy of fossil fuels. *Chemistry–An Asian Journal*, 6(3):768–784, 2011.

[12] A Aspden. Distributed burning in chemical and thermonuclear flames. In *25th International Colloquium on the Dynamics of Explosions and Reactive Systems*, 2015.

[13] A Aspden. A numerical study of diffusive effects in turbulent lean premixed hydrogen flames. *Proceedings of the Combustion Institute*, 36:1997–2004, 2017.

[14] A Aspden, J Bell, M Day, and F Egolfopoulos. Turbulence-flame interactions in lean premixed dodecane flames. *Proceedings of the Combustion Institute*, 36:2005–2016, 2017.

[15] A Aspden, J Bell, M Day, S Woosley, and M Zingale. Turbulence-flame interactions in type ia supernovae. *The Astrophysical Journal*, 689(2):1173, 2008.

[16] A Aspden, J Bell, M Day, S Woosley, and M Zingale. Turbulence-Flame Interactions in Type Ia Supernovae. *The Astrophysical Journal*, 689:1173–1185, December 2008.

[17] A. Aspden, J Bell, and S Woosley. Distributed flames in type Ia supernovae. *The Astrophysical Journal*, 710(2):1654, 2010.

[18] A Aspden, M Day, and J Bell. Characterization of low Lewis number flames. *Proceedings of the Combustion Institute*, 33(1):1463–1471, 2011.

[19] A Aspden, M Day, and J Bell. Lewis number effects in distributed flames. *Proceedings of the Combustion Institute*, 33(1):1473–1480, 2011.

[20] A Aspden, M Day, and J Bell. Turbulence–flame interactions in lean premixed hydrogen: transition to the distributed burning regime. *Journal of Fluid mechanics*, 680:287–320, 2011.

[21] A Aspden, M Day, and J Bell. Turbulence-chemistry interaction in lean premixed hydrogen combustion. *Proceedings of the Combustion Institute*, 35(2):1321–1329, 2015.

[22] A Aspden, M Day, and J Bell. Towards the distributed burning regime in turbulent premixed flames. *Journal of Fluid Mechanics*, 871:1–21, 2019.

[23] A Aspden, N Nikiforakis, S Dalziel, and J Bell. Analysis of implicit les methods. *Communications in Applied Mathematics and Computational Science*, 3(1):101, 2008.

[24] D Ballal and A Lefebvre. The structure and propagation of turbulent flames. *Proceedings of the Royal Society of London. A. Mathematical and Physical Sciences*, 344(1637):217–234, 1975.

[25] C Balos, D Gardner, Carol S Woodward, and D Reynolds. Enabling gpu accelerated computing in the sundials time integration library. *Parallel Computing*, 108:102836, 2021.

[26] D Barnes. Effective solutions for rural electrification in developing countries: Lessons from successful programs. *Current Opinion in Environmental Sustainability*, 3(4):260–264, 2011.

[27] G Batchelor. *An Introduction to Fluid Mechanics*. Cambridge University Press, 1967.

[28] M Baum, T Poinsot, D Haworth, and N Darabiha. Direct numerical simulation of h2/o2/n2 flames with complex chemistry in two-dimensional turbulent flows. *Journal of Fluid Mechanics*, 281:1–32, 1994.

[29] J Bechtold and M Matalon. The dependence of the markstein length on stoichiometry. *Combustion and flame*, 127(1-2):1906–1913, 2001.

[30] J Bell, R Cheng, M Day, and I Shepherd. Numerical simulation of lewis number effects on lean premixed turbulent flames. *Proceedings of the Combustion Institute*, 31(1):1309–1317, 2007.

[31] J Bell, M Day, J Grcar, and M Lijewski. Active control for statistically stationary turbulent premixed flame simulations. *Communications in Applied Mathematics and Computational Science*, 1(1):29–51, 2007.

[32] J Bell, M Day, and M Lijewski. Simulation of nitrogen emissions in a premixed hydrogen flame stabilized on a low swirl burner. *Proceedings of the Combustion Institute*, 34(1):1173–1182, 2013.

[33] J Bell, M Day, I Shepherd, M Johnson, R Cheng, J Grcar, V Beckner, and M Lijewski. Numerical simulation of a laboratory-scale turbulent v-flame. *Proceedings of the National Academy of Sciences*, 102(29):10006–10011, 2005.

[34] L Berger, A Attili, and H Pitsch. Intrinsic instabilities in premixed hydrogen flames: Parametric variation of pressure, equivalence ratio, and temperature. part 1-dispersion relations in the linear regime. *Combustion and Flame*, 240:111935, 2022.

[35] L Berger, A Attili, and H Pitsch. Intrinsic instabilities in premixed hydrogen flames: parametric variation of pressure, equivalence ratio, and temperature. part 2–non-linear regime and flame speed enhancement. *Combustion and Flame*, 240:111936, 2022.

[36] L Berger, K Kleinheinz, A Attili, and H Pitsch. Characteristic patterns of thermodiffusively unstable premixed lean hydrogen flames. *Proceedings of the Combustion Institute*, 37(2):1879–1886, 2019.

[37] T Boningari and P Smirniotis. Impact of nitrogen oxides on the environment and human health: Mn-based materials for the nox abatement. *Current Opinion in Chemical Engineering*, 13:133–141, 2016.

[38] R Borghi. *On the Structure and Morphology of Turbulent Premixed Flames*. 1985.

[39] R Borghi. On the structure and morphology of turbulent premixed flames. In *Recent Advances in the Aerospace Sciences: In Honor of Luigi Crocco on His Seventy-fifth Birthday*, pages 117–138. Springer, 1985.

[40] R Borghi, M Destriau, and G De Soete. *Combustion and Flames, Chemical and physical principles*. Editions Technip, Paris, 1998.

[41] P Bradshaw. *An Introduction to Turbulence and its Measurement*. Pergamon Press, 1971.

[42] K Bray. Turbulent transport in flames. *Proceedings: Mathematical and Physical Sciences*, 451(1941):231–256, 1995.

[43] K Bray, P Libby, and J Moss. Unified modeling approach for premixed turbulent combustion—part i: General formulation. *Combustion and flame*, 61(1):87–102, 1985.

[44] K Bray and J Moss. A unified statistical model of the premixed turbulent flame. *Acta Astronautica*, 4(3-4):291–319, 1977.

[45] E Burke, F Güthe, and R Monaghan. A comparison of turbulent flame speed correlations for hydrocarbon fuels at elevated pressures. In *Turbo Expo: Power for Land, Sea, and Air*, volume 49767, page V04BT04A043. American Society of Mechanical Engineers, 2016.

[46] M Burke, M Chaos, Y Ju, F Dryer, and S Klippenstein. Comprehensive h2/o2 kinetic model for high-pressure combustion. *International Journal of Chemical Kinetics*, 44(7):444–474, 2012.

[47] R Cant, S Pope, and K Bray. Modelling of flamelet surface-to-volume ratio in turbulent premixed combustion. In *Symposium (International) on Combustion*, volume 23, pages 809–815. Elsevier, 1991.

[48] R Cant, S Pope, and K Bray. Modelling of flamelet surface-to-volume ratio in turbulent premixed combustion. In *Symposium (International) on Combustion*, volume 23, pages 809–815. Elsevier, 1991.

[49] N Chakraborty and R Cant. Effects of lewis number on scalar transport in turbulent premixed flames. *Physics of Fluids*, 21(3), 2009.

[50] N Chakraborty and R Cant. Effects of lewis number on flame surface density transport in turbulent premixed combustion. *Combustion and Flame*, 158(9):1768–1787, 2011.

[51] N Chakraborty, M Klein, and N Swaminathan. Effects of lewis number on the reactive scalar gradient alignment with local strain rate in turbulent premixed flames. *Proceedings of the Combustion Institute*, 32(1):1409–1417, 2009.

[52] J Chen and H Im. Stretch effects on the burning velocity of turbulent premixed hydrogen/air flames. *Proceedings of the combustion institute*, 28(1):211–218, 2000.

[53] P Clavin and J Graña-Otero. Curved and stretched flames: the two markstein numbers. *Journal of fluid mechanics*, 686:187–217, 2011.

[54] P Clavin and F Williams. Effects of molecular diffusion and of thermal expansion on the structure and dynamics of premixed flames in turbulent flows of large scale and low intensity. *Journal of Fluid Mechanics*, 116:251–282, 1982.

[55] G Damköhler. Der einfluss der turbulenz auf die flammengeschwindigkeit in gasgemischen. *Zeitschrift für Elektrochemie und angewandte physikalische Chemie*, 46(11):601–626, 1940.

[56] G Darrieus. Propagation d'un front de flamme. *La Technique Moderne*, 30:18, 1938.

[57] P Davidson. *Turbulence: an introduction for scientists and engineers*. Oxford university press, 2015.

[58] M Day and J Bell. Numerical simulation of laminar reacting flows with complex chemistry. *Combustion Theory and Modelling*, 4(4):535–556, 2000.

[59] M Day, J Bell, P Bremer, V Pascucci, V Beckner, and M Lijewski. Turbulence effects on cellular burning structures in lean premixed hydrogen flames. *Combustion and Flame*, 156(5):1035–1045, 2009.

[60] M Day, J Bell, X Gao, and P Glarborg. Numerical simulation of nitrogen oxide formation in lean premixed turbulent H2/O2/N2 flames. *Proceedings of the Combustion Institute*, 33(1):1591–1599, 2011.

[61] M Day, S Tachibana, J Bell, M Lijewski, V Beckner, and R Cheng. A combined computational and experimental characterization of lean premixed turbulent low swirl laboratory flames ii. hydrogen flames. *Combustion and Flame*, 162(5):2148–2165, 2015.

[62] J Driscoll. Turbulent premixed combustion: Flamelet structure and its effect on turbulent burning velocities. *Progress in Energy and Combustion Science*, 34(1):91–134, 2008.

[63] A Du, C Min, and F Gibou. Second-order accurate computation of curvatures in a level set framework using novel high-order reinitialization schemes. *Journal of Scientific Computing*, 35:114–131, 2008.

[64] D Dunn-Rankin. *Lean combustion: technology and control*. Academic Press, 2011.

[65] L Esclapez, M Day, J Bell, A Felden, C Gilet, R Grout, M Frahan, E Motheau, A Nonaka, L Owen, B Perry, J Rood, N Wimer, and W Zhang. Pelelmex: an amr low mach number reactive flow simulation code without level sub-cycling. *Journal of Open Source Software*, 8(90):5450, 2023.

[66] T Falkenstein, S Kang, L Cai, M Bode, and H Pitsch. Dns study of the global heat release rate during early flame kernel development under engine conditions. *Combustion and Flame*, 213:455–466, 2020.

[67] A Favre. Statistical equations of turbulent gases. *Problems of hydrodynamics and continuum mechanics*, pages 231–266, 1969.

[68] D Fernández-Galisteo, V N Kurdyumov, and P Ronney. Analysis of premixed flame propagation between two closely-spaced parallel plates. *Combustion and Flame*, 190:133–145, 2018.

[69] S Firoz. A review: advantages and disadvantages of biodiesel. *International Research Journal of Engineering and Technology*, 4(11):530–533, 2017.

[70] C Frouzakis, N Fogla, A Tomboulides, C Altantzis, and M Matalon. Numerical study of unstable hydrogen/air flames: Shape and propagation speed. *Proceedings of the combustion institute*, 35(1):1087–1095, 2015.

[71] R Goldman. Curvature formulas for implicit curves and surfaces. *Computer Aided Geometric Design*, 33(7):632–658, 2005.

[72] D Goodwin, H Moffat, I Schoegl, R Speth, and B Weber. Cantera: An object-oriented software toolkit for chemical kinetics, thermodynamics, and transport processes. https://www.cantera.org, 2023. Version 3.0.0.

[73] S Gordon. *Computer program for calculation of complex chemical equilibrium compositions, rocket performance, incident and reflected shocks, and Chapman-Jouguet detonations*, volume 273. Scientific and Technical Information Office, National Aeronautics and Space . . . , 1976.

[74] F Gouldin. An application of fractals to modeling premixed turbulent flames. *Combustion and flame*, 68(3):249–266, 1987.

[75] F Grinstein, L Margolin, and W Rider. *Implicit Large Eddy Simulation: Computing Turbulent Fluid Dynamics*. Cambridge University Press, 2007.

[76] Ö Gülder. Turbulent premixed flame propagation models for different combustion regimes. In *Symposium (International) on Combustion*, volume 23, pages 743–750. Elsevier, 1991.

[77] D Haworth and T Poinsot. Numerical simulations of lewis number effects in turbulent premixed flames. *Journal of fluid mechanics*, 244:405–436, 1992.

[78] B Helenbrook and C Law. The role of landau-darrieus instability in large scale flows. *Combustion and Flame*, 117(1-2):155–169, 1999.

[79] I Hernandez, C d'Auzay, R Penning, E Shapiro, and J Hughes. Thermo-diffusive flame speed adjustment and its application to hydrogen engines. Technical report, SAE Technical Paper, 2023.

[80] T Howarth and A Aspden. An empirical characteristic scaling model for freely-propagating lean premixed hydrogen flames. *Combustion and Flame*, 237:111805, 2022.

[81] T Howarth, M Day, P Pitsch, and A Aspden. Thermal diffusion, exhaust gas recirculation and blending effects on lean premixed hydrogen flames. *Proceedings of the Combustion Institute*, 40(1):105429, 2024.

[82] H Im and S Chaudhuri. How" mixing" affects propagation and structure of intensely turbulent, lean, hydrogen-air premixed flames. *arXiv preprint arXiv:2405.17197*, 2024.

[83] H Im and J Chen. Preferential diffusion effects on the burning rate of interacting turbulent premixed hydrogen-air flames. *Combustion and flame*, 131(3):246–258, 2002.

[84] R Iyer, J Kelly, and A Elgowainy. Vehicle-cycle and life-cycle analysis of medium-duty and heavy-duty trucks in the united states. *Science of the Total Environment*, 5:766–790, 2023.

[85] S Kadowaki, T Aung, T Furuyama, K Kawata, T Katsumi, and H Kobayashi. Effects of pressure and heat loss on the unstable motion of cellular-flame fronts caused by intrinsic instability in hydrogen-air lean premixed flames. *Journal of Thermal Science and Technology*, 16(2):JTST0021–JTST0021, 2021.

[86] B Karlovitz, D Denniston, D Knapschaefer, and F Wells. Studies on turbulent flames: A. flame propagation across velocity gradients b. turbulence measurement in flames. In *Symposium (international) on combustion*, volume 4, pages 613–620. Elsevier, 1953.

[87] M Katragadda, N Chakraborty, and R Cant. A priori assessment of algebraic flame surface density models in the context of large eddy simulation for nonunity lewis number flames in the thin reaction zones regime. *Journal of Combustion*, 2012(1):794671, 2012.

[88] M Katsuki, Y Mizutani, T Yasuda, Y Kurosawa, K Kobayashi, and T Takahashi. The effect of initial conditions on the propagation of a premixed flame in a mixing layer. *Combustion and flame*, 74(1):9–18, 1988.

[89] R Kee, J Warnatz, and J Miller. Fortran computer-code package for the evaluation of gas-phase viscosities, conductivities, and diffusion coefficients.[chemkin]. Technical report, Sandia National Labs., Livermore, CA (USA), 1983.

[90] A Klimov. Premixed turbulent flames-interplay of hydrodynamic and chemical phenomena. *Flames, lasers, and reactive systems*, pages 133–146, 1983.

[91] H Kobayashi. Experimental study of high-pressure turbulent premixed flames. *Experimental thermal and fluid science*, 26(2-4):375–387, 2002.

[92] A Kolmogorov. Dissipation of energy in the locally isotropic turbulence. *Dokl. Ajad. Nauk. SSSR*, 1941.

[93] A Kolmogorov. Local structure of turbulence in an incompressible liquid for very large reynolds numbers. *Dokl. Ajad. Nauk. SSSR*, 1941.

[94] A Kolmogorov. (a) the local structure of turbulence in incompressible viscous fluid for very large reynolds numbers, and (b) dissipation of energy in the locally isotropic turbulence. *Royyal Society of London Proceedings Series*, 1991.

[95] G Lagioia, MP Spinelli, and V Amicarelli. Blue and green hydrogen energy to meet european union decarbonisation objectives. an overview of perspectives and the current state of affairs. *International Journal of Hydrogen Energy*, 48(4):1304–1322, 2023.

[96] L Landau. On the theory of slow combustion. *Acta Physicochim*, 1944.

[97] P Lapenna, L Berger, and F Creta. Hydrogen laminar flames. In *Hydrogen for Future Thermal Engines*, pages 93–140. Springer, 2023.

[98] S Lapointe and G Blanquart. Fuel and chemistry effects in high Karlovitz premixed turbulent flames. *Combustion and Flame*, 167:294–307, 2016.

[99] S Lapointe, B Savard, and G Blanquart. Differential diffusion effects, distributed burning, and local extinctions in high Karlovitz premixed flames. *Combustion and Flame*, 162(9):3341–3355, 2015.

[100] C Law. *Combustion Physics*. Cambridge University Press, 2006.

[101] C Law and C Sung. Structure, aerodynamics, and geometry of premixed flamelets. *Progress in energy and combustion science*, 26(4-6):459–505, 2000.

[102] H Lee, A Abdelsamie, P Dai, M Wan, and A Lipatnikov. Influence of equivalence ratio on turbulent burning velocity and extreme fuel consumption rate in lean hydrogen-air turbulent flames. *Fuel*, 327:124969, 2022.

[103] H Lee, P Dai, M Wan, and A Lipatnikov. Influence of molecular transport on burning rate and conditioned species concentrations in highly turbulent premixed flames. *Journal of Fluid Mechanics*, 928:A5, 2021.

[104] H Lee, P Dai, M Wan, and A Lipatnikov. A dns study of extreme and leading points in lean hydrogen-air turbulent flames–part i: local thermochemical structure and reaction rates. *Combustion and Flame*, 235:111716, 2022.

[105] H Lee, P Dai, M Wan, and A Lipatnikov. A dns study of extreme and leading points in lean hydrogen-air turbulent flames-part ii: Local velocity field and flame topology. *Combustion and Flame*, 235:111712, 2022.

[106] H Lee, P Dai, M Wan, and A Lipatnikov. Lewis number and preferential diffusion effects in lean hydrogen–air highly turbulent flames. *Physics of Fluids*, 34(3), 2022.

[107] H Lee, P Dai, M Wan, and A Lipatnikov. A numerical support of leading point concept. *International Journal of Hydrogen Energy*, 47(55):23444–23461, 2022.

[108] A Lipatnikov. *Fundamentals of Premixed Turbulent Combustion*. CRC Press, 2012.

[109] A Lipatnikov and J Chomiak. Turbulent flame speed and thickness: phenomenology, evaluation, and application in multi-dimensional simulations. *Progress in Energy and Combustion Science*, 28(1):1–74, 2002.

[110] C Liu, S Shy, M Peng, C Chiu, and Y Dong. High-pressure burning velocities measurements for centrally-ignited premixed methane/air flames interacting with intense near-isotropic turbulence at constant reynolds numbers. *Combustion and Flame*, 159(8):2608–2619, 2012.

[111] Z Lu and Y Yang. Modeling pressure effects on the turbulent burning velocity for lean hydrogen/air premixed combustion. *Proceedings of the Combustion Institute*, 38(2):2901–2908, 2021.

[112] Z Lu and Y Yang. Modeling of the turbulent burning velocity for planar and bunsen flames over a wide range of conditions. *Acta Mechanica Sinica*, 38(3):121504, 2022.

[113] A Majda and J Sethian. The derivation and numerical solution of the equations for zero mach number combustion. *Combustion science and technology*, 42(3-4):185–205, 1985.

[114] T Mantel and R Borghi. A new model of premixed wrinkled flame propagation based on a scalar dissipation equation. *Combustion and flame*, 96(4):443–457, 1994.

[115] G Markstein. *Nonsteady Flame Propagation*. Pergamon Press, 1964.

[116] M Matalon. On flame stretch. *Combustion science and technology*, 31(3-4):169–181, 1983.

[117] M Matalon. The darrieus–landau instability of premixed flames. *Fluid Dynamics Research*, 50(5):051412, 2018.

[118] M Matalon, C Cui, and J Bechtold. Hydrodynamic theory of premixed flames: effects of stoichiometry, variable transport coefficients and arbitrary reaction orders. *Journal of fluid mechanics*, 487:179–210, 2003.

[119] M Matalon and B Matkowsky. Flames as gasdynamic discontinuities. *Journal of Fluid Mechanics*, 124:239–259, 1982.

[120] C Min. On reinitializing level set functions. *Journal of computational physics*, 229(8):2764–2772, 2010.

[121] C Min and F Gibou. A second order accurate level set method on non-graded adaptive cartesian grids. *Journal of Computational Physics*, 225(1):300–321, 2007.

[122] S Mohan and M Matalon. Numerical methodology for spontaneous wrinkling of centrally ignited premixed flames–linear theory. *Combustion Theory and Modelling*, 25(5):940–967, 2021.

[123] V Mohan, M Herbert, M Klein, and N Chakraborty. A direct numerical simulation assessment of turbulent burning velocity parametrizations for non-unity lewis numbers. *Energies*, 16(6):2590, 2023.

[124] S Muppala, N Aluri, F Dinkelacker, and A Leipertz. Development of an algebraic reaction rate closure for the numerical calculation of turbulent premixed methane,

ethylene, and propane/air flames for pressures up to 1.0 mpa. *Combustion and flame*, 140(4):257–266, 2005.

[125] G Nivarti. *The bending effect in turbulent flame propagation*. PhD thesis, Apollo - University of Cambridge Repository, 2017.

[126] A Nonaka, J Bell, M Day, C Gilet, A Almgren, and M Minion. A deferred correction coupling strategy for low mach number flow with complex chemistry. *Combustion Theory and Modelling*, 16(6):1053–1088, 2012.

[127] A Nonaka, M Day, and J Bell. A conservative, thermodynamically consistent numerical approach for low mach number combustion. part i: Single-level integration. *Combustion Theory and Modelling*, 22(1):156–184, 2018.

[128] F Omole, O Olajiga, and T Olatunde. Challenges and successes in rural electrification: a review of global policies and case studies. *Engineering Science & Technology Journal*, 5(3):1031–1046, 2024.

[129] S Osher, R Fedkiw, and K Piechor. Level set methods and dynamic implicit surfaces. 2004.

[130] P Pelce and P Clavin. Influence of hydrodynamics and diffusion upon the stability limits of laminar premixed flames. *Journal of Fluid Mechanics*, 124:219–237, 1982.

[131] R Pember, L Howell, J Bell, P Colella, W Crutchfield, W Fiveland, and J Jessee. An adaptive projection method for unsteady, low-mach number combustion. *Combustion Science and Technology*, 140(1-6):123–168, 1998.

[132] D Peng, B Merriman, S Osher, H Zhao, and M Kang. A pde-based fast local level set method. *Journal of computational physics*, 155(2):410–438, 1999.

[133] N Peters. Laminar flamelet concepts in turbulent combustion. In *Symposium (International) on combustion*, volume 21, pages 1231–1250. Elsevier, 1988.

[134] N Peters. The turbulent burning velocity for large-scale and small-scale turbulence. *Journal of Fluid Mechanics*, 384:107–132, 1999.

[135] N. Peters. *Turbulent Combustion*. Cambridge University Press, 2000.

[136] H Pitsch. Large-eddy simulation of turbulent combustion. *Annual Review of Fluid Mechanics*, 38(1):453–482, 2006.

[137] T Poinsot and D Veynante. *Theoretical and numerical combustion*. RT Edwards, Inc., 2005.

[138] S Pope. The probability approach to the modelling of turbulent reacting flows. *Combustion and Flame*, 27:299–312, 1976.

[139] S Pope. *Turbulent flows*. Cambridge University Press, 2000.

[140] L Prandtl. 7. Bericht über Untersuchungen zur ausgebildeten Turbulenz. *ZAMM-Journal of Applied Mathematics and Mechanics/Zeitschrift für Angewandte Mathematik und Mechanik*, 5(2):136–139, 1925.

[141] Y Rastigejev and M Matalon. Numerical simulation of flames as gas-dynamic discontinuities. *Combustion theory and modelling*, 10(3):459–481, 2006.

[142] R Rehm and H Baum. The equations of motion for thermally driven, buoyant flows. *Journal of research of the National Bureau of Standards*, 83(3):297, 1978.

[143] O Reynolds. An experimental investigation of the circumstances which determine whether the motion of water shall be direct or sinuous, and of the law of resistance in parallel channels. *Philosophical Transactions of the Royal society of London*, (174):935–982, 1883.

[144] L Richardson. *Weather prediction by numerical process*. University Press, 1922.

[145] M Rieth, A Gruber, and J Chen. The effect of pressure on lean premixed hydrogen-air flames. *Combustion and Flame*, 250:112514, 2023.

[146] P Ronney. Some open issues in premixed turbulent combustion. In *Modeling in Combustion Science: Proceedings of the US-Japan Seminar Held in Kapaa, Kauai, Hawaii, 24–29 July 1994*, pages 1–22. Springer, 1995.

[147] G Russo and P Smereka. A remark on computing distance functions. *Journal of computational physics*, 163(1):51–67, 2000.

[148] C Rutland and A Trouvé. Direct simulations of premixed turbulent flames with nonunity lewis numbers. *Combustion and Flame*, 94(1-2):41–57, 1993.

[149] B Savard and G Blanquart. An a priori model for the effective species lewis numbers in premixed turbulent flames. *Combustion and Flame*, 161(6):1547–1557, 2014.

[150] B Savard and G Blanquart. Broken reaction zone and differential diffusion effects in high Karlovitz n-C7H16 premixed turbulent flames. *Combustion and Flame*, 162(5):2020–2033, 2015.

[151] R Saye. High-order methods for computing distances to implicitly defined surfaces. *Communications in Applied Mathematics and Computational Science*, 9(1):107–141, 2014.

[152] J Schlup and G Blanquart. Validation of a mixture-averaged thermal diffusion model for premixed lean hydrogen flames. *Combustion Theory and Modelling*, 22(2):264–290, 2018.

[153] H Schmid, P Habisreuther, and W Leuckel. A model for calculating heat release in premixed turbulent flames. *Combustion and Flame*, 113(1-2):79–91, 1998.

[154] Y Shim, S Tanaka, M Tanahashi, and T Miyauchi. Local structure and fractal characteristics of h2–air turbulent premixed flame. *Proceedings of the Combustion Institute*, 33(1):1455–1462, 2011.

[155] X Shu, Y Guo, W Yang, K Wei, and G Zhu. Life-cycle assessment of the environmental impact of the batteries used in pure electric passenger cars. *Energy Reports*, 7:2302–2315, 2021.

[156] A Skiba, T Wabel, C Carter, S Hammack, J Temme, and J Driscoll. Premixed flames subjected to extreme levels of turbulence part i: Flame structure and a new measured regime diagram. *Combustion and Flame*, 189:407–432, 2018.

[157] D Spalding. Mixing and chemical reaction in steady confined turbulent flames. In *Symposium (International) on combustion*, volume 13, pages 649–657. Elsevier, 1971.

[158] G Stokes. On the effect of the internal friction of fluids on the motion of pendulums. 1851.

[159] M Sussman, A Almgren, J Bell, P Colella, L Howell, and M Welcome. An adaptive level set approach for incompressible two-phase flows. *Journal of Computational Physics*, 148(1):81–124, 1999.

[160] M Sussman, P Smereka, and S Osher. A level set approach for computing solutions to incompressible two-phase flow. *Journal of Computational physics*, 114(1):146–159, 1994.

[161] E Tingas. *Hydrogen for Future Thermal Engines*. Springer, 2023.

[162] C Towery, A Poludnenko, J Urzay, J O'Brien, M Ihme, and P Hamlington. Spectral kinetic energy transfer in turbulent premixed reacting flows. *Physical Review E*, 93(5):053115, 2016.

[163] A Trouvé and T Poinsot. The evolution equation for the flame surface density in turbulent premixed combustion. *Journal of Fluid Mechanics*, 278:1–31, 1994.

[164] L Tseng, M Ismail, and G Faeth. Laminar burning velocities and markstein numbers of hydrocarbon-air flames. *Combustion and Flame*, 95(4):410–426, 1993.

[165] H Uranakara, S Chaudhuri, H Da e, P Arias, and H Im. A flame particle tracking analysis of turbulence–chemistry interaction in hydrogen–air premixed flames. *Combustion and Flame*, 163:220–240, 2016.

[166] D Veynante and L Vervisch. Turbulent combustion modeling. *Progress in energy and combustion science*, 28(3):193–266, 2002.

[167] X Wang, T Jin, Y Xie, and K Luo. Pressure effects on flame structures and chemical pathways for lean premixed turbulent h2/air flames: Three-dimensional dns studies. *Fuel*, 215:320–329, 2018.

[168] J Warnatz. Influence of transport models and boundary conditions on flame structure. In *Numerical Methods in Laminar Flame Propagation: A GAMM-Workshop*, pages 87–111. Springer, 1982.

[169] X Wen, L Berger, L Cai, A Parente, and H Pitsch. Thermodiffusively unstable laminar hydrogen flame in a sufficiently large 3d computational domain–part i: Characteristic patterns. *Combustion and Flame*, page 113278, 2023.

[170] X Wen, T Zirwes, A Scholtissek, H Böttler, F Zhang, H Bockhorn, and C Hasse. Flame structure analysis and composition space modeling of thermodiffusively unstable premixed hydrogen flames—part i: Atmospheric pressure. *Combustion and Flame*, 238:111815, 2022.

[171] D Wilcox. *Turbulence modeling for CFD*, volume 2. DCW industries La Canada, CA, 1998.

[172] F Williams. A review of some theoretical considerations of turbulent flame structure. In *AGARD Conference Proceeding, 1975*, 1975.

[173] F Williams. *Combustion theory*. CRC Press, 2018.

[174] M Yao and G Blanquart. Isolating effects of large and small scale turbulence on thermodiffusively unstable premixed hydrogen flames. *arXiv preprint arXiv:2311.18131*, 2023.

[175] A Yapicioglu and I Dincer. A review on clean ammonia as a potential fuel for power generators. *Renewable and sustainable energy reviews*, 103:96–108, 2019.

[176] P Yeung and S Pope. Lagrangian statistics from direct numerical simulations of isotropic turbulence. *Journal of Fluid Mechanics*, 207:531–586, 1989.

[177] M Yue, H Lambert, E Pahon, R Roche, S Jemei, and D Hissel. Hydrogen energy systems: A critical review of technologies, applications, trends and challenges. *Renewable and Sustainable Energy Reviews*, 146:111180, 2021.

[178] I Zeldovich, G Barenblatt, V Librovich, and G Makhviladze. Mathematical theory of combustion and explosions. 1985.

[179] Y Zeldovich and D Frank-Kamenetzkii. The theory of thermal propagation of flames. *Russian Journal of Physical Chemistry*, (12):100–105, 1938.

[180] W Zhang, A Almgren, V Beckner, J Bell, J Blaschke, C Chan, M Day, B Friesen, K Gott, D Graves, M Katz, A Myers, T Nguyen, A Nonaka, M Rosso, S Williams, and M Zingale. Amrex: a framework for block-structured adaptive mesh refinement. *Journal of Open Source*, 4(37):1370, 2019.

[181] W Zhang, A Myers, K Gott, K Almgren, and J Bell. Amrex: Block-structured adaptive mesh refinement for multiphysics applications. *The International Journal of High Performance Computing Applications*, 35(6):508–526, 2021.

[182] Z Zhou, F Hernández-Pérez, Y Shoshin, J van Oijen, and L de Goey. Effect of soret diffusion on lean hydrogen/air flames at normal and elevated pressure and temperature. *Combustion Theory and Modelling*, 21(5):879–896, 2017.

[183] V Zimont. Theory of turbulent combustion of a homogeneous fuel mixture at high reynolds numbers. *Combustion, Explosion and Shock Waves*, 15:305–311, 1979.

[184] V Zimont. Gas premixed combustion at high turbulence. turbulent flame closure combustion model. *Experimental thermal and fluid science*, 21(1-3):179–186, 2000.

[185] V Zimont and A Sabelnikov. Criteria for combustion rate in a turbulent flow of a combustible mixture. *Abstracts of presentations on the All-Union school-conference on combustion theory*, 1975.

[186] V Zimont and V Sabelnikov. Abstracts of presentations on the all-union school-conference on combustion theory. *Abstracts of presentations on the All-Union school-conference on combustion theory*, 1975.